ABSTRACT

Title of dissertation:	Phase Tracking Methods for X-ray Pulsar-Based Spacecraft Navigation
	Kevin Anderson, Doctor of Philosophy, 2021
Dissertation directed by:	Professor Darryll J. Pines Department of Aerospace Engineering

X-ray pulsars are potential aids to spacecraft navigation due to the periodicity, uniqueness, and stability of their signals. As the load on the deep space network increases in the future, techniques to navigate with less frequent communication will become desirable. Improved methods of x-ray pulsar-based spacecraft navigation (XNAV) are developed, analyzed, and confirmed over multiple simulated scenarios. A phase-tracking algorithm modeled at the level of individual photon arrivals provides improvements over the current state of the art, and a novel phase maximum likelihood estimator (MLE) is proposed. Relaxing the constant signal frequency assumption with a second-order Taylor polynomial phase model and feedback of frequency and frequency derivative from a third-order digital phase-locked loop is shown to overcome previous phase tracking difficulties due to low flux with millisecond period pulsars (MSPs), which have the best navigation characteristics.

Empirical MLE tests are performed to determine threshold observation times for convergence to the Cramer-Rao Bound. A lower limit is identified due to Poisson statistics and an upper limit due to orbit dynamic stress. For a 1 m^2 detector, one second for the Crab pulsar and 4000 seconds for the lowest flux MSPs are required. An analytical method is presented to predict the necessary threshold observation times for signals with pulse widths under 0.15 cycles.

Simulations are performed for dynamic stress conditions including two heliocentric trajectories, a cislunar trajectory, and three Earth orbits. The Crab pulsar and four MSPs: B1821-24, B1937+21, J0218+4232, and J0437-4715 are investigated. Position errors of 2 to 7 km are shown for most of the MSPs along the interplanetary and cislunar trajectories. B1821-24 tracks on the Earth orbits with 1 – 2 m^2 detectors with 2.5 – 3.5 km error. B1937+21 and J0218+4232 require larger detector areas.

An extended Kalman filter combines multiple pulsar phase tracking range measurements for various observation schedules. Scenarios with one and three detectors are considered. Position error under 3 km is demonstrated for an interplanetary trajectory. Phase tracking shows great promise for deep space navigation and more limited potential in scenarios with greater orbital dynamics.

Phase Tracking Methods for X-ray Pulsar-Based Spacecraft Navigation

by

Kevin Anderson

Dissertation submitted to the Faculty of the Graduate School of the University of Maryland, College Park in partial fulfillment of the requirements for the degree of Doctor of Philosophy
2021

Advisory Committee:
Professor Darryll J. Pines, Chair/Advisor
Professor Derek A. Paley
Professor Robert M. Sanner
Professor Raymond J. Sedwick
Professor Wojciech Czaja

Acknowledgments

I would like to acknowledge some of the people who generously contributed their time, kindness, patience, and expertise throughout my time as a Ph.D. student.

To Dr. Suneel Sheikh for his unwavering support, availability, and willingness to chat about x-ray pulsar research throughout the years. Your guidance and mentorship was invaluable in completing this process.

To the current and former employees at ASTER Labs Inc. including Chuck Hisamoto, Pat Doyle, and Isaac Allen for their work on developing the XPRESS software and making it available for my use. Also for help over the course of my research with different areas such as orbit modeling.

To my undergraduate researchers Arjun Argawal and Thomas Bain for all their help and hard work and particularly for their help with characterizing x-ray detector types and accelerometers for spacecraft.

To the entire NASA Goddard NICER and SEXTANT teams for their willingness to let me use their laboratory equipment and include me in meetings on the SEXTANT mission before launch, and particularly, to Dr. Keith Gendreau, Dr. Jason Mitchell, Dr. Luke Winternitz, and Dr. Munther Hassouneh for all their help and sharing of their time.

To Sheron Williams and Danica Lovelace for all their time and help in securing regular meetings with Dr. Pines even when scheduling was tight.

To my undergraduate research adviser Dr. Demoz Gebre-Egziabher for inspiring me to go onto graduate school.

To all my friends in the Montgomery County Road Runners Club, particularly Rodney Rivera and Kelly Dunston, for providing a social outlet through an isolating process.

To my committee: Dr. Derek Paley, Dr. Robert Sanner, Dr. Ray Sedwick, and Dr. Wojciech Czaja for your help and guidance through my graduate school years. Also to Dr. Sean Humbert who started as a member of my committee before leaving the University of Maryland.

To my research mentor Dr. Darryll Pines for all of his support and encouragement throughout the years. It was always an honor and joy to work with you.

And lastly to my family including my Mom, Dad, and brother Ryan for their love and support though the years. In particular, to my partner Jayna Resman, without whom I could not have completed this process, for all your patience, support, and love.

Table of Contents

List of Tables

List of Figures

List of Abbreviations

ARE	Admiralty Research Establishment
ARGOS	Advanced Research and Global Observation Satellite
APSR	Accretion-powered Pulsar
AU	Astronomical Unit
CAST	China Academy of Space Technology
CLT	Central Limit Theorem
DARPA	Defense Advanced Research Projects Agency
DoD	US Department of Defense
ΔDOR	Delta Differential One-Way Range
DPLL	Digital Phase Locked Loop
EKF	Extended Kalman Filter
ESA	European Space Agency
GEO	Geostationary Equatorial Orbit
GLINT	Gamma-ray source Localization-Induced Navigation and Timing
GNSS	Global Navigation Satellite System
GPS	Global Positioning System
GRID	Gamma Ray Incidence Detector
GSFC	Goddard Spaceflight Center
GXLT	Goddard X-Ray Laboratory Testbed
HASP	High Altitude Student Platform
HAXDT	High Altitude X-ray Detector Testbed Payload
HTPC	High Time-resolution Photon Counter
ICRF	International Celestial Reference Frame
IMU	Inertial Measurement Unit
ISS	International Space Station
JPL	Jet Propulsion Laboratory
LEO	Low Earth Orbit
LOS	Line-of-Sight
MLE	Maximum Likelihood Estimator
MSL	Mars Science Laboratory
MSP	Millisecond Period Pulsar
MXS	Modulated X-Ray Source
NCO	Numerically Controlled Oscillator
NHPP	Non-Homogeneous Poisson Process
NICER	Neutron-star Interior Composition ExploreR
NRL	Naval Research Lab
RMS	Root Mean Square
RPSR	Rotation-powered Pulsar
RXTE	Rossi Timing Explorer
SBIR	Small Business Innovations Research
SDD	Silicon Drift Detector
SEXTANT	Station Explorer for X-ray Timing and Navigation Technology
SDD	Silicon Drift Detector
SNR	Signal-to-Noise Ratio

SOCRATES	Signal of Opportunity CubeSat for Ranging and Timing Experiments
SSB	Solar System Barycenter
TCB	Barycentric Coordinate Time
TDB	Barycentric Dynamic Time
TDRS	Tracking and Data Relay Satellite
TOA	Time-of-Arrival
TSXS	Timing-Resolved Soft X-ray Spectrometer
VLBI	Very Long Baseline Interferometer
XDET	Time-Tagging X-Ray Detector
XDPG	X-Ray Digital Pulse Generator
XNAV	X-ray pulsar-based Navigation
XPNAV-1	X-ray Pulsar Navigation-I Satellite
XRC	X-ray Concentrator Optics

Chapter 1: Introduction

1.1 Motivation

For navigation on Earth and for spacecraft in low Earth orbit, the Global Positioning System (GPS) provides accurate and reliable position and velocity estimates. Many spacecraft missions are planned for beyond the orbit of the GPS satellites and into interplanetary space. Current deep space navigation methods are greatly reliant on Earth-based processing and on mission specific relative position estimates using imaging of target objects. Increased load on Earth communication systems for navigation and a more generally applicable navigation system that is not mission dependent are reasons to look for new ways to leverage spacecraft instruments to solve for position measurements.

X-ray pulsars have shown many desirable characteristics for navigation. They have periodic, reliable signals from which time and position measurements can be made. Drawbacks exist, though. Their low fluxes of X-ray output and low signal-to-noise (SNR) ratios need to be overcome by any system hoping to leverage stable X-ray pulsar signals as navigational aids. Previous research has demonstrated the feasibility of X-ray pulsar-based navigation. Recent developments in X-ray detector technologies and analyses of pulsar signal modeling and parameter estimation have moved the use of variable X-ray sources for spacecraft navigation from an interesting potential idea to a future reality.

The weak signals of X-ray pulsars create the need for methods that work with lower flux in order to extend their uses to a wider range of pulsars. Algorithms for position estimation that extract the signals from the noise over shorter observations than previous methods and that extend to some of the most desirable low flux X-ray pulsars are investigated in this dissertation.

1.2 History of Spacecraft Navigation

The different types of spacecraft navigation for various missions can be described as orbit determination, orbit propagation, and orbit navigation [1]. Orbit determination is the process of estimating a spacecraft orbit using repeated observations of the spacecraft from ground-based stations. The set of measurements are combined together to generate the best possible estimate the spacecraft's state dynamics. Orbit propagation is the process of propagating forward in time the spacecraft's state dynamics using models of the forces acting on the spacecraft. The state dynamics are numerically integrated to give an estimate of position and velocity. Orbit navigation is the process of determining the spacecraft's state parameters using external sensors and blending the data together. The navigation state includes time, position, velocity, acceleration, attitude, and attitude rate. The navigation solution is calculated autonomously on the spacecraft with its sensors. X-ray pulsar-based navigation falls in the category of orbit navigation. X-ray detectors will be used to incorporate data to help determine the spacecraft's navigation solution. The method of navigation for a spacecraft is chosen based on mission parameters including orbit, science objectives, and tolerance for uncertainty in the navigational state.

Navigation of spacecraft along interplanetary trajectories and Earth orbits is a challenging problem that requires ground-based tracking to correct the estimated state. An analytical solution for the spacecraft trajectory can be studied prior to launch by propagating the model of the vehicle's dynamics, but unmodelled disturbances cause the position error from the planned path to grow over time and become too large for successful guidance and control of the spacecraft. Either orbit determination methods using observations from Earth ground stations or measurements from onboard sensors can be used to correct the navigation solution during the course of the mission [1].

Knowledge of time at a spacecraft is important for operations including performing science mission objectives, determining the location of nearby objects, and communicating with the Earth. A clock with nanosecond accuracy is needed to track radio signals received at a spacecraft from Earth with accuracies of a few tenths of a meter [2]. To maintain the tracking accuracy the clock needs to be stable within one part in 10^{13} [1]. Currently available atomic clocks for spacecraft applications are typically accurate within one part in $10^9 - 10^{15}$ per day [1].

Attitude determination for a spacecraft is needed to keep the payload instruments targeted properly. This is essential for performing the science objectives of a mission and for many of the navigation sensors that determine position as well as keeping a line of communication open to Earth-based ground stations. Various types of sensors are available to solve for a vehicle's attitude and attitude rate. Gyroscopes on a spacecraft can provide an estimate of the rate of rotation relative to an inertial frame. Earth-orbiting spacecraft can use magnetometers that measure the magnetic field or Earth horizon sensors that can orient a satellite to an Earth frame of reference [1]. For spacecraft throughout the solar system, sun sensors, star cameras, and star trackers can be used to leverage celestial objects for attitude determination. This is possible because on short time scales the vast distance of the stars allow a spacecraft to use the star positions as a fixed background to determine attitude and attitude rate.

When it comes to position determination, various types of sensors have been developed to support a spacecraft's navigation system. There have been methods that were developed to use fixed intensity celestial sources. The relative position of a spacecraft to a known object can be deduced from starlight during the instance of occultation, when a known celestial body passes in front of a star [3]. If a spacecraft is near a celestial body with an atmosphere, the spacecraft's range to the body can be estimated using the refraction of starlight as a stellar object passes behind the local bodies atmosphere [4]. These methods are limited to when a spacecraft is near a celestial body that has sufficiently well-known properties.

Most space vehicle operations to date have relied primarily on Earth-based navigation solutions [2, 5, 6]. Radar range and optical tracking methods have been the most popular means for tracking and maintaining continuous spacecraft orbit determination [1, 6–8]. Radar range systems compute a spacecraft's position by computing the range and range-rate to the spacecraft along the radial direction from the tracking station. The primary method for doing this relies on the spacecraft reflecting signals transmitted from an Earth observing station and measuring the round-trip time [1]. Accuracies on the order of a few meters in range and fractions of mm/s in range-rate are achievable, but the error in the other two axes is much larger [5]. The Vikings spacecraft missions to Mars achieved position accuracies under 50 km [2] and subsequent missions have improved these accuracies greatly. Processing multiple radar measurements over time allows the spacecraft's orbital elements to be computed.

The position solution of a spacecraft can be propagated ahead in time using orbital mechanics and the knowledge of the solar system's gravitational potential field and any other disturbing forces such as atmospheric drag. The propagated orbit determination solution is compared over time with the processed radar measurements to correct for errors and keeps the orbit solution within the missions required parameters [1].

There are many sources of error that effect the radar ranging process. The radar system requires precise knowledge of each observation station's position on the Earth, which requires extensive surveys of each antenna [1, 5]. The uncertainty in the knowledge of the solar system ephemeris data also affects the measurement. Each new spacecraft fly-by improves the knowledge of the ephemeris data of the target celestial object. An unavoidable error in the position estimate grows as the distance from the Earth observation stations increases. The transmitted radar beam and the reflected signal travel in a cone of uncertainty, which degrades the position estimate along the transverse direction as a linear function of distance [1].

Active transmitters can be used by spacecraft for orbit determination to improve the range and range-rate measurement accuracies [5]. The radial velocity of the spacecraft is measured by measuring the Doppler frequency shift of the transmitted signal. The observation station sends a ping to the spacecraft and the active transmitter is used to re-transmit the signal back to Earth. Transverse axes errors still exist as well as the growth in error due to distance from Earth [1].

Deep space navigation solutions for the past sixty years have primarily been provided by the NASA Deep Space Network (DSN) [10]. The DSN produces precise spacecraft range and range-rate data that can be used to compute position and velocity solutions. The system consists of three ground stations, placed roughly 120°apart, at Goldstone California, USA, Madrid, Spain and Canberra, Australia [9]. Each ground station is a tracking station and data processing center that provides telecommunication and orbit determination of deep space vehicles. The DSN started in 1957 to support initial Earth satellite monitoring and has expanded to become the primary deep space communications and navigation system [10]. The DSN has been used to support U.S. and international missions to all of the solar system planetary bodies and beyond to as far as the heliopause [11]. The primary purpose of the DSN is to provide two-way communication and data transfer between the Earth and a spacecraft [10].

Multiple techniques have been designed to use the DSN to track signals from spacecraft and use these to compute range, range-rate, and angular position [12,13]. This includes one-way, two-way, and three-way tracking techniques, where three-way tracking uses different ground stations for the uplink and downlink. Interferometry is used to combine the signals received at two of the ranging stations to improve the range accuracy.

Using Very Long Baseline Interferometery (VLBI) techniques can provide high accuracy for the angular position measurements [14]. VLBI uses observations by antennas with well known relative locations to simultaneously track the downlink signal from a spacecraft. The differential time delay between the stations gives an measurement of the relative angle between the tracking stations and the planar radio wave arriving from the spacecraft [10, 14]. Further improvements to the spacecraft angular position measurements can be provided by simultaneously observing a secondary radio source, typically a quasar, that is at a known position in the sky. The systematic errors in the DSN can be effectively removed by looking at the difference between the differential one-way range to the spacecraft and the known radio source [12]. This is called a delta differential one-way range (ΔDOR) measurement and it mitigates a large portion of the off-axis errors perpendicular to the line-of-sight to the spacecraft [10]. The newest techniques allow the DSN to provide position and velocity solutions with about 2 nrad of angular measurement error or 0.3 km of position error per astronomical unit (AU) of distance from the Earth [10, 15].

The DSN provides accurate radial position, but it requires extensive ground operations and scheduling of observations. The availability of the tracking stations might become an issue as the number of missions supported increases. It has been suggested that the load on the DSN could be reduced by augmenting its solution with additional measurements provided by other means of navigation [10].

Optical tracking measurements can be produced in a similar way to radar ranging to provide estimates of spacecraft position and orbit determination [7]. Optical tracking determines the position of a spacecraft by reflecting visible light off of the vehicle. Optical measurements are limited by weather and other environmental conditions [1]. Some optical systems rely on comparing pictures of the spacecraft to the fixed background of stars. This type of system struggles to provide real-time measurements due to th extensive human processing required [1].

When a spacecraft's mission includes investigating a known planetary body then imaging of the target can provide augmentation to the spacecraft navigation system. Video imaging of an investigated planet can be used to determine an estimate of the position of the spacecraft relative to the target body by comparing the images to known parameters of the target such as diameter and orientation with respect to other objects [3]. If the mission requires orbiting the target body then this relative position information is sufficient to support the science mission objectives. The absolute position can be determined by combining the relative position with the high accuracy of the position estimate of the planetary object from solar system dynamics.

The cost of vehicle operations continually increases especially for constellations of multiple spacecraft and formations of small satellites. This promotes the desire for methods of autonomous operation of a navigation system and decreased reliance on Earth-based solutions [4, 16]. This requires using onboard sensors to allow the spacecraft to compute internally its navigation and guidance information [1]. Even if not completely independent, a reduction of the labor-intensive portions of vehicle control is desirable.

1.2.1 Current Spacecraft Navigation State of the Art

The current state of the art for spacecraft navigation varies depending on the type of orbit and the mission parameters. There are different primarily used methods for Earth orbits and interplanetary/deep space trajectories. For vehicles operating in Earth orbit the Global Positioning System (GPS) can provide a complete navigation solution including: reference time, position, velocity, attitude, and attitude rate [18, 19]. For higher altitude Earth orbits the GPS navigation solution starts to degrade and then becomes unavailable. Also malfunction or interference might interrupt GPS service. For deep space missions, a combination of Earth-based radar ranging and imaging of a target planet are used to form accurate navigation solutions. These methods require human interpretation of the data and ground-based processing.

Many current techniques for Earth orbit and deep space navigation are summarized in Table 1.1 and 1.2 including pros and cons of each method [1]. This table includes state of the art methods and newer concepts with the potential for use in navigation. Detailed overviews of each method of navigation can be found in [6], [17], and [20]. The last column in Table 1.2 compares the level of position estimate accuracy that is achievable by each method.

There are a range of drawbacks to the listed navigation methods included restrictions on their applicability. The operating range for each method is listed in Table 1.2. Some of the techniques are only applicable for spacecraft in Earth orbits. Using the GPS and the NASA Tracking and Data Relay Satellite (TDRS) system is only available for a spacecraft operating in low Earth orbit (LEO) up to just below the orbit of the GPS satellites themselves. These systems each have high accuracy. The GPS provides the possibility for an autonomous full navigation solution. The TDRS tracking system generates a navigation solution using the same hardware the spacecraft uses to communicate data back to the Earth, but it requires ground-based processing. The TDRS tracking system is mainly used for NASA spacecraft. Both the GPS and the TDRS systems require system maintenance. [1]

Some of the methods listed in Table 1.2 only provide attitude and angular rate measurements, but they are included for completeness. In particular, the use of inertial measurement units (IMUs) and star sensors or star trackers provide only attitude measurements and not position. IMUs require an external aid to maintain stability, but they are usable on spacecraft throughout the solar system and provide estimates of angular rate and acceleration. Star sensors and trackers use instruments that are already in a spacecraft's payload for science purposes and leverages them for attitude measurements, but these instruments are relatively high cost. [1]

Some of the methods listed in Table 1.1 are newer concepts that are potentially autonomous, but their applicability is dependent on celestial geometry. These methods are relatively untested on spacecraft missions. These techniques include a star/moon sextant, a Sun, Earth, and Moon observer, and stellar refraction. The star/moon sextant is an instrument that could provide autonomous attitude and position measurements, but it requires fairly heavy hardware with high power usage. It requires being near a celestial body with a moon. A Sun, Earth, and Moon observer could provide autonomous attitude and position measurements for a spacecraft operating in the Earth-Moon system. It uses existing attitude sensing hardware, but the convergence and accuracy of the position measurements depends of the geometry of the Sun, Earth, and Moon. Stellar refraction also could provide autonomous attitude and position measurements using existing attitude sensing hardware, but it requires the spacecraft to be near a celestial body with an atmosphere with known parameters. [1]

The traditional approach for spacecraft position tracking has been ground-based radiometric tracking and the DSN in particular for deep space trajectories. This method is well established and uses mature spacecraft technologies. These methods are applicable as long as the spacecraft is covered by the ground stations and is scheduled for regular communications. Radiometric tracking techniques require extensive Earth-based processing and the accuracy of position estimates decrease as the distance from the Earth increases, particular in the off axis dimensions [10]. A standard method for supplementing the DSN navigation solution is to use optical navigation with imaging of a target body. This leverages science hardware already on the spacecraft and provides high accuracy. Drawbacks of target body imaging include needing the spacecraft to be near a celestial body that has a known, detailed model and the need for ground processing of the images.

There has been recent research into using onboard cameras to aid in autonomous navigation. When far enough away from a planet to view the full limb, the apparent edge against the dark sky background, measurements of the center and diameter of the planet can provide a relative line of sight and distance measurement [20,21]. This can be performed with any planetary body of known dimensions. When close enough to distinguish surface features with an onboard camera, these can be compared to an database of known features for use in navigation [20, 22]. Also, vision navigation algorithms are being investigated for space applications [23, 24].

Table 1.1: Pros and Cons for Methods of Deep Space and Earth Orbit Navigation [1, 6, 17, 20].

Method	Pros	Cons
GPS	Full navigation solution High accuracy	Only applicable in Earth orbit Requires system maintenance
Target Object Imaging	Uses existing science hardware High accuracy	Only applicable near target Detailed models of target needed Might require ground processing
TDRS Tracking	High Accuracy Same hardware for navigation and sending data	Only Earth orbit and NASA missions Processing on the ground
Inertial Measurement Unit	Widely usable Provides angular rate and acceleration	Only attitude Requires an external aid
DSN / Ground-Based Radiometric Tracking	Traditional approach High accuracy close to Earth	Intensive ground processing Requires system coverage Accuracy decreases with distance from Earth
Star Sensor	Uses instruments already in payload	High cost Only attitude
Star/Moon Sextant	Potentially autonomous	Heavy instrument High power usage Mostly untested
Sun, Earth, & Moon Observer	Uses attitude-sensing hardware Potentially autonomous	Mostly untested Performance depends on geometry
Stellar Refraction	Uses attitude-sensing hardware Potentially autonomous	Mostly untested Requires a star passing behind a nearby object

Table 1.2: Operating Ranges and Accuracy for Methods of Deep Space and Earth Orbit Navigation [1, 6, 17, 20].

Method	Operating Range	Position Measurement Accuracy
GPS	LEO (< GPS)	15 - 100 m (in LEO)
Target Object Imaging	Near Target Object	10 - 100 m
TDRS Tracking	LEO	50 m
Inertial Measurement Unit	LEO to Interplanetary	N/A
DSN / Ground-Based Radiometric Tracking	LEO to Interplanetary	1- 100 km
Star Sensor	LEO to Interplanetary	N/A
Star/Moon Sextant	LEO to GEO	250 m
Sun, Earth, & Moon Observer	LEO to GEO	100 - 400 m (in LEO)
Stellar Refraction	LEO	150 m - 1 km

1.3 Pulsar Science Background

Throughout human history, celestial sources have served as aids for navigation. The majority of the sources used have been stars with steady visible radiation. Variable celestial sources have also been observed over the past few centuries [25]. Edmond Halley published a list in 1715 of all 6 variable stars known at the time [26]. Observations and discoveries have shown there are several classes of variable celestial sources that vary in intensity and emit throughout the electromagnetic spectrum including the X-ray and gamma-ray bands [27, 28].

A particular subset of variable celestial sources that has attractive properties for use in a navigation system are rotating neutron stars, otherwise known as Pulsars [1]. The first pulsar was discovered in the radio band in 1967 by Bell and Hewish [29]. Subsequently, pulsars have been discovered that emit radiation throughout the electromagnetic spectrum [30, 31]. It has been theorized that neutron stars are formed following a supernova of a massive star [32, 33]. During the collapse, pulsars are spun up to high rotational rates due to the conservation of angular momentum.

Pulsars have very strong magnetic fields. Charged particles are accelerated along the field lines, and beams of radiation across the electromagnetic spectrum are expelled from the pulsar's magnetic poles [34]. If there is a misalignment of the pulsar's spin axis with its magnetic field axis an observer will sense a pulse of radiation when the pulsar's magnetic pole sweeps across the observer's line of sight to the pulsar [34].

No two neutron stars are formed in exactly the same manner, which causes their periodic pulse profiles to be unique. Since many pulsars possess unique, periodic, and extremely stable signals, they can be used in navigation through methods to triangulate position from their signals [1]. Pulsars can be potentially used as position, time, and attitude beacons for spacecraft operations [1,34]. In fact, a specific subset called millisecond period pulsars (MSPs) have been shown to match the stabilities of today's atomic clocks [35–37]. MSPs are thought to be recycled pulsars that are very old and have been spun up to high rates due to accretion from a companion star. They have low dissipation rates along with their high stability [34]. Detecting pulsar signals in the X-ray band (0.1 - 100 keV) is the most attractive for spacecraft navigation because it allows for the use of smaller detectors compared to optical and radio-band instruments, on the order of one square meter versus tens of square meters [34].

Most of the astronomical observations of pulsar sources have been done in the radio band because these emissions can be received on the Earth's surface. X-rays are absorbed by the Earth's atmosphere and thus the use of pulsar emissions in these wavelengths is limited to space and planetary body applications [34]. This has resulted in suggested methods to use pulsar radio signals for navigation [38], but significant improvement would need to be made in detector technology in order to make this feasible for space missions. Consequently, there is greater focus on methods to observe pulsars in the X-ray band to test a possible X-ray pulsar-based navigation (XNAV) system and provide updated timing models. The All-Sky Monitor (ASM) instrument aboard the Rossi Timing Explorer (RXTE) has served the role of monitoring the X-ray sky in the past [39]. Currently, the Neutron-star Interior

Composition ExploreR (NICER) and Station Explorer for X-ray Timing and Navigation Technology (SEXTANT), designed and launched by the NASA Goddard Space Flight Center (GSFC), serves these purposes attached to the International Space Station (ISS) [40,41]. These combined missions perform phase-resolved spectroscopy of rapidly spinning neutron stars and have demonstrated real-time X-ray pulsar navigation using MSPs, respectively.

From the history of pulsar observations conducted by the astronomical community over the past fifty years a catalog of pulsar parameters and properties can be developed. This information is collected together in one place for use in spacecraft navigation in [1]. For specific pulsars that have a long history of observations, accurate time histories can be logged of their periodic signals and used as pulsar timing models. Updates are made frequently by astronomical community as new measurements of each pulsar signal are made. Use of pulsars for navigation will require frequent study of each considered pulsar to characterize the signal parameters. When a new pulsar is discovered it takes an extended time of observations before the model parameters and time history are known to a high enough accuracy for use in navigation.

Variable X-ray sources have a variety of energy sources for their emissions and their variability is either produced by intrinsic or extrinsic mechanisms [1,34]. In general there are rotationally-powered pulsars (RPSRs) and accretion-powered pulsars (APSRs) [42]. The energy source for RPSRs is the stored rotational kinetic energy of the neutron star itself. The X-ray pulsations occur either due to magnetosphere or thermal emissions [28]. MSPs are rotationally-powered and they are some of the best timing sources. The brightest RPSR by far is the Crab Pulsar (PSR B0531+21) [43]. Unfortunately, the Crab Pulsar is a young bright source, and these tend to have relatively poor timing stability, whereas older sources such as recycled MSPs, that are the best timing sources, have dimmer fluxes by orders of magnitude [34].

APSRs are neutron stars in binary systems that have stellar material transferred from a companion star. The flow of the stellar material through the pulsars magnetic field causes hot spots on the star's surface. The changing view of these hot spots causes the pulsations as the APSR rotates. APSRs tend to be brighter but less stable than RPSRs due to the unsteadiness of the accretion process [44, 45]. Due to the more complicated nature of their signal modeling and poorer timing characteristics, APSRs will be ignored in this dissertation in favor of focusing on RPSRs.

Various types of detectors have been utilized throughout the history of X-ray astronomy missions including: gas proportional counters with collimators, microchannel plates, charge-coupled device semiconductors, scintillators, and focusing optics with small solid state detectors [46]. The HEAO-1 telescope and the USA experiment demonstrated the use of collimators to limit the field-of-view of the instrument [47, 57]. The use of coded aperture masks was demonstrated on the HETE-II mission. Grazing incidence mirrors were demonstrated by the Chandra X-ray Observatory and the RXTE mission [34, 39]. The instruments used throughout history have been optimized for science objectives and not for engineering purposes as an element of an operational XNAV system [34]. An essential component of a

XNAV system will be the detector, optimized for the energy profiles of pulsars selected for use. Likely candidates for use in such a system are solid-state detectors with their sensitivity being maximized to the medium (2-10 keV) energy band [34].

The naming convention for pulsars consists first of PSR for pulsar or an acronym corresponding to the mission that discovered the pulsar, such as XTE for X-ray timing explorer. The second portion of the name denotes the location in the sky they were discovered in hours and minutes of right ascension followed by degrees and minutes of declination. There is a B or a J added to the beginning of the location to denote if the position is stated in the B1950 or the J2000 epoch coordinate frame, respectively [48].

1.4 Previous Pulsar-Based Navigation Research

Since shortly after the discovery of the first pulsar it has been suggested that observations of these signals could be used as a high quality celestial clock and beacons for navigation. In 1971, Reichley, Downs, and Morris investigated using pulsars as a celestial clock for Earth-based systems [49]. Signal stability was demonstrated over long observations and pulse timing resolution on the order of fractions of a millisecond was achieved [49, 50]. In 1980, Downs and Reichley used decade-long DSN observations to demonstrate methods to determine pulse times of arrival from pulsar signals [52]. In the 1980s and 1990s, several studies were performed by Allan, Matsakis, Taylor, and others that demonstrated that several pulsars provide timing standards of similar quality to atomic clocks [37, 51]. From this early research, pulsars were conjectured to be possible celestial time standards to be used as clocks for spacecraft navigation.

In 1974, Downs was the first to propose using the signals from radio pulsars to perform navigation on an orbiting spacecraft [53]. The proposed method used 3 to 9 omni-directional antennas to get a three-dimensional position estimate from a record of the signal phase. The antennas were of a pyramidal shape with 2 m of area per side in order to provide full sky coverage. An accuracy of 150 km was projected with twenty-four hours of integration time. This study did not incorporate relativistic effects between the spacecraft and the inertial origin at the Solar System Barycenter (SSB), and it was assumed that phase cycle ambiguities were corrected using existing navigation methods.

In 1988, Wallace investigated the issues of using radio celestial sources, including pulsars, for navigation on the Earth [54]. Radio-based systems would require large antennas to detect sources from among the wide range of other broadband radio signals that might obscure weak pulsar signals. Also, the low signal intensity would require long integration times to build up an acceptable signal-to-noise ratio [52, 53]. Pulsars emitting optical pulsations have limited use in a navigation system due to the small number of sources discovered [55]. Large aperture telescopes would be required to detect a sufficient number of photons due to the dimness of the known optical pulsars.

During the 1970s, the first pulsars that emitted energy in the X-ray band of 1-20 keV were discovered. In 1981, Chester and Butman proposed using the first discovered X-ray pulsars as navigational aids for an Earth-orbiting satellite [56].

The accuracy was limited due to the poor noise characteristics of the known X-ray pulsars. Their proposed algorithm for navigation compared the pulse time of arrivals from pulsars between a distant spacecraft and a satellite in Earth orbit. They predicted that an accuracy of 150 km could be achieved after a full day of measurements with a 0.1 m^2 detector [56]. They didn't provide supporting analysis to demonstrate that this was a reasonable detector size, but it was the first study to clearly show the benefits of X-ray emitting sources for spacecraft applications [1].

As part of the design of the NRL-801 Unconventional Stellar Aspect (USA) experiment for the Advanced Research and Global Observation Satellite (ARGOS) satellite, launched by the US Air Force in conjunction with the Naval Research Lab (NRL), in 1993 Wood proposed a comprehensive study of using X-ray sources for navigation. This included using objects emitting in the X-ray band that were not pulsars and proposed methods for determining attitude, position, and time [57]. The USA experiment was flown in 1999 and the details will be discussed further in the section below on past and present flight experiments of pulsar-based navigation techniques.

Hanson in 1996 completed a Ph.D. dissertation at Stanford as part of the NRL development effect. He detailed using pulsars for spacecraft attitude determination with the use of a two-axis gimbaled detector [58]. Possible attitude accuracies on the order of 0.1 - 0.01 degrees were shown by comparing to data from the HEAO-1 spacecraft [47]. Hanson also explored the potential for using X-ray sources for autonomous timekeeping by using a phase-locked loop to keep accurate time.

In 1993, Becker and Trumper presented findings demonstrating that the binary

MSP J0437-4715, previously only known as a radio pulsar, also emits X-rays [60]. This combined with similar discoveries for other MSPs greatly improved the expected accuracy of potential X-ray pulsar-based navigation systems [1]. These advancements accelerated the study of potential XNAV systems. In 2004, the European Space Agency (ESA) published a study investigating the feasibility of relying on pulsar timing information for spacecraft navigation [61].

In 2005, Sheikh completed a Ph.D. dissertation at the University of Maryland giving an extensive study of spacecraft navigation using variable celestial X-ray sources [1]. This was the first study to include a wide range of position determination methods utilizing X-ray pulsar signals. The contributions included a comprehensive variable celestial X-ray source catalog along with a figure of merit to determine how good a pulsar is for navigation, new techniques to model pulse times of arrival to analyze range accuracy, new time transfer equations for spacecraft traveling in our solar system, many algorithms for absolute and relative position determination, methods of delta-correction position estimation, and a navigation Kalman filter was designed to blend spacecraft dynamics with pulsar-based range measurements [1]. Sheikh was the first to validate methods of position determination using X-ray pulsars with flight data, from the USA experiment.

In 2005 to 2006, the Defense Advanced Research Projects Agency (DARPA) XNAV Phase I Program investigated methods for using MSPs for navigation [62]. This effort focused on and produced many advances in the areas of source characterizations, detector development, and navigation algorithms design. Work was performed toward a planned demonstration of the system architecture on an ISS flight. The program did not proceed to Phase II of flight test development. As part of the DARPA XNAV Program the first laboratory facility to simulate X-ray pulsars was developed at NASA GSFC [76]. This program also validated algorithms for spacecraft position determination using previous flight data from the USA experiment [62]. Also in 2005, Woodfork performed research on using X-ray pulsars to aid in GPS satellite orbit determination for his Master's thesis [63].

In 2007, Golshan and Sheikh proposed using a combination of a maximum likelihood phase estimator and a second-order digital phase locked loop (DPLL) to perform pulse phase estimation and tracking [64]. The proposed algorithm was the first to attempt to track the phase of a pulsar signal using shorter update blocks than could be achieved with previous pulsar signal processing techniques that build up profiles by folding back long observations over the pulsar period and perform cross-correlation with high signal-to-noise templates. The DPLL develops an internal model of the pulsar signal. The proposed algorithm was tested in simulations using the signal of the Crab pulsar. A threshold effect, where the accuracy of the MLE phase estimate diverges from the Cramer-Rao lower bound, was demonstrated when the observation time was too low and only limited photons are detected. The threshold effect of the MLE for phase was further investigated in [65].

There have been many Small Business Innovations Research (SBIR) grants through NASA, between 2006 and 2014, with various small businesses including ASTER Labs, CrossTrac, and Microcosm.Through the NASA GSFC, between 2006 and 2010, there was a SBIR focusing on XNAV and time determination that proceeded through Phases I, II, and III. Between 2010 and 2014 there was a GSFC

SBIR focusing on deep space navigation and timing architecture simulation that went through Phase I and II.

There was a GSFC SBIR looking into X-ray detection and processing models for spacecraft navigation and timing that went through Phases I, II, and III between 2010 and 2014. Many different aspects of XNAV and supporting research were investigated through these SBIR grants including in 2008 when Sheikh and Graven looked into using XNAV to augment DSN tracking for interplanetary space missions [10]. In 2012 there was a NASA SBIR called GLINT (Gamma-ray source Localization-Induced Navigation and Timing) that looked at using Gamma-ray pulsars and bursts as aids for spacecraft navigation.

In 2021, ASTER Labs has a Phase I SBIR called HYNAV with NASA to investigate the use of a potential hybrid navigation system that would use various signals of opportunity to produce measurements and combine them. This program is looking at periodic signals like X-ray and radio pulsar and burst type signals including gamma ray and fast radio bursts.

In 2008, Rodin investigated concepts of using an ensemble of pulsar signals to form a new time scale [66]. Between 2009 and 2011 a DARPA program called XTIM studied the use of pulsars for time transfer and developed an instrument to form a pulsar timescale to backup the GPS system. This instrument was never launched to test in space.

Emadzadeh completed a Ph.D. dissertation at UCLA in 2009 on techniques for relative navigation using X-ray pulsars [67]. Doyle in his Master's thesis in 2013 investigated relative navigation further, focusing on using bright, possibly aperiodic

X-ray sources [68]. Doyle also presented the detector used in the University of Minnesota High Altitude X-ray Detector Testbed (HAXDT) that has been flown on multiple balloon missions of the High Altitude Student Platform (HASP) at Louisiana State University. The HAXDT has the goal of demonstrating future hardware for XNAV experiments in near space environments [68].

In 2013 Deng and Hobbs published research on interplanetary spacecraft navigation using pulsars [69]. In particular, they addressed the question of what the optimal techniques for extrapolating pulsar phase estimates are when there is timing noise present [70]. Tran, in 2014, presented statistical prediction models to provide lower bounds on the performance of pulse phase estimation for X-ray pulsars using both deterministic and Bayesian frameworks [71]. These bounds provide a less computationally expensive means of determining the threshold observation time compared to traditional Monte Carlo simulations.

In 2015 Hisamoto and Sheikh investigated using celestial gamma-ray sources as aids for spacecraft navigation [72]. This research was part of the GLINT SBIR grant. Relative navigation algorithms are presented for a pair of satellites observing the same Gamma-ray burst. Correlation of the observed Gamma-ray burst profiles at the two spacecrafts can provide a range measurement between the satellites along the line-of-sight to the source of the burst [72].

In 2016, China launched XPNAV-1 as the first dedicated X-ray pulsar navigation test satellite. XPNAV-1 is the first in a three step sequence [73] to demonstrate X-ray pulsar navigation. The core objective is to validate the ability of observing pulsars in the soft X-ray band with its hardware, which has been done before by other X-ray telescope spacecraft like RXTE [39]. XPNAV-1 has two X-ray detectors of different types. The three goals set in order to meet the core objective are to test the performance of the X-ray detectors in outer space, to detect typical pulsar signal X-ray photons to create pulse profiles, and to accumulate long observations of data to measure pulsar timing parameters [73]. It is unclear if any onboard demonstration of position determination using these observations is planned during the XPNAV-1 mission or whether this will be only possible with subsequent satellites in the series.

The NICER instrument was designed at NASA GSFC and launched in 2017 and attached to the ISS. A companion program to NICER at GSFC, SEXTANT, has the mission of demonstrating real-time X-ray pulsar navigation using MSPs in flight for the first time. The architecture of the SEXTANT mission is overviewed in [74] and [75]. As part of the development work for SEXTANT, a ground testbed called the Goddard X-ray Laboratory Testbed (GXLT) was to emulate detection of a pulsar signal using a X-ray emitter along with a silicon drift detector (SDD) [76].

Both NICER/SEXTANT and the Chinese XPNAV program are discussed further in the section on flight experiments below. Recently, research on XNAV has picked up in the United States, China, and Europe and it is a fast moving field looking to support turning XNAV into an attractive and reliable choice for future deep space missions. A summary of some of the major previous contributions to research in using pulsars as aids for navigation, including XNAV, is contained in Tables 1.3 and 1.4.

In recent years, particularly in China, there has been increased research into hybrid navigation methods. These works investigate the use of XNAV combined with other methods of spacecraft navigation to form an improved overall orbit solution. These methods are mission specific and dependent on other available sources of navigation information. Examples of some of the measurements used in combination with XNAV solutions that have been investigated in simulations include: optical image observations of the moons of Mars, Phobos and Deimos [77], radio measurement information and relative XNAV from a Mars orbiter simultaneously observing pulsars [78], combining with traditional celestial navigation techniques [79], the use of an ultraviolet sensor to image planets and stars to reduce the orbit error [80], and the use of Doppler radial velocity measurements relative the sun [81].

1.4.1 Flight Experiments to test X-ray Pulsar-based Navigation

There have been multiple past, present, and future flight experiments to test X-ray pulsar-based navigation Some have not made it out of the planning stages and some have gone on to varying levels of success in demonstrating the utility of celestial X-ray sources navigational aids. Figure 1.1 illustrates the history of proposed and realized flight tests with a plot of the altitude of the mission vs. time of launch, or program time period. Tables 1.5 and 1.6 provide an overview of the history of government funded programs that investigated navigation using celestial X-ray sources. Tables 1.7 and 1.8 provide a detailed comparison of the different past and present flight experiments to test X-ray pulsar-based navigation.

In 1999, ARGOS was launched and operated until 2000 by the US Air Force

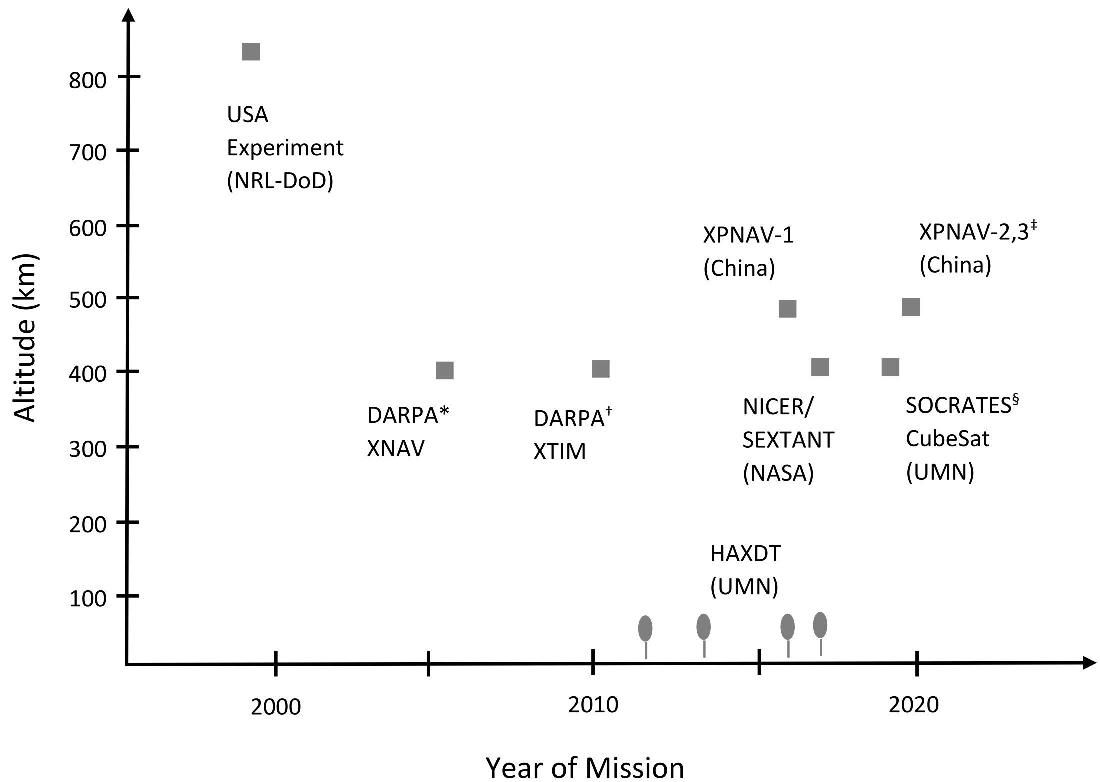

Figure 1.1: History of celestial X-ray source-based navigation flight tests.
* Development of an ISS instrument for XNAV and related supporting research that did not proceed to a flight demonstration
† Pulsar timing instrument developed but not flown
‡ Satellites to improve on XPNAV-1 and test relative navigation
§ CubeSat developed at the University of Minnesota

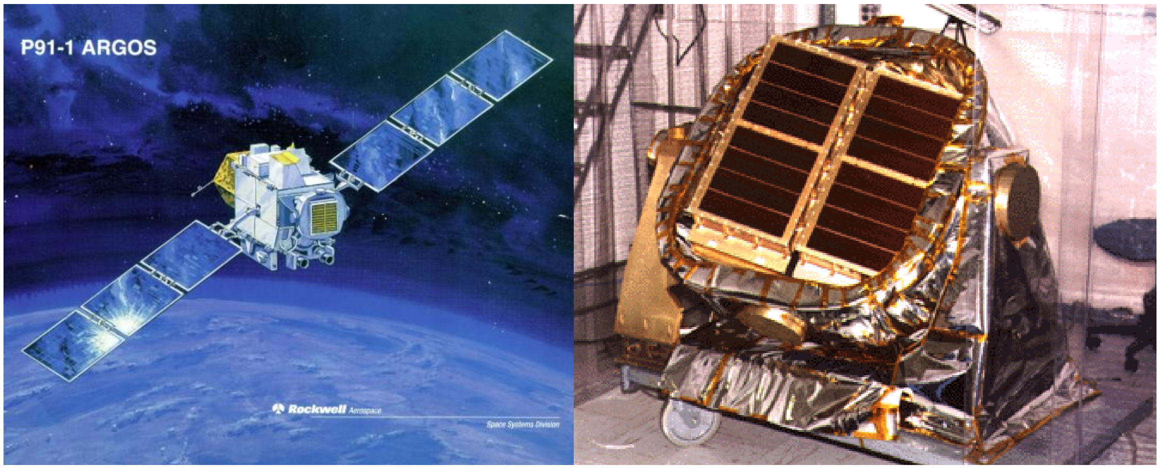

Figure 1.2: Picture of ARGOS satellite on the left and the detector for the USA experiment on the right. [82]

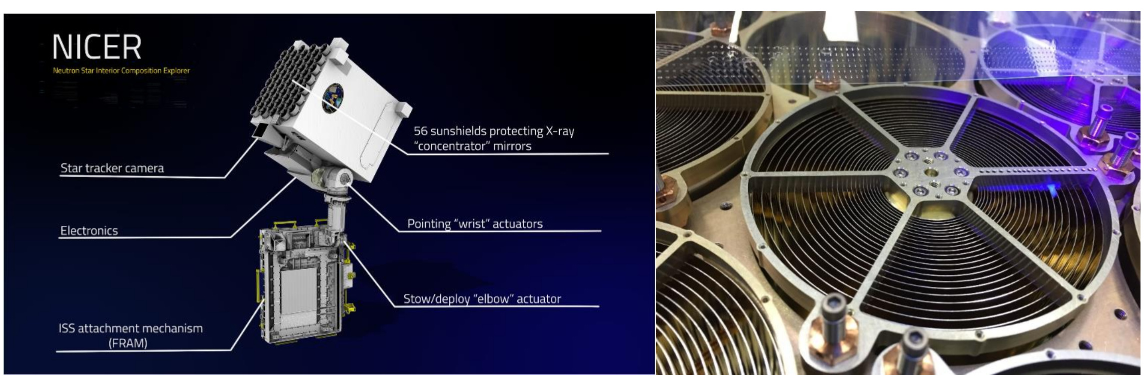

Figure 1.3: Diagram of the NICER instrument attached to the ISS on the left and close up of one of the detectors on the right. 40

Figure 1.4: Diagram of the XPNAV-1 Satellite. A mock-up of the TSXS detector is provided. [73]

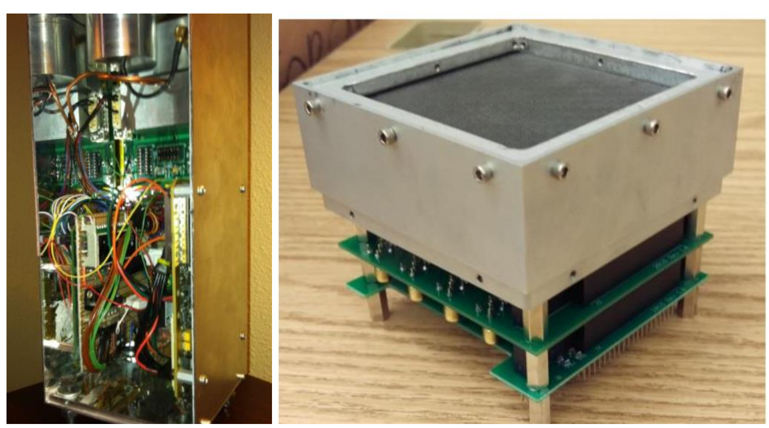

Figure 1.5: Picture of the UMN HAXDT on the left with a close up of the detector (GRID) on the right. [87]

under the US Department of Defense (DoD) Space Test Program. ARGOS carried nine payloads in a sun synchronous LEO orbit with an approximate altitude of 830 km. One of the payloads was the NRL USA experiment. This was the first spacecraft flown with the goal of exploring navigation techniques with celestial X-ray sources. This mission concentrated on binary X-ray sources, but it also considered sources beyond pulsars and broadly investigated navigation concepts beyond just position estimation including time determination. The USA experiment contained two gas filled proportional counter X-ray detectors with areas of $1000cm^2$ and timing resolutions of 2 ms in the 1 to 15 keV energy band. The USA experiment ended early due to a loss of gas in the detector chamber of the X-ray detector that was hypothesized to have been caused by a micrometeorite strike [1, 82–84].

The DARPA XNAV Phase I program operated from 2005 to 2006. Work was performed toward a planned demonstration of the system architecture on an ISS flight. The project did not proceed to Phase II, which ended the planned flight demonstration. Groundwork was laid for future missions to test celestial X-ray navigation techniques including source characterization, detector development, and initial navigation algorithm design [62].

NICER was launched in June 2016 and is currently attached to the ISS in LEO with an altitude between 402 and 407 km. The aim of this mission is to perform gravitational, electromagnetic, and nuclear physics studies of neutron stars. The primary area of interest is the interior composition of neutron stars. The low altitude of the ISS presents some limitations, but two to four objects are still observable per each orbit. NICER is made up of an array of 56 X-ray detectors. Each detector is made up of X-ray concentrator optics (XRC) and a silicon drift detector (SDD). The XRC has an aperture diameter of 10 cm and focuses X-ray photons onto the 2 mm diameter SDD. The timing resolution is 100 ns in the energy band of 0.2 to 12 keV. The total detector area is 1800 cm^2 [40].

In conjunction with NICER, SEXTANT is using the same system architecture to attempt to use MSPs to perform real-time orbit determination for the first time with celestial X-ray sources [74, 75]. The initial goal to estimate position to an uncertainty under 10 km with two weeks of measurements was achieved with initial on orbit results as seen in [76]. SEXTANT will sequentially observe 11 MSPs to perform position determination and maintain that orbital position estimate starting from a rough initial measurement provided by the GPS receiver onboard NICER [76]. Two different orbital position determination tests will be performed. The first will use ground-based pulsar timing models provided by radio observatories and the second will use X-ray timing models generated by NICER during the mission. Attempts at position determination with uncertainty under 1 km will be made as flight and instrument time allows [85].

The China Academy of Space Technology (CAST) has proposed a three-step X-ray pulsar-based navigation space demonstration scheme [73]. This program is made up of three planned rounds of satellites, the first of which, X-ray pulsar navigation-I (XPNAV-1), successfully launched in November of 2016. XPNAV-1 will gather data from 8 different pulsars, 4 isolated rotation-powered and 4 binaries, in order to confirm the ability to accurately observe X-ray pulsars [73]. The next satellite was planned to be launched around 2 to 3 years after XPNAV-1, but it has been delayed. It will have a larger detector to gather X-ray pulsar signal data to build a pulsar parameter database. This second satellite will also perform an onboard test of their pulsar navigation algorithm after 3 to 5 pulsars are adequately modeled and timed with enough observations [73]. The final step is to build a constellation of satellites to demonstrate X-ray pulsar-based navigation and accurate timing from pulsar signals.

The XPNAV-1 satellite is in a sun synchronous LEO orbit of approximately 500 km in altitude. Orbit and power constraints limit the continuous observation times of each X-ray source to 90 minutes. There are two X-ray detectors on the spacecraft that are used independently of each other due to power restrictions. The Time-Resolved Soft X-ray Spectrometer (TSXS) has a collecting area of 30 cm^2 and uses a lens of nested mirrors to focus the photons onto a SDD. The TSXS provides 1.5 μs of timing resolution in the 0.5 to 10 keV energy band. The High Time-resolution Photon Counter (HTPC) uses a collimator to provide a field-of-view of 2 degrees that yields a 1200 cm^2 collecting area and a microchannel plate X-ray detector to count photons in the 1 to 10 keV energy band with 100 ns of timing resolution. The HTPC provides a larger collecting area and better timing resolution than the TSXS [73].

The primary objectives for the XPNAV-I satellite are to demonstrate the X-ray detector hardware in space, detect photons from X-ray pulsars in order to generate pulse profiles, and to gather long periods of X-ray data to determine X-ray pulsar timing. So far XPNAV-1 has demonstrated the ability of the TSXS to observe soft X-ray photons through 192 observations of the Crab pulsars of durations ranging from 10 to 90 minutes [73]. Further research is planned to study how to use these observations to help with orbit determination.

The University of Minnesota has launched multiple small X-ray detectors on high altitude balloons since 2012 through the High Altitude Student Platform (HASP) at Louisiana State University. These missions used the High Altitude X-ray Detector Testbed (HAXDT) payload on the balloon to test small X-ray detectors in space-like conditions to demonstrate their feasibility for an X-ray pulsar-based navigation system [87]. These flights reached an altitude of approximately 36 km, with 1% of the Earth's atmosphere, and they lasted around 20 hours. The detector type used was an avalanche photodiode with a plastic organic scintillator and it was sensitive to the range of photon energies between 100 keV and 5 MeV. The 2014 mission successfully recorded 3.6 photons events per second [88]. This data was used to help characterize the background x-ray noise to aid in future use in spacecraft navigation. More recent missions, since 2016, have used a similar detector, the Gamma Ray Incidence Detector (GRID), that collects high-energy photons from Gamma-ray bursts to evaluate the performance for a future University of Minnesota and ASTER Labs joint CubeSat mission, the Signal of Opportunity CubeSat for Ranging and Timing Experiments (SOCRATES).

1.4.2 State of the Art in X-ray Pulsar-based Navigation

Through the last few decades of developments in research on using X-ray celestial sources for navigation a baseline approach to X-ray pulsar-based navigation

(XNAV) has been defined that uses X-ray observations of MSPs [34]. Approaches using single axis ranging and extensions similar to global navigation satellite systems (GNSS) have been developed to determine accurate spacecraft orbit solutions. The single axis ranging techniques were developed to leverage the fact that most current X-ray detector designs can only observe a single point in space [1,98]. For the GNSS-like techniques, lateration concepts are used to estimate the range from an inertial origin along the lines-of-sight to multiple sources. These concepts either require multiple detectors that can each observe a single pulsar or a future detector system that is developed to monitor the whole sky and provide simultaneous observations [61, 65, 89].

Methods of XNAV require that observations of the pulsars are timed within an inertial frame that is stationary with respect to the pulsar [34]. There are standard methods that provide equations for time conversion from the observer's proper time to coordinate time based on the spacecraft clock motion and the experienced gravitational potential [18, 90–94]. For most pulsar observations the inertial SSB coordinate frame is taken to be the International Celestial Reference Frame (ICRF) whose axes are aligned with the equator and the equinox of J2000 [95]. The reference time scale is either the Barycentric Coordinate Time (TCB) or the Barycentric Dynamic Time (TDB) [95].

Many methods have been developed for position and velocity determination using X-ray sources. These techniques can be split into those that determine position and velocity in an absolute sense in three-dimensions in an inertial reference frame and those that work in a delta-correction sense where updates to estimate range and range-rate values are generated from pulsar measurements [34]. For absolute position determination it is necessary to know the specific pulse cycle that is observed from the source. Methods of pulse cycle ambiguity resolution have been developed that are similar to approaches used by the GPS system [65].

The primary method for spacecraft navigation compares the pulse time-of-arrival (TOA) measured at the spacecraft detector to the predicted arrival time based on the pulsar timing model at the SSB. This provides a TOA timing residual that is the standard measurement in a XNAV system [34]. This is also the approach used by astrophysicists to determine characteristics of a pulsar's signal [96]. A common approach uses a single detector to provide corrections to range estimates using the TOA residual. The TOA residual provides an estimate of the error in range along the LOS to the source pulsar, which can be blended with the estimated position from an orbit propagator to maintain an accurate solution for the navigational state [34].

Another technique that can provide nearly continuous position updates versus the infrequent updates of the TOA residual difference method is phase tracking. Phase tracking can estimate and lock onto the phase and frequency of the observed pulsar signal using the known timing model [64]. An estimate of the spacecraft's orbit in the inertial frame is produced by comparing the tracking with the expected parameters of the source signal. Over short intervals, tens to hundreds of seconds, updates of the spacecraft motion are estimated [64]. DPLLs can be used to ensure proper tracking of the pulsar signal [1, 58]. The current state of the art of phase tracking a pulsar signal is presented by Golshan and Sheikh in [64]. The Golshan and Sheikh phase tracking algorithm breaks an observation into small blocks over which the detected signal frequency is assumed constant, equivalent to a constant spacecraft velocity with respect to the pulsar, and uses a maximum likelihood phase estimator, with an constant frequency internal phase model, to estimate the phase at the beginning of the entire observation. The change of this estimated phase over time corresponds to the Doppler phase shift due to the motion of the spacecraft over the observation. A second-order DPLL is used to smooth the MLE phase estimates and track the observed pulsar signal [64].

Table 1.9 provides an overview of the different types of algorithms considered for estimating parameters of an X-ray pulsar signal for use in navigation. The pros and cons of each main technique are presented. The techniques are separated by two different factors. First, whether the individual pulsar photon data is processed in a batch in a large single set or in a continuous mode where the data is used as soon as it is available. Second, whether the algorithm uses binned photon data or single event processing. In algorithms using binning, the pulsar signal data is represented by the number of photons that arrive in time bins of fixed small duration. For algorithms with single event processing each individual photon event is time-tagged and these photon event times are used to compute the pulse TOA. [34] These combinations yield four possibilities to divide the types of pulsar signal processing algorithms.

The technique of binning photons and using batch processing is the traditional astronomy approach for computing the pulse TOA. This method relies on epoch folding to assemble all of the measured photon events into a pulse profile. The photons are collected into finite size bins and many pulses are folded back together to create a measured profile that is compared to the known profile to estimate the pulse TOA [89]. For example, cross-correlation or nonlinear least squares might be used to estimate the pulse TOA [67]. This provides a good single TOA solution, but information is lost in the binning process. Also, 10^4 seconds or more pass between subsequent measurements, and no information is available to update the position of the spacecraft between the measurements [34].

When time-tagged photons are batch processed the entire photon history is used to create the pulse TOA. No information is lost when time-tagging the photons as opposed to binning. Thus, this method provides the best possible pulse TOA solution. The drawbacks are that 10^4 seconds or more pass between subsequent measurements, and no information is available to update the position of the spacecraft between the measurements [34]. Also, the computational burden is larger than with binning. An example of batch processing time-tagged photons is using an MLE to estimate the pulse TOA using the entire observation of photon event times [67].

Using continuous processing with binned photons is similar to a communications approach to Poisson data. The photons are collected into finite size bins and then the pulsar signal is extracted from the background noise using a DPLL [58]. A DPLL is a type of control system where the phase of the output signal is driven to be in-lock with an input signal and thus contain information from the input [59]. This provides continuous measurements, but information is lost in the binning process and the loop filter of the DPLL limits the bandwidth of the measurements to 10 μHz or less [34].

Ideally, continuous processing with time-tagged photons would be able to provide single photon processing and measurement updates, but currently there are no algorithms that have the capability of providing an estimate update using the information contained in a single photon. The closest current algorithms get to continuous processing is using small batches of photons event times [64]. This method provides good single TOA solutions and has the maximum use of the photon time information with nearly continuous measurements, on the order of tens or hundreds of seconds between updates [34]. An example of using small batches of photon event times is the MLE-DPLL cascade of the phase tracking algorithm proposed by Golshan and Sheikh [64]. The drawbacks include a higher processing burden and possibly lower position estimate accuracies depending on the MLE batch size.

Velocity determination can be performed using the observed Doppler shift of a pulsar signal. This is done by measuring the pulsar's observed signal frequency and comparing this to the expected source frequency. Second and higher order relativistic Doppler effects need to be included to increase the measurement accuracy [97]. Observations from multiple pulsars can be combined to provide a three-dimensional velocity measurement [34].

The standard method to incorporate the position and velocity information derived from pulsar signals into the spacecraft navigation system is to use an extended Kalman filter (EKF). The equations to perform this filtering were presented by Sheikh in 2005 [1, 98]. These techniques blend numerically integrated spacecraft orbit dynamics with the pulsar observation measurements. It has been demonstrated that errors in position and velocity can be removed using these filtering techniques [98]. There has also been research into the best ways to use X-ray pulsar signals to compute relative navigation solutions between two spacecraft or a spacecraft and a pulsar observatory. The details of these methods will not be discussed in depth because the main focus of this dissertation is on phase tracking techniques for determining a single spacecraft's absolute position.

1.5 Contributions

This dissertation describes a comprehensive investigation of methods of phase tracking X-ray pulsar signals as a means of spacecraft navigation. The contributions are split into two major categories. The first deals with verification and testing a previously proposed method for phase tracking and the second deals with the definition and performance of a novel extension to the originally considered phase tracking algorithm in order to address some of the drawbacks with lower flux pulsars that are attractive for navigation.

The Golshan and Sheikh phase tracking method introduced in [64] was experimentally validated using the Crab pulsar signal and the NASA Goddard X-ray Laboratory Testbed (GXLT). The use of the GXLT tests the phase tracking algorithm under conditions including x-ray photon generation and detection that were previously only considered using ideal models in computer simulations. This is done using an x-ray pulsar emulator and an x-ray detector set up inches apart in a lab at NASA Goddard and developed by the NICER/SEXTANT team.

For the first time the drawbacks to the phase tracking algorithm for millisecond period pulsars (MSPs) are described. Most of the pulsars with the best characteristics for use in spacecraft navigation are MSPs, or other pulsars that have much lower flux than the Crab pulsar, so this demonstrates the need for an extension to the phase tracking algorithm. The assumption of constant signal frequency over each block needs to be relaxed in order to use reasonably sized x-ray detectors for use in space.

Phase tracking is a method that is an improvement on the state of the art in XNAV measurement processing. It provides a greater number of measurements than previous methods that rely on the comparison of pulse time of arrival measurements. Phase tracking provides the potential for range and range rate measurements. It also has greater durability to catch potential errors in the measurements due to naturally occurring signal glitches or instrument errors. This motivated the development of phase tracking methods to overcome the difficulties with low flux pulsars.

An extension to the phase-tracking algorithm is presented that assumes a constant signal frequency derivative over each block, which allows for the frequency to vary. An MLE for phase at the start of each block is determined using an internal phase model that increases by one order to a third order Taylor polynomial. The higher order phase model in the MLE uses feedback of the frequency and frequency derivative provided by a third-order DPLL in order to still provide estimates of the phase at the start of each block.

The MLE performance for the Crab pulsar and four MSPs: B1821-24, B1937+21, J0218+4232, and J0437-4715 is empirically determined and compared to the Cramer-Rao lower bound (CRLB) using a range of deep space trajectories and Earth orbits.

The MLE is tested with a trajectory with constant acceleration along the line-of-sight to the pulsar observed in order to test the MLE with a case where the dynamics can be matched exactly by the internal phase model. The threshold observation time required for the MLE phase error to converge to the CRLB is determined for each of the pulsars considered. The MLE is also tested with unmodeled trajectory dynamics and an upper limit on the observation time is determined where the increased dynamic stress causes the MLE phase error to diverge from the CRLB.

An analytical method to quickly predict the threshold observation time required for the error to converge to the CRLB is derived. This works well for three of the five pulsars, but fails for the two pulsars with the largest pulse widths. The analytical prediction method is investigated with a series of artificial pulsar profiles with various pulse widths to test its range of applicability.

The performance of the new phase-tracking algorithm is investigated in simulations for observing individual pulsars along the same trajectories used with the MLE by itself. Phase tracking was demonstrated with simulations for four millisecond period pulsars and the Crab pulsar over a variety of different orbital environments: the MSL and Cassini cruise trajectories; a cislunar trajectory; and the DirecTV, GPS, and ISS orbits. The main product of these simulations is an approximate level of error that is achievable for the phase estimates when in phase-lock.

An extended Kalman filter was used to incorporate one-dimensional range measurements from the phase tracking algorithm from multiple pulsars to produce a three-dimensional navigation solution. The individual pulsar phase tracking simulations were used to determine the level of measurement accuracy to consider when generating measurements for the Kalman filter. Position tracking performance was shown with under 4 km position error and 8 cm/s velocity error for the MSL trajectory, cislunar trajectory, and DPLL orbit. This performance is comparable to other XNAV methods, and these are the first results for phase tracking millisecond period pulsar signals successfully. Various schedules and detector scenarios were included, both modeling an EKF with measurements from three detectors simultaneously and from a single detector in sequence. This is the first work to combine phase tracking pulsar estimates into a three-dimensional filtering model.

1.6 Dissertation Overview

Chapter 2 introduces the aspects of modeling X-ray pulsar signals that will be useful for the phase-tracking methods investigated in this dissertation. First, pulsar timing models that detail when particular pulses of the periodic signal of a chosen pulsar will arrive at the solar system barycenter are discussed. Next, the modeling of photon event times received at an X-ray detector from a pulsar signal as a non-homogeneous Poisson process (NHPP) is detailed along with the consequences of this model. The pulsar rate function that is used for the NHPP model is presented along with plots of examples for a set of pulsars that will be used throughout this dissertation in simulations. The evolution of the phase of a pulsar signal at the detector on a moving spacecraft is discussed for both cases of constant and varying observed signal frequency. The chapter concludes by presenting the maximum likelihood estimator for phase of a pulsar signal.

Chapter 3 introduces the method of phase tracking a pulsar signal as used for spacecraft navigation. The main building blocks of the phase tracking algorithm are introduced as well as previous research in the area. Motivation is given for tracking phase by connecting a spacecraft's position and velocity with the phase and frequency of a pulsar signal observed by a detector on the spacecraft. In particular, the method for phase tracking developed by Golshan and Sheikh in [64] is introduced. The use of digital phase-locked loops (DPLLs) for pulsar signal tracking is described including a discussion of the difference between the ways DPLLs are being used for pulsar signals versus common practice. This includes an example demonstrating the use of a DPLL for frequency modulation (FM) signal demodulation.

The method of phase tracking introduced by Golshan and Sheikh is investigated and confirmed using both lab experiments with the NASA Goddard X-ray Laboratory Testbed (GXLT) and computer simulations. The method is used to track the phase of the Crab pulsar signal for a series of simulated detector trajectories. The accuracy of the MLE for phase estimation is also compared. The final section of Chapter 3 introduces the difficulties that are encountered when extending the Golshan and Sheikh phase tracking method to millisecond period pulsars (MSPs), which have fluxes much lower than the Crab pulsar. It is demonstrated that there is a trade-off between the accuracy of the ML-phase estimates and the dynamic stress of the spacecraft trajectory. Either the block length or the detector size must be increased to accommodate navigation with MSPs. The case is presented that modifications to the standard Golshan and Sheikh phase tracking algorithm are necessary to track MSPs for navigation with a reasonable sized x-ray detector.

In Chapter 4 the Cramer-Rao Lower Bound (CRLB) for the estimation of the phase of a pulsar signal is introduced, and the performance of the proposed MLE for phase estimation is compared to the CRLB. First, the derivation of the CRLB is presented, where the particular bound of most interest is the one for the case of changing signal frequency. A proposed extension to the MLE for pulsar signal phase estimation is introduced in order to relax the constant signal frequency assumption present in the standard Golshan and Sheikh phase tracking algorithm. This allows for the use of longer blocks for phase tracking MSPs. The performance of this proposed MLE is evaluated and compared to the CRLB using a variety of MSPs that are well suited for navigation. The empirical performance of the MLE is determined for a variety of trajectories and Earth orbits. A method for quickly predicting the threshold observation time that is required for a particular pulsar and orbit to have MLE accuracy that is near the CRLB is presented.

Chapter 5 presents and discusses the complete proposed phase-tracking algorithm that allows for varying observed signal frequency and the use of MSPs that have much lower flux than the Crab pulsar. The third-order phase-lock loop and the method for feeding back the current frequency and frequency-derivative values to the MLE are introduced. The method for transient-free acquisition for the DPLL using previous navigation measurements is presented. The performance of the phase tracking algorithm is determined for a range of Earth orbits, a cislunar trajectory and the MSL and Cassini cruise trajectories using the Crab pulsar and four MSPs: B1821-24, B1937+21, J0218+4232, and J0437-4715. The expected standard deviation of the error for each pulsar with each orbit is determined when in phase-lock.

Chapter 6 presents the results of complete scenarios utilizing different observation schedules of the five pulsars and the range of orbits considered in Chapter 5. An extended Kalman filter (EKF) is implemented to combine the phase-tracking estimates together. This is accomplished by providing the EKF with the levels of error expected for each estimated position instead of generating actual position estimates from a set of simulated photons. This is done due to the computational burden of generating days of simulated photon event times. Both a three detector and a single detector scenarios are considered for the MSL trajectory, cislunar trajectory, and DirecTV orbit.

Chapter 7 presents conclusions from this work and identifies areas for future research in pulsar signal phase tracking and pulsar-based spacecraft navigation in general. There are also multiple appendices included to supplement this dissertation. Appendix A presents the method used to simulate realizations of the non-homogeneous Poisson processes representing pulsar signals. Appendix B lists and discusses types of X-ray detectors that could be used for spacecraft navigation. Appendix C contains additional background on the theory of maximum likelihood estimation including an example with computation of an estimate using a simplified model. Appendix D contains background on accelerometers available for use in space.

Table 1.3: Previous Contributions to XNAV Research

Year	Name (Institution)	Description	Refs.
1974	Downs (NASA JPL)	First to propose using radio pulsars for spacecraft navigation	53
1981	Chester & Butman (NASA JPL)	Proposed X-ray pulsars for interplanetary navigation	56
1988	Wallace (ARE, Slough)	Looked at using "radio stars" for Earth navigation	54
1993	Wood (NRL)	Proposed using X-ray pulsars for navigation in near Earth orbit	57
1996	Hanson (Stanford)	Doctoral thesis on X-ray pulsars for attitude and time	58
1999	USA Experiment (NRL)	X-ray sources to perform Earth orbit attitude determination	82–84
2004	ESA ARIADNA	Feasibility study of pulsar timing for space navigation	61
2005	Sheikh (University of Maryland)	Doctoral thesis giving an extensive study of spacecraft navigation using X-ray pulsars. Included source catalog, new time transfer equations, many absolute and relative position determination algorithms, and a navigation Kalman filter to blend pulsar-based range measurements. Validated approach with USA Experiment flight data.	1
2005	DARPA XNAV	Source characterization, detector development, and navigation algorithm formulation to assist a planned ISS flight demonstration that did not proceed	62
2005	Woodfork (Air Force Institute of Technology)	Master's thesis on GPS satellite orbit determination with X-ray pulsars	63

Table 1.4: Previous Contributions to XNAV Research continued.

Year	Name (Institution)	Description	Refs.
2009	Emadzadeh (UCLA)	Doctoral thesis on relative spacecraft navigation using X-ray pulsars	67
2015	Hisamoto & Sheikh (ASTER Labs)	Proposed using gamma-ray sources as aids for spacecraft navigation	72
2016 - Present	XPNAV-1 (Chinese Academy of Sciences)	First Chinese satellite in a series planned to test X-ray pulsar navigation	73
2017- Present	NICER/SEXTANT (NASA GSFC)	Instrument on the ISS to demonstrate real-time X-ray pulsar navigation using MSPs	$40, 75, 85$

Table 1.5: History of Government Funded X-ray Pulsar-Based Navigation Research.
* Position accuracy from studies using previously collected USA experiment data.

Program Name	Year	Comments	Position Accuracy (km)
USA Experiment	1988 - 2000	First spacecraft flown with goal of exploring navigation techniques with celestial X-ray sources	N/A
ESA	2004	Study of the feasibility of relying on pulsar timing info for spacecraft navigation	N/A
DARPA XNAV	2005 - 2006	Work on a potential ISS flight demonstration of XNAV. Mission support work on detectors, modeling and nav algorithms. Demonstrated XNAV using old USA experiment data. Did not proceed to Phase II of flight demonstration development.	1 - 10*
NASA SBIRs: ASTER Labs, CrossTrac, Microcosm	2006 - 2014 2021	• XNAV and Time Determination, Phase I, II, and III, GSFC, 2006 - 2010 • Deep Space Navigation and Timing Architecture Simulation, Phase I and II, GSFC, 2010 - 2014 • X-ray Detection and Processing Models for Spacecraft Navigation and Timing, Phase I, II, and III, GSFC, 2010 - 2014 • GLINT, NASA, 2012 • HYNAV, GSFC, 2021	N/A
DARPA XTIM	2009 - 2011	Developed instrument to form a pulsar timescale to backup GPS. Not launched.	N/A

Table 1.6: History of Government Funded X-ray Pulsar-Based Navigation Research Continued. Current flight missions.
* Predicted position accuracy shown using ground testbed.

Program Name	Year	Comments	Position Accuracy (km)
China XPNAV-1	2016 - Present	First of a series of spacecraft to test X-ray pulsar navigation methods. First satellite is a detector demonstration to verify the ability to detect and reconstruct X-ray pulsar signals.	N/A
NASA NICER/SEXTANT	2017 - Present	Joint mission with instrument on ISS to study the internal physics of neutron stars and demonstrate real-time XNAV with MSPs	1 - 10*

Table 1.7: Comparison of Flight Experiments to Test XNAV.

Launch Year	Name	Mission Description	Navigation Method
1999	USA Experiment	First spacecraft flown to investigate navigation methods with celestial X-ray sources	Attitude determination, Occultation methods
2012, 2014, 2016, 2017	UMN HAXDT	High Altitude Balloon to aid detector development	N/A
2016	XPNAV-1	Observe X-ray pulsars for use in future XNAV missions.	N/A
2017	NICER/SEXTANT	Instrument attached to the ISS to estimate position using MSPs	Position determination using EKF with MLE of MSP signals
2018/2019	UMN CubeSat	LEO CubeSat to detect Gamma Ray bursts and hard X-rays	Relative navigation correlating burst profiles
2018 - 2020	XPNAV-2, 3	Larger detector to create database and test XNAV. Third step is a constellation.	TBD, Relative positioning for constellation

Table 1.8: Details for XNAV Flight Experiments.

Name	Sensors Used (Type of Detector)	Area (cm^2)	Timing Resolution (μs)	Energy Range keV
USA Experiment	Gas proportional counter	1000	2	1 - 15
UMN HAXDT	Avalanche photodiode with plastic organic scintillator	64	4	10 - 600
XPNAV-1	TSXS - silicon drift detector with focusing optics HTPC - microchannel plate with collimator	30	1.5	0.5 - 10
NICER/SEXTANT	X-ray concentrator optics with a silicon drift detector	1800	0.1	0.2 - 12

Table 1.9: X-ray Pulsar-based Navigation Methods and Comparisons [34].

Method	Pros	Cons
Binned Photons w/ Batch Processing (Epoch Folding) [89]	- Traditional approach from astronomy - Good single TOA solution	- Information lost in binning - 10^4 sec or more between measurements - No position information available between measurements
Time-Tagged Photons w/ Batch Processing (Epoch Folding)	- Best possible single TOA solution - No info lost in time-tagging of photons	- 10^4 sec or more between measurements - No position information available between measurements - Processing burden is high
DPLL w/ Binning Photons [58]	- Similar to communications approach - Continuous measurements	- Information lost in binning - DPLL loop filter limits the measurement bandwidth to under 10 μHz
Time-Tagged Photons w/ Continuous Processing (MLE-DPLL Phase Tracking) [64] (Method investigated in this dissertation)	- Position estimate after small batch of photons - Nearly continuous measurements - Good single TOA solution	- Possibly lower position estimate accuracy depending on MLE batch size - High processing burden

Chapter 2: X-ray Pulsar Signal Model

2.1 Overview

In order to be used for spacecraft navigation the signal of an X-ray pulsar must be understood and accurately modeled. In this chapter the aspects of modeling an X-ray pulsar signal that are useful for phase-tracking are introduced and discussed.

Pulsar timing models that are used to predict when a particular pulse from a pulsar will arrive at the solar system barycenter are discussed in Section 2.2. These models are determined by the astronomical community using the history of observations of each pulsar combined with new ongoing observations of the pulsar.

The modeling of the photon event times measured from a detected X-ray pulsar signal as a non-homogeneous Poisson Processes (NHPP) is discussed in Section 2.3 including the definition of and requirements to be an NHPP along with consequences that result from the use of this model in the phase estimation process.

The pulsar rate function used for the NHPP model is presented and discussed in Section 2.4. Plots of templates for the pulse profiles used throughout this dissertation for the Crab pulsar and MSPs used in simulations are also included and discussed in Section 2.4.

The evolution of the phase of the pulsar signal at the detector on a moving spacecraft is discussed in Section 2.5. Both the constant observed signal frequency case resulting from a detector that is stationary or moving at a constant range-rate with respect to the pulsar and the time-varying observed signal frequency case are considered along with their corresponding Poisson rate functions.

The maximum likelihood estimator (MLE) for the phase of the pulsar signal is derived and discussed in Section 2.6.

2.2 Pulse Timing Models

A pulsar's timing model can be accurately measured over long observations. These models are used to predict when specific pulses from a source will arrive in our solar system [1]. For navigation this can be extended to predicting when certain pulses are expected to arrive at a detector observing the pulsar. Thus, it will be necessary for a spacecraft using XNAV to have an almanac of pulse timing models for each pulsar it plans to track.

Pulsars that have been known to astronomers for a long time have well determined pulse timing models built up using the entire history of observations of the pulsar. Observations continue at large Earth-based radio telescopes and aboard spacecraft with X-ray and radio detectors to track pulsars, which regularly provide updated models [1]. These updates can be sent periodically to a spacecraft using X-ray pulsar-based navigation methods.

Pulse timing models can be represented as the total accumulated phase of a pulsar's signal over time. An initial signal number Φ_0 is chosen at a fiducial time,

t_0 at the Solar System Barycenter (SSB), which is used as an inertial reference location. The total phase can be modeled as a function of time and broken down into fractional and whole integer components [34],

$$\Phi(t) = \phi(t) + N(t), \tag{2.1}$$

where ϕ is the fractional portion of the pulse period and N is the number of integer cycles since t_0. This can also be expressed in terms of the pulse signal frequency and its derivatives

$$\Phi(t) = \Phi(t_0) + f[t - t_0] + \frac{\dot{f}}{2}[t - t_0]^2 + \frac{\ddot{f}}{6}[t - t_0]^3, \tag{2.2}$$

where $\Phi(t)$ is the total phase at time t, t_0 is a reference time at the SSB, and f, $\dot{f}$, and $\ddot{f}$ are frequency and its derivatives valid at time t_0. Eq. (2.2) is known as the pulsar spin equation or pulsar spin down law [30, 31], and it is equivalent to a Taylor polynomial expansion of the total phase if the only parameters included in the model are pulse signal frequency and its derivatives.

Higher order frequency derivative terms might need to be added to the timing models for some pulsars depending on the accuracy of the residuals. The timing models for binary pulsars need to incorporate other orbit parameters to accurately account for the complex dynamics present in such a system [99].

Parameters related to the angular coordinates of the source might be required including right ascension, declination, proper motion, and parallax. Pulse timing models are valid for the energy band of the electromagnetic spectrum from which they are developed. For timing measurements made in the radio band the dispersion measure, which is the column density of free electrons along the line-of-sight to the pulsar from the detector, needs to be included in the model [34]. Extra observations and modeling are necessary to extrapolate to other energy bands.

Most of the X-ray pulsars that have the timing characteristics that make them useful for navigation are also bright radio pulsars. Ground-based radio telescopes routinely observe these pulsars for long-term pulsar timing studies [34].

2.3 Non-Homogeneous Poisson Process

In the X-ray domain of the electromagnetic spectrum the primary measurement at a detector is the time that individual photons arrive, known as the photon event time. The relatively low flux of MSPs in the X-ray band allows the individual photons to be resolved at a detector. The photon event times govern a counting process. The rate of these arrivals is dictated by the periodic nature of the pulsar signals. Thus, the counting process determined by the event times of X-ray photons at a spacecraft detector can be modeled as a non-homogeneous Poisson process (NHPP) with a quasi-periodic rate function [64]. The number of photons arriving in a given interval from a pulsar is a Poisson random variable with quasi-periodic rate function $\lambda(t)$. The method used to simulate a realization of an NHPP is discussed in Appendix A. Types of X-ray detectors that potentially could be used for spacecraft navigation are discussed in Appendix B.

The following three axioms need to be satisfied for an arrival process to be a Poisson process [102, 103].

1. The probability that one arrival occurs in an infinitesimal time interval Δt is

given by

$$\Pr[1, \Delta t] = \lambda(t)\Delta t, \Delta t \rightarrow 0. \tag{2.3}$$

2. The probability that more than one arrival occurs in Δt is zero when $\Delta t \rightarrow 0$.

3. The number of arrivals occurring in a given interval is independent from the numbers arriving in all other disjoint intervals.

The expectation of a Poisson process as a function of time, $\lambda(t)$, is often called the rate function [64]. For a Poisson process with a time varying rate function $\lambda(t)$ the probability that k arrivals occur in an interval of time (a,b) is given by the following, [64, 101, 104]

$$\Pr[k; (a, b)] = \frac{\left(\int_a^b \lambda(t)dt\right)^k}{k! \exp\left(\int_a^b \lambda(t)dt\right)}. \tag{2.4}$$

Four consequences stemming from the NHPP model are as follows: [64, 100]

1. The probability that zero photons will arrive in an interval (a,b) is

$$\Pr[0; (a, b)] = \exp\left[-\int_a^b \lambda(t)dt\right]. \tag{2.5}$$

2. The probability that exactly one photon arrives in an infinitesimal interval of length Δt centered at time t is

$$\Pr[1; (t - \Delta t/2, t + \Delta t/2)] = \lambda(t)\Delta t \quad \text{as } \Delta t \rightarrow 0. \tag{2.6}$$

3. The probability of more than one photon arriving in an interval of length Δt is zero when $\Delta t \rightarrow 0$.

4. The number of photons arriving in a given interval is independent from those of all other disjoint intervals.

These consequences of the NHPP model for the photon event times will be used to facilitate estimation of the phase of the pulsar signal in subsequent sections.

2.4 Pulsar Rate Function

The rate function $\lambda(t)$ includes all the photons arriving at a detector. Both source photons arriving at a rate of R_s photons per second (ph/s) and background photons arriving at a rate of R_b ph/s are counted together. The pulse fraction ρ gives the ratio of pulsed to steady emissions from the source pulsar. The rate function is driven by the composition of the normalized pulse profile function specific to the observed pulsar, $h(\phi)$, and the observed phase at the detector, $\phi_{det}(t)$ [64]. It is expressed as

$$\lambda(t) = \beta + \alpha h(\phi_{det}(t)) \qquad (ph/s), \tag{2.7}$$

where α and β are the effective source and background photon arrival rates, respectively. These parameters group together the background photon rate with the non-pulsed source photon rate as follows

$$\alpha = \rho R_s \qquad (ph/s) \tag{2.8}$$

$$\beta = R_b + (1 - \rho) R_s \qquad (ph/s). \tag{2.9}$$

The ratio of α to β gives the signal-to-noise ratio (SNR) of the pulsar corresponding to a given detector. The pulse profile function $h(\phi)$ defines the pulsed nature of the source photons and is unique to a particular pulsar; it is normalized to satisfy $min_{\phi \in (0,1)} h(\phi) = 0$ and $\int_0^1 h(\phi) d\phi = 1$. The domain of the pulse profile function is extended beyond (0,1) by letting $h(m + \phi) = h(\phi)\ \forall m \in \mathbb{Z}$ [64]. The normalized pulse profile for each pulsar is created from a high SNR template [1]. The high SNR templates are created using epoch folding, which is the synchronous averaging of all photon events over the expected pulsar period to create a binned histogram that averages together all of the detected pulses from the source. The expected pulse period is determined from the pulse timing model for the pulsar as discussed in Section 2.1. The templates use long observation times and sometimes combine multiple observations with the same instrument in order to increase the SNR [1].

Examples of the pulse profile functions for the pulsars that will be considered and used in simulations throughout this dissertation are included in Figures 2.1 , 2.2 , 2.3 , 2.4 , and, 2.5 . Each figure contains a plot of two periods of the template for the pulse profile. The pulse profile template for the Crab pulsar is included in Figure 2.1, PSR B1821-24 is included in Figure 2.2, PSR B1937-21 is included in Figure 2.3, PSR J0218-4232 is included in Figure 2.4, and PSR J0437-4715 is included in Figure 2.5 . As can be seen in the figures, the pulse profiles vary greatly depending on the pulsar. The Crab profile has one main pulse along with a smaller sub-pulse. The profile for PSR J0218+4232 has a main pulse and a secondary pulse that is not much weaker. The profile for PSR J0437-4715 has only a single main pulse. The profiles for PSR B1821-24 and PSR B1937+21 have a main pulse along with many smaller pulses throughout each cycle.

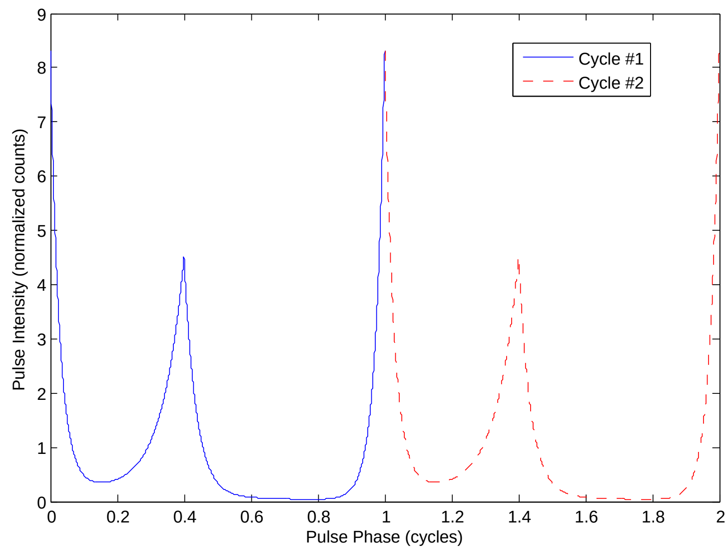

Figure 2.1: Two periods of the template for the Crab pulsar profile used in simulations.

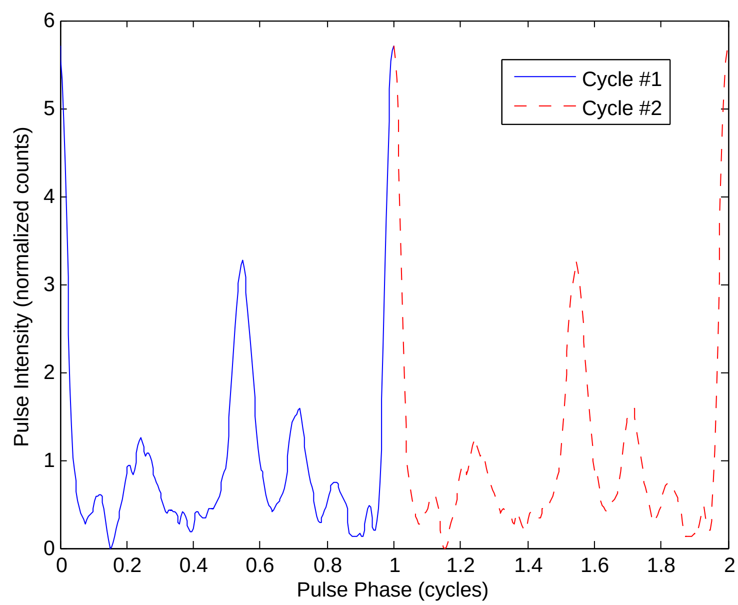

Figure 2.2: Two periods of the template for the B1821-24 pulsar profile.

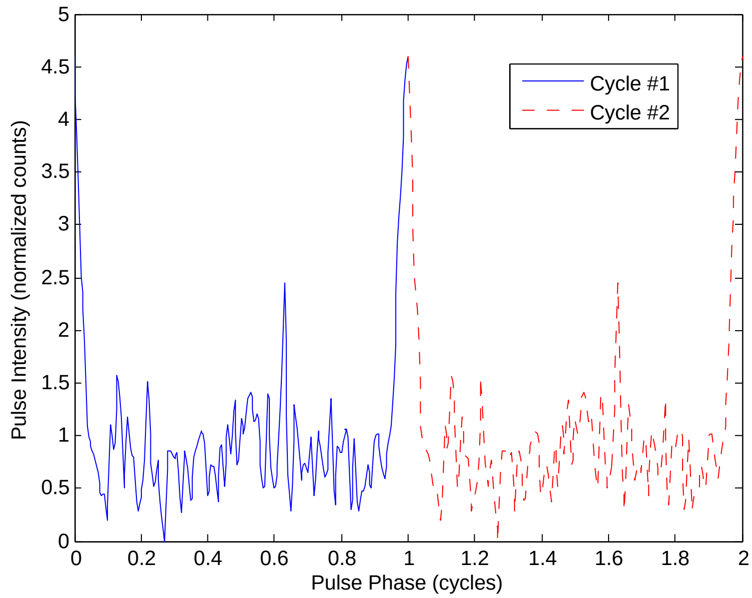

Figure 2.3: Two periods of the template for the B1937+21 pulsar profile.

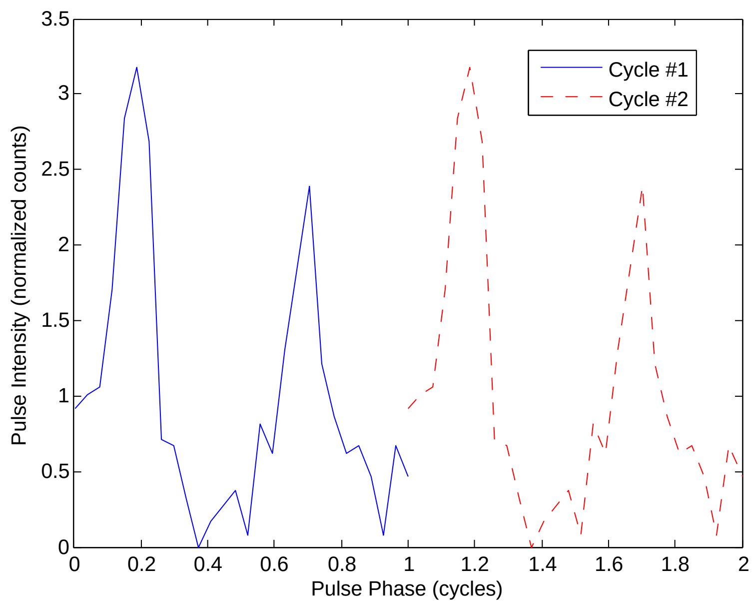

Figure 2.4: Two periods of the template for the J0218+4232 pulsar profile.

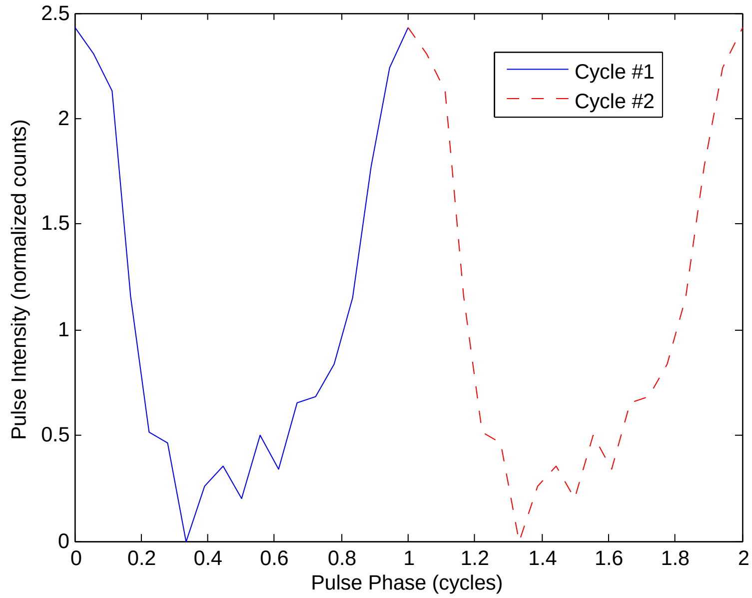

Figure 2.5: Two periods of the template for the J0437-4715 pulsar profile.

2.5 Evolution of Phase at a Detector Aboard a Spacecraft

The phase observed at the detector, $\phi_{det}(t)$, is given as the sum of the initial phase θ_0 at a reference time t_0 and the accumulation of phase since t_0, $\theta(t)$. The total phase can be expressed as the integral of the observed signal frequency over an observation interval (t_0,t) as follows:

$$\phi_{det}(t) \equiv \theta_0 + \theta(t) = \theta_0 + \int_{t_0}^{t} f(t')dt'. \tag{2.10}$$

The observed signal frequency at the detector can be broken into pulsar source frequency and Doppler frequency components: [64]

$$f(t) = f_s + f_d(t) = f_s\left(1 + v(t)/c\right), \tag{2.11}$$

where f_s is the pulsar source frequency, $f_d = f_s v(t)/c$ is the Doppler frequency shift, $v(t)$ is the range-rate of the spacecraft along the line-of-sight direction to the pulsar, and c is the speed of light. In this dissertation, the source frequency is considered constant, and the second and higher-order relativistic Doppler effects are ignored. These simplifications do not significantly limit the applicability of the results since source frequency variations are often forecast and can be accounted for using pre-processing [64]. Under these assumptions, the phase accumulated since the beginning of an observation interval is made up of a term due to the source frequency and a Doppler phase term: [64]

$$\theta(t) = f_s(t - t_0) + \int_{t_0}^{t} f_d(t')dt'. \tag{2.12}$$

The Doppler phase term is the integral of the Doppler frequency and contains information about the dynamics of the spacecraft, $\theta_d(t) = \frac{f_s}{c}\int_{t_0}^{t} v(t')dt'$. If the detector is stationary or moving at a constant range-rate then the observed signal frequency is constant and the Poisson rate function is periodic [64]. Otherwise, the variations in $\theta_d(t)$ due to the dynamics of the spacecraft cause the rate function to be quasi-periodic and the observed signal frequency at the moving detector to vary.

Total frequency will be considered, instead of f_s and f_d, to model the phase dynamics of Eq. (2.12) in a way that will allow for phase estimation using feedback of frequency and frequency derivative information from a phase-locked loop in order to allow for changing observed frequency during the estimate. The total phase at the detector is expressed as a Taylor series in terms of phase, frequency, and frequency derivatives at a particular time t_0. In order to consider a signal with varying observed signal frequency this series is approximated by a second-order Taylor polynomial as follows:

$$\phi_{det}(t) = \theta_0 + f(t - t_0) + \frac{\dot{f}}{2}(t - t_0)^2, \tag{2.13}$$

where θ_0, f, and $\dot{f}$ are the phase, frequency, and frequency derivative, respectively, at time t_0. Using these three parameters the pulsar rate function can be written as:

$$\lambda(t; \theta_0, f, \dot{f}) = \beta + \alpha h \left(\theta_0 + f(t - t_0) + \frac{\dot{f}}{2}(t - t_0)^2 \right). \tag{2.14}$$

This is equivalent to computing f_d in Eq. (2.12) assuming the acceleration is constant. The models in Eqs. (2.12) and (2.13) are explored next for constant and time-varying signal frequency.

2.5.1 Constant Observed Signal Frequency

When the detector is stationary or is moving at a constant range-rate with respect to the pulsar, the observed signal frequency will be constant. Also, the period change of the pulsar over the observation time interval should be negligible [64]. In this section a constant signal frequency model is developed for the rate function. First, notice that with constant observed signal frequency, $f = f_s(1 + v/c)$, the phase at the detector is given linearly as follows [64],

$$\phi_{det}(t) = \theta_0 + f(t - t_0). \tag{2.15}$$

Solve for the Poisson rate function by substituting Eq. (2.15) into Eq. (2.7), which gives

$$\lambda(t; \theta_0, f) = \beta + \alpha h(\theta_0 + f(t - t_0)). \tag{2.16}$$

This shows the functional dependence of the rate function on θ_0 and f and that λ is strictly periodic due to the periodicity of h when the observed signal frequency is constant.

2.5.2 Time-Varying Observed Signal Frequency

The observed phase at the detector has a term contributed by the Doppler effects when the frequency is varying [64]. In this case,

$$\phi_{det}(t) = \theta_0 + \int_{t_0}^{t} f(t')dt' = \theta_0 + \int_{t_0}^{t} [f_s + f_d(t')]dt' = \theta_0 + f_s(t - t_0) + \theta_d(t). \tag{2.17}$$

Now plug Eq. (2.17) into Eq. (2.7) to get the quasi-periodic Poisson rate function for the time-varying frequency case

$$\lambda(t) = \beta + \alpha h(\theta_0 + f_s(t - t_0) + \theta_d(t)). \tag{2.18}$$

This model must be used if the radial speed with respect to the pulsar is varying considerably over the observation interval.

Pulsar signals sporadically undergo glitches due to their internal physics which can significantly alter their spin rates [48]. After a glitch occurs the signal needs to be characterized again, and a new pulse timing model needs to be developed before that pulsar can be used again for navigation. This phenomenon is infrequent enough that this does not limit the proposed navigation scheme when a range of pulsars is available for use.

2.6 Maximum-Likelihood Phase Estimation

A method is desired to estimate parameters of the pulsar signal observed at a detector given a set of observed photon event times. The primary parameter that will be estimated in this dissertation is the phase of the observed signal at the beginning of the observation interval. Observed signal frequency is another parameter to be estimated in certain scenarios. In this dissertation a maximum-likelihood estimator will be used to estimate these pulsar signal parameters. This is the standard approach for phase estimation given Poisson data [102].

The main advantage of the MLE over other possible estimators of pulsar signal phase is that it is asymptotically efficient [64, 67]. The estimator being asymptotically efficient means that it achieves the Cramer-Rao lower bound (CRLB) on the variance of the estimator as the sample size tends to infinity [67]. The CRLB will be discussed further and compared to the performance of the MLE for signal phase in Chapter 5. There are other advantages and disadvantages as compared to nonlinear least-squares and cross-correlation methods [67].

The Maximum-Likelihood Estimator (MLE) for θ_0 and f can be derived following the approach of [64] and [102] for the constant frequency model. The goal is to estimate these parameters based on a set of photon event times, which are either a computer simulated realization of the NHPP or an experimentally detected realization of the NHPP. Additional background for MLEs including an example with computation is included in Appendix C.

Assume that the pulse profile function $h(\phi)$, effective source arrival rate α, and effective background arrival rate β are all known. Consider an observation interval $(t_0, t_0 + T_{obs})$ and a set of photon events $\{t_k\}_{k=0}^{K}$ with $t_0 < t_k < t_0 + T_{obs} \;\; \forall k$. These photon events are a realization of the NHPP for the pulsar with rate function $\lambda(t; \theta_0, f)$ given by Eq. (2.16). The aim is to estimate the model parameters θ_0 and f.

The first step is to compute the K-dimensional joint probability density function (pdf) of the NHPP realization, $f(\{t_k\})$. This is achieved by considering infinitesimal intervals of length Δt_k centered around each $t_k, k = 1, 2, \cdots, K$. The joint pdf can be computed by looking at the probability that one and only one photon arrives within each interval and none outside of them [64], i.e.,

$$
\begin{aligned}
f(\{t_k\})\Delta t_1 \Delta t_2 \cdots \Delta t_K = \Pr[0; (t_0, t_1 - \Delta t_1/2)] \\
\times \Pr[1; (t_1 - \Delta t_1/2, t_1 + \Delta t_1/2)] \\
\times \Pr[0; (t_1 + \Delta t_1/2, t_2 - \Delta t_2/2))] \times \cdots \\
\times \Pr[1; (t_K - \Delta t_K/2, t_K + \Delta t_K/2)] \\
\times \Pr[0; (t_K + \Delta t_K/2, t_0 + T_{obs})]. \qquad (2.19)
\end{aligned}
$$

From the consequences of the NHPP model, plug Eqs. (2.5) and (2.6) into Eq. (2.19). Now take $\Delta t_k \to 0$ for all $1 \leq k \leq K$. This yields the joint pdf evaluated at the observed photon event times,

$$
f(\{t_k\}) = \exp\left[-\int_{t_0}^{t_0 + T_{obs}} \lambda(t; \theta_0, f) dt \right] \prod_{k=1}^{K} \lambda(t_k; \theta_0, f), \qquad (2.20)
$$

which is the likelihood function [64]. The desired MLE solves for the values of θ_0 and f at which the likelihood function is maximized. It is equivalent to consider the logarithm of the likelihood function (LLF), which is easier to maximize,

$$LLF(\tilde{\theta}_0, \tilde{f}) \equiv \sum_{k=1}^{K} \log[\lambda(t_k; \tilde{\theta}_0, \tilde{f})] - \int_{t_0}^{t_0+T_{obs}} \lambda(t_k; \tilde{\theta}_0, \tilde{f}) dt. \tag{2.21}$$

Here log is the natural logarithm, and $\tilde{\theta}_0$ and $\tilde{f}$ are the values at which the LLF is computed. In most cases, the integral in Eq. (2.21) can be dropped since it displays a minimal dependence on the search model parameters. This minimal dependence holds when the observation interval lasts many cycles of the signal at the expected frequency ($\tilde{f}T_{obs} \gg 1$) [64]. The optimization problem that needs to be solved by the MLE is as follows:

$$(\hat{\theta}_0, \hat{f}) = argmax_{\tilde{\theta}_0 \in \Theta, \tilde{f} \in \Omega} \sum_{k=1}^{K} \log[\beta + \alpha h(\tilde{\theta}_0 + \tilde{f}(t_k - t_0))], \tag{2.22}$$

where Θ and Ω are the search spaces for phase and frequency, respectively. The optimization domain is non-convex with many local maximums. Thus, solving this maximization is done by brute force with nested, iterative grid-searches. Each iteration searches a smaller region, but with greater precision around the output of the previous iteration. The simulation methods used will be discussed in a later section. There are also more sophisticated methods that attempt to decrease the MLE run time. For example, [105] uses a discrete Fourier transform procedure to increase speed, but it sacrifices the guarantee that the output is a maximum.

If it is assumed that the signal frequency and Doppler shift are known, then Eq. (2.22) reduces to a phase-only optimization,

$$\hat{\theta}_0 = argmax_{\tilde{\theta}_0 \in \Theta} LLF(\tilde{\theta}_0, f_{ref}), \tag{2.23}$$

where f_{ref} is the a-priori known signal frequency. It was shown in [64] that the performance of this MLE is optimal since it achieves the Cramer-Rao performance bound after a certain threshold. Figure 2.6 contains an example of the top level of a grid search performed to maximize the LLF over phases in the interval $\Theta = [0, 1)$ using Eq. (2.23). The grid tested phases every 0.005 cycles. A clear peak is observed that corresponds to the estimate of the phase at the beginning of the observation interval computed by the MLE.

If the observed signal frequency is constant, the measurement of the initial phase θ_0 by the MLE and knowledge of the frequency f, either a-priori or from the MLE, is sufficient to determine the phase over the entire observation interval. This is because the phase at the detector has a linear dependence on θ_0 and f if the signal frequency is constant, as seen in Eq. (2.15).

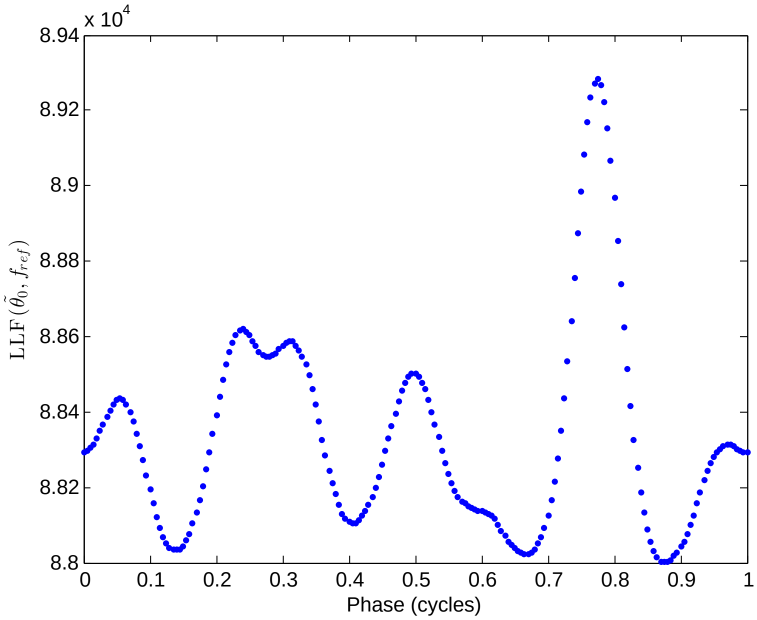

Figure 2.6: Example plot of the top level of an MLE grid search showing values of the LLF evaluated at a range of phases every 0.005 cycles from 0 to 1 that is used to estimate the phase at the start of an observation of a PSR B1821-24 signal simulated on a detector moving at a constant acceleration along the line-of-sight to the pulsar.

Chapter 3: General Phase Tracking

3.1 Overview

This chapter introduces the method of phase tracking a pulsar signal as used for spacecraft navigation. The various building blocks used to track pulsar signal phase are introduced along with a discussion of previous research in the area.

Motivation for tracking phase as a method of spacecraft navigation is discussed in Section 3.2. This includes providing relations connecting a spacecraft's position and velocity with the phase and frequency of a pulsar signal observed at a detector on the spacecraft.

In Section 3.3, the method developed in [64] by Golshan and Sheikh for phase tracking pulsar signals is introduced. This method consists of breaking an observation of photon event times into one second intervals and estimating the initial phase using an MLE on each set of photons. The phase estimates are smoothed with a second-order digital phase locked loop (DPLL).

The use of digital phase-locked loops for pulsar signal tracking is described in Section 3.4. A discussion of the difference between the ways DPLLs are being used for pulsar phase tracking versus common practice is included along with an example demonstrating the use of a DPLL for frequency modulation (FM) signal demodulation.

In Section 3.5, the method of phase tracking introduced by Golshan and Sheikh in [64] is investigated and confirmed using lab experiments with the NASA Goddard X-ray Laboratory Testbed (GXLT) and computer simulations. The method is tested to track the phase of the Crab pulsar signal for a series of simulated detector trajectories. The accuracy of the MLE for phase estimation is also compared between computer simulations and experiments with the GXLT. The use of the GXLT tests the phase tracking algorithm under conditions including x-ray photon generation and detection that were previously only considered using ideal models in computer simulations.

Section 3.6 provides a discussion of difficulties that are encountered when extending the Golshan and Sheikh phase tracking method of [64] to millisecond period pulsars (MSPs). The flux is too low for the method to be used in the same manner as with the Crab pulsar without either increasing the block length or the detector size. There is a trade-off between the accuracy of the ML-phase estimates and the dynamic stress of the spacecraft trajectory. Most of the pulsars with the best characteristics for use in spacecraft navigation are MSPs. The case is made that modifications to the phase tracking algorithm are needed for it to be used with MSPs and a reasonable sized x-ray detector.

3.2 Motivation for Phase Tracking

The phase and frequency of a pulsar signal as observed at a detector moving through space can provide a direct link to the spacecraft's one-dimensional position and velocity along the LOS to the pulsar through the following equations [106]:

$$x = c\left[\frac{\phi - \phi_0}{f_s} - t\right] + x_0 \tag{3.1}$$

$$\dot{x} = v = \frac{c}{f_s}\left(f - f_s\right) = \frac{c}{f_s} f_d, \tag{3.2}$$

where x is the position of the spacecraft at time t, x_0 is the position of the spacecraft at the initial time $t_0 = 0$, ϕ is the phase of the pulsar signal at time t, ϕ_0 is the initial phase at time $t_0 = 0$, f_s is the source frequency of the pulsar, which is assumed constant, f_d is the Doppler frequency shift of the observed signal to first order and c is the speed of light. Eq. (3.1) can be modified to instead relate the change in position over a change in time with the evolution of the observed phase. This removes the reference position x_0 and can be written in a more compact form

$$\Delta x = c\left[\frac{\Delta\phi}{f_s} - \Delta t\right], \tag{3.3}$$

where Δx is the change in a spacecraft's position over a change in time Δt and $\Delta\phi$ is the change in the observed signal phase over the same time.

Tracking the phase and frequency of an observed pulsar signal over time provides an estimate of the trajectory of a spacecraft through the links to position and velocity using Eqs. (3.1) and (3.2). This motivates research into methods of extracting estimates of phase and frequency from observations of a pulsar signal onboard a spacecraft.

3.3 Previous Pulsar Phase Tracking Methods

When a spacecraft's trajectory curves with respect to the line-of-sight (LOS) to a pulsar the observed frequency of that pulsar's signal as determined at a detector onboard the spacecraft cannot be considered constant. Thus, for a spacecraft in orbit that is tracking a pulsar signal it is necessary to have a means of estimating the phase of the signal at the detector over time. This can be done through methods of phase tracking.

The previous work on pulsar signal phase tracking by Golshan and Sheikh [64] broke the observations of photons arriving at a spacecraft's detector into sets or blocks one second in length. This block size was chosen to allow the observed signal frequency to be considered constant over each individual block. Over each block an MLE was used to estimate the phase of the pulsar signal at the middle of the block. The phase model used in the MLE was linear and was based on Eq. (2.13) with $\dot{f} = 0$. A second-order DPLL was then used to smooth the estimates from successive blocks to better account for modeling errors and noise. The second-order DPLL provides an estimate of the phase and Doppler frequency for each block. The DPLL is updated each block with a new MLE phase estimate and continues to give its own estimates as long as it remains in lock. Figure 3.1 outlines the flow of the process that takes the photon events observed during a block and returns the estimate of

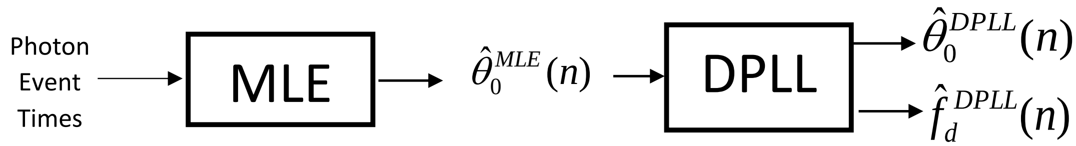

Figure 3.1: Each block of photon event times is processed through the MLE-DPLL cascade outlined in this diagram to reduce phase tracking errors [64].

phase and frequency corresponding to the time at the center of the block. Figure 3.2 demonstrates in a diagram the phase-tracking method introduced by Golshan and Sheikh. The sequence $\hat{\theta}_0$ provides information about the navigational state of the spacecraft.

3.4 Discussion of Digital Phase-Locked Loops

An overview of the digital phase-locked loop (DPLL) used in the phase tracking algorithm is presented in this section. The concepts are discussed in a broad fashion to set up for the extension to higher order DPLLs in the later chapters of this dissertation. Figure 3.3 contains a conceptual block diagram illustrating the flow of a DPLL. The diagram represents the tasks performed by the DPLL during a single update interval, which is equal to the block length that the total observation of photon events is divided into for the phase tracking algorithm. Figure 3.3 shows the interactions of the major components of the DPLL. The ideal phase extractor computes the difference between the ML-estimate of phase and the model phase

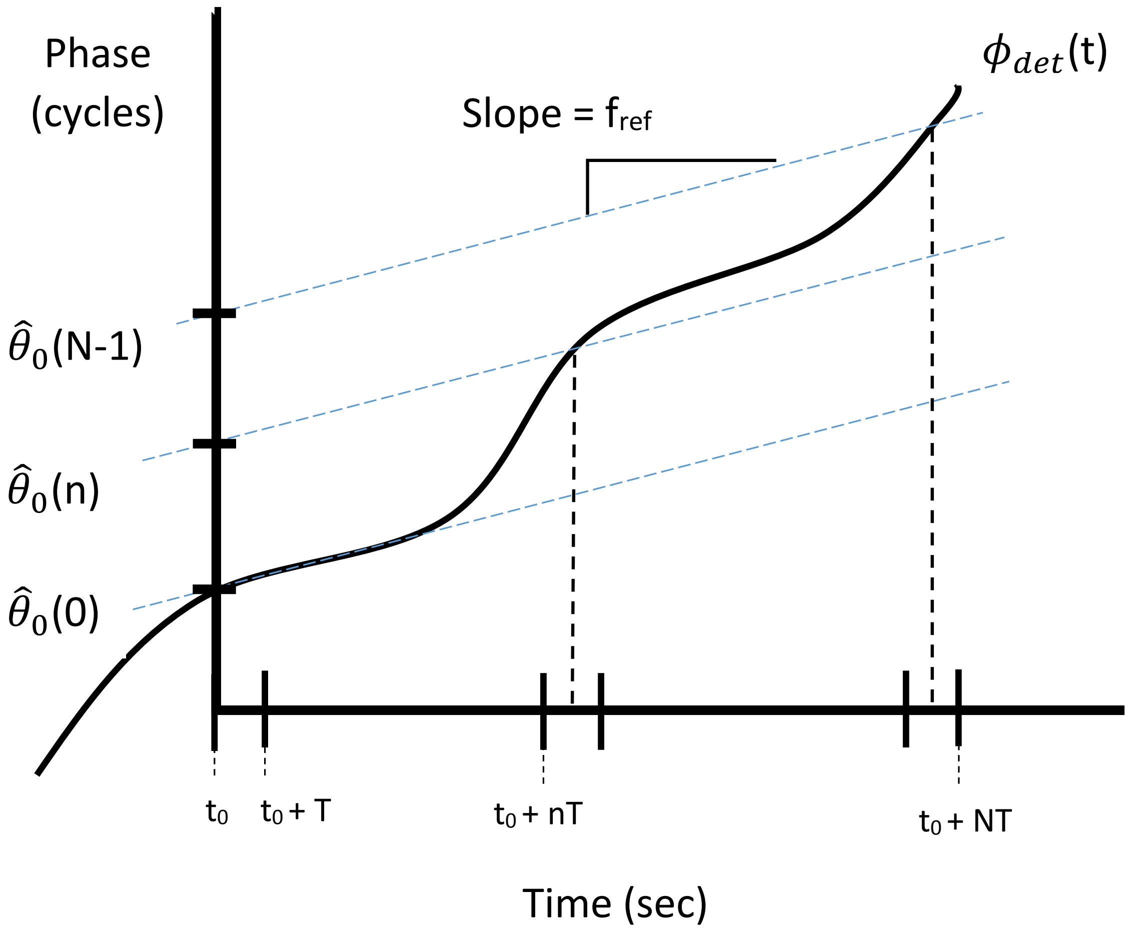

Figure 3.2: This diagram demonstrates the pulse phase-tracking concept introduced by Golshan and Sheikh in [64].

generated by the numerically controlled oscillator (NCO). Outputs of the phase, frequency, and frequency derivative of the DPLL signal model are used in the next iteration of the phase tracking algorithm depending on the order of the DPLL.

The phase extractor is considered to be ideal and directly uses the nth MLE phase measurement as the input signal phase for the nth block:

$$\tilde{\phi}(n) = \hat{\theta}_0^{MLE}(n) - \hat{\phi}^{DPLL}(n), \tag{3.4}$$

where $\tilde{\phi}(n)$ and $\hat{\phi}^{DPLL}(n)$ are the residual phase and the DPLL model phase referenced to the beginning of the block, respectively, for the nth update interval. This difference is carried out without wrapping around the phase. The state of the loop filter is updated using the residual phase as a phase error feedback. For a third order filter this is formulated as follows:

$$\hat{f}^{DPLL}(n+1)T = K_1\tilde{\phi}(n) + K_2\sum_{i=1}^{n}\tilde{\phi}(i) + K_3\sum_{i=1}^{n}\sum_{j=1}^{i}\tilde{\phi}(j), \tag{3.5}$$

where K_1, K_2, and K_3 are the loop constants, which are set according to their relationships with B_L, root-specific decay rate, and root-specific damping as derived in [107], and $\hat{f}^{DPLL}(n+1)T$ is the phase change per update interval T. For a second-order DPLL, $K_3 = 0$. Outputs can be generated for derivatives of the frequency of the DPLL signal by solving for them in terms of the accumulator values [107]. For example, the frequency derivative output for the nth block is

$$\dot{f}^{DPLL}(n) = \frac{K_3}{T^2}\sum_{i=1}^{n}\tilde{\phi}(i). \tag{3.6}$$

The sequence $\hat{f}_d^{DPLL}(n+1)T$ drives a numerically controlled oscillator (NCO), which sets the amount the current NCO phase must be advanced to achieve the model phase at the center of the next block [107]. This model phase is given by the phase accumulation at baseband of the NCO as follows:

$$\hat{\phi}^{DPLL}(n+1) = \hat{\phi}^{DPLL}(n) + \hat{f}^{DPLL}(n+1)T + \hat{\dot{f}}^{DPLL}(n+1)\frac{T^2}{2}. \qquad (3.7)$$

Under the formulation of the DPLL in [107], the model phase, frequency, and frequency derivative values are referenced to the center of each block. Care must be taken when computing the phase residual because the MLE phase estimate is for the beginning of the block. Thus, the DPLL model phase must be translated back to the start of the nth update interval before being used in Eq. (3.4). In order to minimize the time before lock is acquired, the transient-free acquisition method of [107] is used. This procedure uses initial estimates of phase, frequency, and frequency derivative to set the values of the accumulators and the residual phase as if a fictitious block of photons has already been processed.

3.4.1 DPLL Example for FM Signal Tracking

An example of a DPLL used to demodulate a frequency modulation (FM) signal is presented in this section to illustrate the relation to more common uses of the DPLL. A good reference for the use of phase-locked loops on FM signals is Chapter 4 of [110].

Frequency modulation transmits a message $m(t)$ by varying the instantaneous frequency $f_i(t)$ of a sinusoidal carrier signal linearly with the message signal $m(t)$ as follows:

$$f_i(t) = f_c + k_f m(t), \qquad (3.8)$$

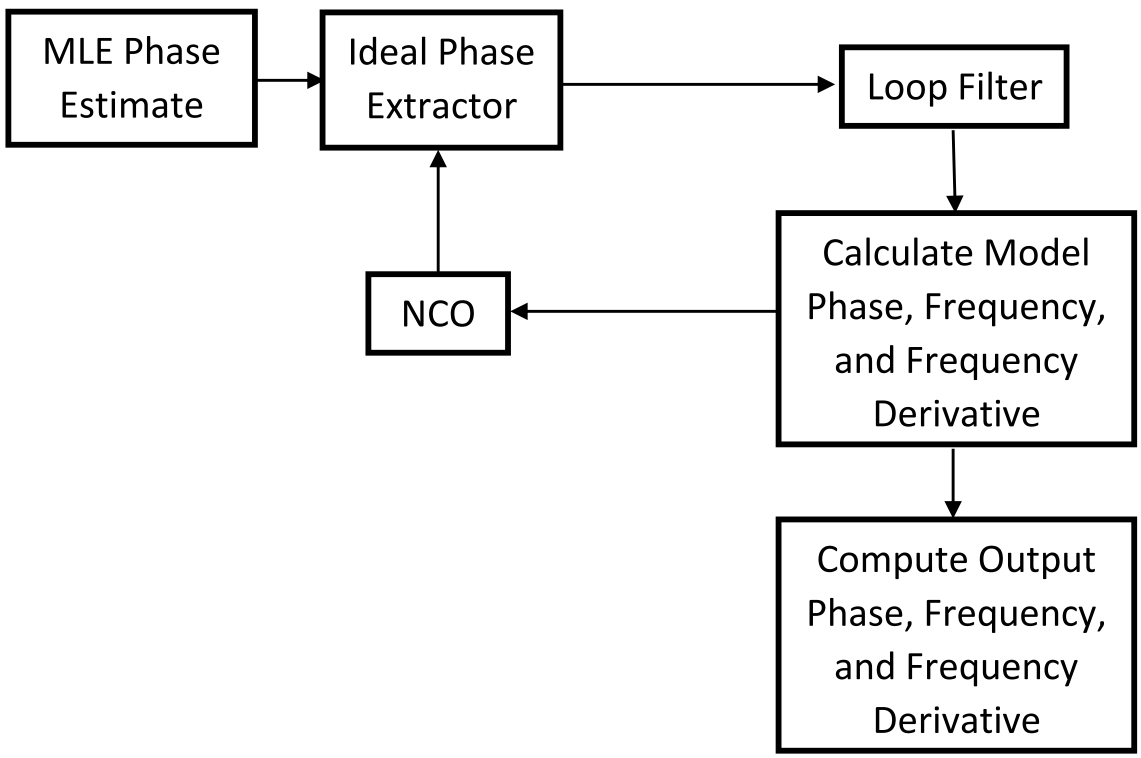

Figure 3.3: This figure is a conceptual block diagram of a DPLL [59]. The diagram represents the tasks performed by the DPLL during a single update interval, which is equal to the block length of the phase tracking algorithm.

where f_c is the frequency of the carrier signal and k_f is the frequency sensitivity of the modulator. An FM signal $s(t)$ is defined as a function of a modulating signal $m(t)$ as

$$s(t) = A_c \sin\left[2\pi\left(f_c t + k_f \int_0^t m(\tau)d\tau\right)\right], \tag{3.9}$$

where A_c is the carrier amplitude [110]. The phase $\phi_1(t)$ of the FM signal is defined in terms of $m(t)$ as

$$\phi_1(t) = 2\pi k_f \int_0^t m(\tau)d\tau. \tag{3.10}$$

A phase-locked loop (PLL) is a negative feedback system that can be used for many applications relating to FM signals including frequency demodulation [110]. A block diagram demonstrating the basic structure of a PLL operating on a FM signal $s(t)$ is included in Figure 3.4. The three major components of the PLL are a multiplier that acts as a phase detector, a loop filter, and a voltage-controlled oscillator (VCO) [110].

The voltage $v(t)$ is the output of the PLL and depending on the design of the PLL it can be driven to be a signal that is in phase-lock with the modulating signal $m(t)$. This allows for the message to be recovered. The voltage-controlled oscillator is a sinusoidal generator that has a frequency that is driven by the voltage output from the loop filter. Thus, the output of the VCO can be defined as

$$y(t) = A_v \cos\left[2\pi\left(f_c t + k_v \int_0^t v(\tau)d\tau\right)\right], \tag{3.11}$$

where A_v is the amplitude of the VCO output and k_v is the frequency sensitivity of the VCO [110]. The phase $\phi_2(t)$ of the VCO signal is defined in terms of the PLL

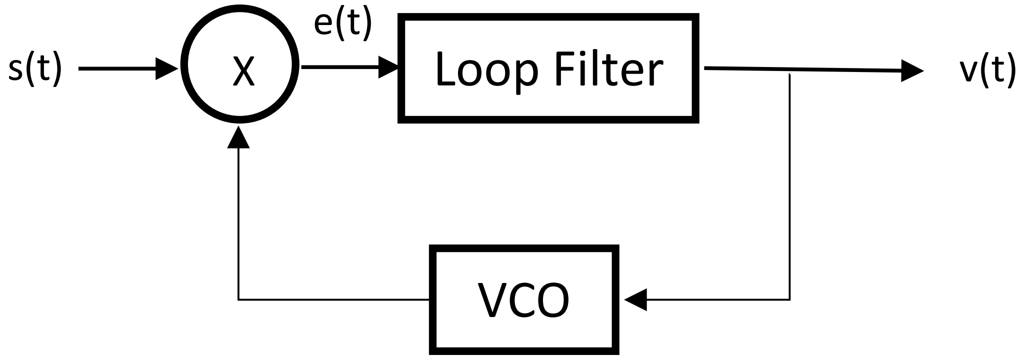

Figure 3.4: Phase-locked loop structure as used to track an FM signal s(t). [110]

output voltage $v(t)$ as

$$\phi_2(t) = 2\pi k_v \int_0^t v(\tau) d\tau. \tag{3.12}$$

Since the PLL loop filter is a low-pass filter the phase detector, which determines the error e(t) after the multiplier seen in Figure 3.4, can be simplified to

$$e(t) = A_c A_v \sin[\phi_1(t) - \phi_2(t)]. \tag{3.13}$$

The loop filter can be digitalized as accumulators as expressed in Eq. (3.5).

Now as a specific example, consider the following two-tone modulating signal

$$m(t) = 0.3 \sin\left(2\pi \frac{f_m}{4} t\right) + 0.2 \cos\left(2\pi f_m t\right). \tag{3.14}$$

This modulating signal is then used to define an FM signal $s(t)$ using Eq. (3.9) with a carrier frequency of $f_c = 100$ kHz and a modulation signal frequency of $f_m = 1$ kHz. The other constants used to define $s(t)$ and the VCO output are included in

Table 3.1. The modulating signal $m(t)$ is plotted for 5 ms in Figure 3.5 along with the phase of the transmitted signal $\phi_1(t)$.

A digital model of the PLL for FM signals will now be presented that acts as a frequency demodulator to recover the phase of the original message $m(t)$. The sampling rate of the FM signal is 3200 kHz. A second-order DPLL was considered with a loop noise bandwidth of $B_L = 200$ kHz, a damping ratio of $\zeta = 0.7071$, and an update interval of T = 0.0003125 ms. The value for the DPLL update interval was set equal to the sampling period of the FM signal. Using the methods of [107] the loop constants were determined by the choice of B_L, T, and ζ to be $K_1 = 0.146248$ and $K_2 = 0.0115498$.

Table 3.1: FM signal and VCO parameters.

Parameter	Value
f_c, kHz	100
f_m, kHz	1
A_c	1
k_f, kHz/V	10
A_v	1
k_v, kHz/V	20

The results of a 5 ms simulation of the operation of the DPLL on the FM signal are presented in Figure 3.6. This figure includes plots of the modulating signal, the recovered output voltage signal, and the phase detector output. It can be seen from the phase detector output that after an initial settling period the phase error is driven close to zero with a small oscillatory error remaining. This results

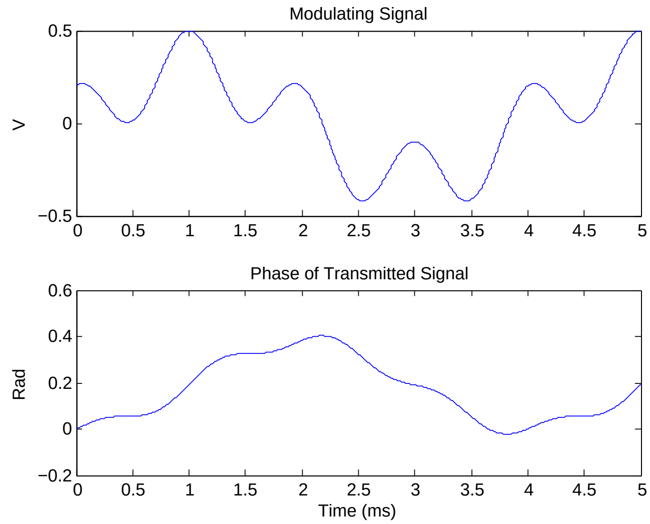

Figure 3.5: The modulating signal $m(t)$ along with the phase of the transmitted signal ϕ_1(t) plotted over 5 ms.

in the recovered signal tracking the modulating signal after an initial settling time of under 0.5 ms. The voltage signal tracks the phase of the modulating signal and recreates the message with an amplitude offset.

This FM signal example provides insight into the use of DPLLs for pulsar applications because there are some similarities between extracting message information from an FM signal and extracting spacecraft dynamic information from an observed pulsar signal. The carrier frequency of the FM signal is like the pulsar signal frequency observed at the inertial reference point, the SSB. The modulating signal that contains the message is like the dynamic motion of the spacecraft. The main difference and complication is that the FM signal can be sampled at a much higher rate than the pulsar signal. Also, there are direct methods of sampling the FM signal whereas the x-ray pulsar signal can only be sampled through probabilistic

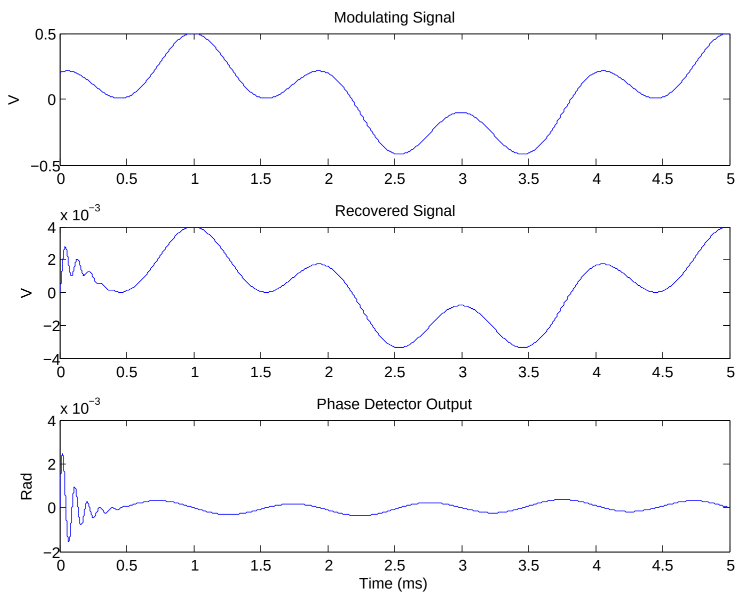

Figure 3.6: This figure compares the recovered voltage signal that is output from the second-order DPLL to the modulating signal of the FM input. The phase detector output is also plotted to show the phase error under the operation of the DPLL.

methods due to the primary measurement being the photon event times. This leads to the need for different methods of phase detection and subsequent complications to the operation of the DPLL.

3.5 Lab Experiments vs. Simulations using the Crab Pulsar

The phase-tracking method proposed by Golshan and Sheikh was previously tested in simulations in [64]. The methods of [108] were used to generate realizations of the NHPP corresponding to the photon event times arriving from a simulation of the Crab pulsar. The Doppler phase profile derived from an observation of the Crab pulsar on-board the RXTE spacecraft was used to add motion effects to the sets of simulated photon event times.

In this dissertation, computer simulations using Matlab were performed to test the MLE for initial phase and the phase tracking algorithm based on the MLE-DPLL cascade proposed in [64] using simulated models of the Crab pulsar. These results were compared to the results of Golshan and Sheikh in [64] as well as experimental results performed for this dissertation using a laboratory based pulsar simulation testbed at the NASA Goddard Space Flight Center (GSFC) called the GSFC X-ray Navigation Laboratory Testbed (GXLT).

In [64], three different flux scenarios corresponding to different α and β values were used to test the MLE and MLE-DPLL cascade over a range of operating conditions. In the simulations to test the MLE and MLE-DPLL cascade in this dissertation, the flux levels were chosen to be similar to the levels anticipated at the

NICER instrument onboard the ISS. These correspond to the values of α and β used to model observation of the Crab pulsar with the GXLT. The parameters used to simulate the signal of the Crab pulsar are included in Table 3.2. These parameters correspond to a detector area of 176.2523 cm^2.

Table 3.2: Crab Pulsar parameters used for Matlab-based XPRESS simulations and GXLT experiments. The GXLT detector area of 176.2523 cm^2 was used.

	B0531+31 (Crab)
f_s, Hz	29.9401
α, ph/s	190
β, ph/s	1510
R_S, ph/cm^2/s	1.54
R_B, ph/cm^2/s	8.1053
ρ (Pulse Fraction)	0.7

3.5.1 Simulation Structure

This section details the Matlab based simulations used to test the phase tracking method introduced by Golshan and Sheikh in [64]. The X-ray Photons and Relativistic Effects Simulation System (XPRESS), developed by ASTER Labs, Inc. and collaborators, was used to simulate the photon event times used for these simulations. The experimental simulations using the GXLT will be discussed in the next section.

First, the MLE and pulse phase tracking MLE-DPLL cascade were tested in a computer simulation environment using MATLAB. The simulated photon event times at the detector are generated by a realization of the NHPP with rate function given by Eq. (2.7). This set of photon events was first generated as if they were located at the solar system barycenter (SSB), and then delay was added in order to account for the offset between the detector and the SSB. The generation of the NHPP realization for the photon event times along with the addition of the geometric and relativistic delay effects were implemented using XPRESS. The NHPP photon generation is completed using the inversion method of non-uniform random variate generation presented in [108] and implemented for the specific example of X-ray pulsar photon generation in [67]. The methods used to produce simulated realizations of the NHPP for photon event times are presented in Appendix A.

The general relativistic delay and Doppler effects must be taken into account to transfer the barycentric set of photon event times at the SSB to a set arriving at the spacecraft detector. To first order, the time transfer corresponding to the geometric delay is given by

$$t_{SSB} - t_{sc} = \frac{\hat{\mathbf{n}} \cdot \mathbf{r}}{c}, \tag{3.15}$$

where t_{SSB} is the time at the SSB, t_{sc} is the time at the spacecraft, $\hat{\mathbf{n}}$ is the unit normal vector pointing from the SSB to the pulsar, and $\mathbf{r}$ is the position vector of the spacecraft with respect to the SSB, as seen in Figure 3.7 [94]. This set of photon events at the spacecraft detector is what is processed by the MLE or MLE-DPLL algorithms. The distance of the pulsar allows the pulses to be assumed to be arriving as uniform wave fronts throughout the solar system, as depicted in Figure 3.7 [94].

An outline of the process used to generate the barycentric photon event times and translate them to a time frame moving with the detector on the spacecraft is

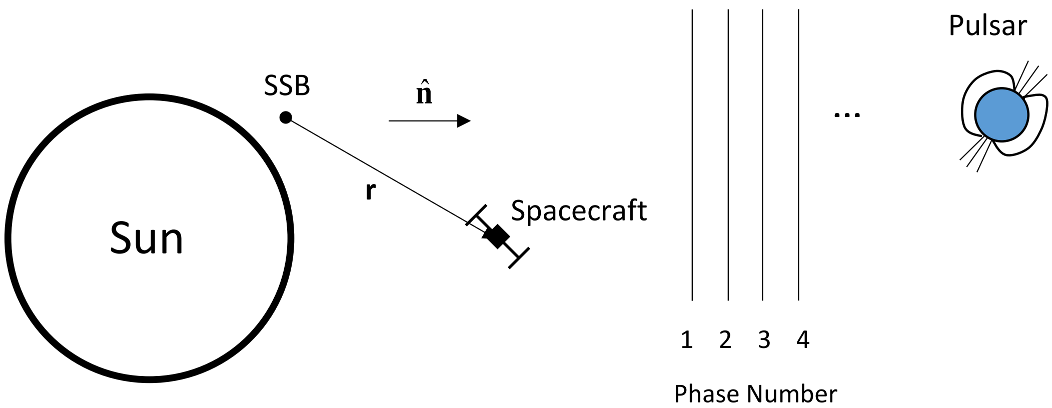

Figure 3.7: The relationship between the spacecraft position, the SSB, and the arriving pulses [94].

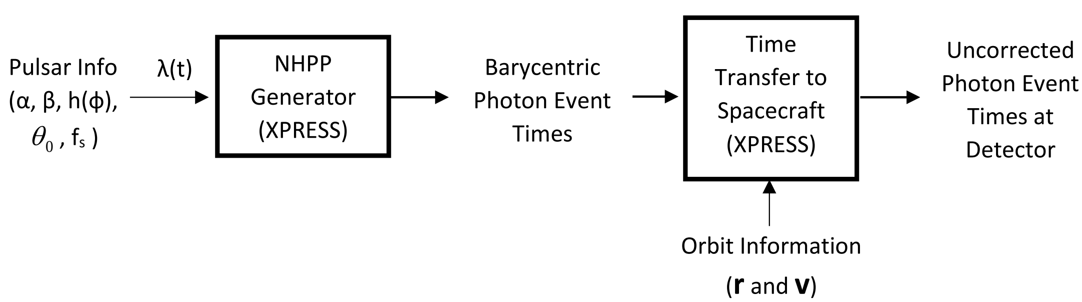

Figure 3.8: Outline of the simulation process to generate photon event times at the SSB and translate them to equivalent event times at a detector on a moving spacecraft.

included in Figure 3.8 . The first step generates the barycentric photon event times as a realization of an NHPP using the rate function defined by the input parameters of the pulsar including α, β, h(ϕ), f_s, and θ_0. The second step performs the time transfer of the barycentric photon event times to an uncorrected set of photon event times at the detector using the truth orbit information for the spacecraft, **r** and **v**. Both steps are performed by XPRESS with the sets of photon event times at the SSB and the spacecraft as outputs. This process uses the truth information about both the pulsar model and the spacecraft orbit to create the sets of photon events as they would arrive at the spacecraft. These photon event times are then used as the measurements to create the estimates of the navigational state of the spacecraft. This process requires the pulsar parameter information, but not the truth trajectory information.

Table 3.3 contains descriptions of the various scenarios tested with simulations of the Crab pulsar. There were three types of trajectories considered, two with constant and one with changing observed signal frequency. All three trajectories consist of the spacecraft moving along a one-dimensional path along the line-of-sight (LOS) to the Crab pulsar. The stationary and constant velocity simulations have constant pulsar signal frequency at the spacecraft. The constant acceleration scenarios have a time-varying pulsar signal frequency that needs to be estimated and tracked at the spacecraft. Two different levels of acceleration were considered to test the phase tracking method under lower and higher dynamic stress represented by accelerations of 0.1 km/s^2 and 5 km/s^2, respectively.

In the constant signal frequency case the MLE algorithm is run using all of the photon events in the entire observation interval. This produces estimates for the phase at the detector at all times in the observation because the phase is given linearly by Eq. (2.15) and the MLE gives estimates of the unknown model parameters. This method is used to test both cases where the detector is stationary and where the detector is moving with a constant range rate with respect to the pulsar.

When the signal frequency is time-varying the observation interval is broken up into blocks of one second, and the pulse phase tracking algorithm is used along with the MLE-DPLL cascade structure. For each block the MLE algorithm is used to estimate the phase at the beginning of the observation using the set of photon times that arrived in the second of the observation considered in that block. The results of these simulations will be presented in Section 3.5.3 and compared to the results from the experimental GXLT simulations. The parameters used for the second-order DPLL in the MLE-DPLL cascade for the phase tracking algorithm are detailed in Table 3.4 . The choices of noise bandwidth $B_L = 0.05$ Hz, update time T = 1 s, and damping ratio $\zeta = 0.707$ together are used to determine the loop constants K_1 and K_2 using the formulations in [107]. The damping ratio was chosen to yield an underdamped response with all of the loop roots having the same decay rate. The noise bandwidth was chosen to balance the responsiveness of the DPLL to the dynamics with the accuracy of the phase estimates.

Table 3.3: Descriptions of the performed simulations with the Crab Pulsar.

Type	θ_0	v_0, km/s	a, km/s^2	Initial f_d, Hz	Observation time, s
Stationary	0.5	0	0	29.9401	10
Constant v	0.5	1	0	29.9402	10
Constant a	0.3	0	0.1	29.9401	200
Constant a	0.5	1	5	29.9402	250

Table 3.4: Settings used for the DPLL parameters in the MLE-DPLL cascade for the Crab pulsar simulations.

DPLL Parameter	Value
T, s	1
B_L, Hz	0.05
ζ	0.707
K_1	0.1199
K_2	0.007658

3.5.2 Experimental Setup

This section describes the GXLT simulations used to test the Golshan and Sheikh phase tracking method. The same scenarios detailed in Table 3.3 for the Matlab-based simulations of the last section were also performed using the GXLT. The results are presented and compared in the next section.

The GXLT is made up of four major components: the X-Ray Digital Pulse Generator (XDPG), which creates a real-time implementation of the pulsar rate signal given in Eq. (2.7), the Modulated X-Ray Source (MXS), which emits the X-ray photons, the Silicon Drift Detector (SDD), which receives the photons and produces a single short pulse using a pulse shaping filter, and the Time-Tagging X-Ray Detector (XDET), which puts a time stamp on the photon pulses from the SDD [41]. The XDPG takes the pulsar definition and the desired phase dynamics derived from the spacecraft motion and creates a real-time implementation of the rate-function at the spacecraft. The XDPG then drives the input of the MXS to generate a realization of the NHPP [41]. Figure 3.9 illustrates the interconnections of the lab equipment and their use in generating the desired X-ray photons.

The simulated sets of photons produced by the GXLT were processed for the different scenarios in the same manner as the Matlab simulated photon event times in the last section. For the constant observed signal frequency case the MLE algorithm is run using the entire observation. In the time-varying observed signal frequency cases, with the constant acceleration trajectories along the LOS to the Crab pulsar, the MLE-DPLL cascade was used with a block time of one second. The same DPLL parameters as outlined in Table 3.4 were used to process the MLE estimates based on the GXLT generated photon event times.

3.5.3 Results

The scenarios listed in Table 3.3 were performed both using Matlab-based simulations and GXLT-based simulations. The area of the detector was set to 176.2523 cm^2 for the Matlab-based simulations to match the GXLT. The parameters of the Crab pulsar signal that correspond to this detector area are listed in Table 3.2 . The background level is determined from the assumed detector noise rejection for

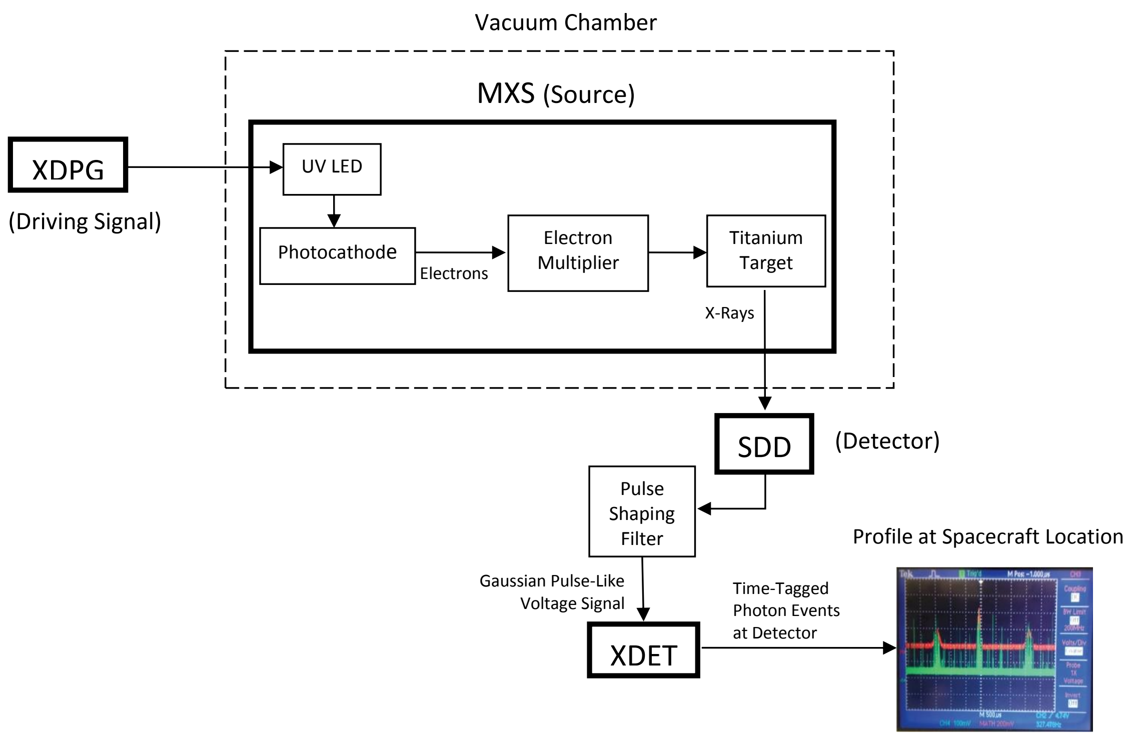

Figure 3.9: Diagram of the GXLT process used to generate X-ray photons that model pulsar emissions received at a moving detector.

the silicon drift detector used in the GXLT along with the model of the Crab pulsar emission physics.

First, the results for the scenarios with a constant observed signal frequency are considered. For the stationary and constant range-rate trajectories, each simulation was performed ten times with unique realizations of the NHPP to get an average of the phase MLE performance for both the Matlab and GXLT simulations. This was done to remove some of the impacts of non-deterministic effects like noise on the accuracy of the MLE algorithm. Each observation was ten seconds in duration. The stationary trajectory consisted of a detector placed at roughly 1 AU along the LOS to the Crab pulsar with the exact distance from the SSB chosen to have an initial phase at the detector of $\theta_0 = 0.5$. The constant velocity trajectory consisted of a detector that started at the same initial position with the same initial phase as the stationary detector, but with a range-rate of 1 km/s along the LOS toward the Crab pulsar.

The MLE results from the Matlab-based simulations and GXLT experiments are displayed in Table 3.5 and Table 3.6, respectively. The Matlab simulated results had 0.077% error from the true initial phase of $\theta_0 = 0.5$ for the stationary trajectory and 0.012% error for the constant velocity trajectory. The results from the GXLT runs had 2.46% error for the stationary trajectory and 1.63% error for the constant velocity trajectory. The GXLT runs had error two orders of magnitude higher than the simulations done in Matlab. This increase in error was likely due to the improved modeling of background and noise using the pulsar emulator and detector in the GXLT. This led to a more realistic simulation and to including error

Table 3.5: MLE results from Matlab simulations.

Type of Run	Average θ_0	Percent Error
Stationary	0.500385	0.077
Constant v	0.50006	0.012

Table 3.6: MLE results from GXLT experiments.

Type of Run	Average θ_0	Percent Error
Stationary	0.512305	2.461
Constant v	0.50816	1.632

sources that were possibly undervalued or ignored in the Matlab simulations. The levels of error for the GXLT simulations were still very reasonable for estimating the phase of the pulsar signal even with the increase over the Matlab simulations.

Next the results for the scenarios with a changing observed signal frequency are presented. Two trajectories with different constant accelerations along the LOS to the Crab pulsar were considered. Both trajectories started near the position of the stationary detector, but were offset for an initial phase of $\theta_0 = 0.3$. The low acceleration case started with zero initial velocity and had a constant acceleration of 0.1 km/s^2. The high acceleration case started with $v_0 = 1$ km/s and had a constant acceleration of 5 km/s^2. The goal of the high acceleration trajectory was to test whether the phase-tracking algorithm could adequately track the trajectory with a significantly higher acceleration and thus increased dynamic stress.

In the phase-tracking algorithm the DPLL update interval was set to one second. The loop phase and frequency for the second-order DPLL were initiated using

$\hat{\theta}_0^{DPLL}(0) = \hat{\theta}_0^{MLE}(0)$ and $\hat{f}_d^{DPLL}(0) = f_s\hat{v}(t_0)/c$ for the first block. The resulting phase and Doppler frequency errors can be converted to line-of-sight position and velocity errors, respectively, by multiplying them by the speed of light divided by the source frequency f_s [64]. Each scenario was simulated for a 200 second observation with both XPRESS in Matlab and the GXLT. The observation is chosen to be much longer than the one used for the constant signal frequency scenario cases since the observation is broken up into blocks for the phase-tracking algorithm with the MLE performed for each block. In the constant signal frequency scenarios a single run of the MLE using the entire observation was performed to estimate the initial phase.

Figure 3.10 contains the results for the Matlab simulated phase tracking using the Crab pulsar with a constant acceleration of 0.1 km/s^2, zero initial velocity, and 0.3 initial phase. The top two plots show the phase outputs and errors of the MLE algorithm and the MLE-DPLL algorithm along with the truth trajectory. It can be seen that they both track the true phase over the observation window, but the error is smaller for the DPLL phase as expected. The equivalent line-of-sight position error is on the order of 20 to 50 km. The bottom two plots show the DPLL frequency state versus the true frequency evolution and the error. The DPLL frequency is tracking with some fluctuation, but with an error on the order of 10^{-3} Hz, equivalently 10 km/s in line-of-sight range-rate error.

Figure 3.11 contains the results for the GXLT-based experimental phase tracking using the Crab pulsar with a constant acceleration of 0.1 km/s^2, zero initial velocity, and 0.3 initial phase. The top plots show the phase outputs of the MLE algorithm and the MLE-DPLL algorithm along with the truth trajectory. It can be seen that they both track the true phase over the observation window, but the error is smaller for the DPLL phase as expected. The equivalent line-of-sight position error is on the order of 100 km. The phase tracks exactly one cycle out of phase, but still tracks the fractional part of the phase accurately, which is the goal. The integer number of cycles can be determined separately through cycle ambiguity resolution for pulsars as discussed in [65]. This process is in many ways analogous to GPS ambiguity resolution. The bottom two plots show the DPLL frequency state versus the true frequency evolution and the error. The DPLL frequency is tracking with some initial fluctuations, but flattens out to a negligible amount. The equivalent line-of-sight range-rate error is on the order of 10 km/s.

The Matlab simulation for the 0.1 km/s^2 constant acceleration scenario had a slightly better range error, between 20 to 50 km, than the GLXT simulation with a level of 100 km. This increased error potentially comes from the cycle slip that caused the GXLT simulation to track one cycle out of phase. This slip of one cycle also caused an extended initial settling period of 100 seconds for the GXLT simulation. Both the Matlab and GXLT simulations had range-rate error on the order of 10 km/s by the end of the observation.

The results for the Matlab simulation and the GXLT experiment for the phase tracking of the Crab pulsar with a detector moving at the increased constant acceleration of 5 km/s^2 with initial velocity of 1 km/s and 0.5 initial phase are displayed in Figure 3.12 and Figure 3.13, respectively. In Figure 3.12 it can be seen that the MLE phase error starts out lower than the DPLL phase error early in the obser-

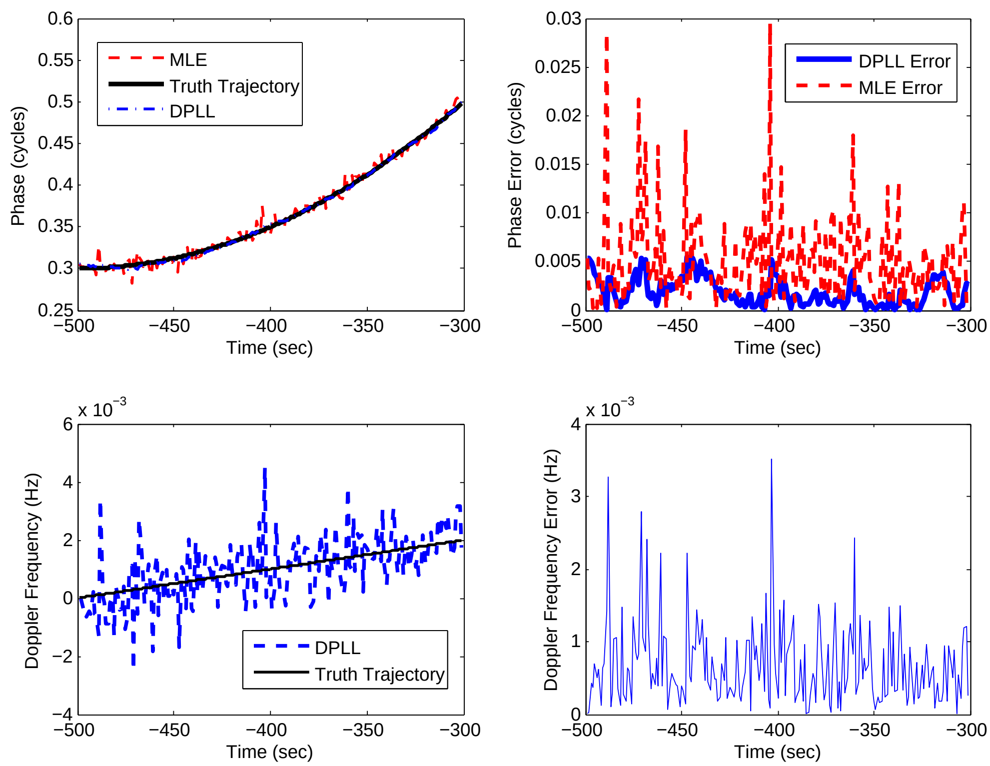

Figure 3.10: Simulation results using the Crab Pulsar and a detector acceleration of 0.1 km/s^2.

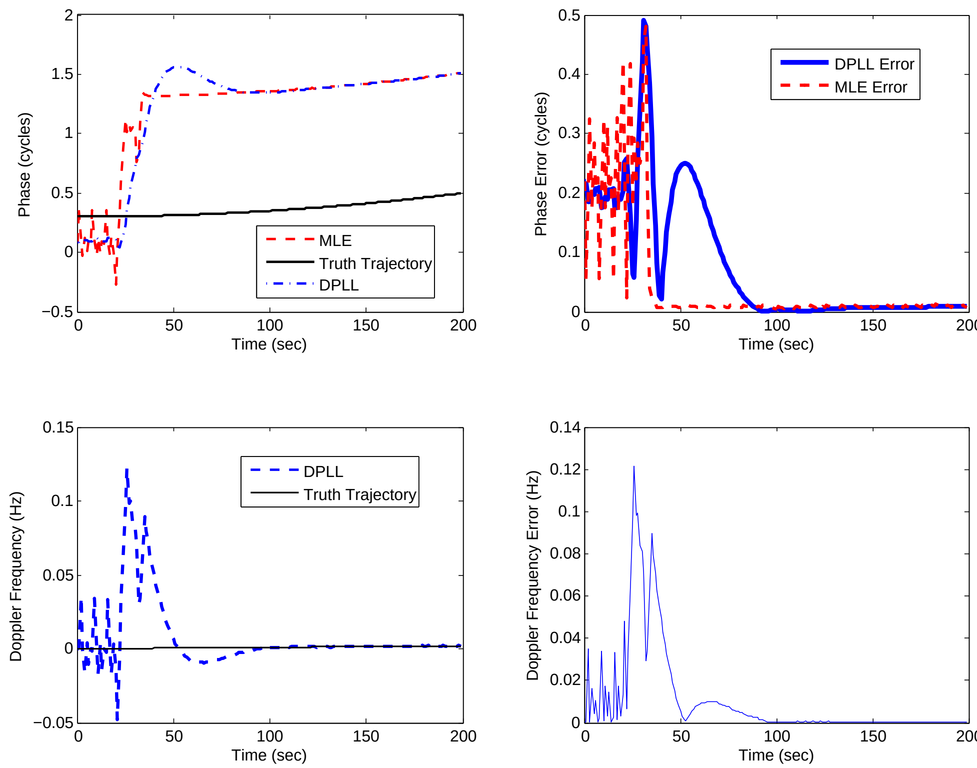

Figure 3.11: Experimental results using the Crab Pulsar and an acceleration of 0.1 km/s^2.

vation, but the error increases over time. After about 125 seconds the decreasing trend of the DPLL phase error improves enough to outperform the MLE alone for the remainder of the observation with steadily decreasing error. By the end of the observation the LOS range error is on the order of 100 km. The Doppler frequency is tracked with an error on the order of 10^{-3} over the entire observation, equivalent to 10 km/s in LOS range-rate error.

In Figure 3.13 it can be seen that the total phase is tracking a few cycles out of phase this time, but the DPLL phase tracks the fractional part with decreasing error over the observation interval. The MLE output error is growing as time progresses. At around 120 seconds the DPLL error improves beyond the increasing MLE error, and the DPLL LOS range error was approximately 20 km by the end of the observation. It can also be seen that the Doppler frequency is being tracked well by the DPLL following an initial fluctuation of over 50 seconds and settles to track with an equivalent LOS range-rate error of 10 km/s.

For the higher acceleration of 5 km/s^2 the GXLT simulation had a better range error of 20 km at the end of the observation compared to 100 km with the Matlab simulation. This discrepancy is largely due to the slower settling of the DPLL error in the Matlab simulation, and for an observation longer than the 250 seconds used in the simulations the levels of error are expected to be similar. The levels of range and range-rate line-of-sight error are similar to the experimental case with the Crab pulsar and a lower acceleration. The level of range-rate error is on the order of 10 km/s by the end of the observation in each of the four constant acceleration scenarios considered. Both runs of the GXLT had an initial settling

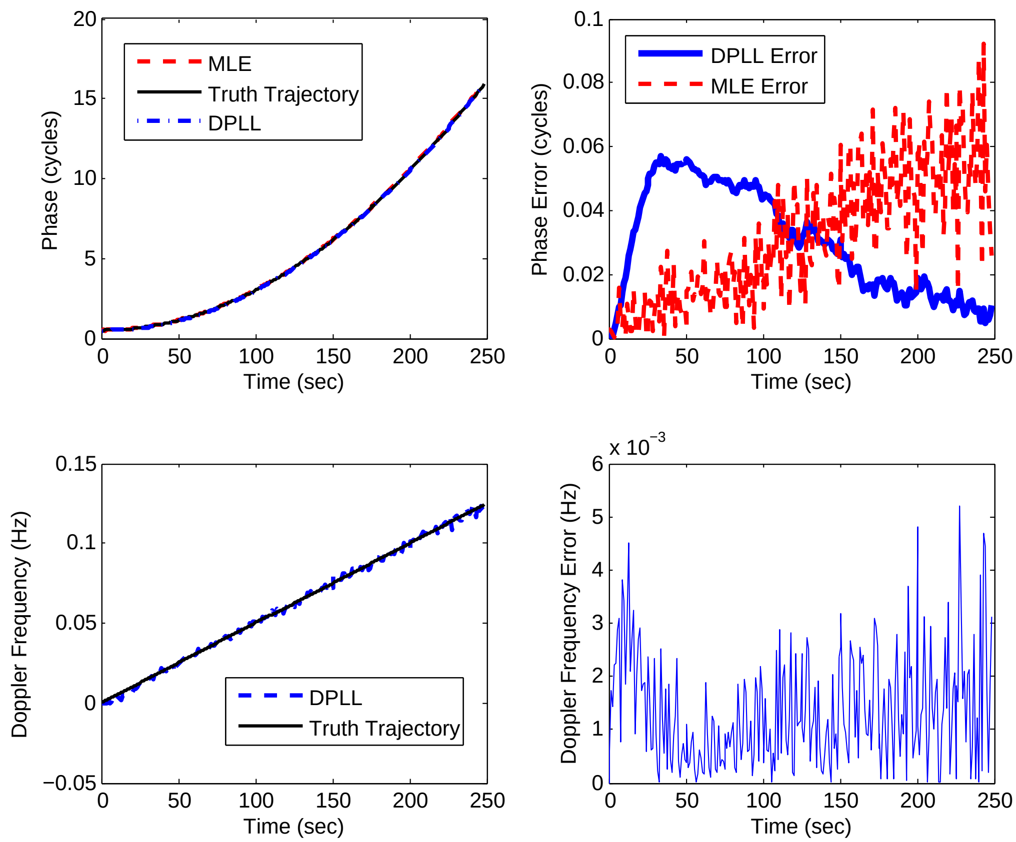

Figure 3.12: Simulation results using the Crab Pulsar and a detector acceleration of 5 km/s^2.

period for the Doppler frequency error that drives the range-rate error. Both runs of the GXLT had at least one cycle slip whereas neither of the Matlab simulations did. This might have been caused by the knowledge of the initial state used in the DPLL being less accurate with the GXLT than with the Matlab simulation models.

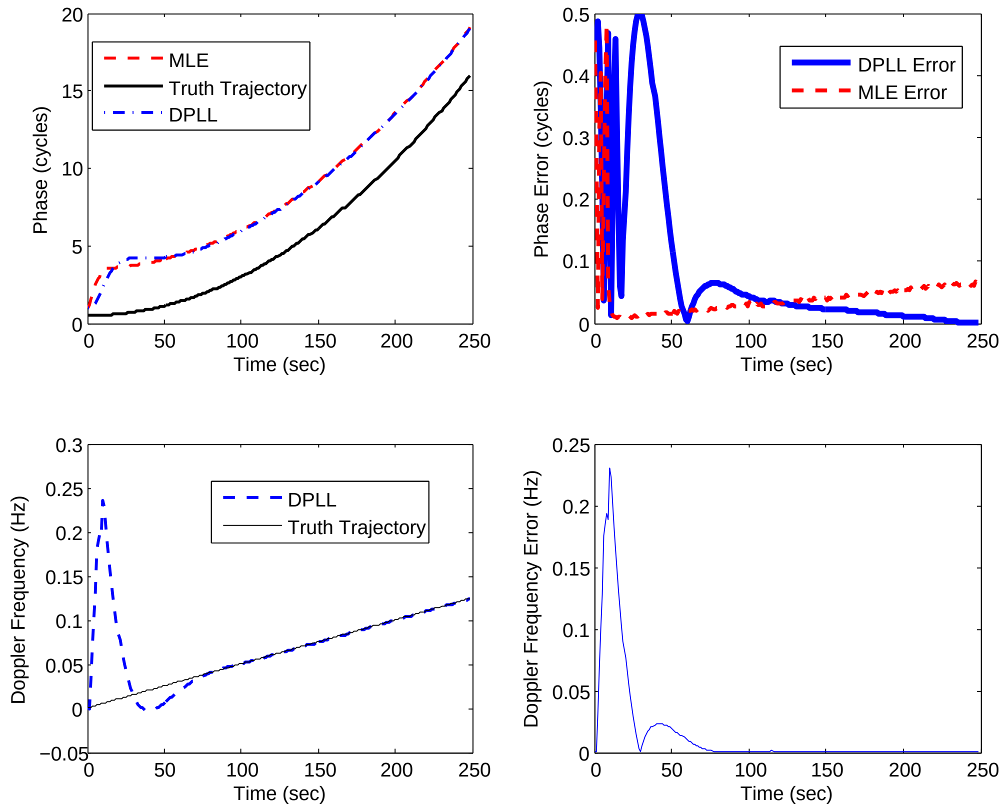

Figure 3.13: Experimental results using the Crab Pulsar and an acceleration of 5 km/s^2.

3.6 Difficulties of the Previous Phase-Tracking Algorithm with MSPs

It was demonstrated in the last section that the phase-tracking algorithm proposed by Golshan and Sheikh in [64] works well when the pulsar being tracked is the Crab pulsar. Many of the pulsars with the most desirable characteristics for use in spacecraft navigation are MSPs. The source flux of the Crab pulsar is many orders of magnitude larger than the flux of the MSPs, which means that the number of photons expected to arrive in one block will be much smaller when tracking an MSP. Table 3.7 contains the effective source and background photon arrival rates of four MSPs, that will be considered throughout this dissertation, along with the total photons per second. These effective rates are calculated assuming the detector area is similar to that of the GXLT of 176.2523 cm^2 and a backgound flux of 0.001 ph/(s cm^2). All four of the pulsars have under 0.21027 expected photons per second with this detector area. This is not feasible since the number of photons arriving during a block of the MLE algorithm needs to be large for the phase estimates to achieve the expected levels of accuracy. Detector areas much larger than the GXLT detector must be considered to allow for more photons to be detected per block from these lower flux pulsars.

Table 3.8 displays expected versus simulated photons per second for a range of detector areas for pulsar B1821-24, a background flux of 0.001 ph/(s cm^2), and a LOS trajectory with an acceleration of 0.1 km/s^2. Simulations were performed using XPRESS to test the number of photons arriving per second versus the expected value for each detector area. The simulated photons per second matches well with

Table 3.7: Examples of MSP flux levels and expected photons per block with the GXLT detector area of 176.2523 cm^2 and a background flux of 0.001 ph/(s cm^2).

Pulsar	α	β	Total photons per second
B1821-24	0.03333636	0.1769326	0.2102690
B1937+21	0.00756369	0.1774836	0.1850473
J0218+4232	0.00855617	0.1794169	0.1879731
J0437-4715	0.00328182	0.1846913	0.1879731

the expected photons per second for all of the detector areas considered as seen in columns two and three of Table 3.8. The detector area needs to be increased to 100000 cm^2 (10 m^2) before the number of photons per second is over 100. The accuracy of the MLE phase estimates will depend on the number of photons per block, which depends on the detector area as well as the block length T. Expected MLE performance is discussed in chapter 4.

The rest of this section considers simulations using PSR B1821-24 with different detector areas, spacecraft trajectories, and block sizes to demonstrate the performance of the phase-tracking algorithm proposed by Golshan and Sheikh in [64] with an MSP. PSR B1821-24 is representative of the performance of the four MSPs considered since they have similar total photons per second as seen in Table 3.7 and all have greatly lower source and background fluxes than the Crab pulsar as seen when comparing to Table 3.2.

First, simulations with the block size set at T = 1 second, as with the Crab pulsar in the last section, will be considered. Figure 3.14 displays the results of a simulation tracking PSR B1821-24 with a 25 m^2 detector along a trajectory with constant acceleration of 0.1 km/s^2. In this simulation numerous outlier ML-estimates

Table 3.8: Expected photons per second verses simulated photons per second for a range of detector areas for pulsar B1821-24, a background flux of 0.001 ph/(s cm^2), and a LOS trajectory with an acceleration of 0.1 km/s^2.

Area, cm^2	Expected Photons per Second	Simulated Photons per Second
176.2523	0.210269	0.21
1000	1.193	1.16
10000	11.93	11.94
50000	59.65	59.37
100000	119.3	119.17
150000	178.95	178.60
250000	298.25	297.68
500000	596.5	596.27
1000000	1193	1192.43

cause the phase-locked loop to slip multiple cycles. The tracking is able to recover, but multiple cycles out of phase. This causes the position error from the DPLL phase estimates to be greater than 100 km for the majority of the observation and the velocity error from the DPLL frequency tracking to be only able to settle to under 50 km/s.

The phase error over time for this simulation, displayed in cycles, is contained in Figure 3.15. From this plot it can be seen that four cycle slips occur over the 200 second simulation and twice the slip is two cycles at once. After each cycle slip the MLE and DPLL estimates are able to recover tracking, but with increased error for over 50 seconds. This performance is not adequate for providing reliable estimates of the navigational state of the spacecraft. Either the area of the detector or the block size T needs to be increased to raise the number of photon event times included in evaluating each ML phase estimate.

Increasing the area of the detector to 50 m^2 and re-running the same simulation resulted in improved tracking performance as seen in Figure 3.16. There are still numerous outlier ML-estimates, but instead of slipping cycles the DPLL phase estimate is able to recover. Near the end of the 200 second observation the tracking does appear to diverge, though. While in-lock, the DPLL settles to approximately 10 km of position error within about 30 seconds of each MLE outlier and to 5 km/s of velocity error within a few seconds of each MLE outlier. This simulation shows that the tracking is tenuous due to the numerous outliers.

Again a larger area was considered in order to try to eliminate the MLE outliers and further decrease the position and velocity errors. Re-running the same simulation, but with a detector area of 100 m^2 resulted in greatly improved tracking performance as seen in Figure 3.17. There are no cycle slips or outlier ML-estimates during the 200 second simulation. The position error from the DPLL phase estimates decreases to under 7 km after 120 seconds of the simulation, and the velocity error remains below 3 km/s. The phase error over time for this simulation is contained in Figure 3.18. It can be seen that the DPLL phase error is lagging the MLE phase error and appears to have a bias in the opposite direction of the true phase of the majority of the ML-estimates. This could be potentially improved with changes to the DPLL noise bandwidth at the expense of higher tracking errors.

From looking at the simulations using PSR B1821-24 for phase-tracking along a constant acceleration trajectory it is apparent that a large area detector would be necessary to obtain adequate tracking results. Areas of 50 – 100 m^2 are not feasible for an X-ray detector on a spacecraft. The phase tracking algorithm of Golshan and Sheikh was investigated further by looking at tracking PSR B1821-24 with a

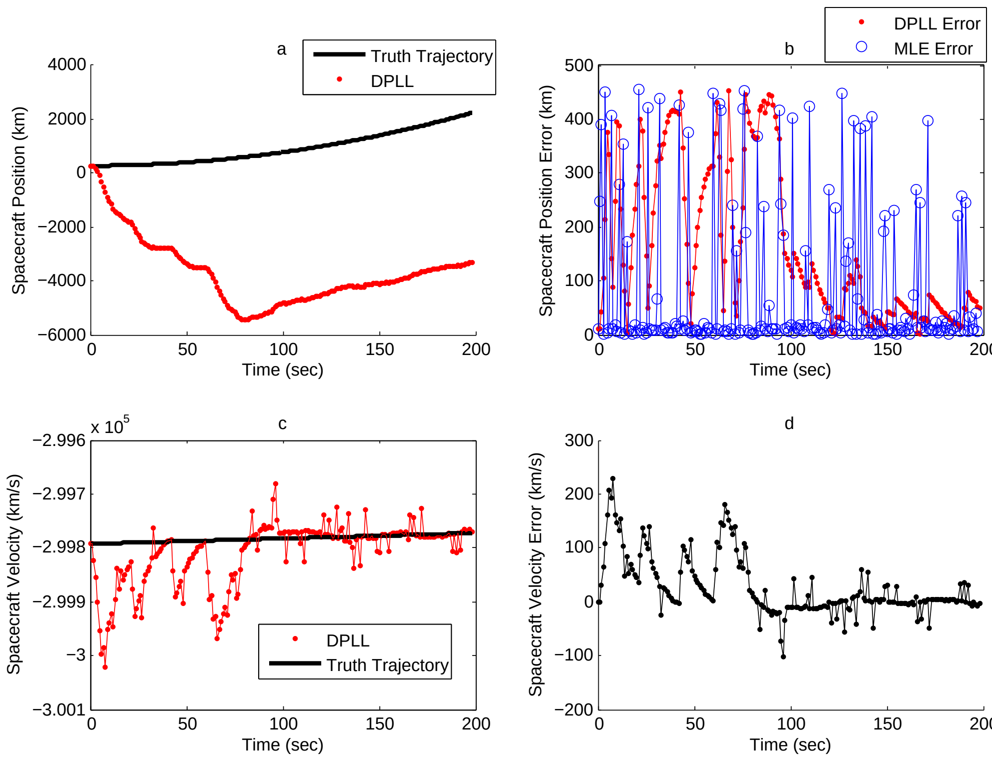

Figure 3.14: Simulation results using PSR B1821-24 and a 25 m^2 detector with an acceleration of 0.1 km/s^2.

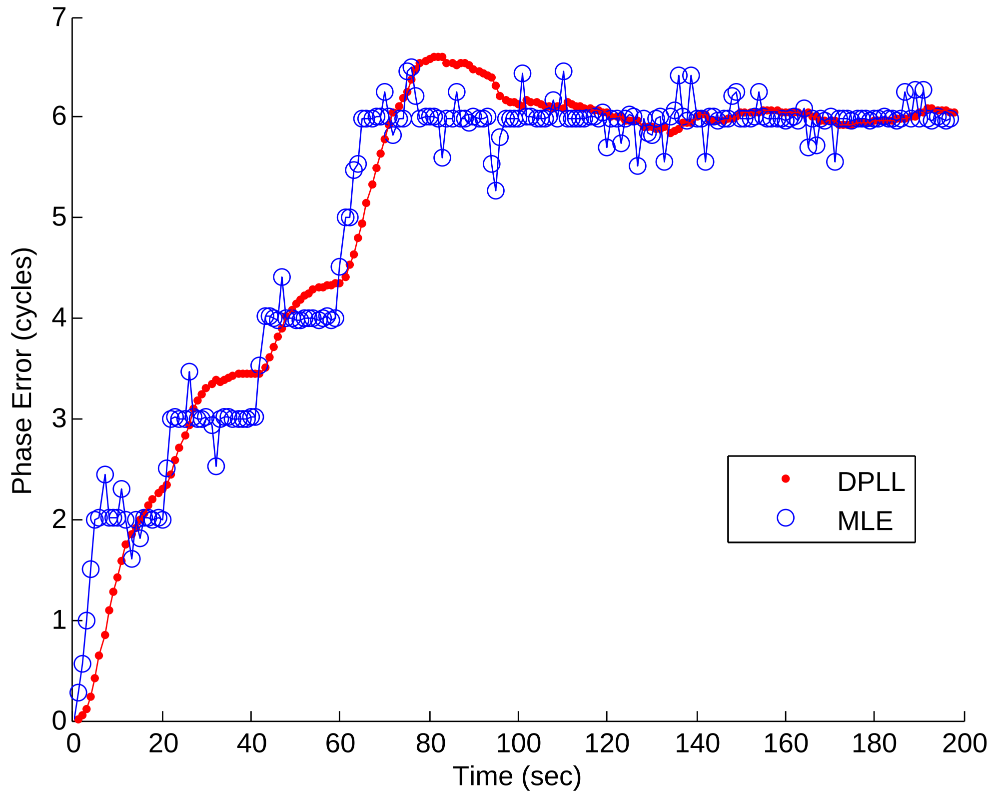

Figure 3.15: Phase error over time with PSR B1821-24 and a 25 m^2 detector with an acceleration of 0.1 km/s^2.

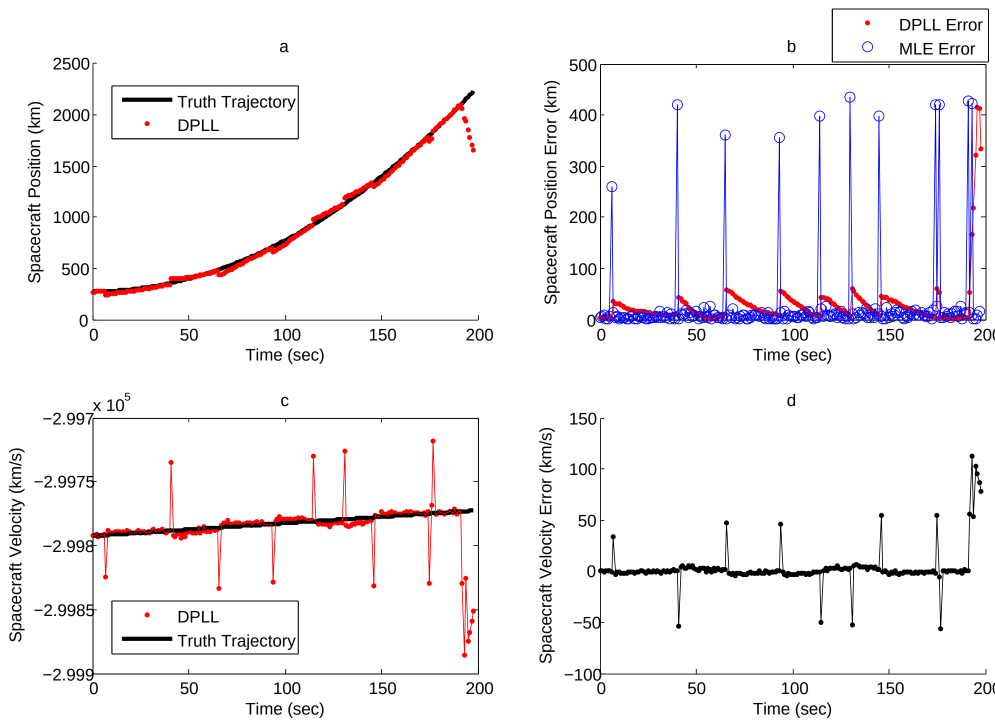

Figure 3.16: Simulation results using PSR B1821-24 and a 50 m^2 detector with an acceleration of 0.1 km/s^2.

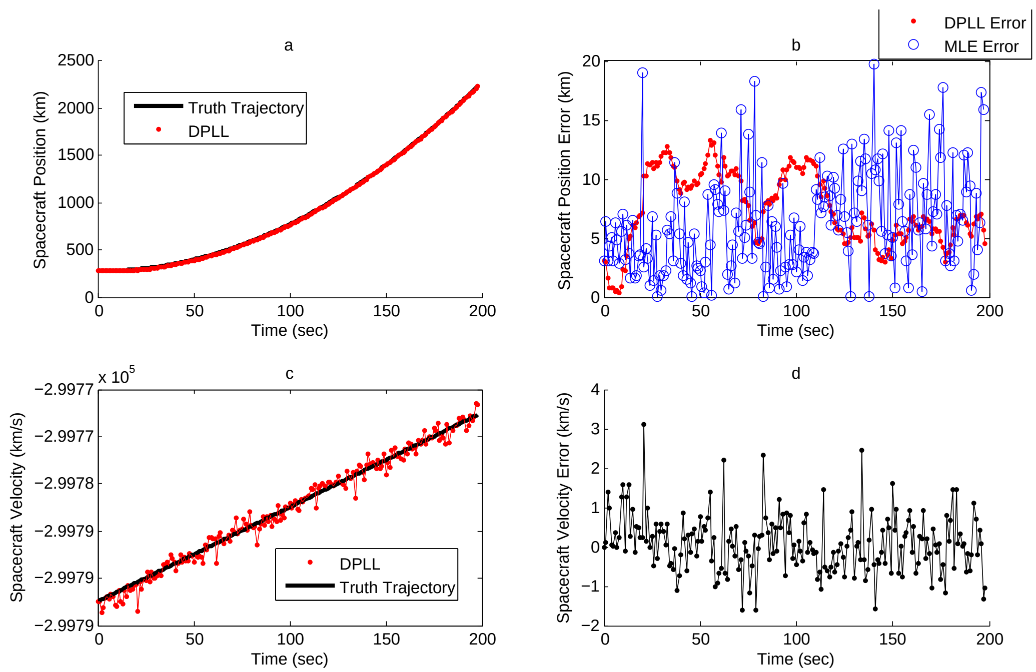

Figure 3.17: Simulation results using PSR B1821-24 and a 100 m^2 detector with an acceleration of 0.1 km/s^2.

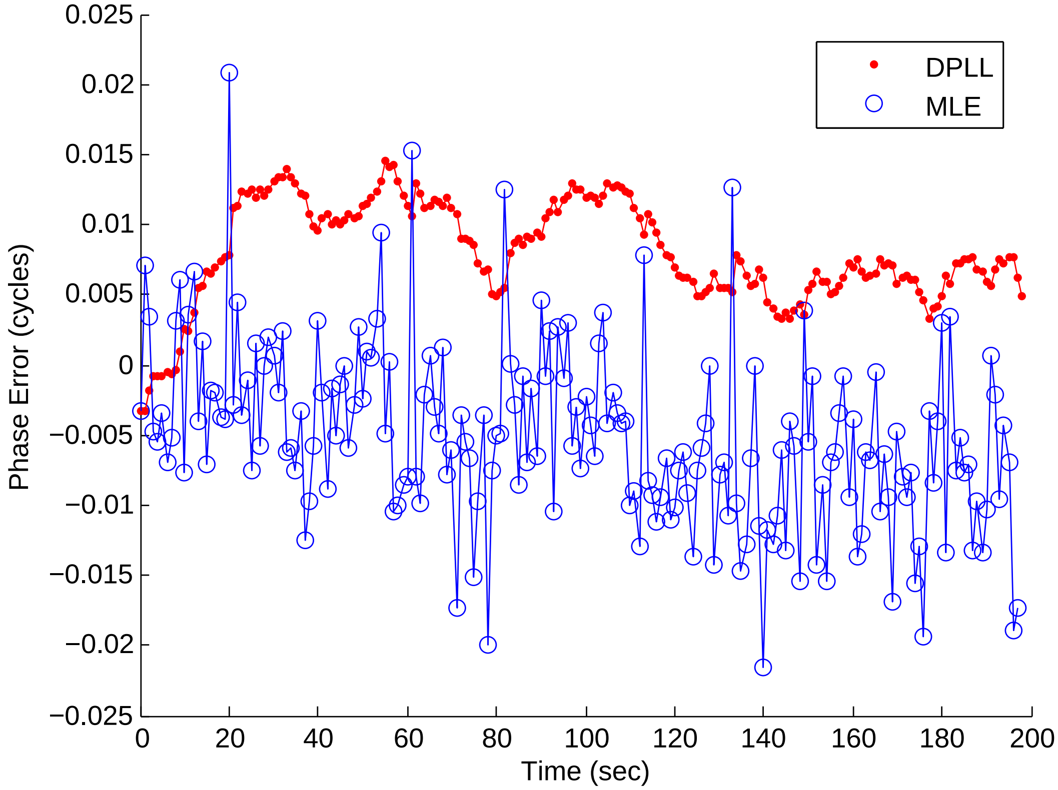

Figure 3.18: Phase error over time with PSR B1821-24 and a 100 m^2 detector with an acceleration of 0.1 km/s^2.

detector on a simulation of a portion of the Mars Science Laboratory's (MSL) cruise trajectory between the Earth and Mars. This was done to assess the performance under a different set of dynamic stress conditions than the constant acceleration trajectory and to consider a more realistic spacecraft application. This trajectory has less dynamic stress along the LOS to the pulsar, but includes three-dimensional motion with regards to the pulsar.

First, different detector areas are considered with a set block size of T = 1 second. Figure 3.19 displays the results of a simulation tracking PSR B1821-24 with a 10 m^2 detector along the MSL trajectory for 200 seconds. From plot (a) in Figure 3.19 it can be seen that the DPLL phase estimates only briefly appear to track the truth trajectory. From plot (b) in Figure 3.19 it can be seen that both the MLE and DPLL position errors fluctuate up to 400 km with no signs of tracking.

Increasing the detector area to 25 m^2 and 50 m^2 produced the simulation results displayed in Figures 3.20 and 3.21, respectively. Both of these simulations have cycle slips followed by short periods of tracking as seen in plots (a) of Figures 3.20 and 3.21. Plots (b) demonstrate that each increase in detector area leads to a reduction in outlier ML-estimates. The cycle slips are still causing large DPLL position errors of up to 400 km in both cases with settling to below 20 km position error and 10 km/s velocity error in between cycle slips in the simulation with the 50 m^2 detector as seen in plots (b) and (d) of Figure 3.21.

Next, since this is already a large detector area, changing the block size T used in the MLE algorithm will be considered. The block size is the other parameter of the phase-tracking algorithm that affects the number of photon event times incorporated

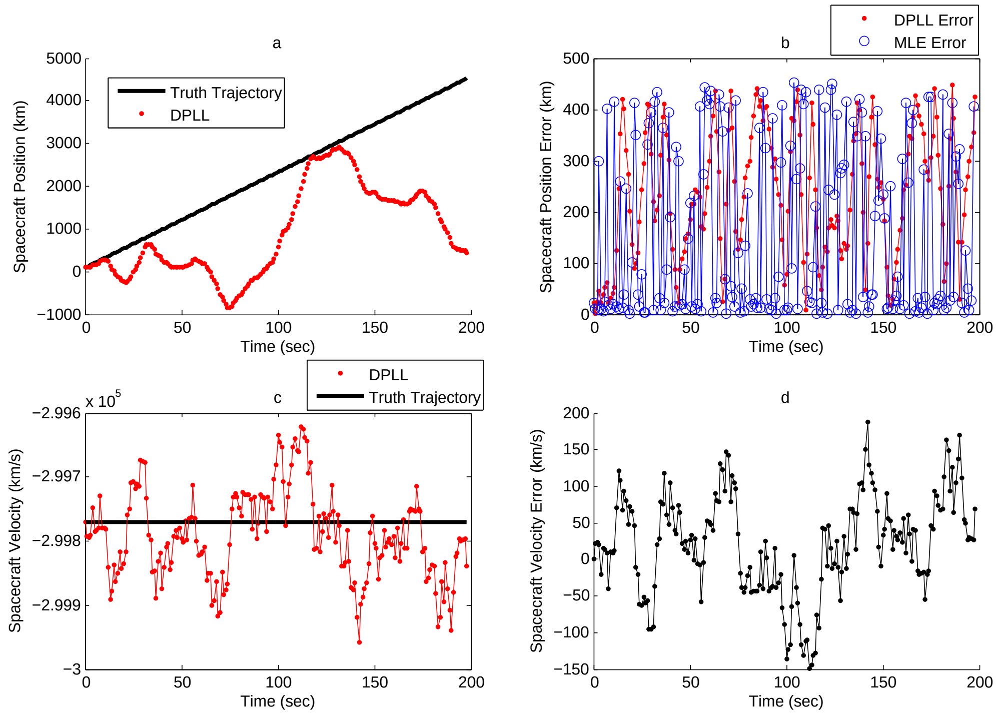

Figure 3.19: Simulation results of tracking PSR B1821-24 with a 10 m^2 detector during the MSL cruise stage and T = 1 second.

into each run of the MLE. The results of increasing to T = 2 seconds and keeping a detector area of 50 m^2 are shown in Figure 3.22. From plot (a) it can be seen that there are no cycle slips in this simulation and in plot (b) it can be seen that there are only two outlier ML-estimates and that the DPLL position error settles to around 25 km after each outlier. From plot (d) it can be seen that the DPLL velocity error settles to under 5 km/s after each outlier. The tracking performance of this simulation is greatly improved over the equivalent simulation with a block size of T = 1. The limits of the improvement resulting from further increases to the block size are considered next.

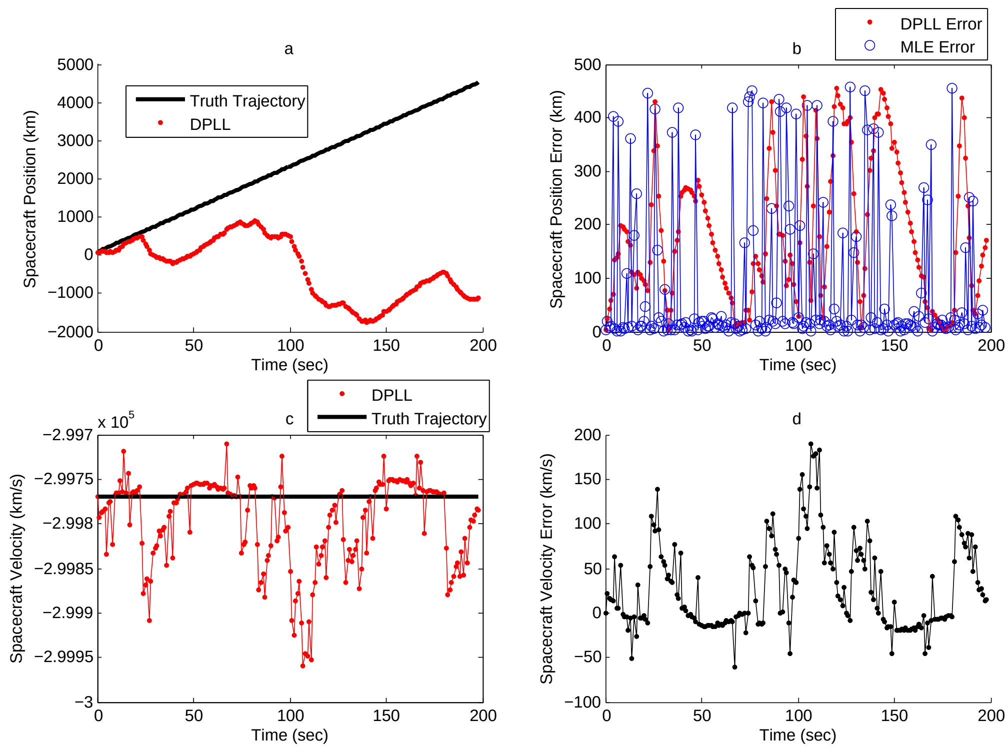

Figure 3.20: Simulation results of tracking PSR B1821-24 with a 25 m^2 detector during the MSL cruise stage and T = 1 second.

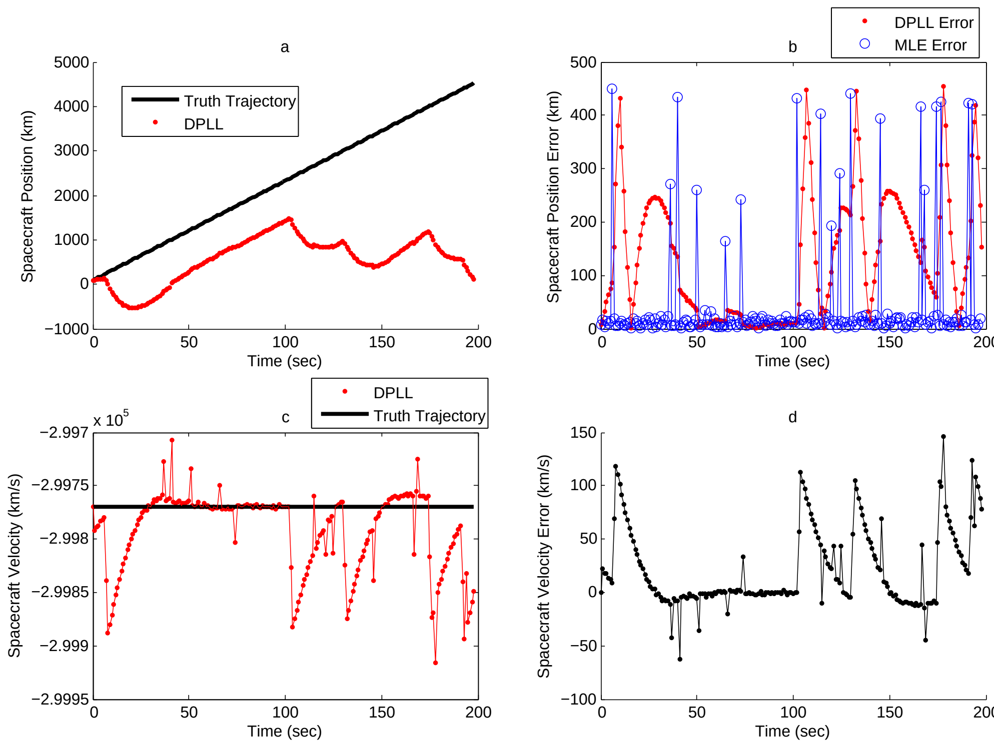

Figure 3.21: Simulation results of tracking PSR B1821-24 with a 50 m^2 detector during the MSL cruise stage and T = 1 second.

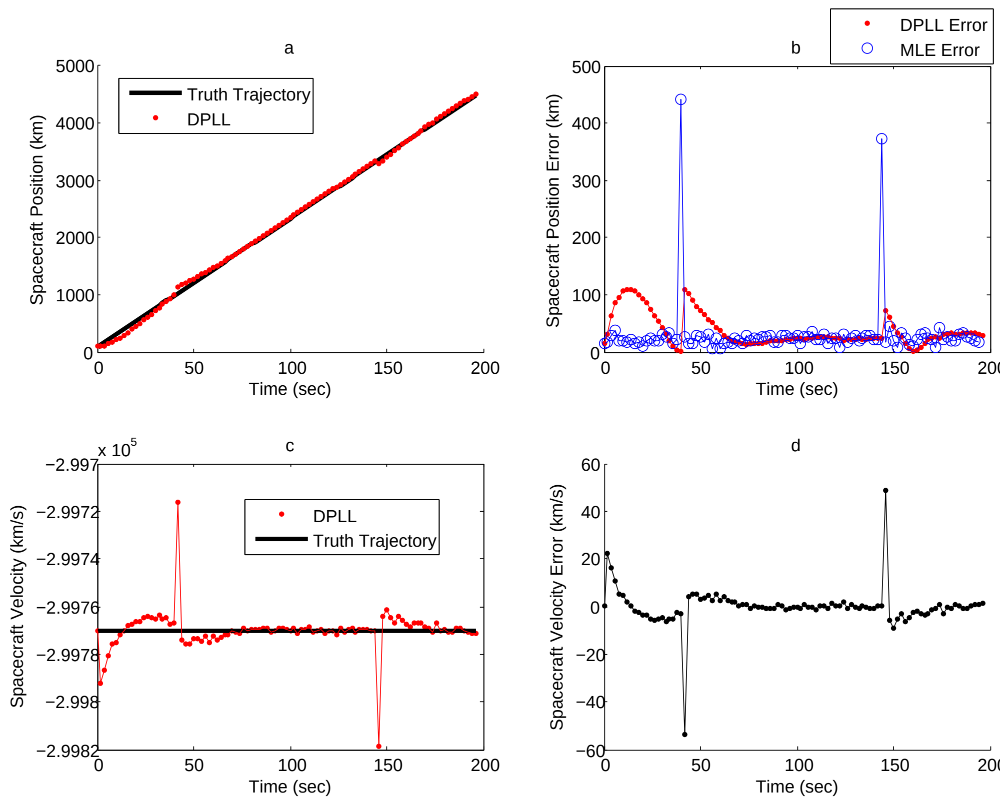

Figure 3.22: Simulation results of tracking PSR B1821-24 with a 50 m^2 detector during the MSL cruise stage and T = 2 seconds.

A range of different block lengths were considered for tracking PSR B1821-24 with a 25 m^2 detector along the portion of the MSL cruise trajectory. A smaller detector area was used in order to test if the improvements in tracking performance seen from a larger block size with a 50 m^2 detector allows for a decrease in area. The results for simulations with T values of 2, 3, 4, 5, and 6 seconds are displayed in Figures 3.23 – 3.27 , respectively. Comparing Figure 3.23 with Figure 3.20 it can be seen that increasing the block size to T = 2 seconds eliminates some of the cycle slips and MLE outliers from the T = 1 second simulation, but a few of them still exist. The MLE position error is under 50 km between the outliers, but the DPLL phase error does not recover fast enough between MLE outliers to provide good tracking. From Figures 3.24 – 3.26 it can be seen that the tracking results with block sizes of T = 3, 4, and 5 seconds are similar to the T = 2 seconds simulation. All of these simulations have a similar number of cycle slips and MLE outliers. In plots (b) of these figures, the level of the MLE position error rises with increasing block size from around 50 km with T = 2 seconds to over 80 km with T = 5 seconds.

In Figure 3.27 it can be see that the tracking performance begins to degrade with the block size increased to T = 6 seconds. Roughly a quarter of the ML-estimates are outliers, which causes the DPLL to never acquire lock. This demonstrates that there is a limit to the benefit of increasing the block size. There is decreasing performance caused by dynamic stress if T is made too large. This results from the assumption that the signal frequency is constant over each individual block when calculating the ML phase estimates. A block length of six seconds appears to be the limit caused by the assumption of constant signal frequency for the

MSL cruise trajectory. Different orbits might allow for different block lengths.

The results from simulations of tracking PSR B1821-24 with a 10 m^2 detector along the MSL cruise trajectory using T values of 4, 5, and 6 seconds are displayed in Figures 3.28 – 3.30 , respectively. Both T = 4 seconds and T = 6 seconds perform better than the original method with T = 1 second, as seen in Figures 3.28 and 3.30, respectively, as compared to Figure 3.19. In both cases the tracking lasts only the first 30 seconds of the simulation, though, and the position errors are up to 100 km. The best tracking results with a 10 m^2 detector are with T = 5 seconds as seen in Figure 3.29. In this case the tracking lasts more than 100 seconds before loss-of-lock, but the position error is still on the order of 100 km. This high position error and the loss-of-lock halfway through the simulation demonstrates that the use of a 10 m^2 detector may not provide adequate tracking results depending on the application.

The simulation results of tracking PSR B1821-24 with a 5 m^2 detector along the MSL cruise trajectory using T = 4 seconds are displayed in Figure 3.31. Four seconds was the block size that had the best tracking performance of the times tested with a detector area of 5 m^2. As can be seen in plots (a) and (b) of Figure 3.31 the phase tracking loses lock within the first 50 seconds and does not recover and the position error is up to 100 km during the period of best tracking performance. Thus, a detector area of 5 m^2 is not feasible for tracking PSR B1821-24 along the MSL cruise trajectory using any choice of block size for the Golshan and Sheikh phase tracking algorithm.

This section demonstrates the need for improvements to the algorithm proposed by Golshan and Sheikh in [64] to extend the concept of phase tracking to MSPs. The significantly lower flux rates of MSPs as compared to the Crab pulsar results in fewer photons arriving at a spacecraft X-ray detector. In order to achieve similar MLE and DPLL performance results, changes need to be made in order for a similar amount of source photons to arrive in each block as with the Crab pulsar. The two parameters of the phase-tracking algorithm that can be changed to cause more photon event times per MLE block are the detector area and the block size T. In this section it was shown that with the block size set at T = 1 second the detector area needs to be increased to 50 to 100 m^2 to achieve adequate tracking of PSR B1821-24 along a constant acceleration trajectory or the MSL cruise trajectory. This large of a detector area is not feasible onboard a spacecraft.

This section also demonstrates that increasing the block size T resulted in improved tracking performance for PSR B1821-24 along the MSL cruise trajectory, but there is a limit to how large T can be made before causing the breakdown of the assumption of constant observed signal frequency due to the dynamic stress. Increasing T allows for the use of a 25 m^2 detector or possibly a 10 m^2 detector, but in both cases the position error is high and these detector areas are probably still not feasible for a spacecraft. Since MSPs are some of the most attractive X-ray pulsars available for spacecraft navigation, the rest of this dissertation will be concentrated on changing the algorithm to allow phase tracking their signals with a more reasonable detector area. The focus will be on changing the algorithm to relax the assumption of a constant signal frequency over each block.

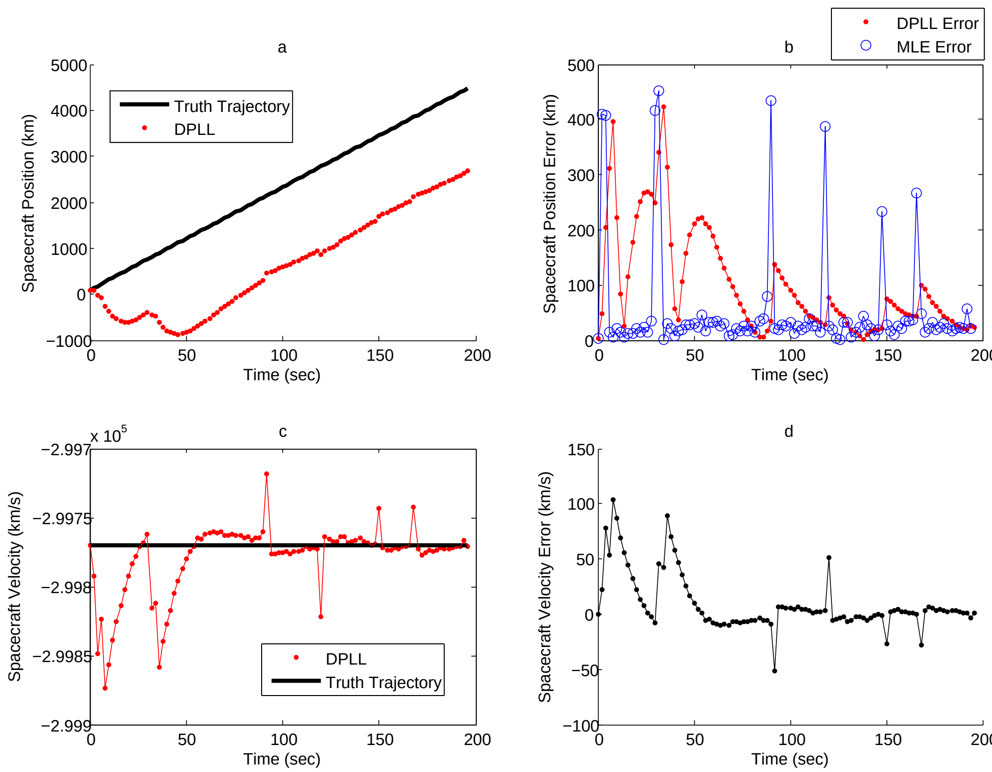

Figure 3.23: Simulation results of tracking PSR B1821-24 with a 25 m^2 detector during the MSL cruise stage and T = 2 seconds.

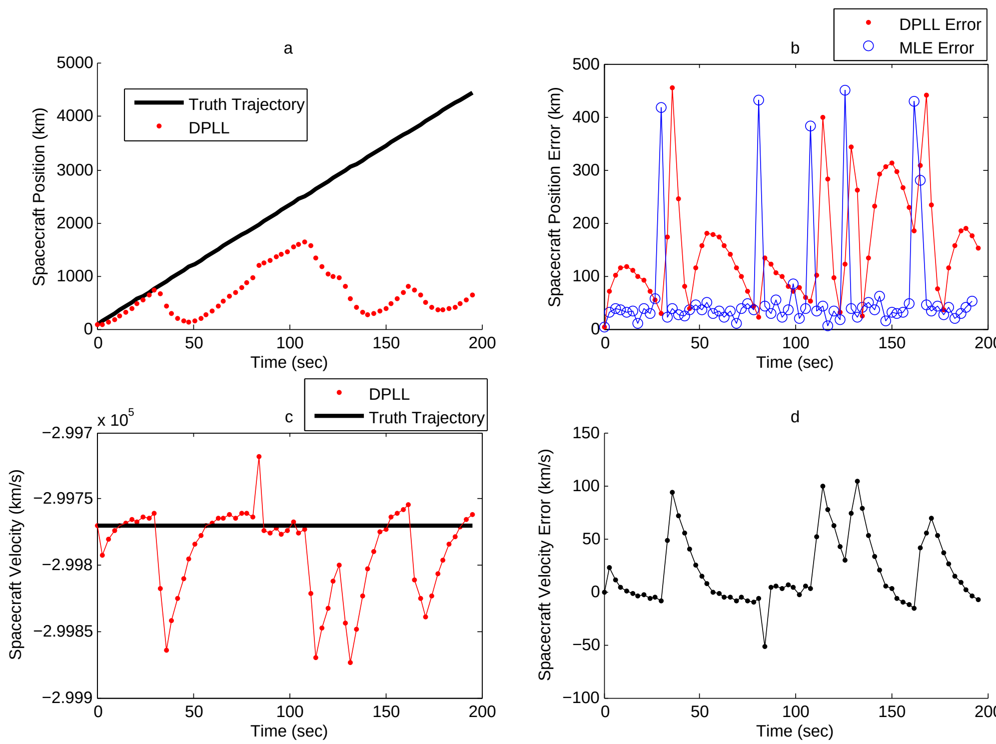

Figure 3.24: Simulation results of tracking PSR B1821-24 with a 25 m^2 detector during the MSL cruise stage and $T = 3$ seconds.

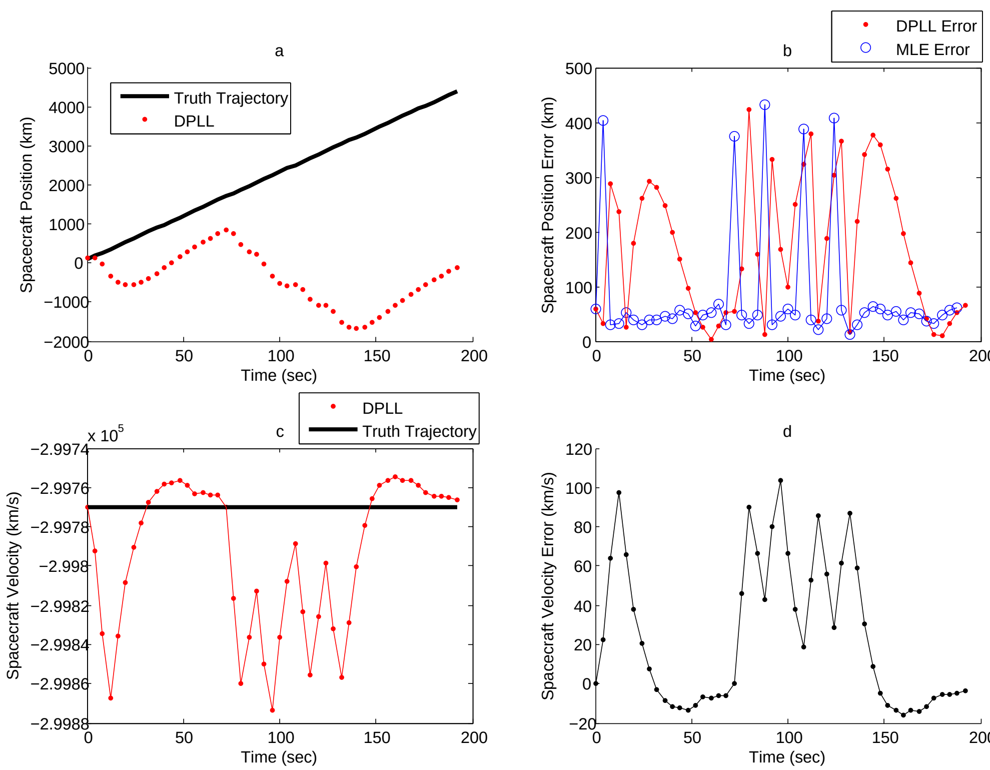

Figure 3.25: Simulation results of tracking PSR B1821-24 with a 25 m^2 detector during the MSL cruise stage and T = 4 seconds.

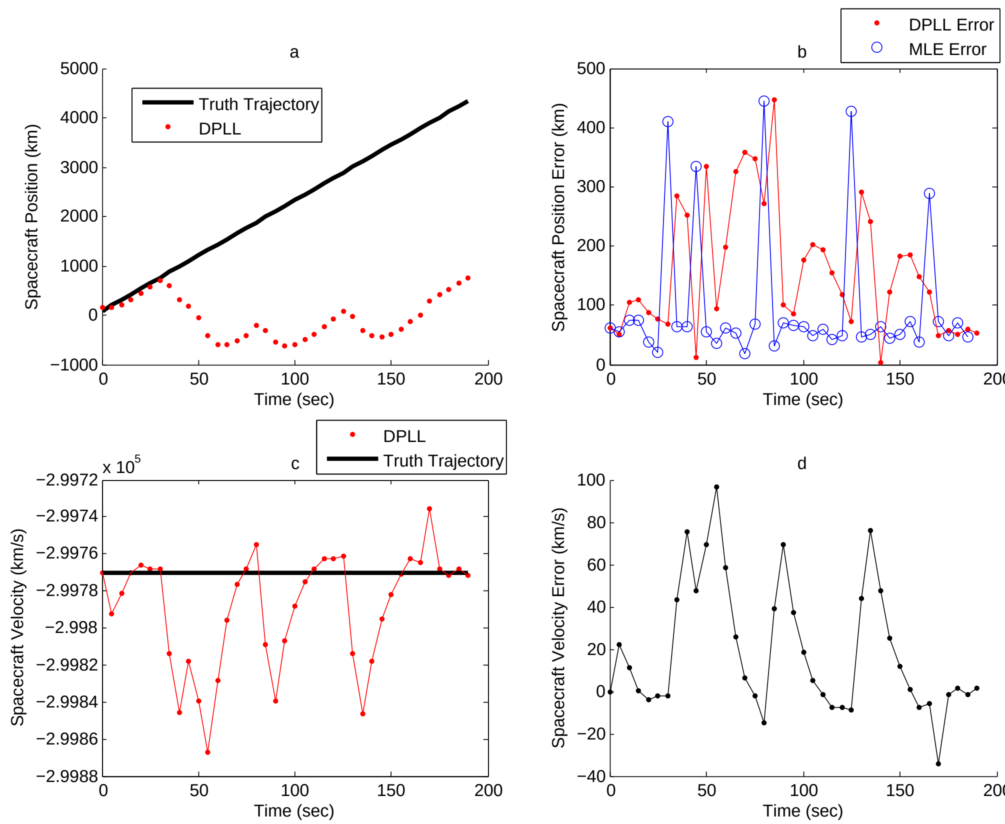

Figure 3.26: Simulation results of tracking PSR B1821-24 with a 25 m^2 detector during the MSL cruise stage and T = 5 seconds.

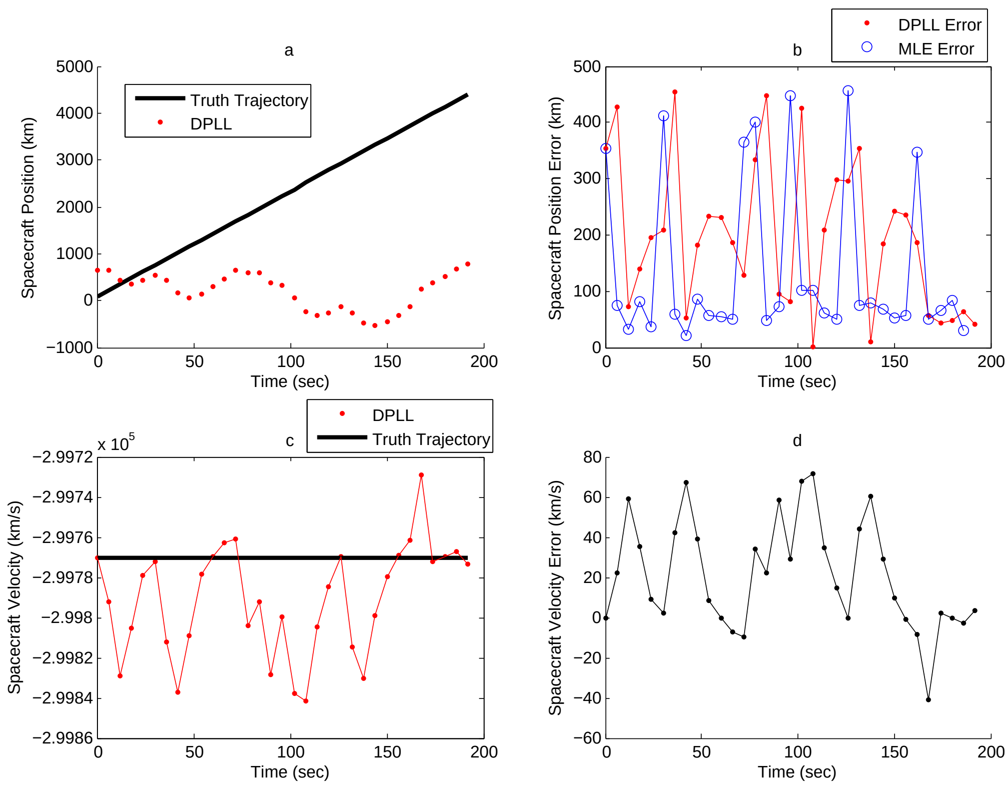

Figure 3.27: Simulation results of tracking PSR B1821-24 with a 25 m^2 detector during the MSL cruise stage and T = 6 seconds.

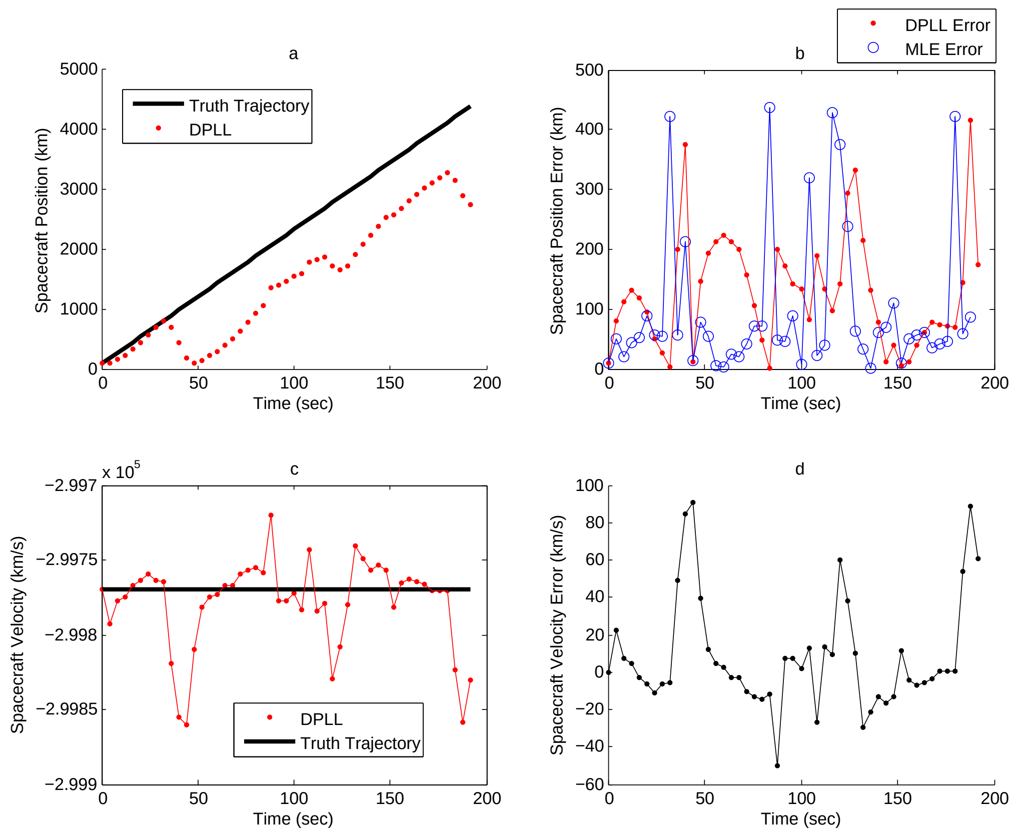

Figure 3.28: Simulation results of tracking PSR B1821-24 with a 10 m^2 detector during the MSL cruise stage and T = 4 seconds.

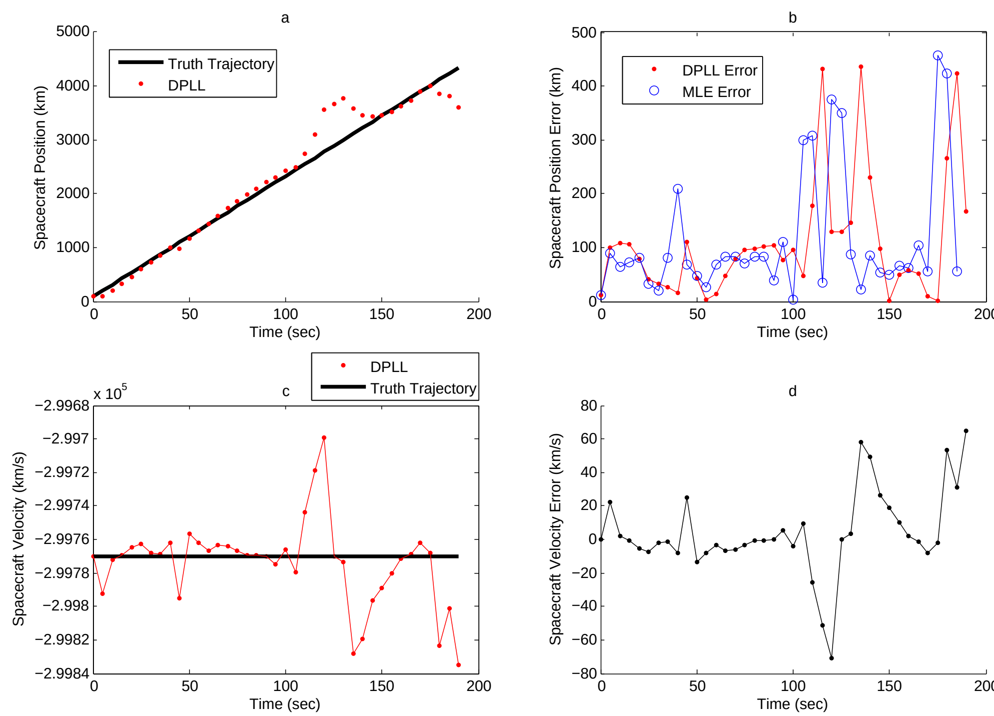

Figure 3.29: Simulation results of tracking PSR B1821-24 with a 10 m^2 detector during the MSL cruise stage and T = 5 seconds.

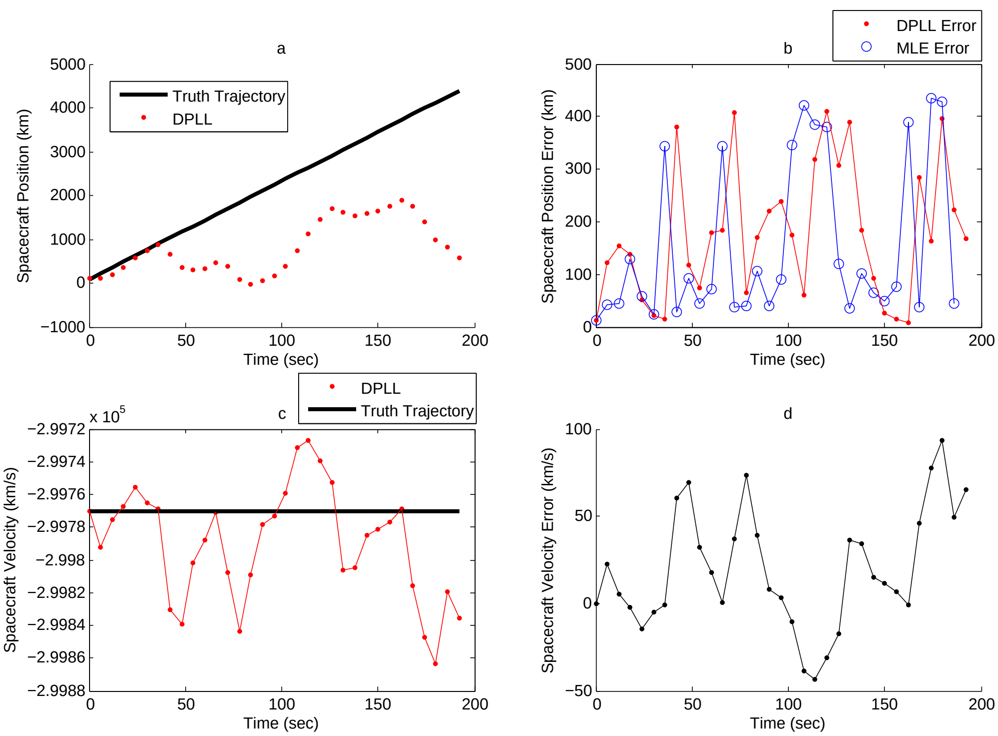

Figure 3.30: Simulation results of tracking PSR B1821-24 with a 10 m^2 detector during the MSL cruise stage and T = 6 seconds.

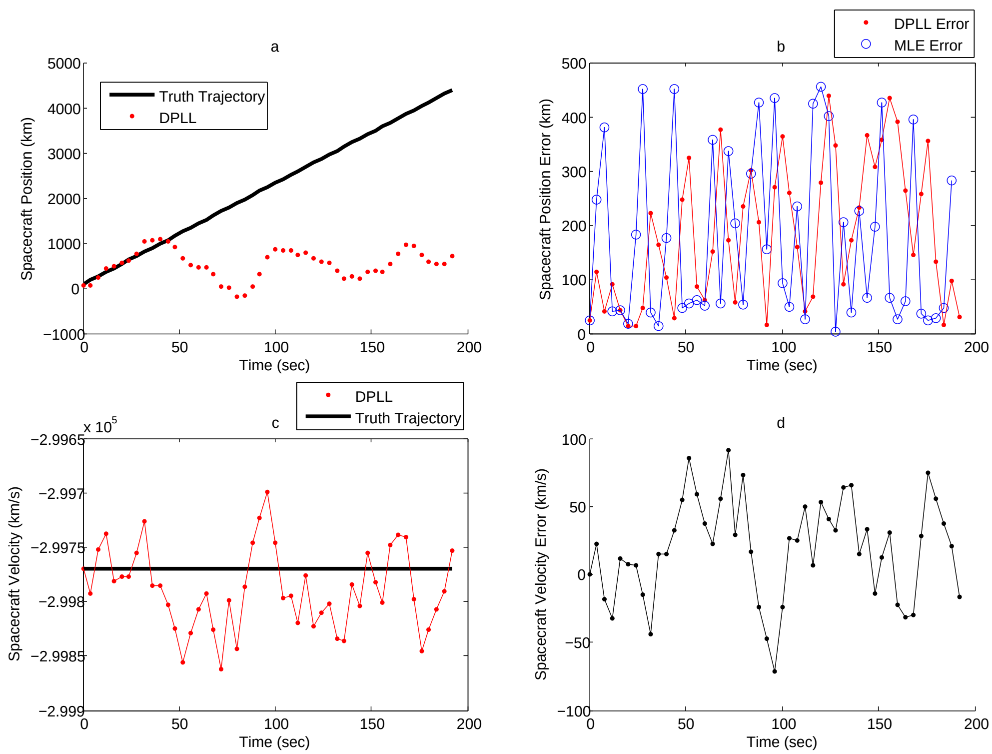

Figure 3.31: Simulation results of tracking PSR B1821-24 with a 5 m^2 detector during the MSL cruise stage and T = 4 seconds.

3.7 Summary

In this chapter, the method of phase tracking of a pulsar signal as used for spacecraft navigation was introduced. The various building blocks for pulsar signal phase tracking were presented along with a discussion of previous research in the area. The use of digital phase-locked loops for pulsar signal tracking was described. The method developed in [64] by Golshan and Sheikh for phase tracking pulsar signals was introduced and investigated and confirmed using lab experiments with the NASA Goddard X-ray Laboratory Testbed (GXLT) and computer simulations.

The method was tested with the Crab pulsar signal for a variety of simulated detector trajectories. The use of the GXLT tested the phase tracking algorithm under conditions including x-ray photon generation and detection that were not previously considered in x-ray pulsar phase tracking simulations.

The difficulties that the Golshan and Sheikh phase tracking method had with millisecond period pulsars was discussed and investigated. The flux is too low for the method to be used in the same manner as with the Crab pulsar without either increasing the block length or the detector size. A detector size of 25 to 100 m^2 was needed to track the B1821-24 signal depending on the orbit considered. There is a trade-off between the accuracy of the ML-phase estimates and the dynamic stress of the spacecraft trajectory. Most of the pulsars with the best characteristics for use in spacecraft navigation are MSPs. This motivates the investigation into changes needed for the phase tracking algorithm to be used with MSPs and a reasonably sized x-ray detector.

Chapter 4: Cramer-Rao Lower Bound and Threshold Observation Time Prediction

4.1 Overview

This chapter introduces a proposed extension to the MLE for signal phase that replaces the assumption of constant signal frequency over the estimation time with the assumption that the signal frequency rate is constant. This allows for the observation time considered for each estimate to be extended, which helps improve the performance with lower flux pulsars including many MSP's.

In order to analyze the performance of the MLE this chapter includes comparisons to the Cramer-Rao Lower Bound (CRLB). The CRLB is introduced and derived in Section 4.2. The CRLB provides a lower bound on the variance that can be achieved by any unbiased estimator of the phase. This provides a way of comparing the MLE phase error to the optimal performance for any given observation time. A lower bound on the variance for a particular estimation problem is extremely useful because it provides a benchmark to compare against as well as demonstrating the physical impossibility of finding an estimator with a variance less than the bound [111].

Section 4.3 investigates the comparison of the empirical performance of the MLE versus the CRLB. A standard detector area of 1 m^2 and a background flux $R_b = 0.001$ ph/(s cm^2) are used and five pulsars are considered: the Crab pulsar, B1821-24, B1937+21, J0218+4232, and J0437-4715. The first subsection introduces the extension of the phase MLE to relax the constant signal frequency assumption. This consists of increasing the order of the Taylor polynomial used to represent the estimator's internal phase model and using a third-order DPLL in the phase tracking algorithm that will provide frequency and frequency derivative estimates back to the MLE at each iteration.

The other two subsections consider the MLE performance over different trajectories that provide a range of levels of dynamic stress during the pulsar observations. First, the scenario where the detector is on a constant acceleration trajectory along the line-of-sight to the target pulsar is considered. This simplified choice allows the performance of the MLE to be tested for its limitations resulting from the underlying Poisson statistics since the vehicle dynamics can be perfectly modeled by the MLE for a constant signal frequency derivative. Second, trajectories with unmodeled dynamics MLE's are considered. This consists of a range of Earth orbits and an interplanetary trajectory that is a portion of the cruise stage of the Mars Science Laboratory (MSL) mission. For each pulsar and trajectory combination the MLE is run for a range of observation times. Each observation time is repeated 100 times using different random seeds and the results are compiled together to give the empirical performance represented as RMS phase error and compared to the CRLB. A threshold phenomenon is observed where the MLE phase error doesn't converge to the CRLB until a certain amount of observation time is reached. For the trajectories with dynamic stress there exists an upper threshold observation time as well that limits the length of time before the MLE phase error diverges from the CRLB. These threshold observation times are determined for each pulsar and trajectory combination.

Section 4.4 presents a method to analytically predict the lower threshold observation time for a given pulsar. This method provides a quick guess of the threshold observation time for a new pulsar before having to perform extensive empirical tests of the MLE. For the five pulsars considered the predicted thresholds are compared to the empirically determined values of the last section. The pulse width of the pulsar phase profile seems to affect the performance of the prediction algorithm. The greater the pulse width the lower the performance. This hypothesis is tested by considering a wider range of pulse widths using artificial pulsar profiles. This was achieved by artificially designing profiles with various pulse widths and combining them with realistic flux levels of PSR J0437-4715 and PSR B1821-24.

4.2 Derivation of Cramer-Rao Lower Bound

The Cramer-Rao Lower Bound (CRLB) for a particular parameter estimation problem places a lower bound on the variance that can be achieved by any unbiased estimator of the parameter [111]. This section will introduce and define the CRLB in general and provide the formulation of the CRLB for the specific case of phase estimation of an X-ray pulsar signal where the detected photons are modeled as a non-homogeneous Poisson Process (NHPP). This will provide a means for measuring the performance of the phase estimation techniques considered in the next two chapters.

The theorem defining the CRLB can be stated as the following [111]: if the probability density function $p(\boldsymbol{X};\boldsymbol{\theta})$ of a random vector $\boldsymbol{X}$ parametrized by the vector $\boldsymbol{\theta}$ satisfies the following regularity condition

$$\mathrm{E}\left[\frac{\partial}{\partial\boldsymbol{\theta}}\log p(\boldsymbol{X};\boldsymbol{\theta})\right] = 0 \quad \forall\boldsymbol{\theta}, \tag{4.1}$$

where the expectation is taken with respect to $p(\boldsymbol{X};\boldsymbol{\theta})$, then the covariance matrix of any unbiased estimator $\hat{\boldsymbol{\theta}}$ of the parameter $\boldsymbol{\theta}$ is bounded by the CRLB [111]. The CRLB is expressed as

$$\mathrm{cov}(\hat{\boldsymbol{\theta}}) \geq \mathrm{I}^{-1}(\boldsymbol{\theta}), \tag{4.2}$$

where I is the Fisher Information matrix as a function of the unknown parameter vector $\boldsymbol{\theta}$. The Fisher Information matrix is defined in terms of the probability mass function, $p(\boldsymbol{X};\boldsymbol{\theta})$, as

$$[\mathrm{I}(\boldsymbol{\theta})]_{ij} = -\mathrm{E}\left[\frac{\partial^2}{\partial\boldsymbol{\theta}_i\partial\boldsymbol{\theta}_j}\log p(\boldsymbol{X};\boldsymbol{\theta})\right], \tag{4.3}$$

where the expectation is taken with respect to $p(\boldsymbol{X};\boldsymbol{\theta})$ and the derivatives are evaluated at the true value for $\boldsymbol{\theta}$ [111].

In the simplified case of a single parameter θ being estimated then the CRLB can be defined as follows [111]:

$$\mathrm{Var}(\hat{\theta}) \geq \mathrm{CRLB}(\theta) \equiv \mathrm{I}^{-1}(\theta) = \frac{1}{-\mathrm{E}\left[\frac{\partial^2}{\partial\theta^2}\log p(\boldsymbol{X};\theta)\right]} . \tag{4.4}$$

This states that the variance of any unbiased estimator of the parameter θ is bounded below by the CRLB given that $p(\boldsymbol{X};\theta)$ satisfies a similar regularity condition as with the vector parameter case stated in Eq. (4.1) [111].

Now consider estimating parameters of an NHPP that will represent the case of detected photons arriving from an X-ray pulsar. Consider an observation of a pulsar signal starting from time t_0 of length T_{obs}. Over this observation interval, photon arrival times are recorded using an x-ray detector. Split the observation interval into N bins of length Δt seconds and create random variables X_n that contain a count of the number of photons that arrived in the n-th bin. This allows a counting process $\boldsymbol{X}$ to be defined as a vector containing the N-point data set of bin counts X_n. This counting process is a NHPP with rate function $\lambda(t;\boldsymbol{\theta})$ defined in terms of parameters of the pulsar and the detector's motion. The probability mass function, $p(\boldsymbol{X};\boldsymbol{\theta})$, for the counting process is parameterized through the rate function by the desired quantities to be estimated, which are phase and the derivatives of phase included in the model [64].

The bin size Δt is taken to be sufficiently small such that the rate can be considered constant over each bin. Each of the bin count variables X_n can then be considered homogeneous Poisson random variables. The constant rate of the n-th bin can be expressed in the following simplified form

$$\lambda_n(\boldsymbol{\theta}) \equiv \lambda(\xi_n;\boldsymbol{\theta}) \tag{4.5}$$

where ξ_n denotes the time interval of the n-th bin, $\xi_n = [t_0 + (n-1)\Delta t, t_0 + n\Delta t)$.

The CRLB for the one-dimensional parameter case will now be demonstrated using Eq. (4.4) following the derivation in [64]. This simplified case consists of a detector that is moving at a constant velocity known to the estimator. This corresponds to having a constant observed signal frequency from the pulsar. The underlying navigation filter provides a value for the velocity to be used over the observation interval. The parameter to be estimated is the phase, θ_0, at the beginning of the observation interval. The probability mass function (pmf) for the Poisson random variables representing the bin counts, X_n, are given as [64, 106]:

$$p(X_n;\theta_0) = \Pr(X_n = x;\theta_0) = \frac{[\lambda_n(\theta_0)\Delta t]^x}{x!}\exp(-\lambda_n(\theta_0)\Delta t). \tag{4.6}$$

The mean and variance of a Poisson random variable are equal [104]. For each term in the Poisson random sequence, X_n, the mean and variance are given as

$$\mathrm{E}(X_n) = \mathrm{Var}(X_n) = \lambda_n(\theta_0)\Delta t. \tag{4.7}$$

Due to X_n being an independent random sequence, the joint pmf, $p(\boldsymbol{X};\theta_0)$, is given by the product of the individual pmfs for the sequence, $p(X_n;\theta_0)$ [64]. The joint pmf is given as

$$p(\boldsymbol{X};\theta_0) = \prod_{n=0}^{N-1} p(X_n;\theta_0) = \prod_{n=0}^{N-1} \frac{[\lambda_n(\theta_0)\Delta t]^{x_n}}{x_n!}\exp(-\lambda_n(\theta_0)\Delta t), \tag{4.8}$$

where the individual pmfs are evaluated as in Eq. (4.6). Taking the natural log of the joint pmf and simplifying yields

$$\log p(\boldsymbol{X};\theta_0) = \sum_{n=0}^{N-1} x_n \log[\lambda_n(\theta_0)\Delta t] - \log(x_n!) - \lambda_n(\theta_0)\Delta t. \tag{4.9}$$

Now to continue evaluating the CRLB, the log of the pmf is differentiated with respect to the parameter to be estimated, θ_0, yielding

$$\frac{\partial}{\partial\theta_0}\log p(\boldsymbol{X};\theta_0) = \sum_{n=0}^{N-1}\left(\frac{x_n}{\lambda_n(\theta_0)\Delta t}\frac{\partial}{\partial\theta_0}\lambda_n(\theta_0)\Delta t - \frac{\partial}{\partial\theta_0}\lambda_n(\theta_0)\Delta t\right). \tag{4.10}$$

Which by simplifying by canceling out Δt gives

$$\frac{\partial}{\partial\theta_0}\log p(\boldsymbol{X};\theta_0)=\sum_{n=0}^{N-1}\left(\frac{x_n}{\lambda_n(\theta_0)}\frac{\partial}{\partial\theta_0}\lambda_n(\theta_0)-\frac{\partial}{\partial\theta_0}\lambda_n(\theta_0)\Delta t\right). \tag{4.11}$$

Taking a second derivative with respect to θ_0 yields

$$\frac{\partial^2}{\partial\theta_0^2}\log p(\boldsymbol{X};\theta_0)=\sum_{n=0}^{N-1}\left[\frac{x_n}{\lambda_n(\theta_0)}\frac{\partial^2}{\partial\theta_0^2}\lambda_n(\theta_0)-\frac{x_n}{\lambda_n(\theta_0)^2}\left(\frac{\partial}{\partial\theta_0}\lambda_n(\theta_0)\right)^2-\frac{\partial^2}{\partial\theta_0^2}\lambda_n(\theta_0)\Delta t\right]. \tag{4.12}$$

Evaluating the expected value of Eq. (4.12) with respect to $p(\boldsymbol{X};\boldsymbol{\theta})$ gives

$$\mathrm{E}\left[\frac{\partial^2}{\partial\theta_0^2}\log p(\boldsymbol{X};\theta_0)\right]=\sum_{n=0}^{N-1}\left[\left(\frac{\mathrm{E}[x_n]}{\lambda_n(\theta_0)}-\Delta t\right)\frac{\partial^2}{\partial\theta_0^2}\lambda_n(\theta_0)-\frac{\mathrm{E}[x_n]}{\lambda_n(\theta_0)^2}\left(\frac{\partial}{\partial\theta_0}\lambda_n(\theta_0)\right)^2\right]. \tag{4.13}$$

Using Eq. (4.7) to substitute for $\mathrm{E}[x_n]$ and simplifying gives

$$\mathrm{E}\left[\frac{\partial^2}{\partial\theta_0^2}\log p(\boldsymbol{X};\theta_0)\right]=\sum_{n=0}^{N-1}\left[-\frac{\Delta t}{\lambda_n(\theta_0)}\left(\frac{\partial}{\partial\theta_0}\lambda_n(\theta_0)\right)^2\right] \tag{4.14}$$

Rearranging and using Eqs. (4.4) and (4.5) gives an expression for the reciprocal of the CRLB

$$\mathrm{CRLB}^{-1}(\theta_0)=\sum_{n=0}^{N-1}\frac{\left[\frac{\partial}{\partial\theta_0}\lambda(\xi_n,\theta_0)\right]^2}{\lambda(\xi_n,\theta_0)}\Delta t\ . \tag{4.15}$$

Now take the limit $\Delta t\to 0$ since the interval Δt was taken to be arbitrarily small. This is equivalent to taking the number of bins $N\to\infty$. This allows the CRLB from Eq. (4.15) to be expressed as an integral evaluated over the entire observation window as follows [64]:

$$\mathrm{CRLB}^{-1}(\theta_0)=\int_{t_0}^{t_0+T_{obs}}\frac{\left[\frac{\partial}{\partial\theta_0}\lambda(\xi_n,\theta_0)\right]^2}{\lambda(\xi_n,\theta_0)}dt\ . \tag{4.16}$$

Plugging in for $\lambda(\xi_n,\theta_0)$ using Eqs. (2.7) and (2.10) gives

$$\mathrm{CRLB}^{-1}(\theta_0)=\int_{t_0}^{t_0+T_{obs}}\frac{\left[\frac{\partial}{\partial\theta_0}\left(\beta+\alpha h(\theta_0+\int_{t_0}^{t}f(t')dt')\right)\right]^2}{\beta+\alpha h(\theta_0+\int_{t_0}^{t}f(t')dt')}dt\ . \tag{4.17}$$

With the simplification of considering a known constant observed signal frequency f corresponding to a constant velocity of the detector with respect to the LOS to the pulsar, the reciprocal of the CRLB can be expressed by plugging Eq. (2.15) into Eq. (2.16) to get

$$\mathrm{CRLB}^{-1}(\theta_0) = \int_{t_0}^{t_0+T_{obs}} \frac{\left[\alpha \frac{\partial}{\partial \theta_0} h(\theta_0 + f(t-t_0))\right]^2}{\beta + \alpha h(\theta_0 + f(t-t_0))} dt \; . \tag{4.18}$$

Now a change of variables from time t to phase ϕ can be performed using Eq. (2.15), which yields

$$\mathrm{CRLB}^{-1}(\theta_0) = \frac{1}{f} \int_{\theta_0}^{\theta_0+fT_{obs}} \frac{\left[\alpha \frac{\partial}{\partial \phi} h(\phi)\right]^2}{\beta + \alpha h(\phi)} d\phi \; , \tag{4.19}$$

where θ_0 is the phase of the observed signal at time t_0 and f is the constant observed signal frequency. By assuming that $fT_{obs} \gg 1$ cycle, the dependence of Eq. (4.19) on θ_0 can be removed since the integrand of Eq. (4.19) is periodic due to the pulse profile function h(ϕ) being periodic [64]. This gives the final form of the CRLB for the case of estimating the initial phase of a pulsar signal considering the observed signal frequency is constant and known, which can be stated as the following bound on the variance of any unbiased estimator of θ_0 [64]:

$$\mathrm{Var}(\hat{\theta}_0) \geq \left[T_{obs} \int_0^1 \frac{\left[\alpha \frac{\partial}{\partial \phi} h(\phi)\right]^2}{\beta + \alpha h(\phi)} d\phi \right]^{-1} \quad (\text{cycle}^2). \tag{4.20}$$

Now instead of simplifying to the case of a known constant observed signal frequency, consider the case of a known initial observed signal frequency and a known constant derivative of the signal frequency. The underlying navigation filter will provide an estimate of the velocity and acceleration of the detector at the start of each observation interval. This provides the initial signal frequency and the derivative of the signal frequency to be used by the estimator during that observation interval. This will be useful when considering the extensions to the phase-tracking procedure proposed in the next chapter that relax the requirement of having a constant signal frequency over each block.

The phase at the detector, in the case of a constant signal frequency derivative $\dot{f}$, can be expressed as a second-order Taylor expansion as in Eq. (2.13). The rate function for the NHPP in this case is given in Eq. (2.14). Plugging Eq. (2.14) into Eq. (4.16) gives the CRLB of estimating initial phase in the case of a known initial observed signal frequency and a known constant derivative of the signal frequency:

$$\mathrm{CRLB}^{-1}(\theta_0) = \int_{t_0}^{t_0+T_{obs}} \frac{\left[\alpha \frac{\partial}{\partial \theta_0} h\left(\theta_0 + f(t-t_0) + \frac{\dot{f}}{2}(t-t_0)^2\right)\right]^2}{\beta + \alpha h\left(\theta_0 + f(t-t_0) + \frac{\dot{f}}{2}(t-t_0)^2\right)} dt \ . \tag{4.21}$$

The changing signal frequency means that the same change of variables from time to phase cannot be made as in Eq. (4.19), and that the effects of the initial time t_0 or the initial phase θ_0 cannot be removed from the bound as in Eq. (4.20) from the known constant signal frequency case. It is necessary to numerically integrate over the entire observation. Other references contain extensions of the CRLB for higher-order parameter estimation using X-ray pulsar signals. The two-dimensional CRLBs for using X-Ray photons arrival times to estimate both the phase and frequency of an observed pulsar signal or the position and velocity of a detector of that pulsar signal are given in [67] and [106], respectively.

4.3 Empirical MLE Performance vs. CRLB

In this section the performance of the proposed MLE for phase of a pulsar signal is evaluated and compared to the CRLB. Particularly, trends are considered across a variety of MSPs that are best suited for navigation. First the proposed extension to the MLE for phase and the phase tracking algorithm is introduced that allows for the assumption of constant frequency over each block to be relaxed.

4.3.1 Extension of the MLE for Phase to Relax the Constant Frequency Assumption

As was shown in Chapter 2, there are drawbacks to the assumption of constant frequency over each block of the phase tracking algorithm proposed by Golshan and Sheikh in [64]. This assumption makes the algorithm unusable for MSP's detected by a reasonably sized x-ray detector for spaceflight.

The proposed update to the phase MLE that will allow the assumption of constant frequency to be relaxed consists of using a second-order Taylor series expansion for the phase at the detector as the MLE's internal model of the phase evolution. The pulsar rate function is given in terms of the phase, frequency, and frequency derivative at a reference time in Eq (2.14). In order to estimate the phase at the beginning of each block of the phase tracking algorithm, values for f and $\dot{f}$ from the underlying DPLL corresponding to the time at the start of the block are used in the second-order Taylor expansion of phase. This requires the use of a third-order

DPLL in the phase tracking algorithm, with loop filter as expressed in Eq (3.5), to be able to provide the outputs of f and $\dot{f}$ at the various times needed. A flow chart outlining this proposed new phase tracking method is contained in Figure 4.1 .

The previous MLE introduced in Chapter 2 and expressed in Eq (2.23) is expanded to this new model for phase evolution at the detector as follows

$$\hat{\theta}_0 = argmax_{\tilde{\theta}_0 \in \Theta} LLF(\tilde{\theta}_0, \hat{f}, \hat{\dot{f}}), \tag{4.22}$$

where Θ is the search space for phase and the LLF for the realization of the NHPP is given as

$$LLF(\tilde{\theta}_0, \hat{f}, \hat{\dot{f}}) \equiv \sum_{k=1}^{K} \log[\lambda(t_k; \tilde{\theta}_0, \hat{f}, \hat{\dot{f}})], \tag{4.23}$$

where log is the natural logarithm, $\tilde{\theta}_0$ is the phase value that the LLF is computed at, and $\hat{f}$ and $\hat{\dot{f}}$ are the previous estimates of the frequency and frequency derivative, respectively. The maximization contour for the LLF is bumpy and requires brute force methods to solve for the MLE using a multiple level grid search as described in Chapter 2.

This new model assumes a constant frequency rate, which is equivalent to a constant acceleration, but allows the signal frequency to vary. This change will allow for phase tracking of a variety of MSPs that have desirable characteristics for use in a navigation system.

4.3.2 MLE Performance with a Constant Acceleration Trajectory

It is important to determine the expected performance of the new MLE for phase of a pulsar signal in order to know the expected quality of estimate for use in

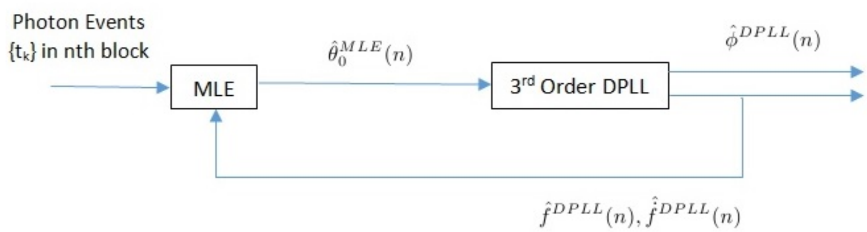

Figure 4.1: Flow chart of the proposed phase tracking method using a second-order Taylor model of phase with feedback of frequency and frequency derivative values.

Table 4.1: Simulation parameters used to determine empirical MLE performance

Detector Area, A	1 m^2
Background Flux, R_b	0.001 ph/(s cm^2)
Number of MLE Runs	100
Type of Orbit	Constant Acceleration along LOS a = 0.01 km/s^2, v_0 = 10 km/s, and $\theta_0 = 0.3$
ML-Phase Estimator	Third-order Taylor Phase Model with known f and $\dot{f}$

the underlying navigation filter. Also, we want to be sure that we are operating the MLE under conditions that will provide an estimate that is useful and this requires knowing the expected variance. In order to test the performance of the MLE, various observation times T were used and the MLE was run 100 times for each value of T. As a measure of the best possible variance for an unbiased estimator of phase, the CRLB was used to compare with the variance of the set of 100 runs of the MLE for each observation time T. For each observation time, the root-mean-square (RMS) of the phase error was used as a measure of the variance of the ML-estimates. This process was performed for a set of pulsars using a standard setup to provide an empirical determination of the MLE performance compared to the CRLB.

Table 4.2: Pulsar scenarios and the corresponding SNR with a 1 m^2 detector

Pulsar Scenario	Effective Source Flux α, ph/s	Effective Background Flux β, ph/s	SNR
B1821-24, $R_b = 0.001$ ph/(s cm^2)	1.89	10.04	0.188
B1821-24 Low SNR, $R_b = 0.002$ ph/(s cm^2)	1.89	20.04	0.094
Crab Pulsar, $R_b = 0.001$ ph/(s cm^2)	10780	4630	2.328
B1937+21, $R_b = 0.001$ ph/(s cm^2)	0.43	10.07	0.042
J0218+4232, $R_b = 0.001$ ph/(s cm^2)	0.49	10.18	0.048
J0437-4715, $R_b = 0.001$ ph/(s cm^2)	0.19	10.5	0.018

The standard setup used the parameters included in Table 4.1. In order to test the MLE performance independent of dynamic stress an orbit that matches the internal model of the phase perfectly was chosen. This orbit is a constant 0.01 km/s^2 acceleration trajectory along the LOS to the pulsar whose signal is being detected. The initial velocity is set as 10 km/s. The initial position is chosen to be a location along the LOS about 1 AU from the SSB corresponding to an initial signal phase of 0.3. A standard detector area of 1 m^2 and a background flux $R_b =$ 0.001 ph/(s cm^2) were used. The Crab pulsar along with four MSPs were considered: B1821-24, B1937+21, J0218+4232, and J0437-4715. Table 4.2 includes the source and background flux parameters for the pulsars simulated as well as the SNR.

There is a link between the estimate of the phase of the pulsar signal and the position of the detector as expressed in Eq. (3.1) while providing the motivation for phase tracking. Thus, the results of the empirical tests of MLE performance can be expressed in terms of RMS position error, which is more intuitive to determine the applicability of the estimator. This is seen by comparing Figures 4.2 and 4.3. Figure 4.2 displays the RMS phase error vs. observation time for PSR B1821-24 for the scenario described in Table 4.1 and Figure 4.3 displays the RMS position error vs. observation time for the same scenario. It can be seen that the trend is the same between the two figures. For all of the rest of the plots the RMS position error will be displayed.

As can be seen in Figure 4.2 there is a threshold observation time at which the RMS phase error of the MLE approaches the CRLB. The threshold value of the update interval, T, was chosen to be the observation time at which the plot becomes parallel to the CRLB. This threshold time is dependent on the SNR of the pulsar signal as seen in Figures 4.3 and 4.4 where the background fluxes are R_b = 0.001 ph/(s cm^2) and R_b = 0.002 ph/(s cm^2), respectively. The threshold value of T increases from 100 seconds to 150 seconds with the increase in background. For the rest of the MLE simulations in this section the background flux was set as R_b = 0.001 ph/(s cm^2) as given in Table 4.1 .

The empirical performance of the MLE was determined for the Crab pulsar, B1937+21, J0218+4232, and J0437-4715 in a similar manner. Each of these pulsars also displayed a threshold phenomenon where there is a minimum observation time required for the RMS position error to converge to the CRLB.

The threshold value of T for each pulsar can be determined by looking at their individual plots. The empirical MLE performance is demonstrated in Figures

4.5, 4.6, 4.7, and 4.8 for the Crab pulsar, B1937+21, J0218+4232, and J0437-4715, respectively. Each plot was created using the standard parameters and scenario of Table 4.1. The empirically determined threshold T values are displayed in Table 4.3 along with the last MLE observation time that contained an outlier estimate and the percentage of outliers for the corresponding observation time. These threshold values of T will be used in the next chapter when determining the update interval to use for the phase tracking algorithm.

The threshold phenomenon can be investigated further by considering plots of the number of photons vs. the phase error over the 100 runs of the MLE for a single observation time. When the observation time considered is at various points along the empirical MLE performance curve in relation to the threshold there are different patterns that can be observed in these plots of the number of photons vs. the phase error.

Consider the scenario with PSR B1821-24 and a background flux of $R_b = 0.001$ ph/(s cm^2), which corresponds to the empirical MLE performance curve in Figure 4.2. For observation times much lower than the threshold T there are a large number of outliers that have phase errors that are far away from the trend of the majority of the estimates as seen in Figure 4.9. For observation times slightly under the threshold T, but in the region where the RMS position error is converging toward the CRLB, there are only a few outliers as seen in Figure 4.10. For observation times larger than the threshold T there are no more outliers and the errors are more randomly distributed, but centered on the true value as seen in Figure 4.11.

From these plots it can be seen that the portion of the empirical MLE perfor-

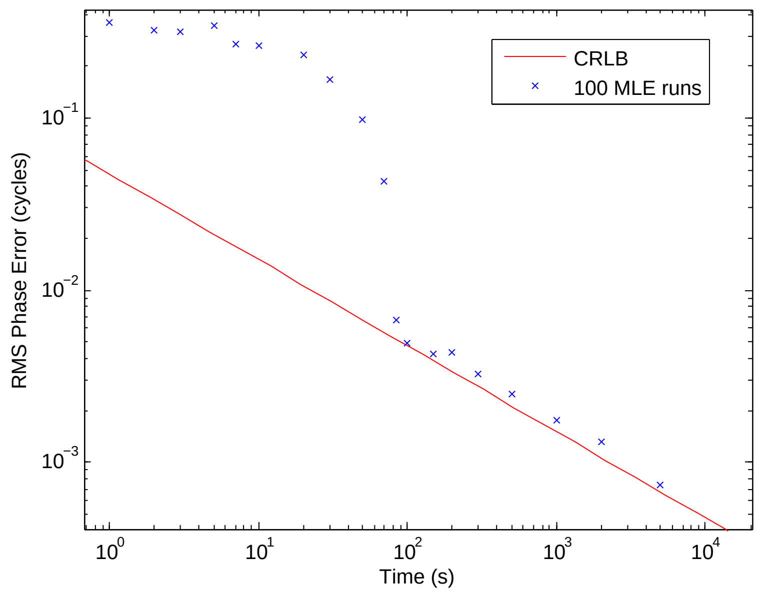

Figure 4.2: MLE Phase RMS error vs. CRLB for PSR B1821-24.

mance curve where the RMS position error is converging to the CRLB, but is still not close to it, is caused by a small number of remaining outliers. Thus, choosing an observation time over the threshold T greatly reduces the likelihood of an outlier phase estimate. The phase tracking algorithm might be more or less sensitive to possible outlier estimates depending on choices made and investigated in the next chapter. This makes knowing this threshold observation time very useful and the number of runs used to create the empirical MLE performance curve relates to the percentage that an outlier is expected at the threshold observation time. When the observation time goes far below the threshold observation time, the RMS position error corresponds to the phase estimate being uniformly distributed on the interval [0, 1). This corresponds to no information being gained by the position estimate.

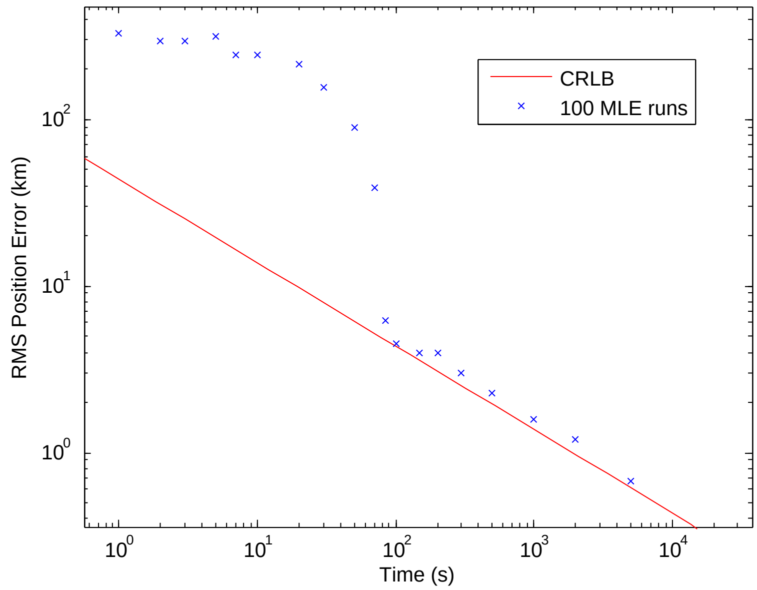

Figure 4.3: Position RMS error vs. CRLB for PSR B1821-24 as determined using the phase MLE.

Table 4.3: Empirically Determined Threshold Values

Pulsar Scenario	Empirical Threshold T, s	Last MLE Run Time with Outliers	Percent of Outliers for Last MLE Run with Outliers
B1821	85	80	1
B1821, Low SNR	150	145	1
Crab Pulsar	0.07	0.05	1
B1937+21	2750	2500	1
J0218+4232	3250	3200	1
J0437-4715	3000	2000	4

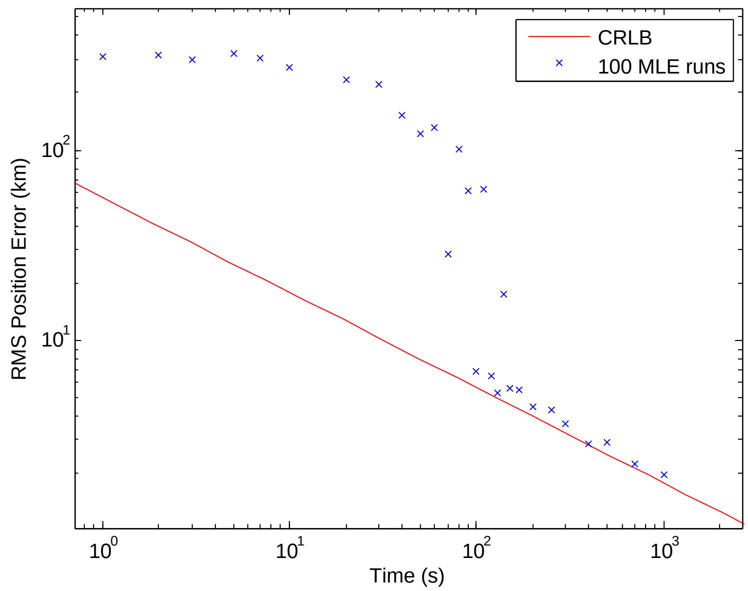

Figure 4.4: Position RMS error vs. CRLB for PSR B1821-24 with increased background flux $R_b = 0.002$ ph/(s cm^2).

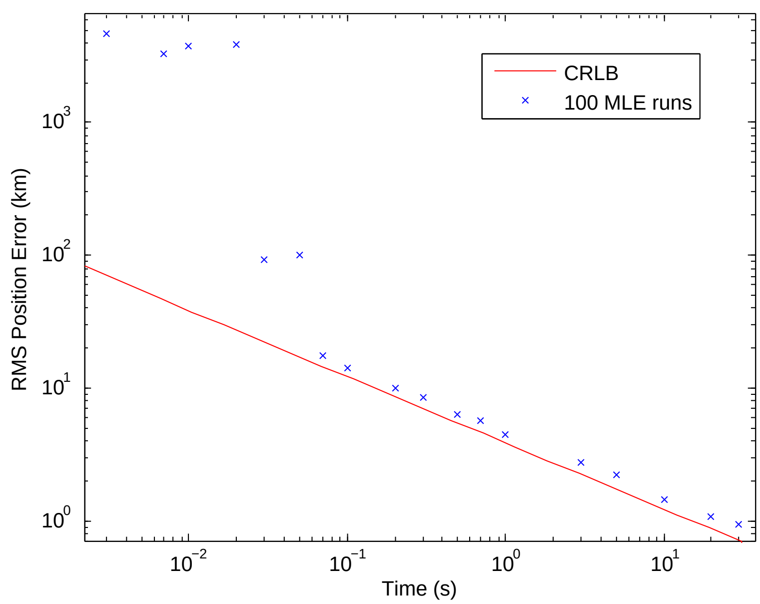

Figure 4.5: Position RMS error vs. CRLB for the Crab Pulsar.

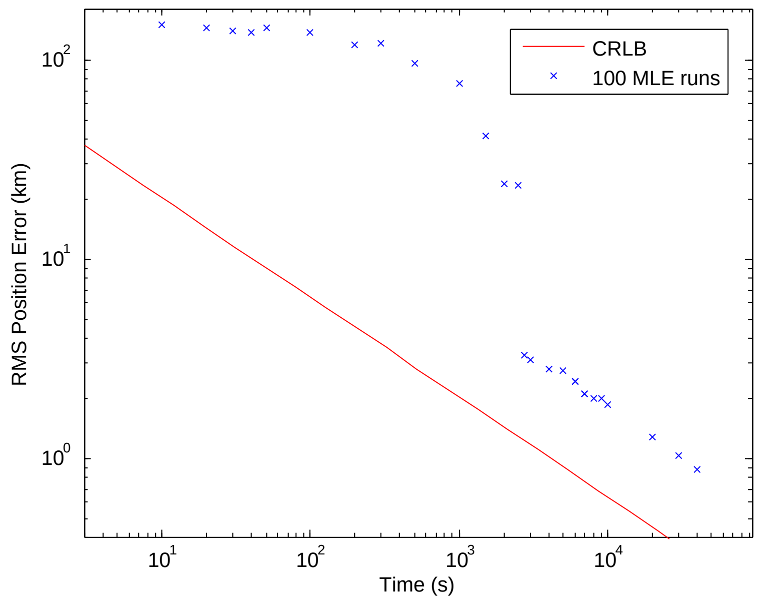

Figure 4.6: Position RMS error vs. CRLB for PSR B1937+21.

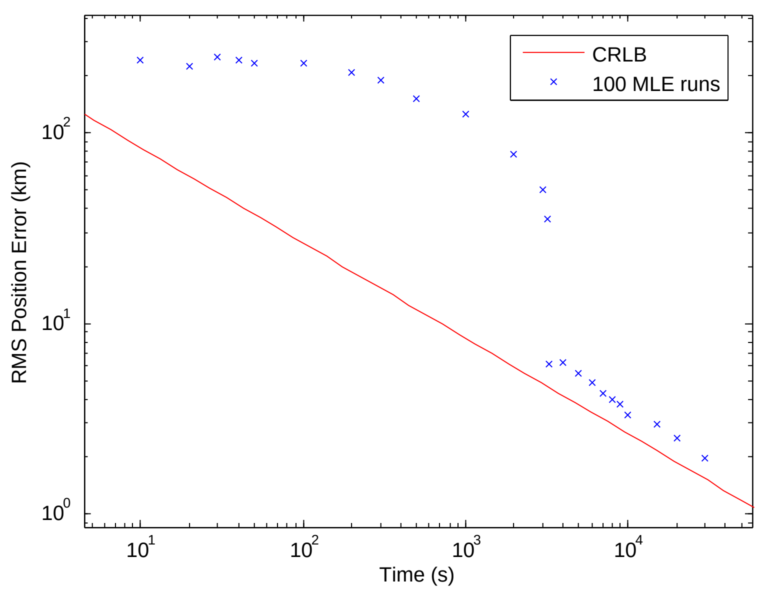

Figure 4.7: Position RMS error vs. CRLB for PSR J0218+4232.

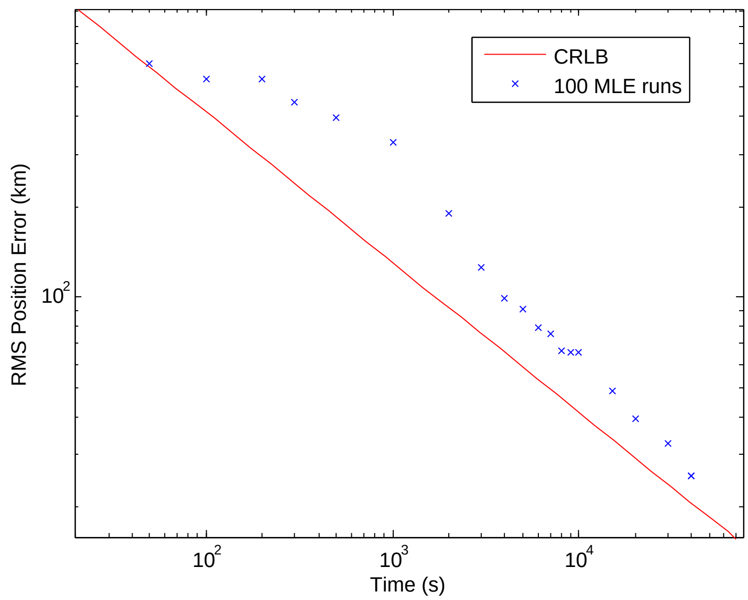

Figure 4.8: Position RMS error vs. CRLB for PSR J0437-4715.

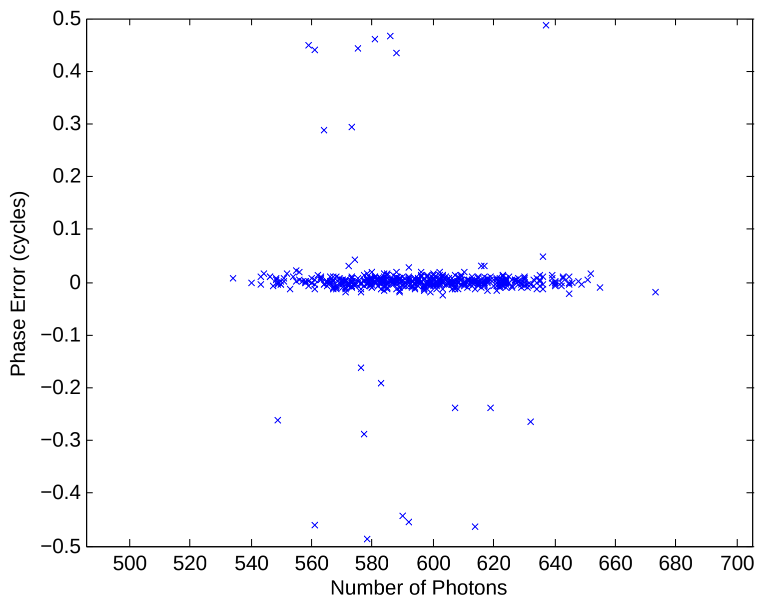

Figure 4.9: Number of Photons vs. Phase Error for PSR B1821-24 with T = 50 s, which is under the threshold.

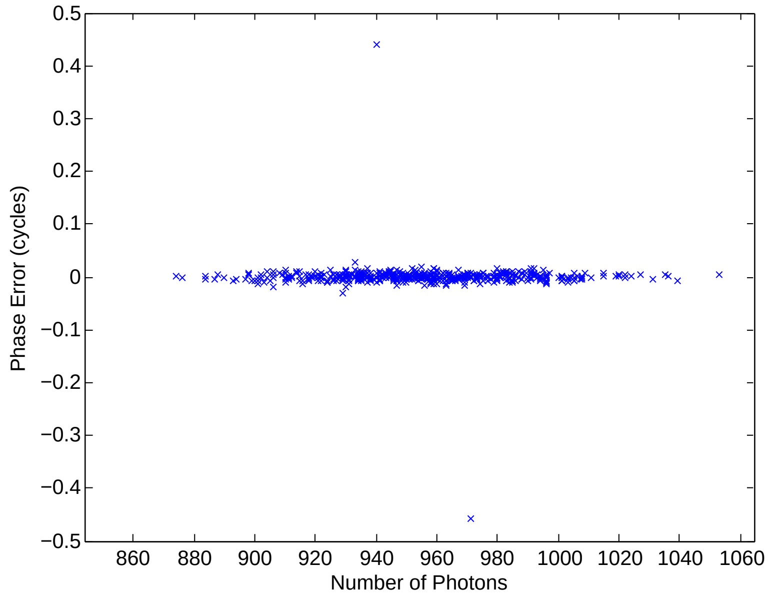

Figure 4.10: Number of Photons vs. Phase Error for PSR B1821-24 with T = 80 s, which is near but below the threshold.

4.3.3 MLE Performance with Unmodeled Trajectory Dynamics

In the previous section the empirical MLE performance was determined when the MLE internal phase model completely captures the dynamics because a constant acceleration can be exactly modeled by a second-order Taylor polynomial. In this section, the empirical MLE performance under dynamic stress is investigated. Looking at any real orbit for a spacecraft will have unmodeled trajectory dynamics that vary from the second-order Taylor model of phase. Three Earth orbits are considered, GPS, ISS, and a DirecTV satellite, as well as one interplanetary trajectory along the cruise stage of the MSL mission. The parameters of the simulations are taken to be the same as in Table 4.1. The detector area, background flux, number

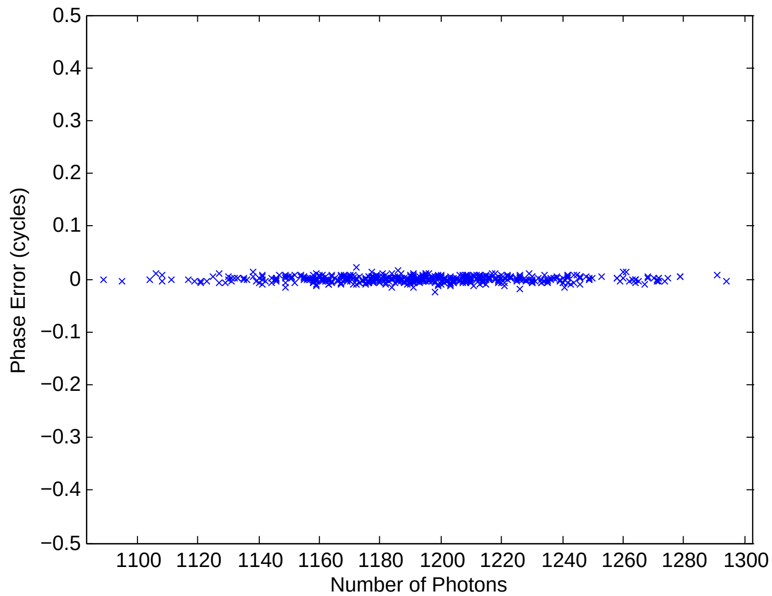

Figure 4.11: Number of Photons vs. Phase Error for PSR B1821-24 with T = 100 s, which is over the threshold.

of MLE runs, and the structure of the ML-phase estimator are all the same as in the last section when considering the constant acceleration trajectory.

For each of the orbits one of the empirical MLE performance curves is included. Figure 4.12 contains the empirical MLE performance curve compared to the CRLB for the ISS orbit with PSR B1821-24. There is a tight window of convergence to the CRLB. Figure 4.13 contains the empirical MLE performance curve for the GPS orbit with PSR B1821-24. The window of convergence to the CRLB is slightly larger than with the ISS orbit. Figure 4.14 contains the empirical MLE performance curve for the DirecTV orbit with PSR B1821-24. The convergence window to the CRLB is longer than the other two Earth orbits. This window is increasing as the dynamic stress decreases. Figure 4.15 contains the empirical MLE performance curve for the

MSL cruise trajectory with PSR B1937+21. For the MSL trajectory there appears to be no upper bound on observation time for the MLE.

The dynamic stress creates an upper limit on the observation time before outlier phase estimates start occurring at a higher than expected frequency. Knowing this observation time is important, so that the update interval of the phase tracking algorithm is set to a value that is in the sweet spot between the lower threshold value that comes from the Poisson statistics and the upper limit that comes from the dynamic stress. This demonstrates the trade-off between wanting a long observation time, so that more photons are detected, but also wanting a short enough observation so that the constant frequency derivative assumption is valid for the trajectory of the detector.

The empirically determined values of the lower threshold T and the upper limit on observation time for the pulsars considered are displayed in Tables 4.4, 4.5, 4.6, and 4.7 for the GPS, ISS, DirecTV satellite, and MSL cruise trajectories, respectively. The upper limits for the Crab pulsar simulations are undetermined due to the high flux. They are not as necessary due to the much lower values for the lower bound on observation time. For all of the orbits, the lower threshold time is 0.05 – 0.07 seconds with the Crab pulsar. For all of the orbits, the thresholds are ordered for the pulsars based on SNR level.

For some pulsars on some of the orbits, the upper and lower thresholds were reported as the same value. In these cases, the MLE performance never fully converged to the CRLB and the observation time with the lowest RMS position error was reported as both thresholds. For the GPS orbit, the lower thresholds for the

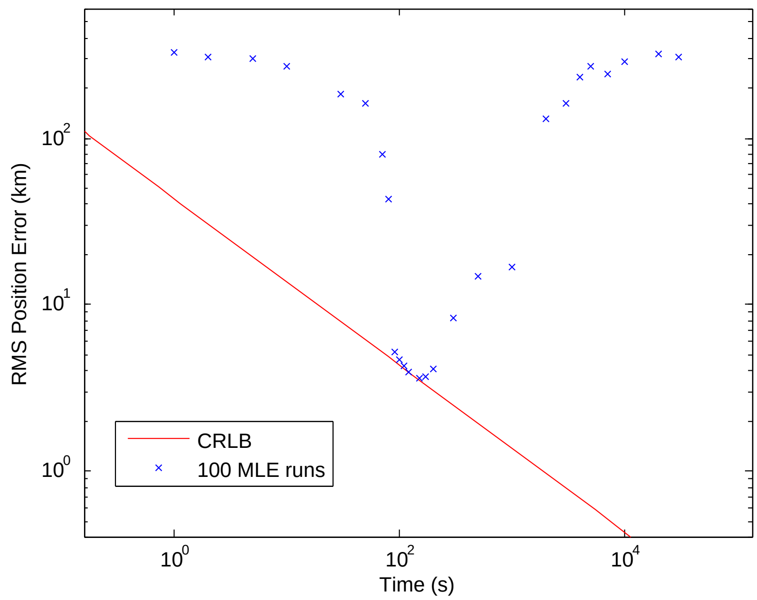

Figure 4.12: MLE Position RMS error vs. CRLB for PSR B1821-24 with the ISS orbit.

MSPs ranged from 80 seconds with B1821-24 to 2000 seconds for the other three, and the upper limit varied from 500 seconds for B1821-24 to 4000 seconds for J0437-4715.

For the ISS orbit, only the Crab pulsar and B1821-24 converged near the CRLB. For B1821-24 the threshold values were 90 and 170 seconds. For the DirecTV orbit, the lower thresholds for the MSPs ranged from 80 seconds with B1821-24 to 5000 seconds with J0437-4715, and the upper limit varied from 1000 seconds for B1821-24 to 5000 seconds for J0437-4715. As seen in Table 4.7 there is no upper limit when tracking the MSL trajectory due to the low dynamic stress. The lower threshold for the MSPs range from 100 seconds with B1821-24 to 5000 seconds with J0437-4715.

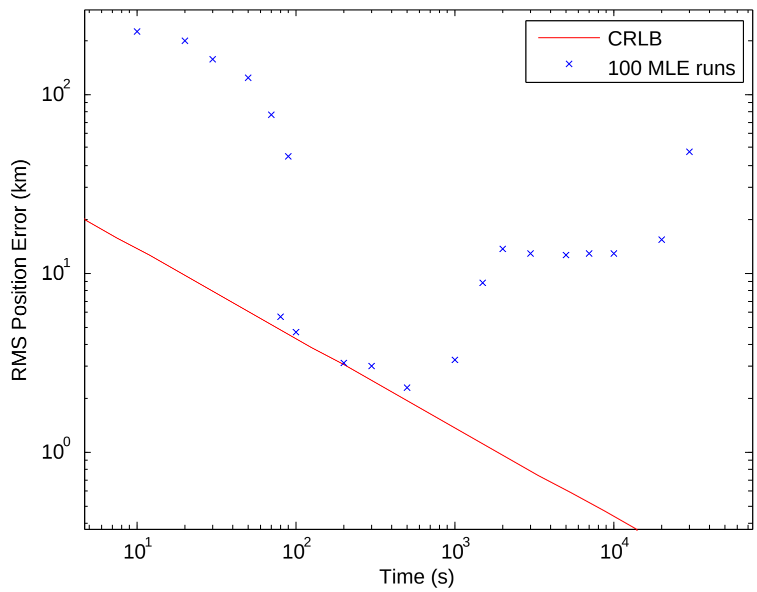

Figure 4.13: MLE Position RMS error vs. CRLB for PSR B1821-24 with a GPS orbit.

Table 4.4: Empirically Determined Upper and Lower Threshold Values for GPS orbit

Pulsar Scenario	Lower Threshold T, s	Upper Limit, s
Crab Pulsar	0.05	N. A.
B1821-24	80	500
B1937+21	2000	2000
J0218+4232	2000	2000
J0437-4715	2000	4000

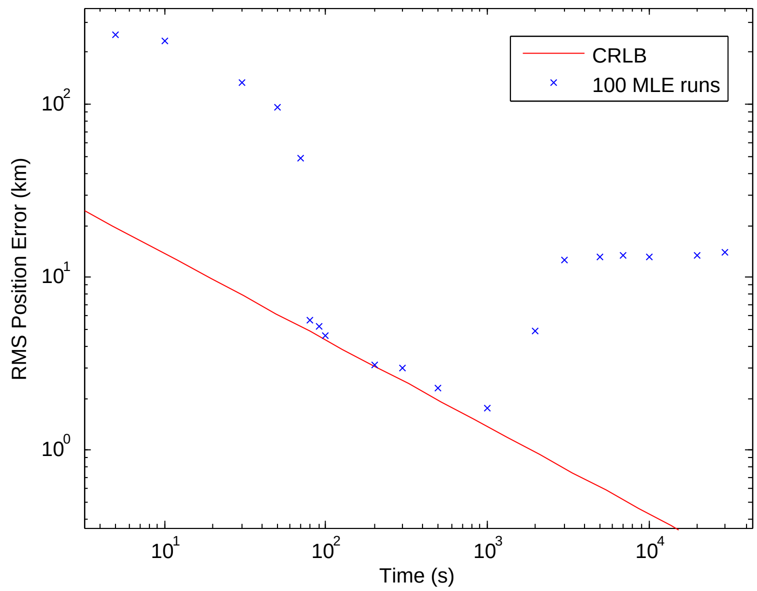

Figure 4.14: MLE Position RMS error vs. CRLB for PSR B1821-24 with a DirecTV satellite orbit.

Table 4.5: Empirically Determined Upper and Lower Threshold Values for ISS orbit

Pulsar Scenario	Lower Threshold T, s	Upper Limit, s
Crab Pulsar	0.07	N. A.
B1821-24	90	170
B1937+21	N. A.	N. A.
J0218+4232	N. A.	N. A.
J0437-4715	N. A.	N. A.

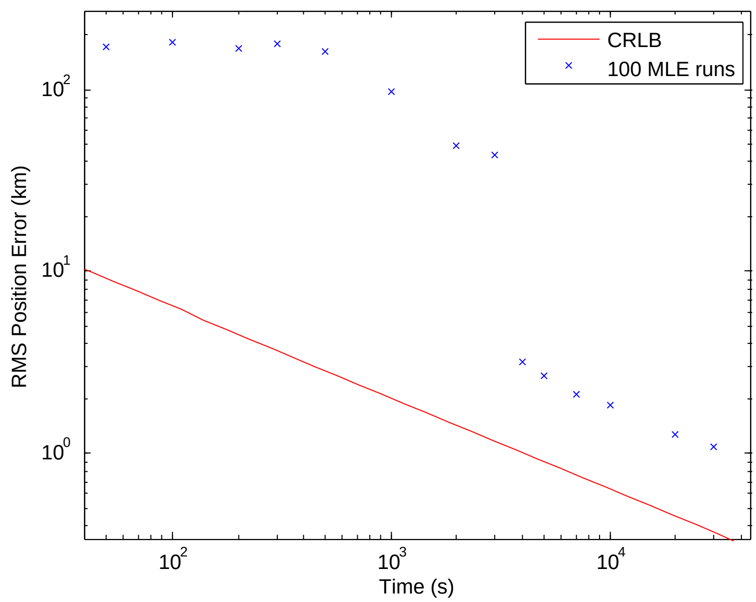

Figure 4.15: MLE Position RMS error vs. CRLB for PSR B1937+21 with the MSL cruise trajectory.

Table 4.6: Empirically Determined Upper and Lower Threshold Values for DirecTV orbit

Pulsar Scenario	Lower Threshold T, s	Upper Limit, s
Crab Pulsar	0.07	N. A.
B1821-24	80	1000
B1937+21	2000	2700
J0218+4232	4000	4000
J0437-4715	5000	5000

Table 4.7: Empirically Determined Upper and Lower Threshold Values for MSL Cruise Trajectory

Pulsar Scenario	Lower Threshold T, s	Upper Limit, s
Crab Pulsar	0.07	N. A.
B1821-24	100	N. A.
B1937+21	4000	N. A.
J0218+4232	4000	N. A.
J0437-4715	5000	N. A.

4.4 Analytical Prediction of Threshold Observation Time

Extensive computation time is needed to create new empirical MLE performance plots like the ones considered in the last section, on the order of days to weeks in Matlab. When considering a new pulsar and orbit combination it is desirable to have a way to predict the threshold observation time necessary to converge to the CRLB without having to wait to compute the MLE for a large number of runs over a range of observation times. This section presents an analytical method to determine an estimate of the threshold T that takes a fraction of the time of creating an empirical performance curve.

The basic idea comes from the underlying grid search process that is used to compute the MLE. A vast number of the outlier phase estimates come from the wrong interval being selected at the top level of the grid search. For a given observation time, determining the probability that the phase estimate will lie in the correct section of the coarse first grid provides a means to estimate the probability that the MLE will produce an outlier. This process can then be used to predict the threshold T value.

Consider the sum that results when generating the LLF while determining the MLE for phase of a pulsar signal, as given in Eq. (4.23). Define random variables X_k that represent the values of the LLF that result from the phase values ϕ_k that correspond to the k-th photon event time as follows:

$$\mathrm{X}_k = \log[\beta + \alpha h(\theta_0 + \phi_k)], \tag{4.24}$$

where θ_0 is the true initial phase, $\phi_k = \int_0^{t_k} f(t)dt$ is the Doppler phase that corresponds to the photon event time t_k, and f is the observed signal frequency of the pulsar. By the central limit theorem (CLT), assuming a large number, K, of photons detected, we know that the LLF sum can be represented by a normal random variable X as follows [109]:

$$\mathrm{X} \equiv \sum_{k=1}^{K} \mathrm{X}_k = \sum_{k=1}^{K} \log[\beta + \alpha h(\theta_0 + \phi_k)] \sim N(\mu_x, \sigma_x^2) \tag{4.25}$$

where N(μ_x,σ_x^2) denotes that X is distributed normally with mean μ_x and variance σ_x^2. The mean of X, μ_x, is defined using the expected value as follows:

$$\mu_x \equiv \mathrm{E}[\mathrm{X}] = \mathrm{E}\left[\sum_{k=1}^{K} \log(\beta + \alpha h(\theta_0 + \phi_k))\right]. \tag{4.26}$$

To calculate μ_x the expectation operator can be brought inside the finite sum

$$\mathrm{E}\left[\sum_{k=1}^{K} \log(\beta + \alpha h(\theta_0 + \phi_k))\right] = \sum_{k=1}^{K} \mathrm{E}\left[\log(\beta + \alpha h(\theta_0 + \phi_k))\right]. \tag{4.27}$$

Now use the definition and properties of the expected value in order to express E[X] as a sum of integrals [109]:

$$\mathrm{E}[\mathrm{X}] = \sum_{k=1}^{K} \int_0^1 \log(\beta + \alpha h(\theta_0 + \phi_k)) f_\Phi(\phi_k; \theta_0) d\phi_k, \tag{4.28}$$

where $f_\Phi(\phi_k; \theta_0)$ is the probability density function of the phase ϕ_k, where ϕ_k is defined mod 1. This pdf can be determined by scaling the rate function given in Eq. (2.7) so that it integrates to 1 as required, which yields:

$$f_\Phi(\phi_k; \theta_0) = \frac{1}{\alpha + \beta} \left[\beta + \alpha h(\theta_0 + \phi_k)\right] \qquad \text{if } \phi_k \in [0, 1). \tag{4.29}$$

Define $f_\Phi(\phi_k; \theta_0) = 0$ for $\phi_k \notin [0, 1)$ in order to satisfy the requirements to be a pdf, which corresponds to ϕ_k being defined as the phase mod 1. Since the ϕ_k's are independent and identically distributed, with K assumed large and using the strong law of large numbers, Eq. (4.28) can be approximated as follows [109]:

$$\mathrm{E}[\mathrm{X}] \approx K \int_0^1 \log(\beta + \alpha h(\theta_0 + \phi)) f_\Phi(\phi; \theta_0) d\phi. \tag{4.30}$$

This expectation can be evaluated through numerical integration using the form of h representing the pulsar considered.

The variance of X, σ_x^2, can be computed by using the fact that the variance of a sum of uncorrelated random variables is equal to the sum of the variances as follows:

$$\sigma_x^2 \equiv \mathrm{Var}[\mathrm{X}] = \mathrm{Var}\left[\sum_{k=1}^{K} X_k\right] = \sum_{k=1}^{K} \mathrm{Var}\left[X_k\right] \tag{4.31}$$

The definition of variance can be used to compute the value of the kth element of this sum as follows:

$$\mathrm{Var}[\mathrm{X}_k] = \mathrm{E}[\mathrm{X}_k^2] - (\mathrm{E}[\mathrm{X}_k])^2, \tag{4.32}$$

where $\mathrm{E}[\mathrm{X}_k]$ is computed as above and $\mathrm{E}[\mathrm{X}_k^2]$ is computed similarly through numerical integration.

Now define a new random variable Z as the difference between the LLF calculation using θ_0 and $\tilde{\theta}_0$, i.e.,

$$\mathrm{Z} = \sum_{k=1}^{K} \log[\beta + \alpha h(\theta_0 + \phi_k)] - \sum_{k=1}^{K} \log[\beta + \alpha h(\tilde{\theta}_0 + \phi_k)], \tag{4.33}$$

where θ_0 is the true initial phase and $\tilde{\theta}_0$ is a value for phase that is used in the grid search to determine the ML-estimate for the initial phase. Then since Z is the difference of two normal random variables, by the CLT following Eq. (4.25), it is a normal random variable itself that satisfies

$$\text{Z} = \text{X} - \text{Y} \sim N(\mu_x - \mu_y, \sigma_x^2 + \sigma_y^2), \tag{4.34}$$

where X and Y are normal random variables that represent the limit of the sums differenced in Eq. (4.33) to define Z [109]. X is as defined in Eq. (4.25). The mean of X is given in Eq. (4.30), and the mean of Y can be computed similarly. Thus the mean of the new random variable Z is given as

$$\mu_z \approx K \int_0^1 \left[\log(\beta + \alpha h(\theta_0 + \phi)) - \log(\beta + \alpha h(\tilde{\theta}_0 + \phi))\right] f_\Phi(\phi; \theta_0) d\phi. \tag{4.35}$$

The variances of X and Y can be determined separately from Eq. (4.31). Then the variance of Z is the sum of the variances of X and Y. Since Z is a normal random variable, its pdf can be defined in terms of its mean and variance as follows [109]:

$$f_Z(z; \theta_0) = \frac{1}{\sigma_z \sqrt{2\pi}} \exp\left[\frac{-(z - \mu_z)^2}{2\sigma_z^2}\right]. \tag{4.36}$$

If $Z < 0$, then the LLF is greater for a phase value $\tilde{\theta}_0$ that is not the true initial phase and this yields an outlier value in the grid search. In this situation the wrong grid section is chosen at the coarse top level of the grid search. Numerical integration can be used to evaluate $\Pr(Z > 0)$ for a particular grid value, $\tilde{\theta}_0$, and a given number of photons, K. By definition of the pdf, $f_Z(z; \theta_0)$ can be used to compute $\Pr(Z > 0)$ as follows: [109]

$$\Pr(Z > 0) = \int_0^\infty f_Z(z; \theta_0) dz. \tag{4.37}$$

To help simplify the numerical integration, the integral can be split in two around μ_z as follows:

$$\Pr(Z > 0) = \int_0^{\mu_z} f_Z(z; \theta_0) dz + \int_{\mu_z}^\infty f_Z(z; \theta_0) dz. \tag{4.38}$$

Then since μ_z is by definition the mean of Z, the second integral in Eq. (4.38) is equal to 0.5, which yields the following simplified expression:

$$\Pr(Z > 0) = \int_0^{\mu_z} f_Z(z;\theta_0)dz + 0.5. \tag{4.39}$$

This expression is simpler to compute than the original in Eq. (4.37) since μ_z is already computed in order to define $f_Z(z;\theta_0)$.

Given a particular top level grid structure, the values for $\Pr(Z_i > 0)$ resulting from each of the incorrect grid choices $\{\tilde{\theta}_0\}_{i=1}^{\mathrm{N}}$ can be multiplied together to get the total probability, $\mathrm{P}_{outlier}$, that there is an outlier phase estimate in the first level of the grid search. Random variable Z_i is defined using Eq. (4.33) for the ith incorrect grid choice $(\tilde{\theta}_0)_i$. The number of photons, K, can be incrementally increased from a given starting value and the computation of $\mathrm{P}_{outlier}$ can be repeated until the probability of being outlier free is above a predefined desired value. This gives the number of photons required, K_{req}, to obtain the given probability that there will not be an outlier. The value for K can be converted to an observation time using the average rate of arrivals for the NHPP model of the pulsar considered. This observation time can be thought of as an estimate of the threshold value of T. The step-by-step procedure for predicting the threshold observation time, $\mathrm{T}_{threshold}$, is expressed in Figure 4.16.

4.4.1 Predicted Threshold vs. Empirically Determined Values

In order to test the proposed analytical procedure to predict the threshold observation time, it was coded in Matlab and run on scenarios that match the

1. Choose a desired probability that the grid search will be outlier free, P_{req}.
2. Choose an initial number of photons K that is large enough to approximate the sums in Eq. 4.25 as normal random variables.
3. Determine the probability of each grid value individually not producing an outlier with K photons. Find all of the probabilities $Pr(Z_i > 0)$.
4. Multiply together all of the individual probabilities that a particular grid value will not produce an outlier, $Pr(Z_i > 0)$, to get the total probability the grid search is outlier free for a given K, $P_{outlier}$.
5. Incrementally increase the number of photons K and repeat steps 3 and 4 until the total probability of being an outlier free estimate is above P_{req}. This is the number of photons required, K_{req}.
6. Get the estimate of the threshold observation time by dividing K_{req} by the number of photons arriving per second at the detector, $\alpha + \beta$. $T_{threshold} = K_{req} / (\alpha + \beta)$

Figure 4.16: Outline of the procedure for analytically predicting the threshold observation time for convergence to the CRLB.

empirical MLE vs. CRLB plots contained in Section 4.3.2. The grid was defined to match the computation used to determine the MLE for phase as presented in Section 4.3.1. The top level of the grid search tests phase values from 0 to 1 every 0.05 cycles. The next grid level centers on the point chosen from the top level and searches 0.05 cycles to each side. This second level search includes the adjacent grid values to the one chosen as corresponding to the maximum in the top level search. Thus, adjacent grid values are permissible because the next level of the grid will double check the region containing the correct phase. For example, if the true phase is 0.3 and the top level grid search chooses 0.25 as corresponding to the maximum, this is acceptable since the next level of the grid will search between 0.2 and 0.3, which still contains the correct value. This also helps account for the cases where the true phase value is near the middle of one of the top level grid intervals. Excluding the adjacent grid values in these cases could increase K_{req} unnecessarily.

The scenarios used to create the MLE vs. CRLB plots contained in Section 4.3.2 used a detector trajectory that had a constant acceleration of 0.01 km/s^2 along the LOS to the pulsar with an initial velocity of 10 km/s and an initial phase of 0.3. This choice of a trajectory with constant acceleration allows the internal MLE phase model, which is defined in Section 4.3.1 as a second-order Taylor series, to match the dynamics perfectly. Thus, the divergence from the CRLB when the observation time is below the lower threshold is due to Poisson statistical noise effects and not trajectory dynamics. This threshold due to Poisson statistics is what is tested by the proposed analytical prediction procedure of the previous section. The same initial phase of 0.3 was used for the test of the analytical prediction method.

As mentioned above, the top level of the grid search is performed on the following set of phase values:

$$\begin{aligned}\tilde{\theta} \in [&0, 0.05, 0.1, 0.15, 0.2, 0.25, 0.3, 0.35, 0.4, 0.45, 0.5,\\ &0.55, 0.6, 0.65, 0.7, 0.75, 0.8, 0.85, 0.9, 0.95, 1]\end{aligned} \tag{4.40}$$

where $\tilde{\theta}$ is a value for phase that is used in the grid search. A matching detector area of 1 m^2 and a background flux of 0.001 ph/(s cm^2) was used for each of the pulsars. As in Section 4.3.2, the pulsars tested were the Crab pulsar, B1821-24, B1937+21, J0218+4232, and J0437-4715. A low SNR scenario with PSR B1821-24 was also considered with a background flux of 0.002 ph/(s cm^2) and compared to the results of Section 4.3.2.

A range of different choices for P_{req} were used: 99%, 99.5%, 99.8%, and 99.9%. These each represent different probabilities that the MLE will not produce an outlier phase estimate. Each value for P_{req} was tested for the five pulsars considered. The resulting predictions of $T_{threshold}$, corresponding to each combination of pulsar and value for P_{req}, are contained in Table 4.8. This table compares all of the predicted required observation times to the empirically determined, in Section 4.3.2, threshold observation time for each pulsar.

For pulsars B1821-24, B1937+21, and B1821-24 with lower SNR the threshold prediction algorithm predicts observation times that are in the ballpark of the empirical determined threshold observation time for convergence to the CRLB. For B1821-24 with both levels of background flux, the prediction algorithm using a 99% probability of the MLE not producing an outlier phase estimate yields an observation time approximately 5 seconds larger than the empirical threshold. For PSR B1937+21 , the prediction algorithm using outlier-free probabilities of 99.5% and 99.8% yield observation times below and above the empirical threshold, respectively.

For the Crab pulsar the analytical prediction algorithm yields a value an order of magnitude less than the empirically determined one. The observation time is much smaller for the Crab than for the other pulsars considered, and a small increase to allow for a buffer over the threshold observation time accounts for the discrepancy in prediction.

The analytical prediction algorithm performs poorly for the other two pulsars considered. For PSR J0218+4232, the predicted necessary observation time is three to four times longer than the empirically determined threshold. Using this value would reduce the performance of the phase tracking algorithm. For PSR J0437-4715, the predicted necessary observation time is much longer than the empirically

Table 4.8: Comparison of Analytic Outlier Free Percentages with Empirical Threshold

Pulsar Scenario	Empirical Threshold T, s	Time for 99% Outlier Free, s	99.5 %	99.8 %	99.9 %
B1821-24	85	90.9	105.5	125.7	141.6
B1821-24 Low SNR	150	154.4	179.2	214.0	238.7
Crab Pulsar	0.07	0.0019	0.0022	0.0027	0.0030
B1937+21	2750	2315.0	2628.0	3058.3	3397.5
J0218+4232	3250	10439.0	12788.1	15887.9	18367.2
J0437-4715	N. A.	87808.4	104224.8	126323.4	143185.9

Table 4.9: Pulse Widths of the Pulsars Considered for Threshold Prediction

Pulsar	Pulse Width (cycle)	Pulse Width (ms)
Crab Pulsar	0.05	1.67
B1821-24	0.018	0.055
B1937+21	0.01348	0.021
J0218+4232	0.15086	0.35
J0437-4715	0.32	1.84

determined threshold and would be unusable as an update time for the phase tracking algorithm.

4.4.2 The Affect of Pulse Width on Threshold Prediction

The prediction algorithm performs well in general for three of the five pulsars considered, but two of them provide results that would be unusable. The two pulsars that have the worst predictions are the ones whose pulse profile shapes have the largest pulse widths. The pulse widths of the pulsars considered are presented in Table 4.9, expressed as both the percentage of a pulse cycle and number of milliseconds. It is hypothesized that the greater the pulse width the more conservative the estimate will be for the threshold prediction. This is potentially caused by the pulse not having a nicely defined peak in a single grid of the phase search for the MLE.

In order to test the effect of pulse width on the performance of the threshold observation time prediction algorithm, a series of artificial pulse profiles were generated. The profiles were created with a range of pulse widths. An example of the artificial pulse profile created with a pulse width of 0.1 cycles is shown over two periods in Figure 4.17. Two different source and background flux levels were considered. One was chosen to match PSR J0437-4715 and the other to match PSR B1821-24. The analytical threshold prediction algorithm was run for each pulse width to achieve a 99% chance of no outliers.

The predicted threshold observation times are plotted versus the pulse widths of the artificial pulse profiles in Figures 4.18 and.4.19 for the B1821-24 and J0437-4715 flux levels, respectively. The empirically determined threshold observation values for the MLE are also included for comparison.

In both figures, a clear trend can be seen where the analytical and empirical threshold values match up well for pulse widths below 0.15 cycles, and then the analytical prediction diverges for larger pulse widths. The prediction becomes more conservative, compared to the empirical results, the larger the pulse width. This matches the hypothesis about the effect of pulse width on the analytical threshold prediction algorithm.

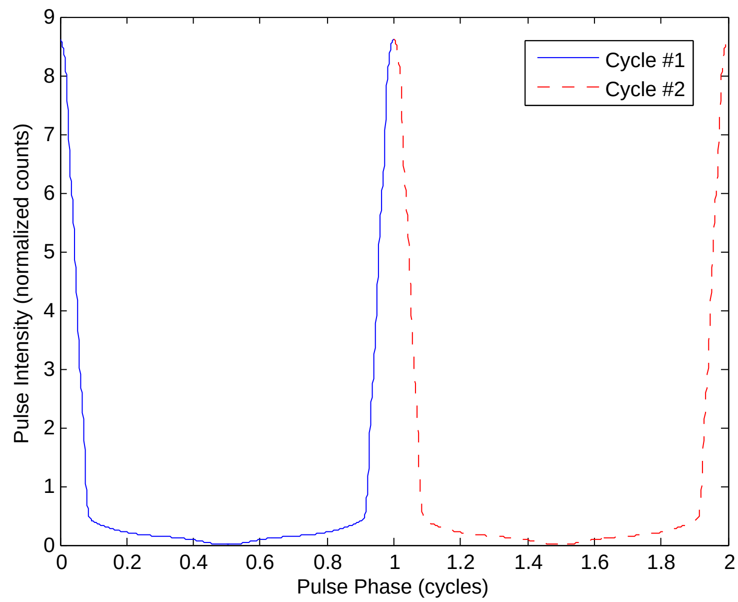

Figure 4.17: Two periods of the template for the pulse profile of an artificial pulsar with a pulse width of 0.1 cycles.

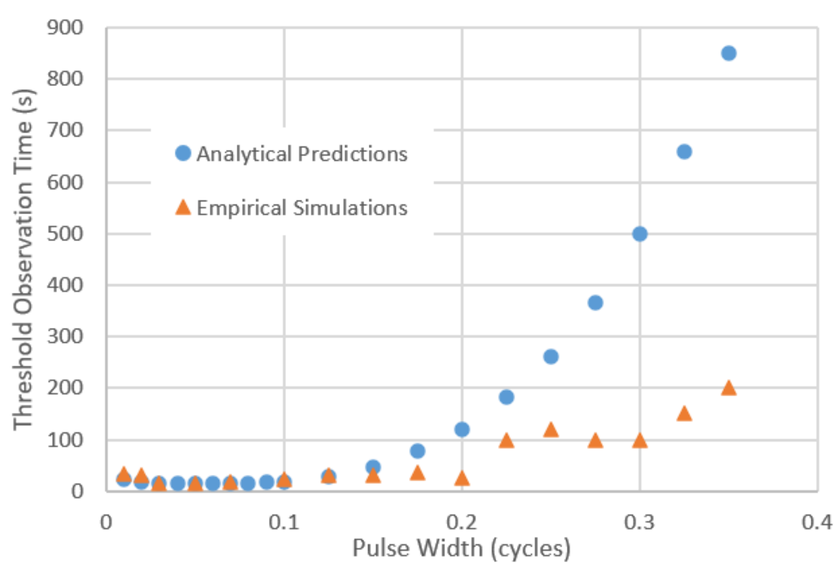

Figure 4.18: The predicted threshold observation time plotted versus the pulse width of an artificial pulse profile with a B1821-24 flux level.

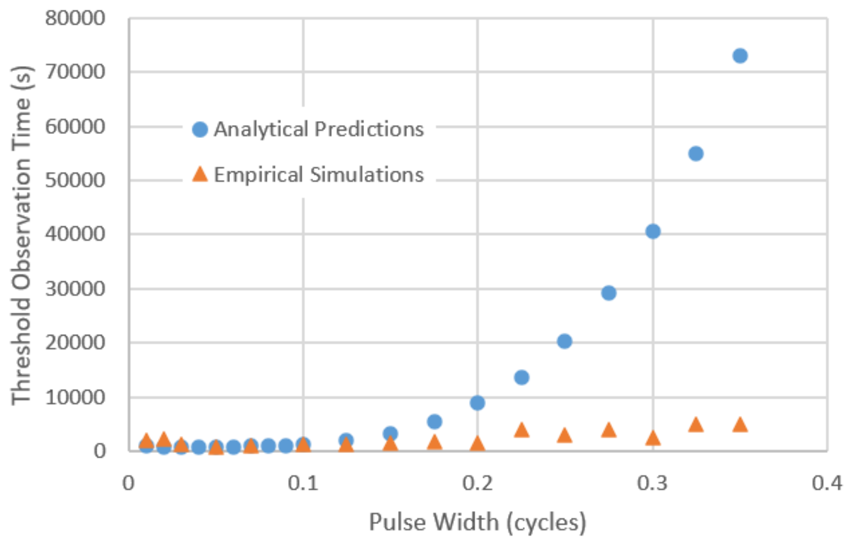

Figure 4.19: The predicted threshold observation time plotted versus the pulse width of an artificial pulse profile with a J0437-4715 flux level.

4.5 Summary

This chapter presents the extension to the algorithm using an MLE for signal phase that allows for the signal frequency to vary over an observation at an assumed constant rate. This is an update over previous methods using MLEs to track the phase of a pulsar signal that relied on the assumption of constant signal frequency or equivalently constant velocity. This extension allows for longer observations to be considered for each estimate, which expands the set of usable pulsars to include low flux MSPs that have signals that are conducive to navigation.

The CRLB for estimating pulsar signal phase was introduced and derived in order to evaluate the performance of the proposed MLE. The empirical performance of the MLE was tested using a standard detector size of 1 m^2 and a background flux $R_b = 0.001$ ph/(s cm^2). Simulations were performed and the results compared to the CRLB for five pulsars: the Crab pulsar, B1821-24, B1937+21, J0218+4232, and J0437-4715. Different orbits and trajectories were considered that provided a range of levels of dynamic stress including a simplified scenario with constant acceleration, an interplanetary trajectory of the cruise stage of the MSL, and various Earth orbits.

In all of the considered scenarios there is a threshold observation time below which the RMS error of the MLE diverges from the CRLB and tends to the uniform distribution as the observation time tends to zero. This observed lower threshold is the result of noise and Poisson effects when the number of photon event times considered for the estimate becomes too small. For the orbits and trajectories with dynamic stress, an upper threshold is also observed where the RMS error of the

MLE diverges again from the CRLB. This is the result of the mismatch between the Taylor series model for the phase and the affects of the dynamic stress on the true phase evolution. This mismatch can become more pronounced the lower the observation time depending on the dynamics of the trajectory.

For all of the orbits, the thresholds are ordered for the pulsars based on SNR level. Only the Crab pulsar and B1821-24 approach the CRLB for the ISS orbit. For the MSL trajectory none of the pulsars had upper thresholds since the dynamic stress was low. For B1821-24 the lower threshold was around $80 - 100$ seconds for all of the orbits, and the upper threshold varied from 170 seconds for the ISS orbit to 1000 seconds for the DirecTV orbit.

Also, a method to analytically predict the lower threshold observation time for a given pulsar was proposed and tested. This method provides a quick means of approximating the necessary observation time per run of the phase MLE for convergence to the CRLB without having to perform extensive and time consuming empirical tests. The analytical prediction algorithm was tested with the same five pulsars as the MLE: the Crab pulsar, B1821-24, B1937+21, J0218+4232, and J0437-4715. The prediction works well for the Crab pulsar, B1821-24, and B1937+21, but has poor results for J0218+4232 and J0437-4715.

The two pulsars with poor results predicted much longer observation times than determined necessary from the empirical testing. These two pulsars had the largest pulse widths of the five pulsars considered, and it was proposed that this had an affect on the algorithm's performance. This hypothesis was tested using artificially designed profiles of various widths with flux levels corresponding to PSR

J0437-4715 and PSR B1821-24. It was shown that the prediction matches up well with the empirically determined observation threshold for pulse widths below 0.15 cycles and diverges for larger widths.

Chapter 5: Phase Tracking with Higher Order Phase Model

5.1 Overview

This chapter discusses and analyzes the performance of the proposed phase tracking algorithm that is based on a higher order phase model. The motivation is to allow for variations in the signal frequency over the blocks of observation time of the pulsar signal used to estimate phase. This method is based on the use of a third-order DPLL with frequency and frequency derivative feedback to an MLE for phase.

Section 5.2 introduces the method of initializing the DPLL using previous estimates of phase, frequency, and frequency derivative in order to acquire lock in a transient-free manner as introduced by Stephens and Thomas in [107]. This is required since the proposed extension to the phase tracking algorithm uses feedback of the frequency and frequency derivative estimates from the DPLL in order to generate ML-estimates of phase. If the DPLL does not start close to a locked state right from start-up then the MLE phase values will not contain useful information, and the DPLL will never be able to acquire lock.

The proposed extension to the Golshan and Sheikh phase tracking algorithm to allow relaxation of the assumption of constant velocity (signal frequency) to an assumption of constant acceleration (signal frequency derivative) is discussed in detail in Section 5.3. Background information on the performance metrics and parameter choices for phase tracking are presented. The theoretical DPLL performance given the MLE error level is investigated. Rules of thumb are shown for the choice of loop noise bandwidth given dynamic stress and the SNR predicted performance.

Section 5.4 begins the presentation of the phase tracking simulation results. The first subsection tests the phase tracking algorithm in the idealized case of a detector moving on a constant acceleration trajectory along the line-of-sight to a pulsar. The pulsars B1821-24, B1937+21, J0218+4232, and J0437-4715 are considered. The results and performance are compared to the drawbacks of the Golshan and Sheikh algorithm demonstrated in Chapter 3. The second subsection adds in error to the initial phase, frequency, and frequency derivative estimates used for transient-free acquisition that corresponds to the expected performance achievable after a hand-off of a navigation state from the Deep Space Network (DSN).

In Section 5.5 the phase tracking algorithm is tested with realistic spacecraft trajectories. Interplanetary trajectories that model portions of the cruise phases of the Mars Science Laboratory (MSL) and Cassini missions are simulated. Three Earth orbits of various altitudes are considered. A cislunar transfer trajectory is also tested to provide an intermediate performance condition between the Earth orbits and heliocentric trajectories. These simulations create varying levels of dynamic stress on the DPLL due to changes in acceleration over the observation blocks of the phase tracking algorithm.

5.2 Initialization of DPLL for Transient-Free Acquisition

If accurate estimates of the signal phase and its time derivatives are known at the moment of start-up of a DPLL for phase tracking a pulsar signal, then the loop sums and loop phase can be initialized with values that allow the loop to start tracking in-lock without transients [107]. This is done by using the method of transient-free acquisition for DPLLs introduced by Stephens and Thomas in [107], which will be outlined in this section. Estimates of time derivatives of the signal phase are necessary up to the order of the DPLL. For a third-order DPLL, estimates of signal phase, signal frequency, and the signal frequency drift rate are necessary for transient-free acquisition.

For a general signal, the necessary information about the signal phase can be supplied by FFT analysis or a priori trajectory estimates [107]. For the pulsar phase tracking problem, the initial information about the signal phase and its time derivatives can be determined from initial estimates of the detector's position and its time derivatives (velocity and acceleration). The estimates of position, velocity, and acceleration can be provided by the previous best knowledge of the spacecraft state provided by either orbit trajectory propagation or some other means of navigation like the DSN.

If the input signal can be represented by an appropriate order polynomial, then steady-state tracking can develop. When the DPLL is operating with steady-state tracking, or in-lock, the residual phase becomes a constant:

$$\tilde{\phi}_n = \tilde{\phi}_{ss}, \tag{5.1}$$

where $\tilde{\phi}_{ss}$ is the constant representing the steady-state phase error. For a third-order loop, Eq. (3.5) can be represented as follows when operating with steady-state tracking [107]:

$$\Delta\phi(n+1) = K_1\tilde{\phi}_{ss} + K_2\sum_{i=1}^{n}\tilde{\phi}(i) + K_3\sum_{i=1}^{n}\sum_{j=1}^{i}\tilde{\phi}(j), \tag{5.2}$$

where estimated model phase rate, $\hat{f}^{DPLL}(n+1)T$, is replaced by differenced input phase, $\Delta\phi(n+1)$, due to the observation that model phase tracks input phase exactly when the DPLL is in steady-state besides noise and a constant phase error offset. The NCO update equation is

$$\hat{\phi}(n+1) = \hat{\phi}(n) + \hat{f}^{DPLL}(n+1)T. \tag{5.3}$$

In order to take higher order differences, the difference operator is defined as follows:

$$\Delta\phi(n+1) = \phi(n+1) - \phi(n). \tag{5.4}$$

The second and third-order differences of Eq. (5.2) can be calculated using Eq. (5.4) to yield

$$\Delta^2\phi(n+1) = K_2\tilde{\phi}_{ss} + K_3\sum_{i=1}^{n}\tilde{\phi}(i) \tag{5.5}$$

$$\Delta^3\phi(n+1) = K_3\tilde{\phi}_{ss}. \tag{5.6}$$

Now for comparison, express the input phase as a Taylor expansion centered about the center of the nth interval, $t = t_n$:

$$\phi(t) = \phi(n) + (t - t_n)\dot{\phi}(n) + \frac{(t-t_n)^2}{2}\ddot{\phi}(n) + \frac{(t-t_n)^3}{6}\dddot{\phi}(n) + \cdots \tag{5.7}$$

Higher order differences of Eq. (5.7) give the following relations between the input phase differences and the input phase derivatives [107]:

$$\Delta\phi(n+1) = T\dot{\phi}(n) + \frac{T^2}{2}\ddot{\phi}(n) + \frac{T^3}{6}\dddot{\phi}(n) + \cdots \tag{5.8}$$

$$\Delta^2\phi(n+1) = T^2\ddot{\phi}(n) + \cdots \tag{5.9}$$

$$\Delta^3\phi(n+1) = T^3\dddot{\phi}(n) + \cdots \tag{5.10}$$

For a third-order DPLL, the Taylor series in Eq. (5.7) can be approximated by the third-order Taylor polynomial. Equating the phase differences in Eqs. (5.2), (5.5), (5.6) with those in Eqs. (5.8) – (5.10) and solving for the steady-state phase error and the values of the two accumulators yields:

$$\tilde{\phi}_{ss} = \frac{T^3}{K_3}\dddot{\phi}(n) \tag{5.11}$$

$$\sum_{i=1}^{n}\tilde{\phi}(i) = \frac{1}{K_3}\left(T^2\ddot{\phi}(n) - K_2\tilde{\phi}_{ss}\right) \tag{5.12}$$

$$\sum_{i=1}^{n}\sum_{j=1}^{i}\tilde{\phi}(j) = \frac{1}{K_3}\left(T\dot{\phi}(n) + \frac{T^2}{2}\ddot{\phi}(n) + \frac{T^3}{6}\dddot{\phi}(n) - K_1\tilde{\phi}_{ss} - K_2\sum_{i=1}^{n}\tilde{\phi}(i)\right) \tag{5.13}$$

These three equations provide expressions for the values of the three unknowns in the system of equations: the steady-state phase error and the two loop sums that are necessary for initializing the DPLL. The unknowns are expressed in terms of the input phase derivatives and the given set of loop constants. An estimate of the starting model phase is also needed in order to complete the initialization [107]. For spacecraft navigation, an initial position estimate along with a model of the pulsar phase ephemeris can be used to provide an estimate of the initial input phase, which then can be differenced with the steady-state phase error to give an estimate of the model phase as follows:

$$\hat{\phi}(n) = \phi(n) - \tilde{\phi}_{ss} \tag{5.14}$$

since tracking error is equal to residual phase. The initial value of the input phase can be provided by an initial stand-alone run of the signal phase MLE or through an initial position estimate of the spacecraft obtained by other means of navigation.

The values of the loop sums and model phase can be calculated from Eqs. (5.11) – (5.14) for a phantom interval n based on the a priori values for signal phase and its derivatives [107]. They correspond to the values of these parameters that would be present under similar conditions with steady-state tracking already established. These quantities are then used to initialize the $(n + 1)$th interval following the processing of the phantom nth interval. Residual phase $\tilde{\phi}(n)$ is replaced by the steady-state phase error $\tilde{\phi}_{ss}$ in Eq. (3.5) when predicting the phase rate for the $(n+1)$th interval since the DPLL is assumed to be tracking in-lock. For subsequent intervals the loop updates are processed in the normal fashion as outlined in Section

3.4. This completes the initialization for the $(n + 1)$th interval as if steady-state tracking has been established and the operation of the DPLL begins in-lock.

When using the DPLL to process the observed signal of a pulsar in practice, the steady-state phase error only develops in cases where the observed signal can be represented by an appropriate polynomial phase model. When the dynamics are less ideal, as with any realistic spacecraft trajectory, the transients will not be completely eliminated by the initialization process [107]. Direct acquisition can be greatly improved for a third-order loop using the above initialization process given estimates of phase and its derivatives. In this case the effect of transients will be reduced and in many cases the DPLL performs as if in-lock from the initial time. For the case when the acceleration can be considered constant over an update interval, the steady-state phase error may be assumed to be zero when tracking with a third-order DPLL. Otherwise, an estimate of the change in acceleration would also be needed in order to determine the value for $\tilde{\phi}_{ss}$ to use for initialization.

5.3 Phase Tracking using a Second-Order Taylor Series Phase Model

In Chapter 3, it was shown that the previous phase tracking algorithm proposed by Golshan and Sheikh in [64] requires either unreasonably large detector areas, on the order of 25 – 100 m^2, or increased block length T in order to track the signal of MSP B1821-24 due to its significantly lower flux than the Crab pulsar. Troubles arise with the constant frequency assumption when the block length T is increased from the one second used in [64]. This assumption is equivalent to requiring that the spacecraft move at a constant velocity over each observation block of length T seconds. As demonstrated in Chapter 3, this constant observed signal frequency assumption breaks down when T is greater than about 6 seconds with a 10 m^2 detector and on a portion of the MSL cruise trajectory that has relatively low dynamic stress. These results motivated the extension of the phase tracking algorithm in a manner that allows for the constant frequency assumption to be relaxed.

The operation of the new phase tracking algorithm is demonstrated in Figure 4.1, which includes a diagram of the flow of the MLE-DPLL cascade with the new algorithm. As explained in Section 4.3.1, the internal phase model for the MLE is increased by one order to a second-order Taylor expansion. The photon events are divided into blocks of length T and the MLE produces an estimate of the phase of the observed pulsar signal at the start of each of these blocks. This change to the MLE model of the phase evolution relaxes the assumption of constant observed signal frequency to an assumption of constant frequency derivative over the length of the block. This corresponds to relaxing the constant velocity assumption to an assumption of constant acceleration. Another significant change from the Golshan and Sheikh phase tracking algorithm is that the estimates of phase from the MLE correspond to the time at the beginning of each individual block instead of back to the start time of the entire observation t_0.

The MLE is computed considering only the initial phase to be a parameter that is to be estimated. Feedback of frequency and frequency derivative values from an underlying third-order DPLL are used to define the second-order Taylor expansion of phase in the internal MLE model. The kth estimate of the MLE uses the kth block of length T from the total observation and uses the frequency and frequency derivative estimates from the $(k-1)$th update of the DPLL. The outputs of the frequency and frequency derivative from the DPLL are referenced to the end of the $(k-1)$th interval in order to match up with the Taylor expansion centered around the beginning of the kth block that is at the heart of the MLE for phase. A third-order DPLL can track constant acceleration with zero steady-state error. In the MLE phase model, the second-order Taylor polynomial truncates the phase as if it is evolving with a constant acceleration.

The equations governing the operation of a third-order DPLL were introduced in Section 3.4. These equations followed the formulation by Stephens and Thomas in [107], which includes prescribed values for the gains of the loop filter, K_1, K_2, and K_3, given desired physical parameters including loop noise bandwidth, B_L, damping ratio, ζ, update time T, and loop order. Tables included in [107] provide specific values for the loop gains. The update time of the DPLL will be considered to be the same as the block size of the observation time considered for each ML-phase estimate.

It is essential that the third-order DPLL start operation in-lock since the MLE relies on accurate estimates of frequency and frequency derivative to use in its internal phase model. If the DPLL is feeding back values of frequency and frequency derivative with high error then the MLE will not be able to produce adequate phase estimates for the DPLL to achieve lock. The transient-free acquisition procedure described in Section 5.2 is used to initialize the DPLL in-lock. The DPLL is defined as operating in-lock as long as the difference between the DPLL phase estimate and the new MLE estimate is small. This phase difference is represented by the ideal phase extractor measurement, $\tilde{\phi}$, given in Eq. (3.4).

When the phase tracking algorithm is operating with the DPLL in-lock, a check for outlier ML-phase estimates is performed at each update to the DPLL. The value, $\tilde{\phi}$, of the ideal phase detector step of the DPLL is checked at each update. If the error between the MLE and DPLL estimates for phase is over a predetermined threshold, the phase estimate from the MLE is rejected as an outlier and the DPLL continues as if $\tilde{\phi} = 0$ for that time step. For the simulations in this section the level that triggers rejection as an outlier is $\tilde{\phi} > 0.1$.

To test the phase tracking performance, the same four MSPs are chosen that were investigated in Chapter 4: B1821-24, B1937+21, J0218+4232, and J0437-4715. For certain scenarios the Crab pulsar will also be considered. The relevant pulsar parameters used in the simulations are displayed in Table 5.1. The parameters listed are as follows: f_s is the constant frequency of the source observed in an inertial frame, α is the effective source flux, β is the effective background flux, R_S is the total flux of photons from the source pulsar, R_B is the flux of background photons, and p_f is the pulse fraction. The relations between these parameters were detailed in the descriptions of pulsar signal modeling in Chapter 2. When computing α and β, the nonpulsed photons arriving from the source pulsar are considered as part of the background. The values correspond to photon detections in the 2 - 10 keV energy range of the X-ray portion of the electromagnetic spectrum with a detector area of 1 m^2.

The pulse profile templates used to simulate the signal of each of the MSPs are displayed in Figures 2.2 – 2.5 plotted over two periods. The flux parameters and profiles listed correspond to those expected at a detector that is sensitive in an energy range from 2 to 10 keV [1, 112–116]. A standard Background flux of $R_B = 0.001$ ph/cm^2/s was considered. This choice was made in order to make easy first order comparisons of the performance across the various pulsars. In future studies and applications on spacecraft missions, properties of the detector and knowledge of the operating environment can be used to get accurate background flux values specific to each pulsar.

Table 5.1: Pulsar parameters used for modeling the MSP signals assuming photon detections in the 2 - 10 keV energy range. A detector area of 1 m^2 was used [1, 112–116].

	B1821-24	B1937+21	J0218+4232	J0437-4715	Crab Pulsar
f_s, Hz	327.8689	641.9268	431.0345	173.9130	29.9401
α, ph/s	1.8914	0.42914	0.48545	0.1862	10780
β, ph/s	10.0386	10.06986	10.17955	10.4788	4630
R_S, ph/cm^2/s	0.000193	0.0000499	0.0000665	0.0000665	1.54
R_B, ph/cm^2/s	0.001	0.001	0.001	0.001	0.001
p_f (Pulse Fraction)	0.98	0.86	0.73	0.28	0.70
W (Pulse Width), ms	0.055	0.021	0.35	1.84	0.67

5.3.1 Theoretical DPLL Performance Given MLE Error Level

The MLE performance was investigated in Chapter 4 using empirical tests to check convergence to the CRLB. The MLE phase estimate can be considered as the input to the DPLL system. Thus, a measure of the expected DPLL phase output performance can be computed when the MLE performance is known. Again considering the Stephens formulation for the DPLL given in [107], the z-transform of the MLE-DPLL system can be expressed as:

$$\Phi_{DPLL}(z) = H(z)\Phi_{MLE}(z), \tag{5.15}$$

where the closed-loop transfer function H(z) is defined as

$$H(z) = \frac{K_1(z-1)^2 + K_2 z(z-1) + K_3 z^2}{(z-1)^3 + K_1(z-1)^2 + K_2 z(z-1) + K_3 z^2}. \tag{5.16}$$

The values for K_1, K_2, and K_3 are the third-order DPLL loop gains corresponding to a choice of B_L and T. If the sequence of MLE error inputs to the DPLL can be assumed to be an uncorrelated sequence that is a stationary process with mean $m_{MLE} = 0$ and variance, σ^2_{MLE}, then the DPLL output errors are also a stationary process with mean $m_{DPLL} = H(1)m_{MLE} \implies m_{DPLL} = 0$ and variance [117], i.e,

$$\sigma^2_{DPLL} = \frac{\sigma^2_{MLE}}{2\pi i} \oint H(z)H(z^{-1})z^{-1}dz, \tag{5.17}$$

where the closed path is the unit circle. Since the path is the unit circle, the conjugate $z^* = z^{-1}$. The integral in Eq. (5.17) can be computed using residues within the unit circle [118]. For simple poles this integral can be computed as [107]

$$\sigma^2_{DPLL} = \sigma^2_{MLE} \sum_i [(z - z_i)H(z)H(z^{-1})z^{-1}]_{z \to z_i} \tag{5.18}$$

where the sum is computed over the set of the poles, z_i, of the integrand within the unit circle. Since $H(z)$ is designed to be stable in the formulation of the DPLL, the three roots of $H(z)$ must all lie within the unit circle and the poles of $H(z^{-1})$ are all outside. Also, there is no pole at $z = 0$ since $\lim_{z \to 0} H(z^{-1}) = K_1 z$ [107]. Thus, only the residues of the 3 poles of H(z) contribute to the computation of σ^2_{DPLL} in Eq (5.18). This gives a prediction of the variance of the DPLL output error at a given time step as a function of the variance of the MLE input error.

The steady-state error of the DPLL can also be given in terms of the jerk stress dynamics and loop filter bandwidth or natural frequency as follows [119]:

$$\tilde{\phi}_{ss} = \frac{dR^3/dt^3}{w_0^3} \tag{5.19}$$

where dR^3/dt^3 is the line-of-site jerk of the detector motion. As can be seen from Eq. (5.19), the steady-state-error is inversely proportional to the tracking loop bandwidth of the DPLL and directly proportional to the third derivative of range, i.e., the jerk stress.

5.3.2 Rule of Thumb for Loop Noise Bandwidth Given Dynamic Stress

Due to the high-level similarities between DPLL usage for GPS tracking and phase tracking of pulsar signals, previous experience with DPLL performance in GPS situations can be applied to give a framework for expected limits on errors and accuracy in pulsar phase tracking. A rule-of-thumb for a tracking threshold for a GPS receiver PLL based on the sources of phase error is given as [119]:

$$3\sigma_{DPLL} = 3\sigma_j + \theta_e \leq 45^\circ \tag{5.20}$$

where σ_{DPLL} is the 1-sigma phase error of the DPLL, σ_j is the 1-sigma phase jitter from all sources except from dynamic stress, and θ_e is the dynamic stress error in the DPLL tracking loop. Keeping the 3-sigma errors from all causes below 45° is a conservative rule-of-thumb threshold for a DPLL tracking loop in GPS applications. This is equivalent to a 1-sigma rule-of-thumb DPLL tracking threshold of 15°. This value is chosen because in a typical GPS receiver the DPLL discriminator error begins to flatten and round off when the input phase increases beyond the 45° level when the carrier-to-noise power ratio decreases toward the thermal noise threshold [119].

For the pulsar phase tracking case, an error larger than 45° greatly increases the probability that the error will take the phase estimate out of the correct search window for MLE. Despite the differences in the formulation of the DPLL for the phase tracking problem versus GPS receivers, this same rule-of-thumb can be used to provide a first check to determine reasonable values for the loop noise bandwidth, B_L, depending on the dynamic stress of the orbits. In order to provide a bound on the choice of loop noise bandwidth based on the physics of the orbits, Eq. (5.20) will be simplified to focus only on the dynamic stress error and look for a best case scenario that disregards the other sources of potential phase jitter.

From [119] the dynamic stress error for a third-order DPLL with minimum mean square error can be defined as follows:

$$\theta_e = 0.4828 \frac{dR^3/dt^3}{B_L^3}, \tag{5.21}$$

where dR^3/dt^3 is the maximum line-of sight jerk dynamics for the trajectory expressed in $°/\mathrm{s}^3$. This can be rearranged to create a rule of thumb for the allowable DPLL loop noise bandwidth given an expected level of dynamic stress. This rule of thumb for B_L is as follows:

$$B_L^3 \geq 0.0107 \frac{dR^3}{dt^3}, \tag{5.22}$$

with the jerk stress, dR^3/dt^3, expressed in $°/s^3$. The jerk stress can be converted from km/s^3 using the wavelength of the pulsar signal. The levels of dynamic stress experienced by a spacecraft in the Earth orbits simulated in this chapter are discussed later in Section 5.5.2.1.

5.3.3 Comparison to SNR-based Performance Rule-of-Thumb

The signal-to-noise ratio (SNR) for the observed X-ray photon flux from a given pulsar can be determined from the ratio of the pulsed component of the signal source counts to the one sigma error in detecting the signal as follows [46] [48]:

$$\text{SNR} = \frac{N_{S_{pulsed}}}{\sigma_{noise}} = \frac{R_S A p_f t_{obs}}{\sqrt{[R_B + R_S(1 - p_f)](A t_{obs} d) + R_S A p_f t_{obs}}}, \tag{5.23}$$

where A is the area of the detector in cm^2, t_{obs} is the length of the observation in seconds, and d is the duty cycle of the pulse, which is defined as the fraction of the pulse width W that spans the pulse period P. The width W is usually given as the full-width at half maximum (FWHM) in seconds, which is the width of the main pulse of the profile measured at 50% of the peak intensity [1]. The noise is made up of the background radiation flux, the portion of the nonpulsed signal component that is detected during the duty cycle of the pulse, and the pulsed signal [48].

A rule-of-thumb calculation was proposed by Sheikh in [48] to estimate the achievable position accuracy based on a single observation as follows:

$$\sigma_{range} = \frac{cW}{2\text{SNR}}, \tag{5.24}$$

where c is the speed of light. The factor of the speed of light is used to convert from the accuracy of the resolution of the arrival time of a pulse. This is just intended to be a back-of-the-envelope calculation, and there are simplifications in the setup that lead to differences with the CRLB for MLE performance.

Table 5.2 presents the SNR values, achievable position accuracies, and other measures of the strength of the pulsed competent of the pulsar signal in terms of α and β for the MSPs considered as well as the Crab pulsar. The observation time chosen corresponds to the threshold observation time needed for the MLE phase RMS error to converge to the CRLB as computed in Chapter 4. The parameters are based on the values included in Table 5.1, and the same detector area and background flux were used.

Two measures are included in Table 5.2 to compare the source and background rates of each pulsar signal. The value for SNR as computed with Eq. (5.23) is tabulated as well as the ratio of the source and background effective photon rates, α and β. Some of the same general trends are apparent across the pulsars. The Crab pulsar and PSR J0437-4715 have the highest and lowest values for each metric, respectively. For the SNR measurement, the signal strength of B1821-24 looks to be worse then B1937+21 and J0218+4232, but the achievable accuracy value is better. The value of the α to β ratio is correlated to the level of position estimation performance we saw for each pulsar for the MLE in Chapter 4.

In Table 5.2 the values for the CRLB for the various pulsars can be compared. These CRLB values correspond to the specific choice of T for each pulsar with the MSL trajectory. PSR B1937+21 has an optimistic CRLB value of 1.19 km for T =

3000 seconds, but in Chapter 4 it was seen that B1937+21 has a bias offset with its performance compared to the CRLB, and this position error will not be achievable. The other pulsar CRLB values compare with each other as expected with the Crab having the smallest value of 1.22 km and J0437-4715 having by far the highest at 68.80 km. B1821-24 and J0218+4232 have performance in the range of 3 to 5 km error. Larger T values were considered for B1821-24, B1937+21, and J0218+4232 in the simulations that follow.

The rule-of-thumb accuracy as computed using Eq (5.24) is also included in Table 5.2. The general trend of which pulsar has the best MLE position tracking results can be seen relating to the σ_{range} value. The achievable accuracy prediction is more optimistic than the CRLB for all of the pulsars, which was discussed above. The prediction is a back-of-the-envelope calculation that is oversimplified as compared to the full CRLB computation.

Table 5.2: Measures of the strength of the pulsed component of the pulsar signals considered. The threshold time corresponds to the observation time necessary to converge to the CRLB.

	B1821-24	B1937+21	J0218+4232	J0437-4715	Crab Pulsar
Threshold Time, s	150	3000	3300	4000	1
SNR	16.091	31.274	19.616	6.260	103.382
α/β	0.1884	0.0426	0.0477	0.0178	2.3283
Achievable Accuracy σ_{range} (km)	0.51	0.10	2.67	44.06	0.77
CRLB(T) (km)	3.55	1.19	4.91	68.80	1.22

5.4 Constant Acceleration Simulations with Transient-Free Acquisition

In this section, the proposed extension to the phase tracking algorithm that relaxes the assumption of constant velocity is tested for a range of MSPs with trajectories that have constant acceleration along the lines-of-sight to each pulsar. This test case is chosen since the internal phase model of the MLE used in the new phase tracking algorithm has the capability to theoretically track an observed signal with constant frequency derivative with zero steady state error. This will be used as an initial test of improvement over the previous pulsar phase tracking research. The trajectory is similar to the one used to test the previous Golshan and Sheikh phase tracking algorithm with the Crab pulsar in Chapter 3. The phase tracking algorithm will be initialized with two different scenarios: true initial state and initial condition error matching a DSN handoff.

The simulated pulsar observation data consists of photon event times formed as a realization of the NHPP that corresponds to the signal model of the pulsar signal as affected by the spacecraft dynamics. This is done in a similar manner to Chapter 3 using the Matlab-based X-ray Photons and Relativistic Effects Simulation System (XPRESS), developed by ASTER Labs, Inc. and collaborators. The process consists of generating an initial set of photon event times at an inertial point, considered to be the SSB, and then time transferring to an uncorrected set of photon events times simulated at the detector using the spacecraft orbit data as outlined in

Figure 3.8 [94]. The NHPP realization is performed using the inversion method of non-uniform random variate generation presented in [108] and implemented for the specific example of X-ray pulsar photon generation in [67] as detailed in Appendix A.

The parameters and conditions necessary to describe the constant acceleration trajectories are presented in Table 5.3. For each pulsar a different artificial trajectory was constructed so that the detector was moving along the LOS to the pulsar considered and the rate of change of the range rate was constant. The same initial conditions for initial phase, range rate, and range rate rate were considered across the set of MSPs. These initial conditions were used to create a standard trajectory and then the unit vector $\hat{\mathbf{n}}$ along the LOS to each pulsar was used to convert the standard design trajectory into one that moved along the LOS. As seen in Table 5.3, the initial phase, θ_0, was chosen to be 0.3 cycles, the initial velocity (range-rate) was 10 km/s, and the constant acceleration (range-rate-rate) was 0.01 km/s^2. The initial position was chosen to be the SSB plus an offset equal to the distance necessary to properly have θ_0 correspond to the phase at time zero of the simulation. This offset was different for each pulsar depending on the source frequency.

For each pulsar, observations of 12 hours were simulated at a detector starting at the initial conditions described and then traveling along the LOS for the length of the simulation. Photon times are simulated as they accumulate at the detector as it moves along the trajectory. This set of photon event times was then processed through the phase tracking algorithm. In order to compensate for the random effects that appear in a particular realization of the NHPP, the simulation was run 10 times with each pulsar using different random number seeds.

Table 5.3: Simulation parameters for the constant acceleration trajectory.

Parameter	Value
Detector Area (A), m^2	1
Initial Phase (θ_0), cycles	0.3
Initial Velocity (v_0) , km/s	10
Constant Acceleration (a), km/s^2	0.01
Total Observation Time, s	43200
Number of Runs Averaged	10

The phase tracking algorithm as illustrated in Figure 4.1 was tested for each scenario consisting of a source pulsar and a constant acceleration trajectory along the LOS to that pulsar. Table 5.4 contains the values for the parameters used for the MLE and DPLL for each of the MSPs considered. The values for block length were chosen based on the threshold plots from Chapter 4 as well as consideration of the predicted equivalent position error of MLE phase estimates determined by the CRLB. The update time T of the DPLL was taken to be equal to the block length of the phase tracking algorithm considering no delay between the MLE computation and the DPLL update. For each pulsar scenario, the total observation was broken up into blocks of T seconds. The set of photon event times occurring in a particular block were collected together and processed through the MLE to give a phase estimate corresponding to the start time of the corresponding block. The ML-phase estimates are computed using the frequency and frequency derivative outputs of the DPLL from the previous block and are fed into the DPLL to update the model for the current block time as seen in Figure 4.1.

Table 5.4: Settings used for the parameters of the third-order DPLL for the constant acceleration trajectory phase tracking simulations with true initial state.

DPLL Parameter	B1821-24	B1821-24	B1937+21	J0218+4232	J0437-4715
Area, m^2	1	1	1	1	5
T, s	200	4000	4000	4000	4000
B_L, Hz	0.0001	0.0001	0.0001	0.0001	0.0001
ζ	0.707	0.707	0.707	0.707	0.707
K_1	0.050	0.546	0.546	0.546	0.546
K_2	0.0011	0.177	0.177	0.177	0.177
K_3	0.0000097	0.0247	0.0247	0.0247	0.0247

The choice of the DPLL loop noise bandwidth B_L takes into account both the expected dynamic stress and the desired output estimation error, as discussed in Section 5.3.1. The bandwidth needs to be high enough to allow for variations resulting from the dynamic stress of the trajectory, but the higher the bandwidth the higher the estimation error [59] [120] [119]. For the constant acceleration trajectory the dynamic stress is theoretically zero since a third-order DPLL perfectly tracks a signal with a constant frequency rate [59]. Thus, the rule-of-thumb for allowable loop noise bandwidth from Section 5.3.2 is not applicable since it depends on the jerk stress level of the orbit. Noise in the phase measurements from the MLE degrades the DPLL performance somewhat, but the internal phase model of the MLE is also third-order, so the error will predominantly be from the Poisson statistics and not dynamic stress. Thus, the values chosen for B_L can be relatively small. The damping ratio was chosen to be the same for all the simulations and corresponded to the standard underdamped response, $\zeta = \frac{1}{\sqrt{2}} \approx 0.707$. Under the Stephens and Thomas formulation of the DPLL in [107], the DPLL gains, $\{K_i\}_{i=1}^{3}$, are directly determined by the choice of the the damping ratio ζ and the product of the update time T and the loop noise bandwidth B_L. The $\{K_i\}_{i=1}^{3}$ values for various combinations of damping ratio and $B_L T$ product are contained in tables in [107]. The particular values used for the combinations of $B_L T$ and ζ for the various pulsars are contained in Table 5.4.

5.4.1 Initial Conditions using True Initial State

First, the phase tracking algorithm will be initialized using the true initial state in order to test the ability to maintain and improve the position estimates over the constant acceleration trajectory. Removing the effects caused by potential initial condition errors allows for a focus on other factors affecting the phase tracking performance. To do this, each simulation uses knowledge of the initial state, given as position, velocity, and acceleration converted to phase, frequency, and frequency derivative and uses these signal properties to initialize the DPLL. This then allows each phase tracking simulation to start with the DPLL perfectly in-lock using the techniques for transient-free acquisition presented in Section 5.2.

5.4.1.1 Investigating the Effects of the Loop Bandwidth Choice with PSR B1821-24

The affect of the choice of B_L on the DPLL and MLE performance is illustrated by comparing the sequence of simulations demonstrated in Figure 5.1, Figure 5.2 and Figure 5.3. These figures all contain results of simulations tracking the constant acceleration trajectory along the LOS to PSR B1821-24 with a block length of T = 200 seconds. Each figure contains three subplots consisting of the position, velocity, and acceleration errors versus time. The position error plot contains points corresponding to the DPLL position error in km, a dotted blue line corresponding to the 1σ error of the MLE, and a solid red line showing the 1σ error of the DPLL. The velocity error plot contains points corresponding to the equivalent velocity error from the DPLL in km/s and a solid red line illustrating the 1σ error. The acceleration plot contains points corresponding to the equivalent acceleration error from the DPLL in km/s^2 and a solid red line showing the 1σ error. Each plot shows the average of 10 runs of the same simulation scenario. This sequence of figures illustrates the effects of reducing the loop noise bandwidth from $B_L = 0.01$ Hz in Figure 5.1 to $B_L = 0.001$ Hz in Figure 5.2 to $B_L = 0.0005$ Hz in Figure 5.3 . There is a change between whether the MLE errors produce better position estimates or the DPLL errors when the loop noise bandwidth changes from 0.01 Hz in Figure 5.1 and 0.001 Hz in Figure 5.2. This demonstrates that if B_L is too large, the DPLL estimates for position might not be improvements on the individual MLE outputs.

Between each of these figures there is a change in the axes scaling for the

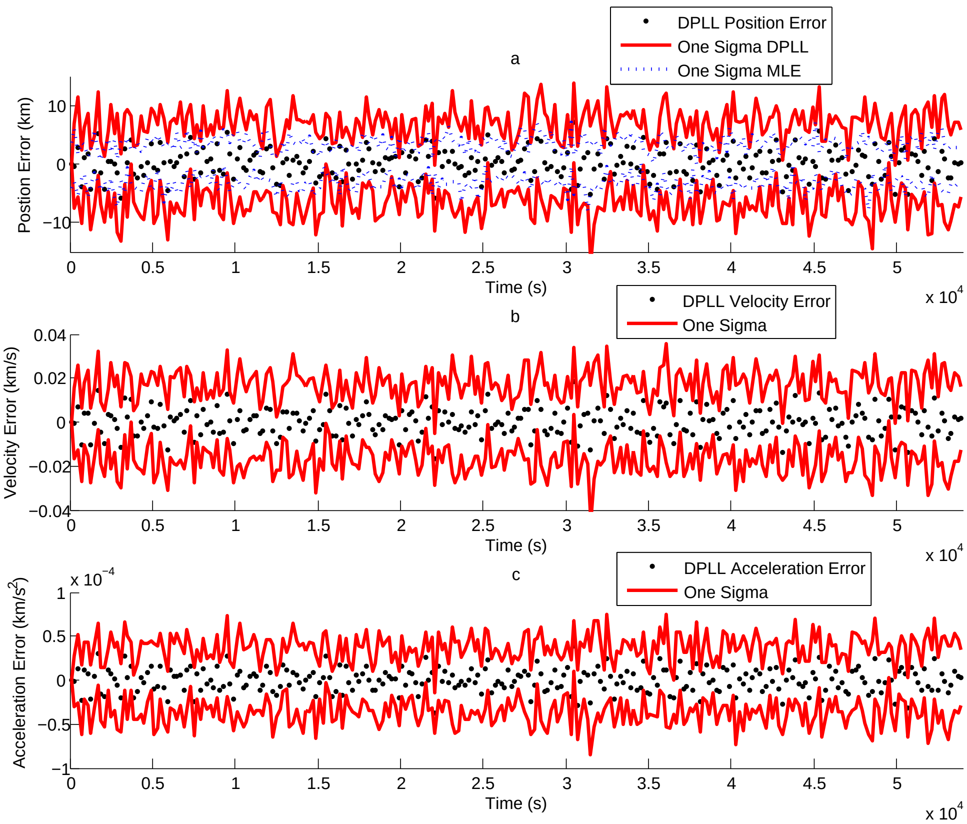

Figure 5.1: Constant acceleration trajectory phase tracking simulation results with true initial state using B1821-24 with T = 200 seconds and B_L = 0.01 Hz. One dimensional tracking results along LOS to pulsar.

velocity and acceleration plots. The results are presented this way in order to distinguish the 1σ error bars from the average error points, but without taking into account the zoom in between each figure, the decrease in velocity and acceleration error as B_L decreases is difficult to observe.

In order to compare the performance of the phase tracking algorithm across various loop noise bandwidth choices, metrics to capture the tracking error over the entire observation and at the end point of the simulation are compiled in Table 5.5.

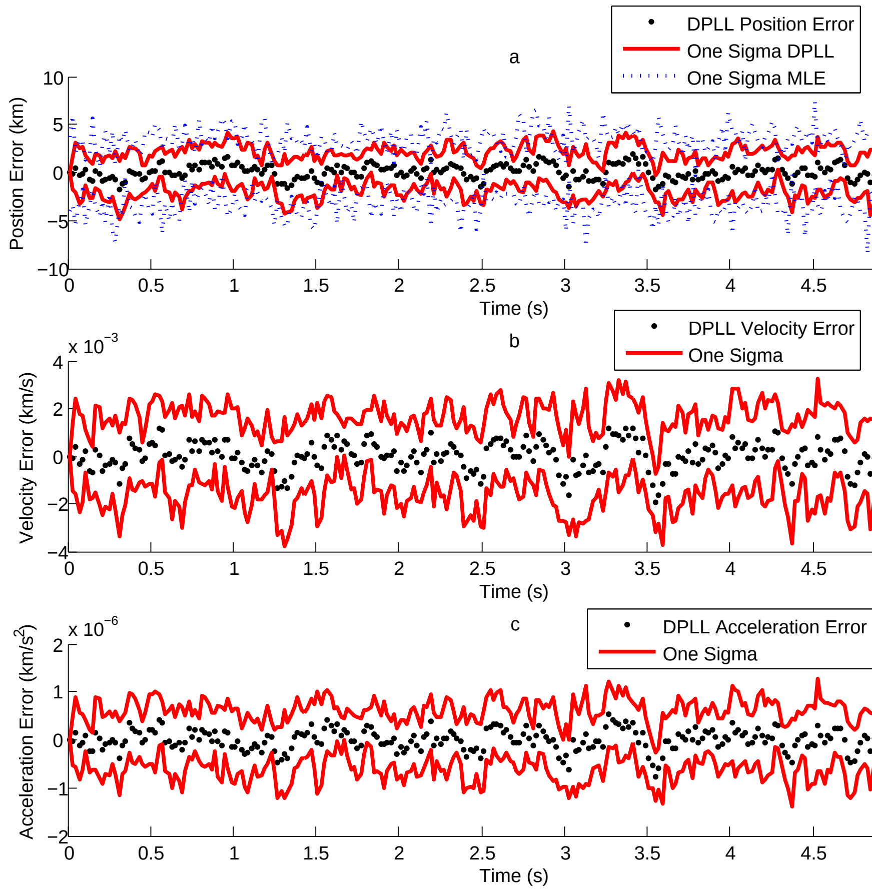

Figure 5.2: Constant acceleration trajectory phase tracking simulation results with true initial state using B1821-24 with T = 200 seconds and $B_L = 0.001$ Hz. One dimensional tracking results along LOS to pulsar.

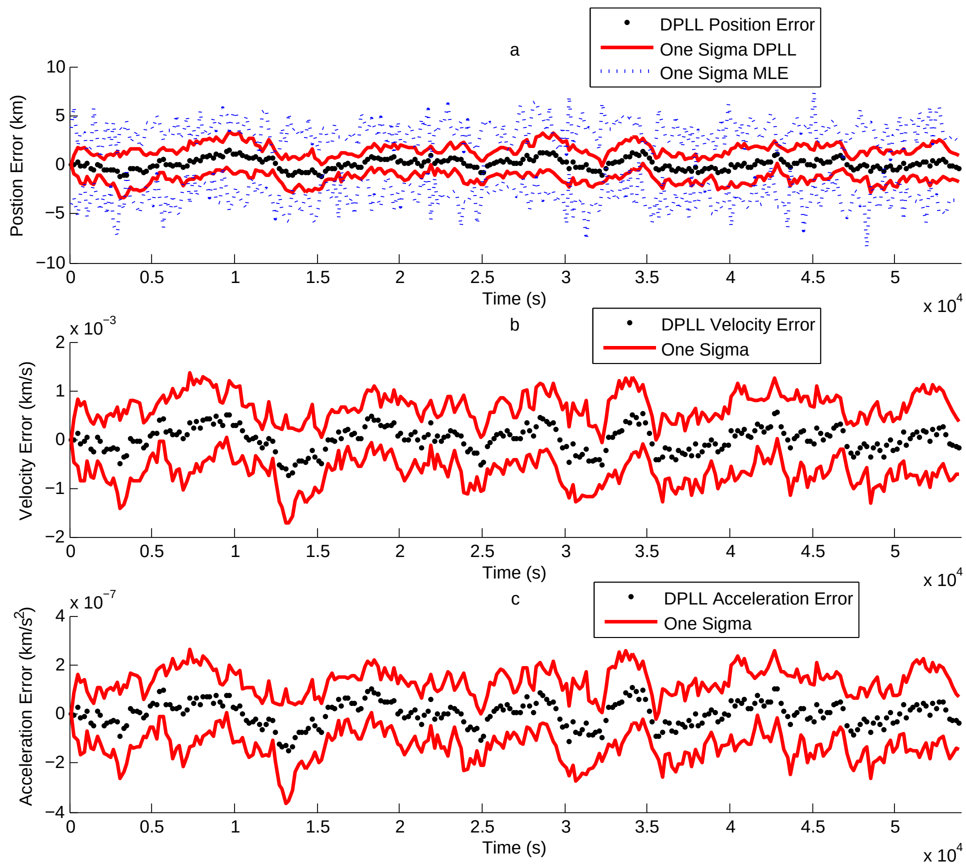

Figure 5.3: Constant acceleration trajectory phase tracking simulation results with true initial state using B1821-24 with T = 200 seconds and $B_L = 0.0005$ Hz. One dimensional tracking results along LOS to pulsar.

These metrics include the average position error of the MLE outputs over the length of each simulation in km, the end point RMS position error in km, which is the DPLL position error at the end of the observation time averaged over the 10 runs of the simulation, the averaged position error in km, which is the DPLL position error averaged over the length of each simulation and over the 10 runs, the end point RMS velocity error in m/s, which is the DPLL velocity error at the end of the observation time averaged over the 10 runs of the simulation, and the averaged velocity error in m/s, which is the DPLL velocity error averaged over the length of each simulation and over the 10 runs. The various loop bandwidths considered above are included in Table 5.5 as well as $B_L = 0.0001$, which will be used to match with simulations using other pulsars later in the section. The results corresponding to $B_L = 0.0001$ are included in Figure 5.4.

Table 5.5: PSR B1821-24 phase tracking performance for various loop noise bandwidths with T = 200 s using the constant acceleration trajectory with true initial state. One dimensional tracking results along LOS to pulsar.

B_L, Hz	0.01	0.001	0.0005	0.0001
Averaged MLE Position Error (km)	3.4564	3.4182	3.4187	3.4183
End Point RMS Position Error (km)	5.49	1.94	1.32	0.54
Averaged Position Error (km)	6.91	2.13	1.53	0.68
End Point RMS Velocity Error (m/s)	13.73	1.59	0.55	0.055
Averaged Velocity Error (m/s)	17.70	1.70	0.70	0.066

The MLE error level stays relatively constant since the block length T is unchanged. When the error from the dynamic stress is low and the block length is chosen large enough to be above the lower threshold of convergence to the CRLB, the MLE error level achieves the CRLB and is only dependent on the block length and detector area. The average and end point DPLL rms position error decreases with each decrease in B_L, as expected, with the end point values decreasing from 5.49 km with $B_L = 0.01$ Hz to 0.54 km with $B_L = 0.0001$ Hz. The velocity errors improve with each decrease in B_L as well, with the velocity end point error decreasing from 13.73 m/s with $B_L = 0.01$ Hz to 5.48 cm/s with $B_L = 0.0001$ Hz. In all cases the end point values for position and velocity DPLL errors are improvements on the position and velocity DPLL errors averaged over the entire simulated observation. This demonstrates that there is some settling going on in the DPLL performance over the length of the simulation.

Generally it will be best to choose the loop noise bandwidth to be small enough to allow the DPLL estimates to be improvements on the MLE outputs, but sometimes this is not possible. There is generally a lower limit to the value of B_L that allows the DPLL to track a given trajectory due to the dynamic stress as discussed in Section 5.3.2. If B_L needs to be chosen to be a value that is too large for the DPLL position estimates to be improvements over the MLEs then this can be accounted for by setting up the navigation EKF, which combines the various phase tracking estimates together from different pulsars, to use the MLE values as inputs instead of the DPLL ones. This will be known prior to performing the phase tracking due to the choice of the DPLL parameters.

The DPLL is not useless in this case even though the MLE outputs are being fed to the EKF instead. This is because the MLE itself would be unable to function as designed without the feedback of frequency and frequency derivative outputs from the DPLL. If there is an outlier MLE value for a particular block this can be detected and the DPLL phase output can be used to replace the rejected value from the MLE to generate the position estimate. The way that the phase tracking algorithm is formulated for extension to orbits with changing observed frequency makes the third-order DPLL and the MLE with a second-order Taylor series internal phase model inseparable. One can not perform without the other. For the constant acceleration trajectory the dynamic stress is negligible. Thus, for each pulsar simulation the value of B_L can be set small enough for the DPLL estimates to be improvements on the individual MLE outputs.

5.4.1.2 Comparing Phase Tracking Results with Various Pulsars

The phase tracking performance with a constant acceleration trajectory with true initial state was further investigated using the other three MSPs previously considered: B1937+21, J0218+4232, and J0437-4715. For pulsars B1937+21 and J0218+4232 a detector area of 1 m^2 was studied to compare directly to the results with PSR B1821-24. For pulsar J0437-4715 the results were poor when considering a detector area of 1 m^2. None of the combinations of T and B_L allowed the DPLL to track over ten runs per simulation due to J0437-4715 having significantly the lowest SNR of the pulsars considered. With T = 4000 seconds and B_L = 0.0001

Hz lock was maintained in seven out of ten simulations, but the average position error was nearly 50 km. In order to still demonstrate the phase tracking potential for J0437-4715, a larger detector area of 5 m^2 was considered.

The results of the phase tracking simulations for the constant acceleration trajectories with knowledge of the initial state, converted to phase, frequency, and frequency derivative to initialize the DPLL, are displayed in Figures 5.4 – 5.8. These figures all display the phase tracking results formatted in the same way as was discussed for Figures 5.1 – 5.3, above. Two different values for loop update time T were considered for B1821-24 with the same loop noise bandwidth of 0.0001 Hz. Figure 5.4 contains the results for T = 200 seconds, which corresponds to using a block time that is a minimum value with a safety margin over the lower bound for convergence to the CRLB. This corresponds to the smallest block times usable for B1821-24. Figure 5.5 contains the results for T = 4000 seconds, which corresponds to the loop update time used for the other MSPs considered. This allows for a more direct comparison of the achievable position errors and general performance between B1821-24 and the other three MSPs. Figure 5.6, Figure 5.7, and Figure 5.8 contain the results for pulsars B1937+21, J0218+4232, and J0437-4715, respectively. The axes for Figure 5.8 are zoomed in compared to those used in Figure 5.6 and Figure 5.7. This zoom was necessary in order to display the results for J0437-4715 due to the significantly worse tracking errors. The similarities in shape at first glance between the J0437-4715 results in Figure 5.8 and the B1937+21 and J0218+4232 results in Figure 5.6 and Figure 5.7, respectively, should not be misread as indicating a similarity in performance.

When comparing the results in Figure 5.4 and Figure 5.5 it can be seen that the DPLL position, velocity, and acceleration results are generally similar between the two scenarios, but the MLE results are significantly more accurate in Figure 5.5 where T = 4000 seconds, as expected. Consequently, the accuracy of the MLE and DPLL results are similar in the position plot of Figure 5.5 since the MLE accuracy increases with the increase in T, but the DPLL accuracy stays roughly the same. The position accuracy results show similar trends in Figure 5.6, Figure 5.7, and Figure 5.8 where T = 4000 seconds in all of these scenarios, and the MLE and DPLL position accuracy levels appear to be similar for pulsars B1937+21, J0218+4232, and J0437-4715. The phase tracking algorithm is able to track each of the pulsars considered and stay in-lock throughout the observation window.

In order to compare the performance of the phase tracking algorithms across the various pulsars, the same metrics used for Table 5.5 above are compiled in Table 5.6. The outliers are removed from the MLE position error average. Table 5.6 also includes the CRLB computed for each pulsar and the corresponding loop update time T. The MLE averages for each pulsar compare well with the CRLB, which is a good check to see that things are performing as expected. The biggest difference is with B1937+21, which was shown to have a bias offset of the CRLB in the empirical performance tests of the MLE in Chapter 4. When looking at the DPLL results in Table 5.6 there are three clear tiers in the performance. PSR B1821-24 is the best with end point position error of 0.54 km and end point velocity error of 5.48 cm/s. PSR B1937+21 and PSR J0218+4232 are in the next tier with end point position errors of 1.72 km and 2.44 km and end point velocity errors of 8.66 cm/s and 21.01

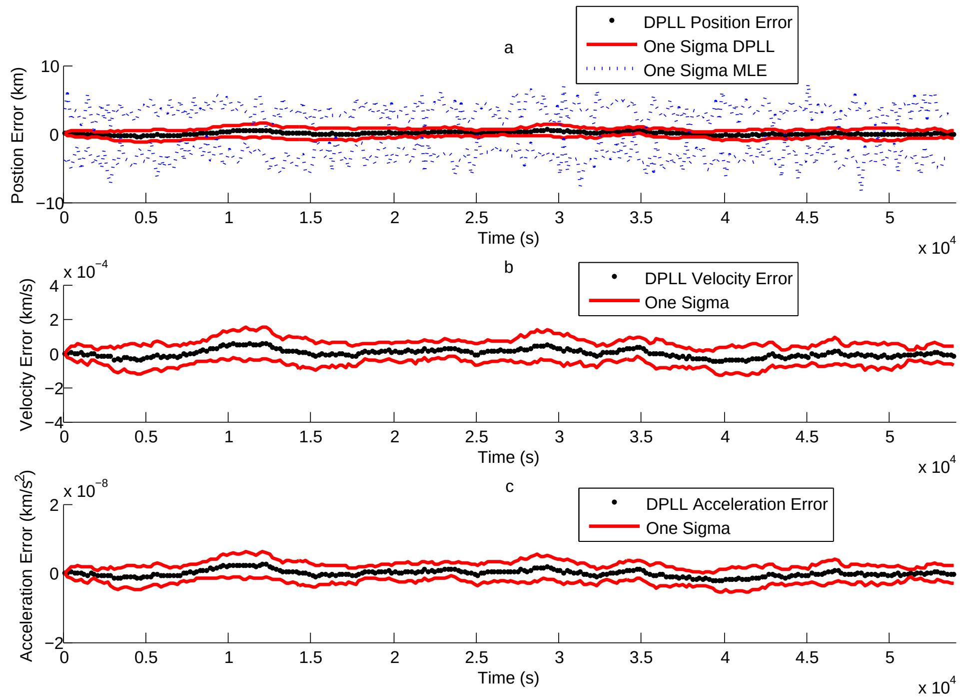

Figure 5.4: Constant acceleration trajectory phase tracking simulation results with true initial state using B1821-24 with T = 200 seconds and $B_L = 0.0001$ Hz. One dimensional tracking results along LOS to pulsar.

cm/s, respectively. PSR J0437-4715 is in a clear worst tier, even with the larger 5 m^2 detector, with a end point position error of 31.9 km and end point velocity error of 179.19 cm/s. The end point and average position and velocity results are roughly similar for each pulsar, which corresponds to not much settling time in the errors. The first three MSPs demonstrated clearly usable and promising phase tracking results and PSR J0437-4715 had poor results that might only be usable under certain circumstances, but the tracking was still able to stay in-lock.

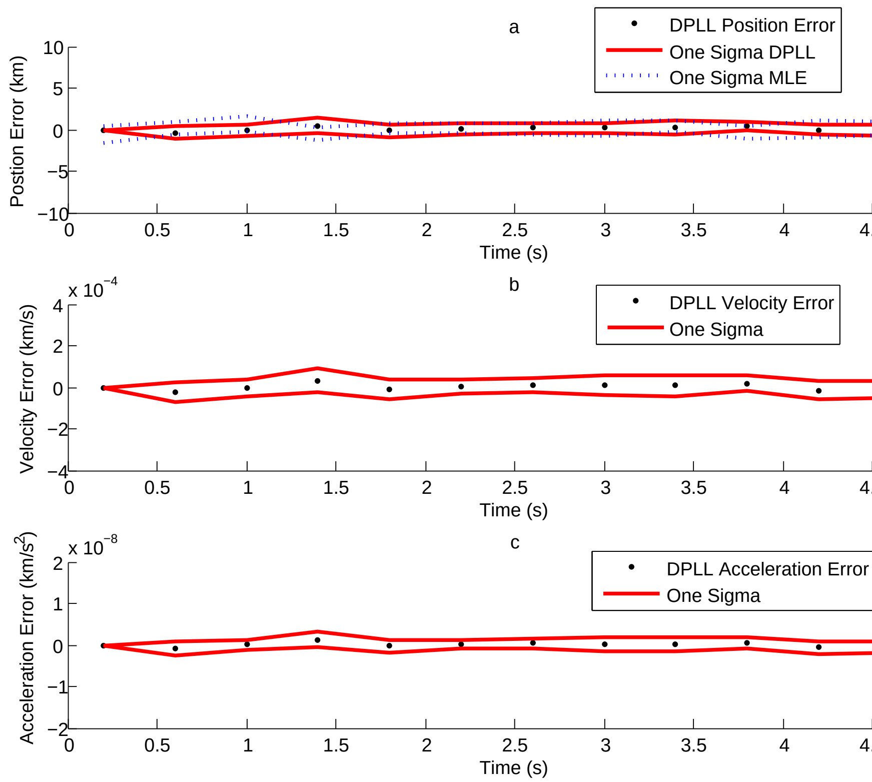

Figure 5.5: Constant acceleration trajectory phase tracking simulation results with true initial state using B1821-24 with T = 4000 seconds and $B_L = 0.0001$ Hz. One dimensional tracking results along LOS to pulsar.

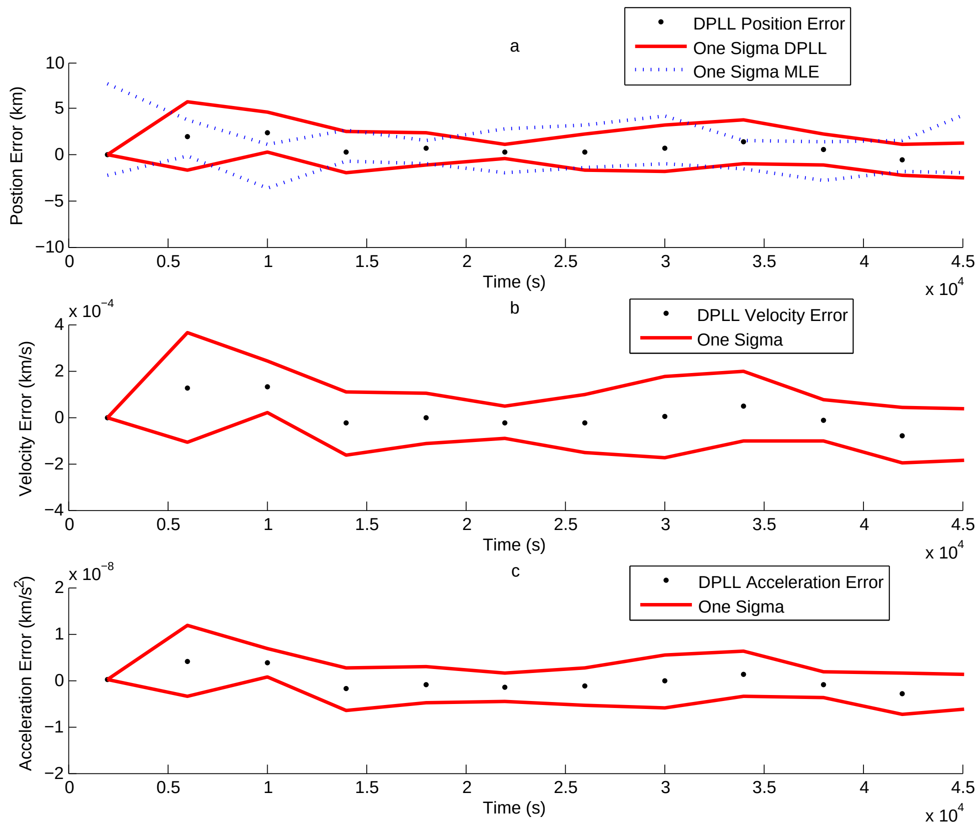

Figure 5.6: Constant acceleration trajectory phase tracking simulation results with true initial state using B1937+21 with T = 4000 seconds and B_L = 0.0001 Hz. One dimensional tracking results along LOS to pulsar.

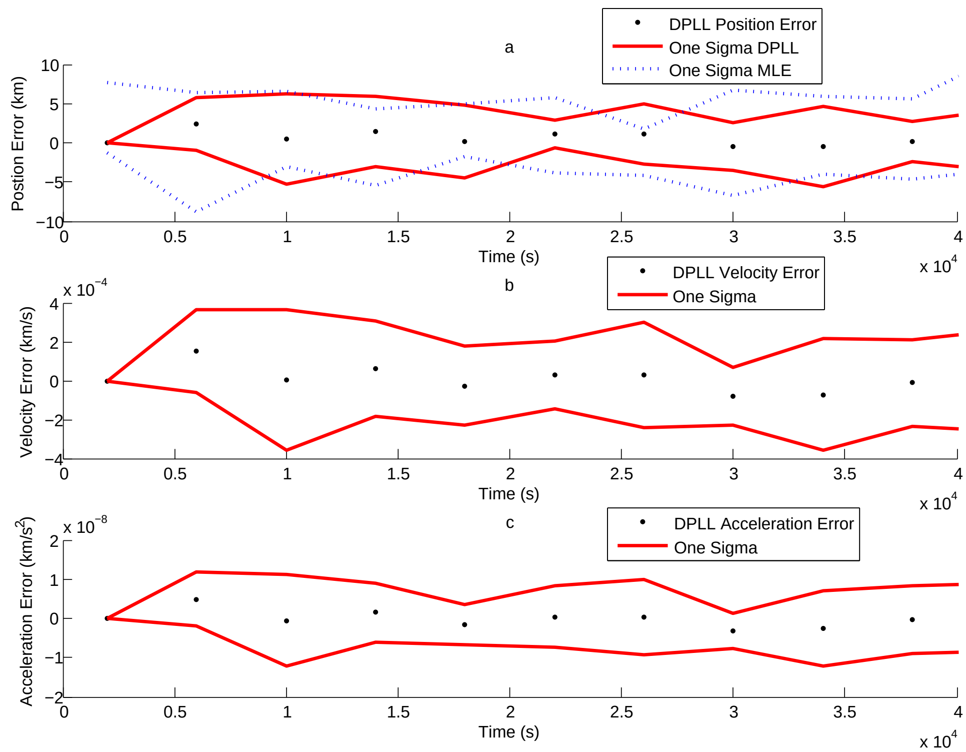

Figure 5.7: Constant acceleration trajectory phase tracking simulation results with true initial state using J0218+4232 with T = 4000 seconds and B_L = 0.0001 Hz. One dimensional tracking results along LOS to pulsar.

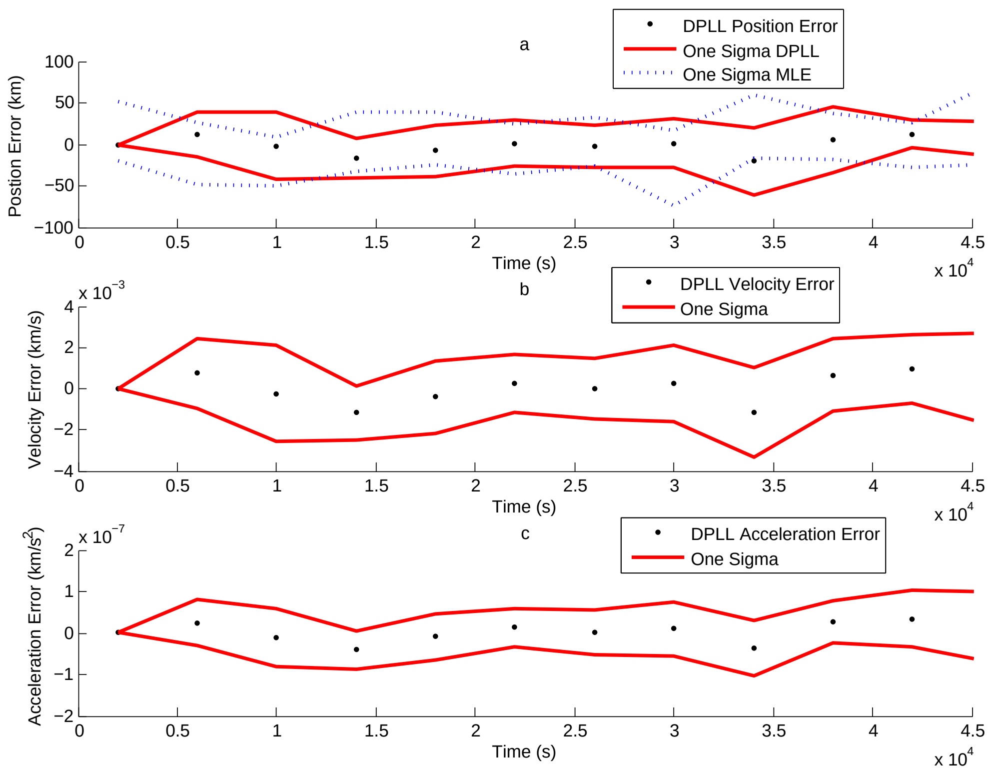

Figure 5.8: Constant acceleration trajectory phase tracking simulation results with true initial state using $5m^2$ detector and J0437-4715 with T = 4000 seconds and $B_L = 0.0001$ Hz. One dimensional tracking results along LOS to pulsar. The scaling of the axes is zoomed in compared to Figures 5.4 – 5.7.

Table 5.6: Results of the constant acceleration trajectory simulations with true initial state. Detector area of 1 m^2 besides 5 m^2 for J0437-4715. One dimensional tracking results along LOS to pulsar.

	B1821-24	B1821-24	B1937+21	J0218+4232	J0437-4715
B_L, Hz	0.0001	0.0001	0.0001	0.0001	0.0001
T, s	200	4000	4000	4000	4000
CRLB, km	3.0707	0.6866	1.0159	4.189	29.2364
Averaged MLE Position Error (km)	3.42	0.82	2.42	5.23	34.42
End Point RMS Position Error (km)	0.54	0.67	1.72	2.44	38.64
Averaged Position Error (km)	0.68	0.70	2.30	3.82	31.90
End Point RMS Velocity Error (cm/s)	5.48	3.89	8.66	21.01	179.19
Averaged Velocity Error (cm/s)	6.60	4.34	13.92	23.44	178.87

5.4.1.3 Comparison to Previous Phase Tracking Methods

The constant acceleration tracking results can be compared back to the results from the last section of Chapter 3 to demonstrate the major improvements the new phase tracking algorithm model has over the previous efforts at phase tracking pulsar signals. In Chapter 3 the drawbacks of the previous phase tracking algorithm were demonstrated with the PSR B1821-24 signal as a representative MSP. In order to track this signal the detector area needed to be 25 to 100 m^2 and the position errors were still on the order of 100 km. The block size for the phase tracking algorithm was not able to be increased over 6 seconds due to the dynamic stress of the constant velocity assumption versus the constant acceleration trajectory. As seen in this chapter, the new phase tracking algorithm that relaxes the assumption to constant acceleration over each block of the MLE and DPLL, is able to track the constant acceleration trajectory with a range of pulsar signals, a 1 m^2 detector area, and position accuracies between 1 – 10 km.

5.4.2 Initial Condition Error Matching DSN Handoff

In order to test the phase tracking algorithm under more realistic start-up conditions, initial error in the values of phase, frequency, and frequency derivative used in the transient-free acquisition process were considered. The initial error was simulated to correspond to a navigation system hand-off from the Deep Space Network (DSN). The achievable position and velocity accuracy from a DSN update will be used to set the initial phase and frequency errors. A position accuracy of 1 km and a velocity error of 1 m/s is used corresponding to the achievable range and range rate measurements from the DSN [10]. The accuracy may be better or worse for specific orbit conditions or with various improvements to the DSN processing, but these values will be used to have a simulation baseline. The acceleration estimate will be considered to be generated from an accelerometer onboard the spacecraft. The acceleration error from the simulated accelerometer is 1 cm/s^2, which is within the range of achievable performance for a spacecraft accelerometer as discussed in Appendix D. This provides a complimentary set of initial conditions that relate together over the estimation time blocks considered. The same constant acceleration trajectories and pulsars of the last section were considered.

The values for phase, frequency, and frequency derivative used to initialize the DPLL in the phase tracking algorithm corresponded to the one-sigma errors from the DSN hand-off and the onboard accelerometer. The initial conditions for each simulation run were chosen using normal random variables with their averages set to the true initial position, velocity, and acceleration values and variances corresponding to 1 km, 1 m/s, and 1 cm/s^2 error in range, range-rate, and range-rate-rate error, respectively. For each pulsar, ten runs of the simulation were performed with different seeds for the random number generator. Each simulation was of a 15 hour observation of the corresponding pulsar. The same methods for parameter selection for the third-order DPLL were used as in the last section with the perfect initial condition case as contained in Table 5.4.

5.4.2.1 Constant Acceleration Phase Tracking Results with Initial Condition Error and a 1 m^2 Detector

First, the pulsars were tested with the same 1 m^2 detector area as in the previous section. The results for pulsars B1821-24, B1937+21, and J0218+4232 are contained in Figures 5.9 - 5.11, respectively. As with the last section, J0437-4715 doesn't track with a 1 m^2 detector. To get tracking to acquire and stay in-lock a detector area of 5 m^2 is needed and these results will be discussed later in the section. Also, the Crab pulsar, which has a much higher flux, will be considered later in the section with a smaller detector area of 1000 cm^2 to demonstrate feasibility. The standard loop noise bandwidth that was used to compare across the pulsars was $B_L = 0.001$ Hz, which is larger than the value of the loop noise bandwidth used in the last section with perfect initial conditions, $B_L = 0.0001$. This change was necessary in order to acquire tracking with the initial condition error, but will make direct comparison back to the results of the last section more difficult since loop noise bandwidth is directly relating to tracking error. The DPLL parameters used for the simulations with pulsars B1821-24, B1937+21, and J0218+4232 are included in Table 5.7.

Metrics comparing the tracking error over the entire observation and at the end point of the simulation are collected in Table 5.8 to compare the performance of the phase tracking algorithms across the various pulsars. Comparing these results with those from the last section in Table 5.6 demonstrates the effects of modeling the initial condition errors representative of a DSN handoff. Again, the MLE averages for each pulsar compare well with the CRLB with the biggest difference for B1937+21. The end-point position and velocity errors are all higher than the corresponding ones in the previous section, as expected due to the loop noise bandwidth being raised an order of magnitude to accommodate the initial condition errors. PSR B1821-24 still has the best tracking performance with end point position and velocity errors of 1.94 km and 1.59 m/s, respectively. The end point position errors are larger for B1937+21 and J0218+4232 with 6.22 km and 19.31 km error, respectively. For these two pulsars the MLE results are outperforming the DPLL position results and would be used in the navigation EKF. For all three pulsars the average position and velocity errors are similar to the end point errors signifying low settling time.

Table 5.7: Settings used for the parameters of the third-order DPLL for the constant acceleration trajectory phase tracking simulations with initial condition error on the order of a hand-off from the DSN.

DPLL Parameter	B1821-24	B1937+21	J0218+4232
T, s	200	4000	4000
B_L, Hz	0.001	0.001	0.001
ζ	0.707	0.707	0.707
K_1	0.360	0.968	0.968
K_2	0.0684	0.881	0.881
K_3	0.00527	0.574	0.574

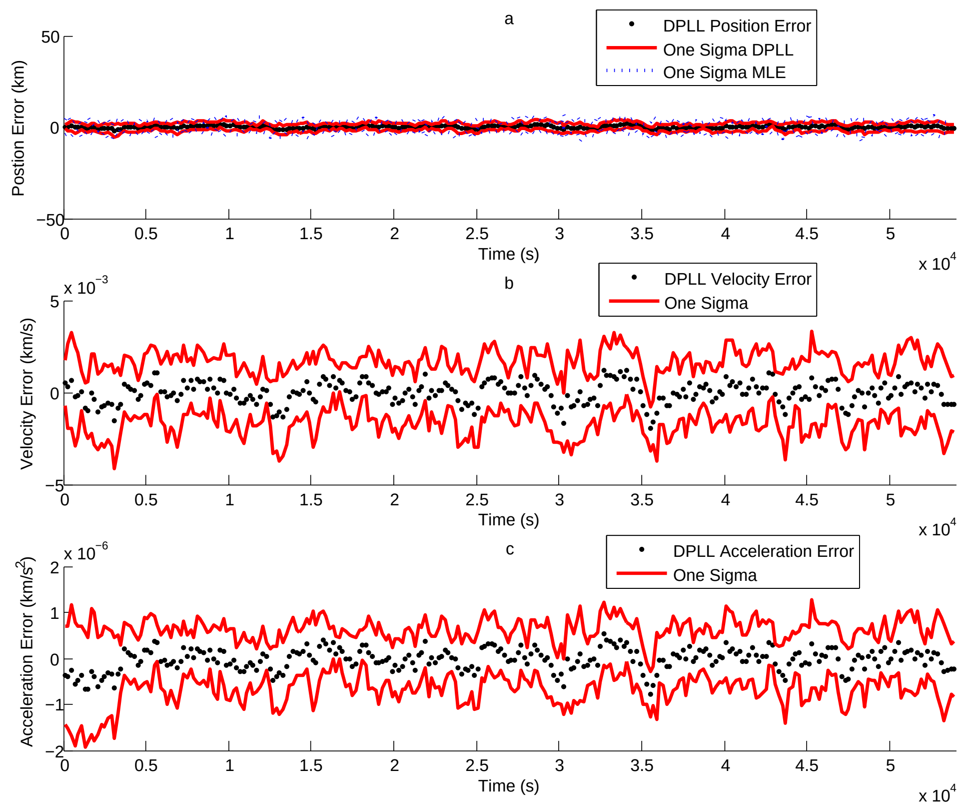

Figure 5.9: Constant acceleration trajectory phase tracking simulation results with DSN plus accelerometer level initial condition error using B1821-24 with T = 200 seconds and $B_L = 0.001$ Hz. Detector area of 1 m^2. One dimensional tracking results along LOS to pulsar.

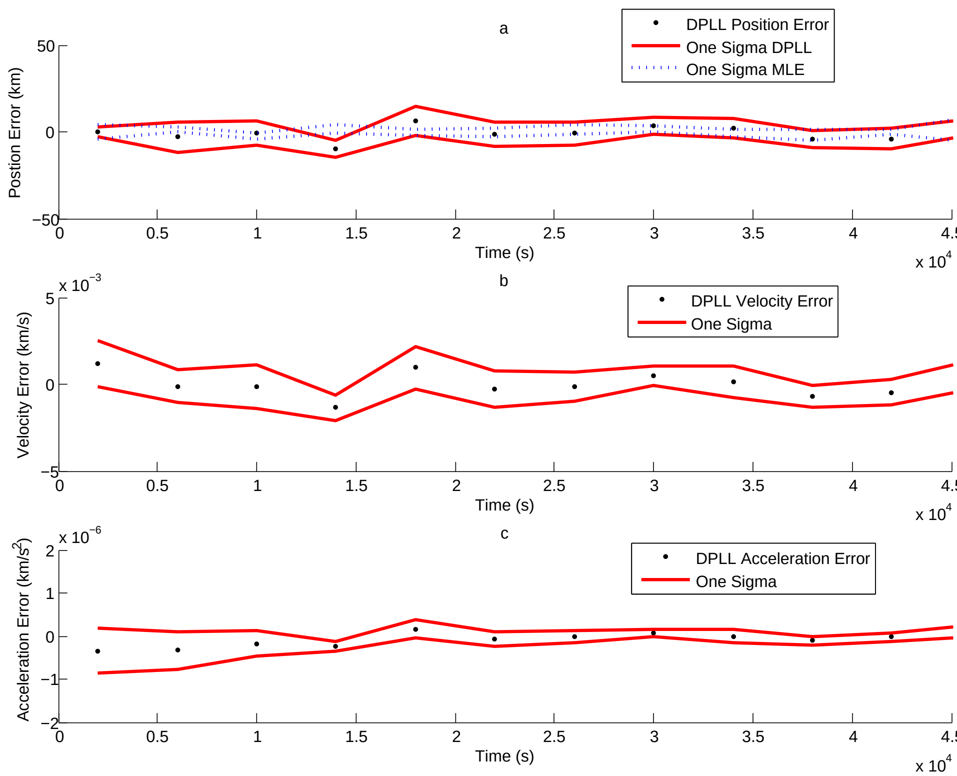

Figure 5.10: Constant acceleration trajectory phase tracking simulation results with DSN plus accelerometer level initial condition error using B1937+21 with T = 4000 seconds and $B_L = 0.001$ Hz. Detector area of 1 m^2. One dimensional tracking results along LOS to pulsar.

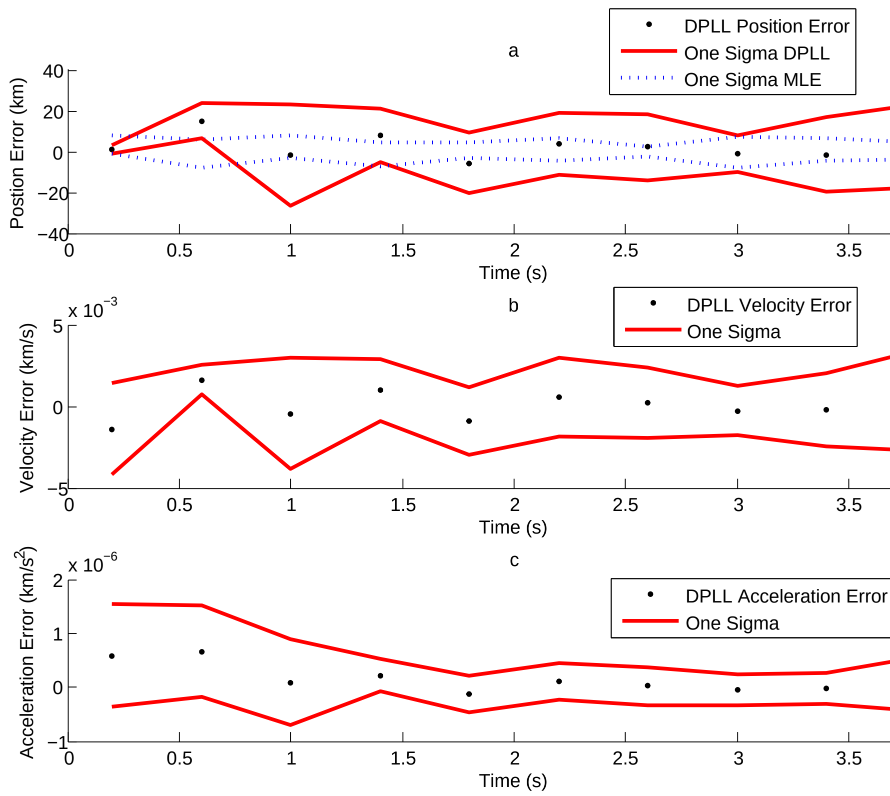

Figure 5.11: Constant acceleration trajectory phase tracking simulation results with DSN plus accelerometer level initial condition error using J0218+4232 with T = 4000 seconds and $B_L = 0.001$ Hz. Detector area of 1 m^2. One dimensional tracking results along LOS to pulsar.

Table 5.8: Results of the constant acceleration trajectory simulations with initialization from DSN and an accelerometer using a detector area of 1 m^2. One dimensional tracking results along LOS to pulsar.

	B1821-24	B1937+21	J0218+4232
B_L, Hz	0.001	0.001	0.001
T, s	200	4000	4000
CRLB, km	3.0707	1.0159	4.189
Averaged MLE Position Error (km)	3.42	2.87	5.29
End Point RMS Position Error (km)	1.94	6.22	19.31
Averaged Position Error (km)	2.14	9.59	16.22
End Point RMS Velocity Error (m/s)	1.59	0.99	2.95
Averaged Velocity Error (m/s)	1.73	1.34	2.25

5.4.2.2 Constant Acceleration Phase Tracking Results with Initial Condition Error and a 2 m^2 Detector

Due to the increase in position errors as compared to the simulations with perfect initial conditions, an increased detector area of 2 m^2 was considered for pulsars B1821-24, B1937+21, and J0218+4232. This was chosen as a size that is small enough to still be feasible for a potential spacecraft and also large enough to demonstrate a range of improved performance over 1 m^2. It will be used to demonstrate the potential value of phase tracking for these three pulsars. Doubling the detector area allows the block update time, T, to be cut in half for each pulsar. A range of different loop noise bandwidths were considered in order to provide a more general view of the feasibility and potential of the proposed phase tracking algorithm. For PSR B1821-24 a few different values of T were investigated as well.

First, the 2 m^2 detector results for PSR B1821-24 are considered. Three different choices for block size were investigated: 100, 500, and 2000 seconds. Figure 5.12, Figure 5.13, and Figure 5.14 contain the phase tracking simulation results for the scenario using PSR B1821-24 with T = 100 seconds and loop noise bandwidths of B_L = 0.001 Hz, B_L = 0.00025 Hz, and B_L = 0.0001 Hz, respectively. Each plot contains the position, velocity, and acceleration errors along with the 1σ DPLL and MLE errors. By comparing these three figures it can be seen that as the loop noise bandwidth is decreased, an initial overshoot is added to the DPLL results along with a progressively longer settling time. In Figure 5.13 it takes roughly 17500 seconds (4.9 hours) for the position, velocity, and acceleration errors to settle for the simulation with $B_L = 0.00025$ Hz. In Figure 5.14 it takes nearly the whole 12 hour simulation time for the DPLL errors to settle for the simulation with $B_L = 0.0001$ Hz.

The results for PSR B1821-24 with T = 500 seconds and loop noise bandwidths of $B_L = 0.00025$ Hz and $B_L = 0.0001$ Hz are included in Figure 5.15 and Figure 5.16, respectively. In this case it can be seen in Figure 5.15 that the settling time has increased to nearly 20000 seconds (5.6 hours) with the increase in block time T for the simulation with $B_L = 0.00025$ Hz. In Figure 5.16 the settling time is again roughly the full 12 hour simulation time for the scenario with $B_L = 0.0001$ Hz. The results for PSR B1821-24 with T = 2000 seconds and loop noise bandwidths of $B_L = 0.00025$ Hz and $B_L = 0.0001$ Hz are included in Figure 5.17 and Figure 5.18, respectively. For this scenario the settling time has increased to roughly 27500 seconds (7.6 hours) as seen in Figure 5.17 with $B_L = 0.00025$ Hz. In Figure 5.18 the settling time for position is taking longer than the 12 hour simulation duration and the velocity and acceleration settle in roughly the full 12 hours for the simulation with $B_L = 0.0001$ Hz. The increase in block time T also adds to the magnitude of the overshoots in position, velocity, and acceleration for the simulations with $B_L = 0.00025$ Hz and $B_L = 0.0001$ Hz. The results for PSR B1821-21 over the various choices of B_L and T are summarized in Table 5.9 including the average MLE error and the end point and average DPLL position, velocity, and acceleration errors.

Comparing the results as T is increased in Table 5.9 demonstrates that the averaged MLE position error improves and is unaffected by choice of B_L, assuming B_L is chosen to be inside the range that allows for tracking of the B1821-24 signal.

The averaged MLE position error decreases from 3.38 km with T = 100 seconds to 1.46 km with T = 500 seconds and to 0.70 km with T = 2000 seconds. The effect of the choice of loop noise bandwidth is apparent in the end point RMS position and velocity error results. These results also show an effect based on the choice of update time, T. For an update time of T = 100 seconds the end point RMS position error improves from 1.67 km with B_L = 0.001 Hz to 0.99 km with B_L = 0.00025 Hz but then worsens to 1.30 km with B_L = 0.0001. With update times of T = 500 seconds and T = 2000 seconds the end point RMS position error worsens from 0.98 km and 0.99 km, respectively with B_L = 0.00025 to 2.06 km and 4.37 km, respectively with B_L = 0.0001 Hz. These results demonstrate that there is a limit to the improvement in the position error due to decreasing the loop noise bandwidth.

The effect on end point RMS velocity error is similar, but depends more on the value of T chosen as well. For T = 100 seconds, the end point RMS velocity error decreases for all three of the decreasing B_L values tested, for T = 500 seconds it remains similar for the two B_L values tested, and for T = 2000 seconds it increases when the B_L level is decreased. Looking at a study of possible B_L and T choices will be needed on a case by case basis for future use of this phase tracking algorithm to determine the best values to use for the particular blend of orbit dynamics, detector model, and pulsar signal parameters. For PSR B1821-24 with the constant acceleration trajectory a loop noise bandwidth of B_L = 0.00025 Hz provides the best results as seen in Table 5.9. This value will be used to compare these results to other pulsars and other orbits in later sections.

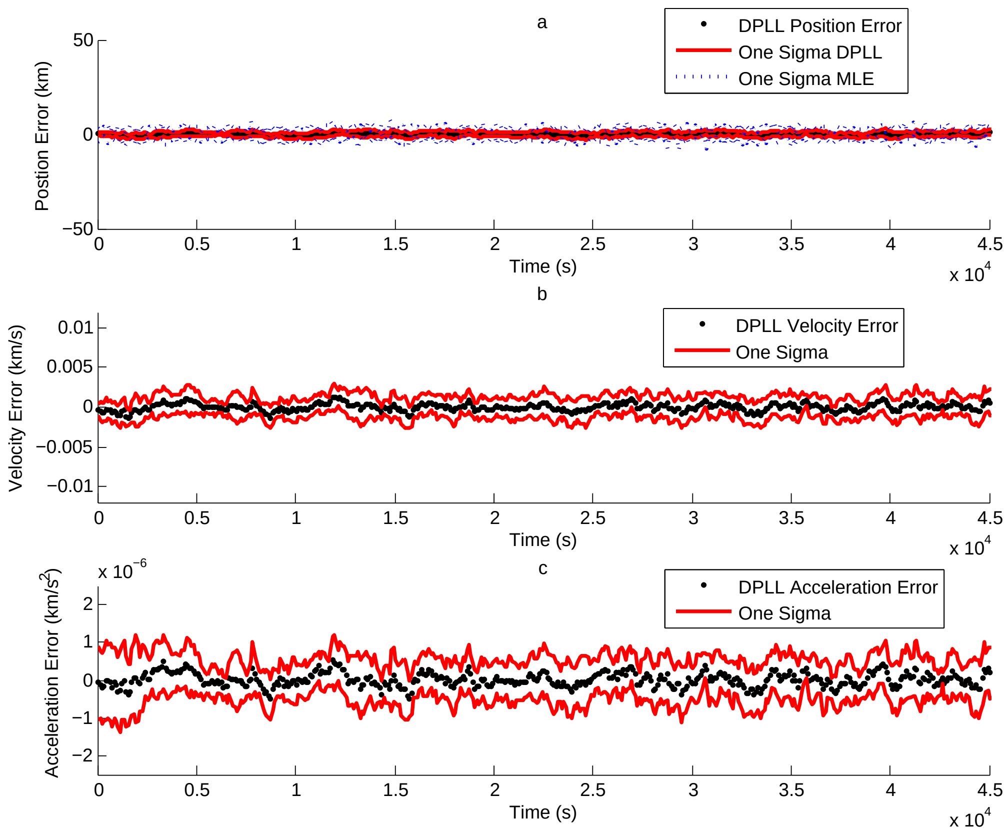

Figure 5.12: Constant acceleration trajectory phase tracking simulation results with DSN plus accelerometer level initial condition error using B1821-24 with T = 100 seconds and $B_L = 0.001$ Hz. Detector area of 2 m^2. One dimensional tracking results along LOS to pulsar.

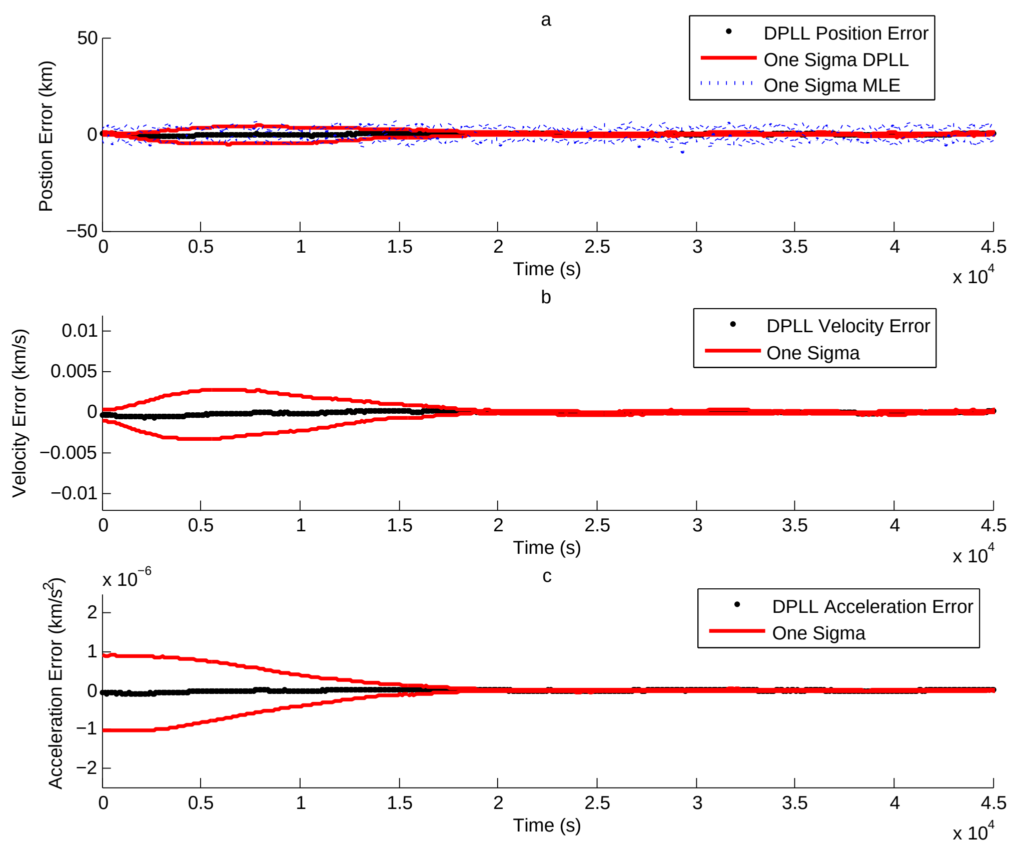

Figure 5.13: Constant acceleration trajectory phase tracking simulation results with DSN plus accelerometor level initial condition error using B1821-24 with T = 100 seconds and $B_L = 0.00025$ Hz. Detector area of 2 m^2. One dimensional tracking results along LOS to pulsar.

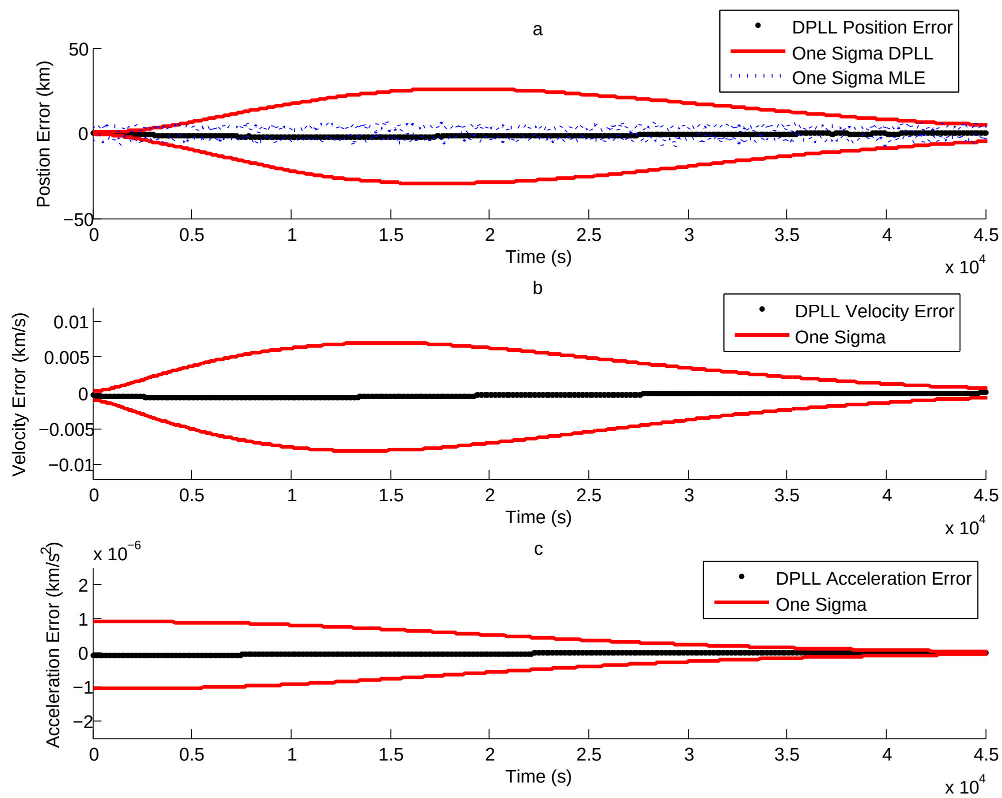

Figure 5.14: Constant acceleration trajectory phase tracking simulation results with DSN plus accelerometer level initial condition error using B1821-24 with T = 100 seconds and $B_L = 0.0001$ Hz. Detector area of 2 m^2. One dimensional tracking results along LOS to pulsar.

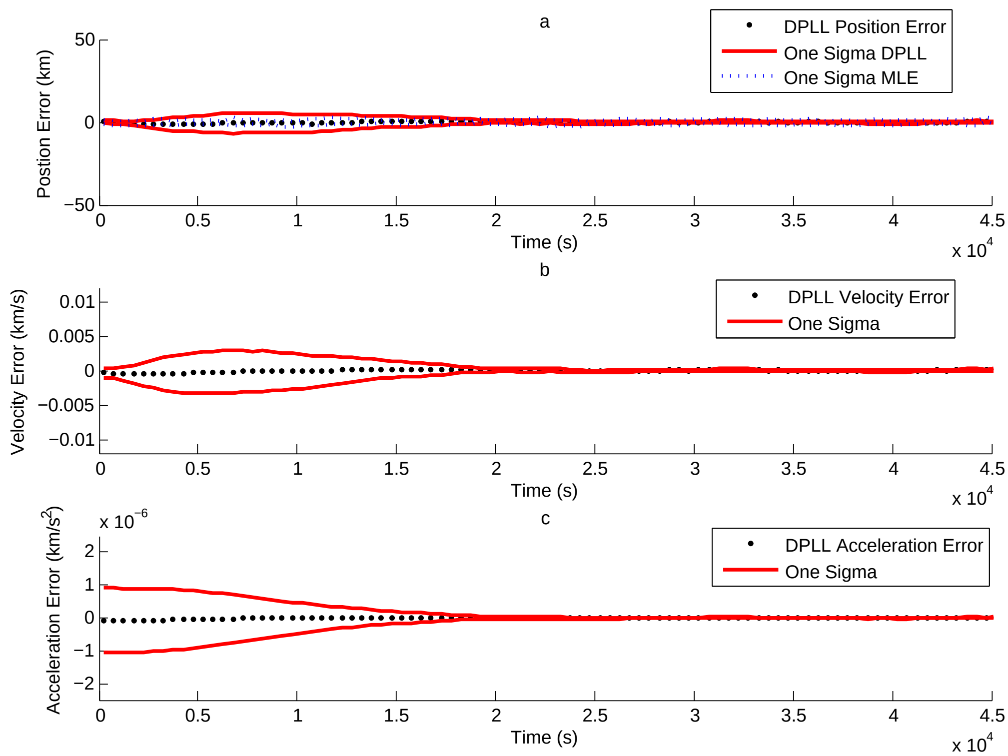

Figure 5.15: Constant acceleration trajectory phase tracking simulation results with DSN plus accelerometer level initial condition error using B1821-24 with T = 500 seconds and $B_L = 0.00025$ Hz. Detector area of 2 m^2. One dimensional tracking results along LOS to pulsar.

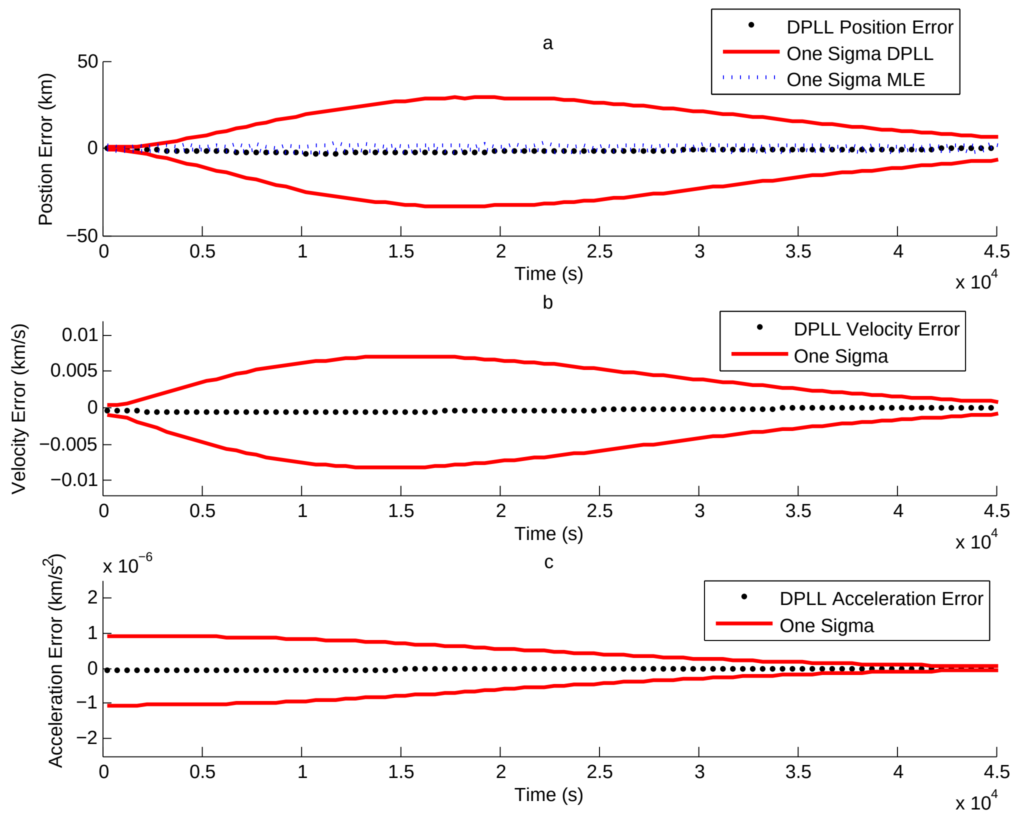

Figure 5.16: Constant acceleration trajectory phase tracking simulation results with DSN plus accelerometer level initial condition error using B1821-24 with T = 500 seconds and $B_L = 0.0001$ Hz. Detector area of 2 m^2. One dimensional tracking results along LOS to pulsar.

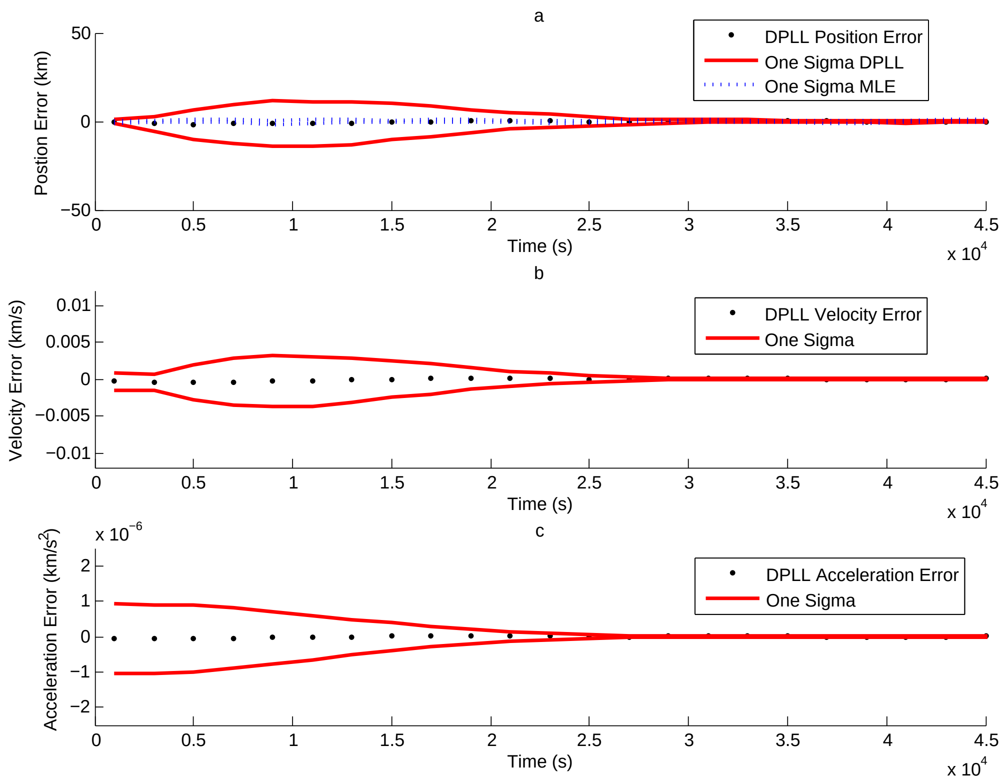

Figure 5.17: Constant acceleration trajectory phase tracking simulation results with DSN plus accelerometer level initial condition error using B1821-24 with T = 2000 seconds and B_L = 0.00025 Hz. Detector area of 2 m^2. One dimensional tracking results along LOS to pulsar.

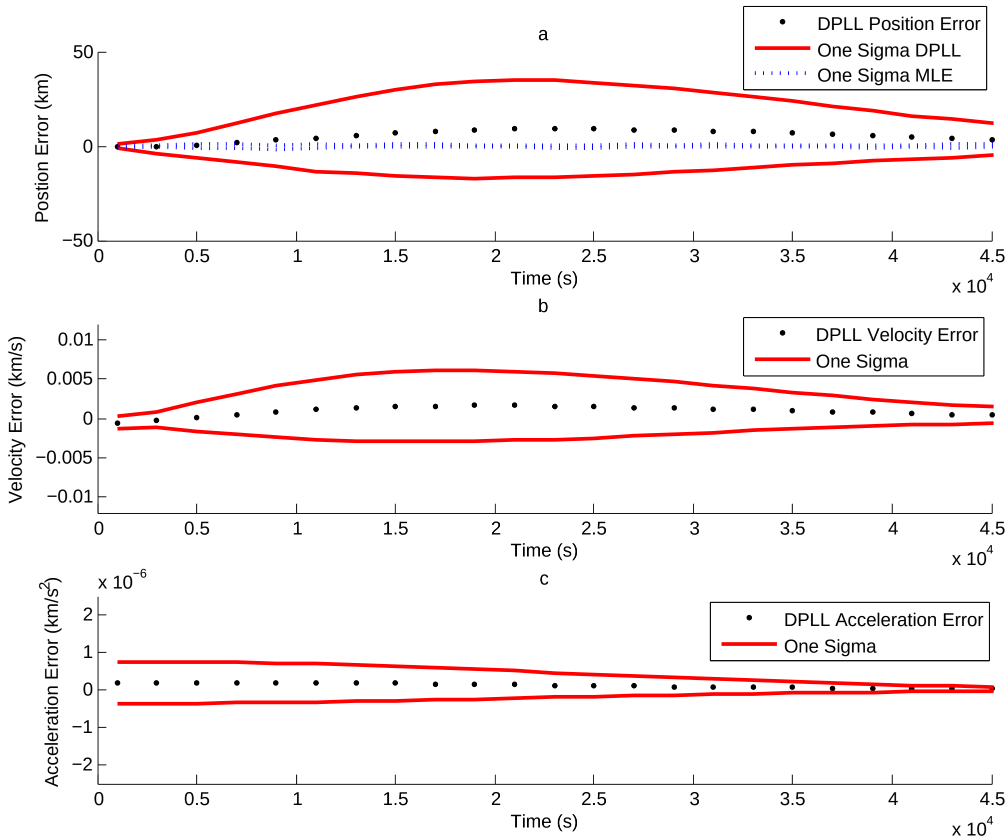

Figure 5.18: Constant acceleration trajectory phase tracking simulation results with DSN plus accelerometor level initial condition error using B1821-24 with T = 2000 seconds and $B_L = 0.0001$ Hz. Detector area of 2 m^2. One dimensional tracking results along LOS to pulsar.

Next, the 2 m^2 detector results for B1937+21 and J0218+4232 are considered. For these two pulsars only a block update time of T = 2000 seconds is investigated, which is half of the block time used for the simulations with a 1 m^2 detector. These two pulsars have similar phase tracking performance, so the results will be demonstrated in pairs of figures for various choices of loop noise bandwidth. Figure 5.19 and Figure 5.20 show the phase tracking results with $B_L = 0.002$ Hz for B1937+21 and J0218+4232, respectively. Figure 5.21 and Figure 5.22 show the phase tracking results with $B_L = 0.001$ Hz. Figure 5.23 and Figure 5.24 show the phase tracking results with $B_L = 0.0005$ Hz. Figure 5.25 and Figure 5.26 show the phase tracking results with $B_L = 0.00025$ Hz. Figure 5.27 and Figure 5.28 show the phase tracking results with $B_L = 0.00015$ Hz. By comparing each of these pairs of plots the general similarity between the tracking performance of B1937+21 and J0218+4232 is demonstrated.

Figures 5.19 – 5.28 demonstrate that the proposed algorithm is able to track both the B1937+21 and J0218+4232 signals in all scenarios of loop noise bandwidth considered. Over these figures, the tracking performance shows various different effects including a few instances of outlier rejection, some overshoot, and settling time changes. For the first plots with $B_L = 0.002$ Hz., in Figure 5.19 and Figure 5.20, the tracking performance is steady over the entire simulation with no overshoot or settling time. As B_L decreases, an overshoot and an increasing settling time starts to appear. First, slow settling appears in the acceleration error for B1937+21 in Figure 5.21 with $B_L = 0.001$ Hz. Overshoot and slow settling then appears somewhat in the position and velocity error as well for B1937+21 with $B_L = 0.0005$ Hz in

Figure 5.23 and in the acceleration error for J0218 with in Figure 5.24. The overshoot becomes much more pronounced and the settling time increases to roughly half of the total simulation time for both pulsars in position, velocity, and acceleration error with $B_L = 0.00025$ Hz. For $B_L = 0.00015$ Hz the settling time increases enough to last nearly the whole simulation time for B1937+21 and the position error never fully settles for J0218+4232. These are similar to the trends for decreasing loop noise bandwidth seen earlier with B1821-24.

The results for B1937+21 and J0218+4232 over the various choices of B_L and T are summarized in Table 5.10 and Table 5.11, respectively, including the average MLE error and the end point and average DPLL position and velocity errors. Comparing the averaged MLE position error to the Cramer-Rao lower bound it can be seen that there is close convergence for J0218+4232 and a bias offset for B1937+21 as expected from the previous results. The end point position and velocity errors decrease for each decrease in loop noise bandwidth for B1937+21 from 15.01 km and 3.77 m/s with $B_L = 0.002$ Hz. to 2.09 km and 0.24 m/s with $B_L = 0.00015$. For J0218+4232 the end point position and velocity errors improve with each decrease in B_L until increasing with the last change to $B_L = 0.00015$ Hz. The best end point performance for J0218+4232 was 5.16 km and 0.83 m/s for position and velocity error, respectively, with $B_L = 0.00025$ Hz. The drawbacks of overshoot and slow settling time show up in the average position and velocity errors.

The simulation performance with a loop noise bandwidth of $B_L = 0.00025$ Hz will be used to compare with the results for B1821-24 in Table 5.9. An update time of T = 100 seconds will be considered for B1821-24 and T = 2000 for B1937+21 and J0218+4232 for the comparison. These are both values of T that provide a little margin over the smallest block times that lead to convergence of the MLE results with the CRLB. PSR B1821-24 greatly outperforms both B1937+21 and J0218+4232 in tracking performance. The end point RMS position error is 0.99 km for B1821-24 compared to 2.55 km and 5.16 km for B1937+21 and J0218+4232, respectively. The end point RMS velocity error is 0.24 m/s for B1821-24 compared to 0.41 m/s and 0.83 m/s for B1937+21 and J0218+4232, respectively. For all three pulsars there is a slow settling time at the beginning of the simulation before these performance levels are achievable with $B_L = 0.00025$ Hz.

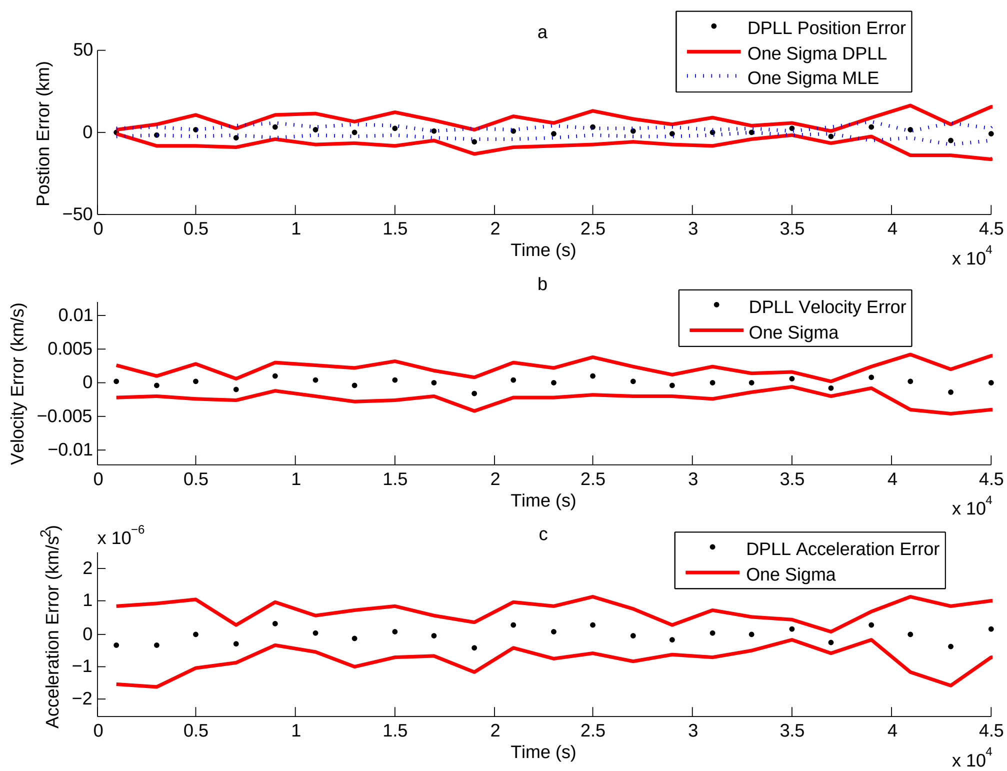

Figure 5.19: Constant acceleration trajectory phase tracking simulation results with DSN plus accelerometer level initial condition error using B1937+21 with T = 2000 seconds and $B_L = 0.002$ Hz. Detector area of 2 m^2. One dimensional tracking results along LOS to pulsar.

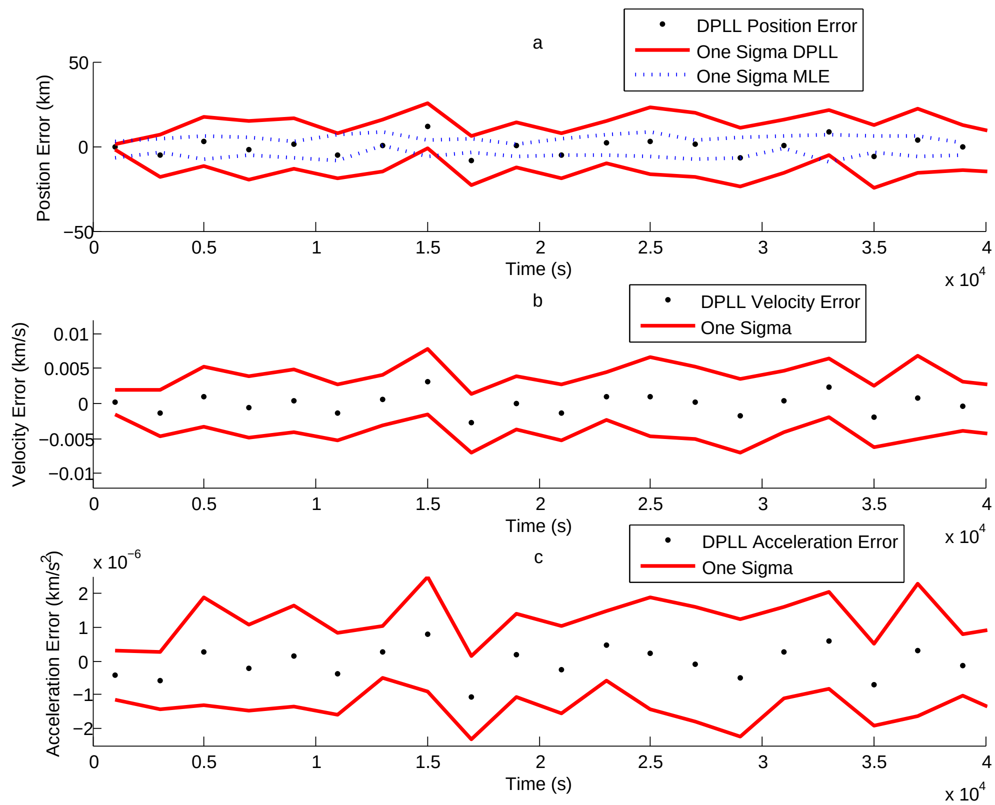

Figure 5.20: Constant acceleration trajectory phase tracking simulation results with DSN plus accelerometer level initial condition error using J0218+4232 with T = 2000 seconds and B_L = 0.002 Hz. Detector area of 2 m^2. One dimensional tracking results along LOS to pulsar.

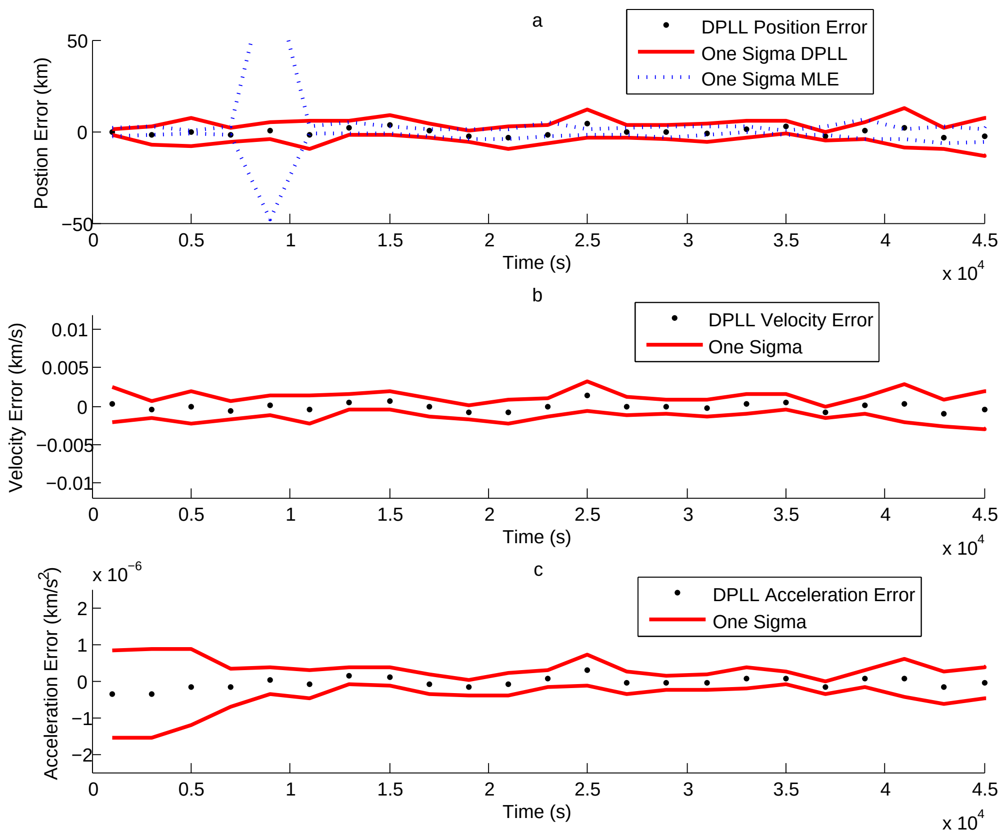

Figure 5.21: Constant acceleration trajectory phase tracking simulation results with DSN plus accelerometer level initial condition error using B1937+21 with T = 2000 seconds and $B_L = 0.001$ Hz. Detector area of 2 m^2. One dimensional tracking results along LOS to pulsar.

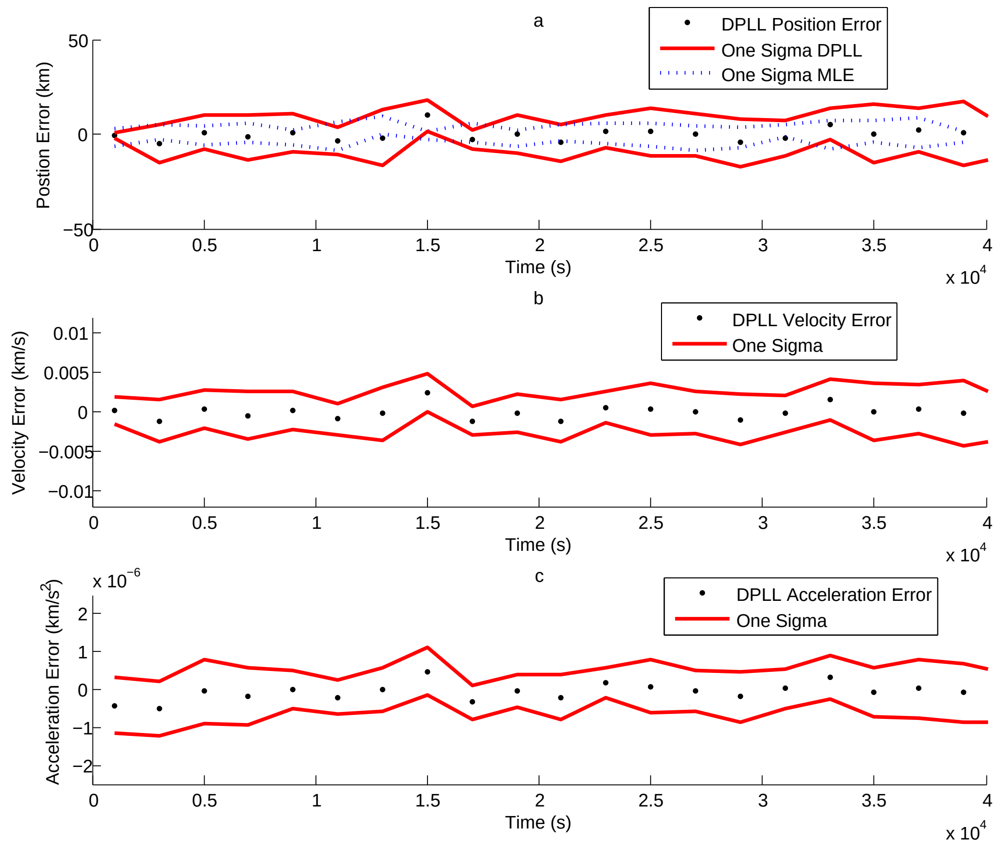

Figure 5.22: Constant acceleration trajectory phase tracking simulation results with DSN plus accelerometer level initial condition error using J0218+4232 with T = 2000 seconds and B_L = 0.001 Hz. Detector area of 2 m^2. One dimensional tracking results along LOS to pulsar.

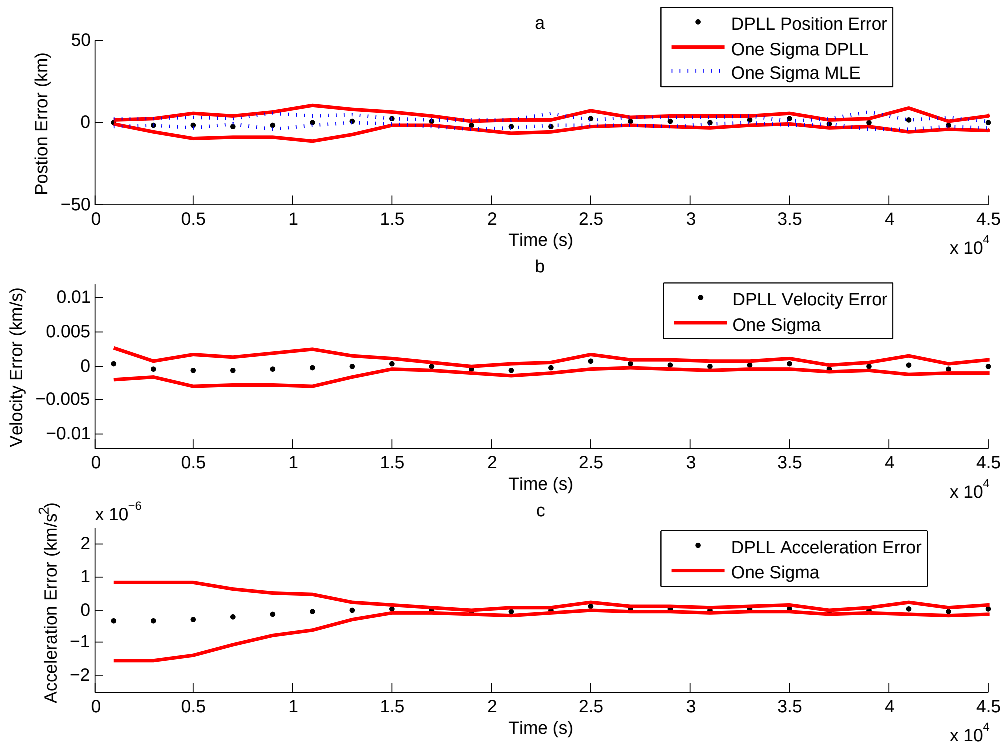

Figure 5.23: Constant acceleration trajectory phase tracking simulation results with DSN plus accelerometor level initial condition error using B1937+21 with T = 2000 seconds and B_L = 0.0005 Hz. Detector area of 2 m^2. One dimensional tracking results along LOS to pulsar.

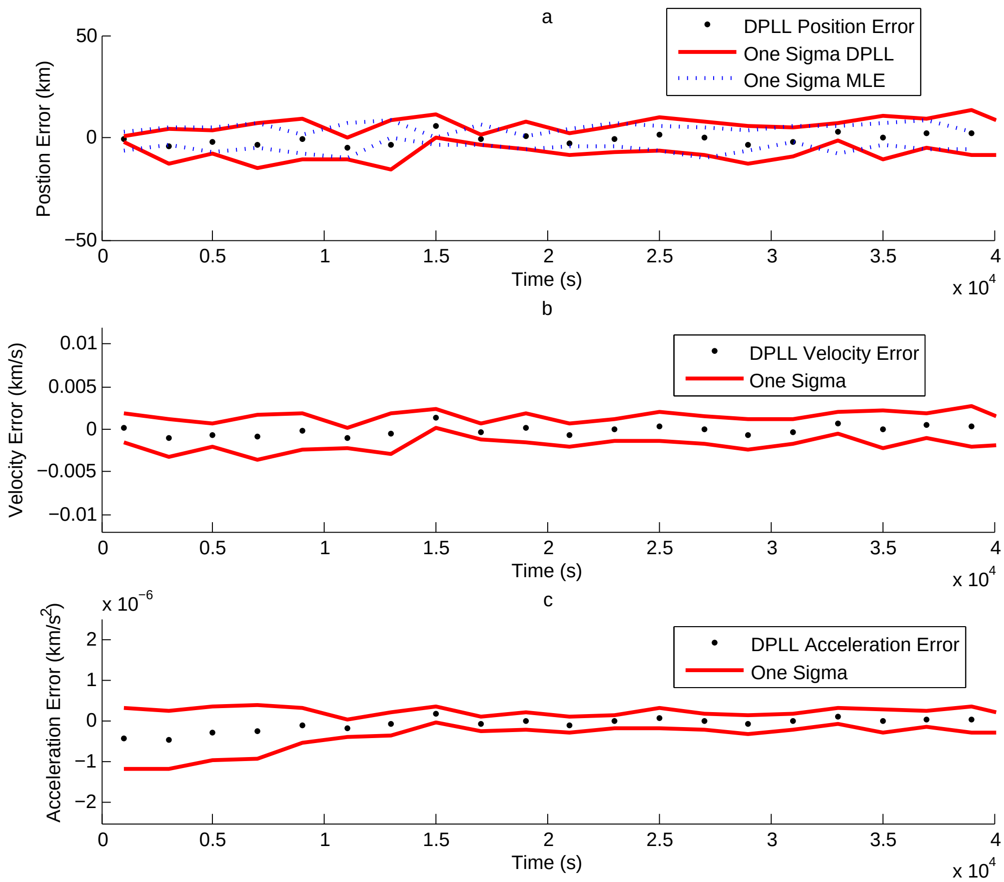

Figure 5.24: Constant acceleration trajectory phase tracking simulation results with DSN plus accelerometor level initial condition error using J0218+4232 with T = 2000 seconds and $B_L = 0.0005$ Hz. Detector area of 2 m^2. One dimensional tracking results along LOS to pulsar.

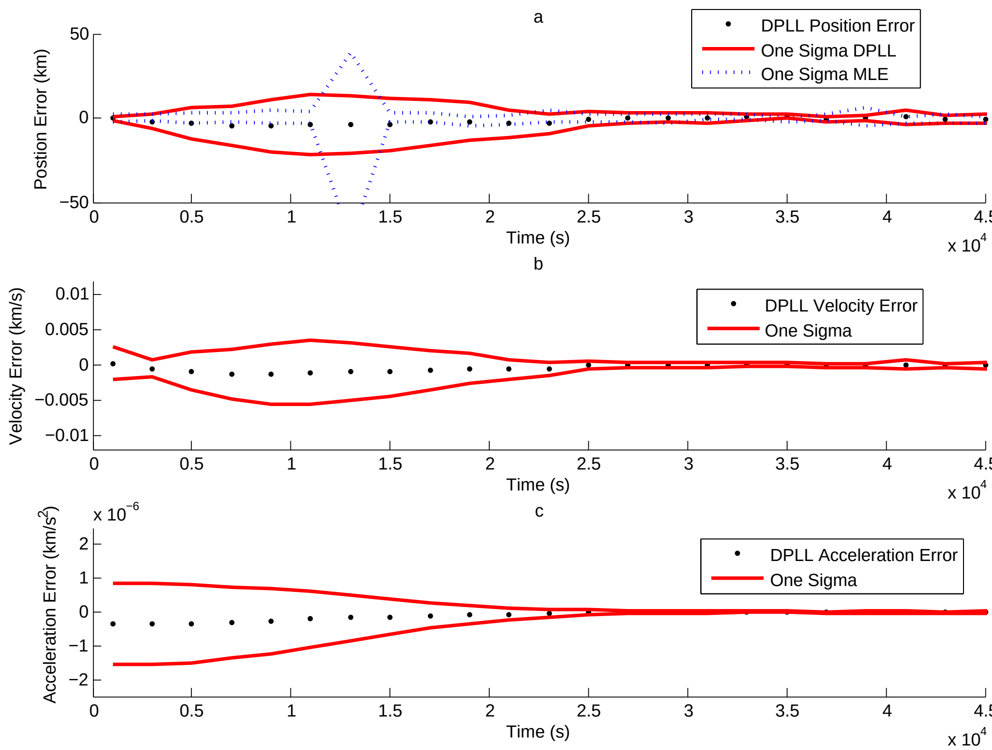

Figure 5.25: Constant acceleration trajectory phase tracking simulation results with DSN plus accelerometer level initial condition error using B1937+21 with T = 2000 seconds and B_L = 0.00025 Hz. Detector area of 2 m^2. One dimensional tracking results along LOS to pulsar.

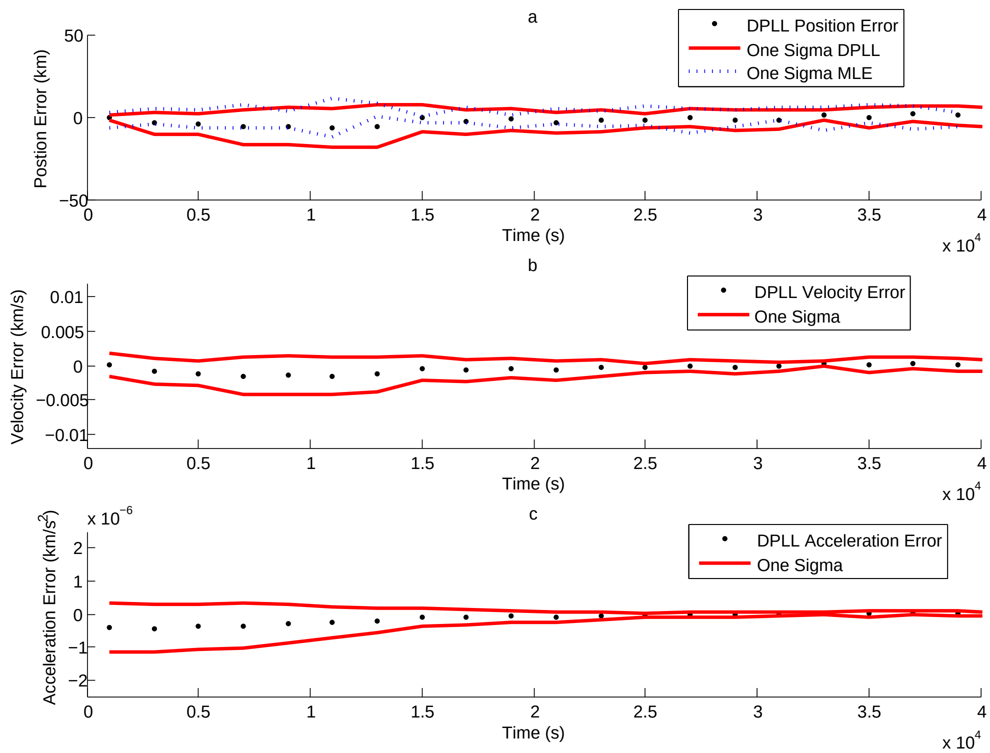

Figure 5.26: Constant acceleration trajectory phase tracking simulation results with DSN plus accelerometer level initial condition error using J0218+4232 with T = 2000 seconds and B_L = 0.00025 Hz. Detector area of 2 m^2. One dimensional tracking results along LOS to pulsar.

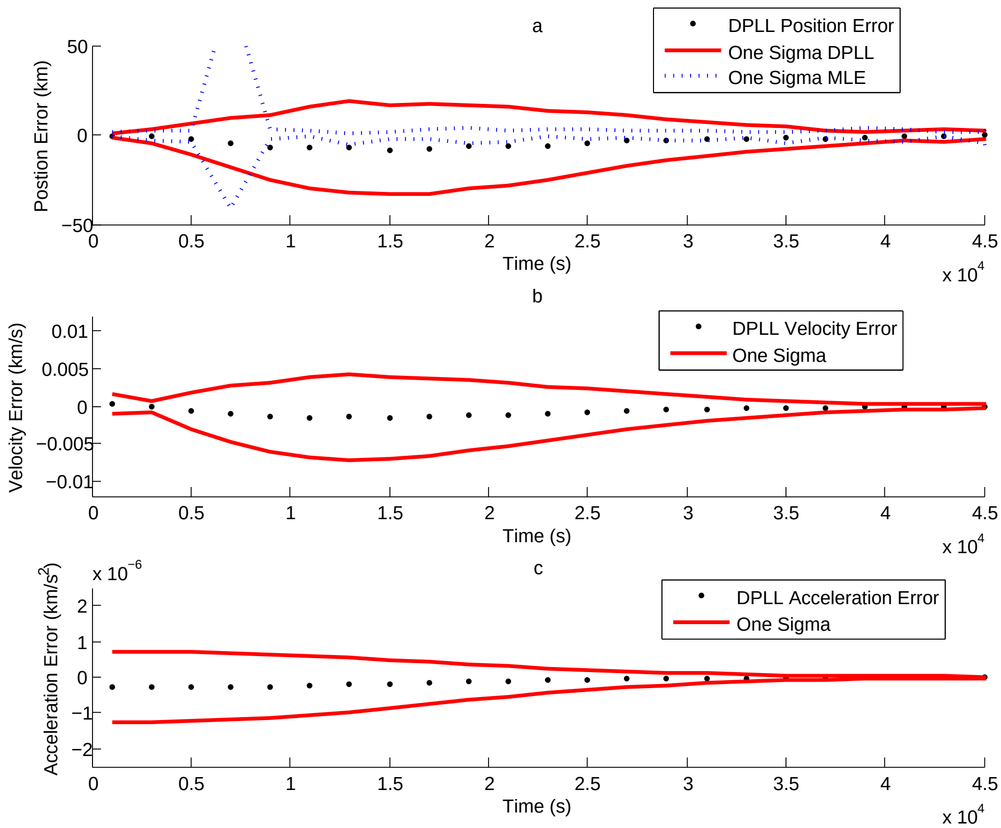

Figure 5.27: Constant acceleration trajectory phase tracking simulation results with DSN plus accelerometer level initial condition error using B1937+21 with T = 2000 seconds and B_L = 0.00015 Hz. Detector area of 2 m^2. One dimensional tracking results along LOS to pulsar.

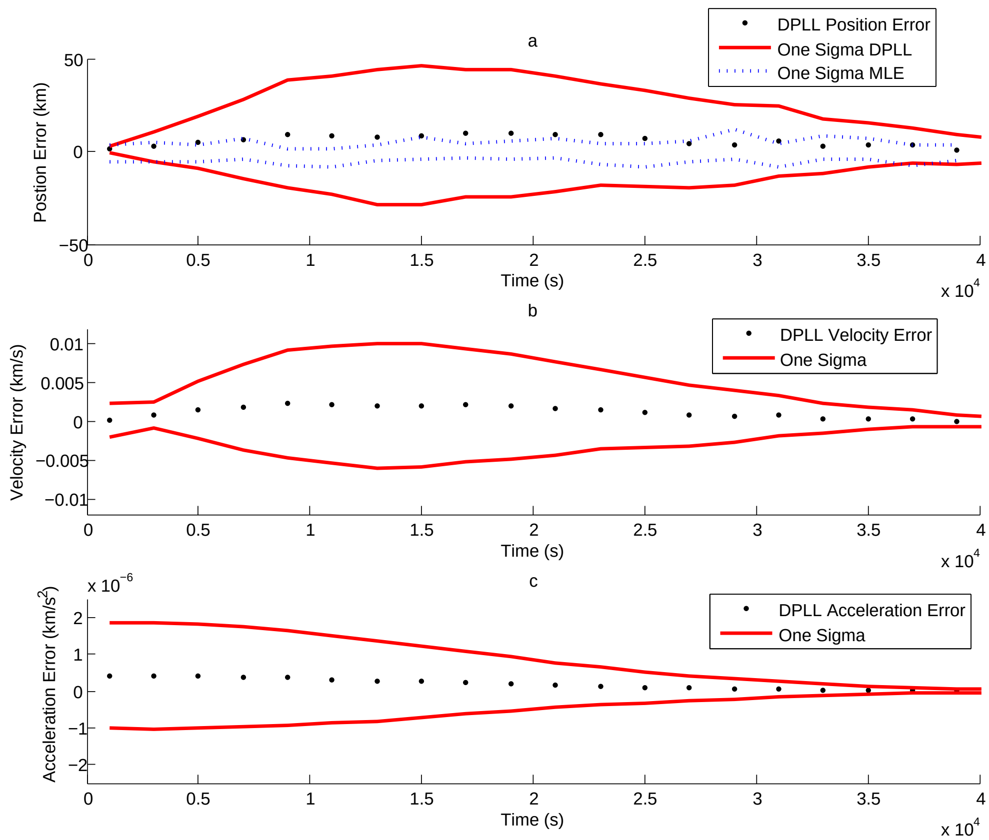

Figure 5.28: Constant acceleration trajectory phase tracking simulation results with DSN plus accelerometer level initial condition error using J0218+4232 with T = 2000 seconds and B_L = 0.00015 Hz. Detector area of 2 m^2. One dimensional tracking results along LOS to pulsar.

Table 5.9: Constant acceleration trajectory simulation results for PSR B1821-24 with initialization from DSN and an accelerometer using a detector area of 2 m^2. One dimensional tracking results along LOS to pulsar.

B_L, Hz	0.001	0.00025	0.0001	0.00025	0.0001	0.00025	0.0001
T, s	100	100	100	500	500	2000	2000
CRLB, km	3.0707	3.0707	3.0707	1.3733	1.3733	0.6866	0.6866
Averaged MLE Position Error (km)	3.38	3.38	3.38	1.46	1.46	0.71	0.70
End Point RMS Position Error (km)	1.67	0.99	1.30	0.98	2.06	0.99	4.37
Averaged Position Error (km)	1.48	1.42	13.61	1.77	15.90	4.00	15.69
End Point RMS Velocity Error (m/s)	1.34	0.24	0.11	0.20	0.19	0.13	0.45
Averaged Velocity Error (m/s)	1.37	0.70	3.48	0.75	3.67	0.97	2.62

Table 5.10: Constant acceleration trajectory simulation results for PSR B1937+21 with initialization from DSN and an accelerometer using a detector area of 2 m^2 and a block update time of 2000 seconds. One dimensional tracking results along LOS to pulsar.

B_L, Hz	0.002	0.001	0.0005	0.00025	0.00015
CRLB, km	1.0159	1.0159	1.0159	1.0159	1.0159
Averaged MLE Position Error (km)	3.78	6.30	3.39	5.54	8.81
End Point RMS Position Error (km)	15.01	10.27	4.26	2.55	2.09
Averaged Position Error (km)	7.96	5.60	4.70	7.13	13.02
End Point RMS Velocity Error (m/s)	3.77	2.37	0.95	0.41	0.24
Averaged Velocity Error (m/s)	2.24	1.44	1.10	1.60	2.64

Table 5.11: Constant acceleration trajectory simulation results for PSR J0218+4232 with initialization from DSN and an accelerometer using a detector area of 2 m^2 and a block update time of 2000 seconds. One dimensional tracking results along LOS to pulsar.

B_L, Hz	0.002	0.001	0.0005	0.00025	0.00015
CRLB, km	4.189	4.189	4.189	4.189	4.189
Averaged MLE Position Error (km)	5.31	5.12	5.30	5.45	5.37
End Point RMS Position Error (km)	18.13	11.15	7.08	5.16	9.65
Averaged Position Error (km)	15.58	10.46	7.65	7.59	23.66
End Point RMS Velocity Error (m/s)	5.73	2.96	1.48	0.83	1.09
Averaged Velocity Error (m/s)	4.42	2.69	1.68	1.59	4.74

The results for the simulations with a 2 m^2 detector area can be analyzed back to the performance with a 1 m^2 detector by comparing the results in Table 5.8 to the B1821-24, B1937+21, and J0218+4232 results in Table 5.9, Table 5.10, and Table 5.11, respectively. Figure 5.29 contains a comparison of the averaged MLE one dimensional range error for B1821-24, B1937+21, and J0218+4232 for B_L choices of 0.001 Hz, 0.00025 Hz, and 0.00015 Hz. Choices of T with B1821-24 varying from 100 seconds to 500 seconds to 2000 seconds are compared for the choices of B_L.

Looking only at the position error and considering the best achievable estimate accuracy, either from the MLE or the end point estimate of the DPLL, there is improvement from 1.94 km to 1.67 km error with B1821-24 and from 5.29 km to 5.12 km with J0218+4232 when the detector area was doubled. For some reason the position error results for B1937+21 decreased from 2.87 km to 6.30 km. This value did correlate back much better to the end point DPLL RMS position error of 6.22 km with 1 m^2. As seen many other times, there is something anomolous going on with the MLE results with B1937+21 that seems unique to its signal profile or modeling.

5.4.2.3 Constant Acceleration Phase Tracking Results with Initial Condition Error Using PSR J0437-4715

The results for the simulation of phase tracking the J0437-4715 signal with a 5 m^2 detector are plotted in Figure 5.30. The block update time used is T = 4000 seconds and the loop noise bandwidth is $B_L = 0.0001$ Hz. The shapes of the

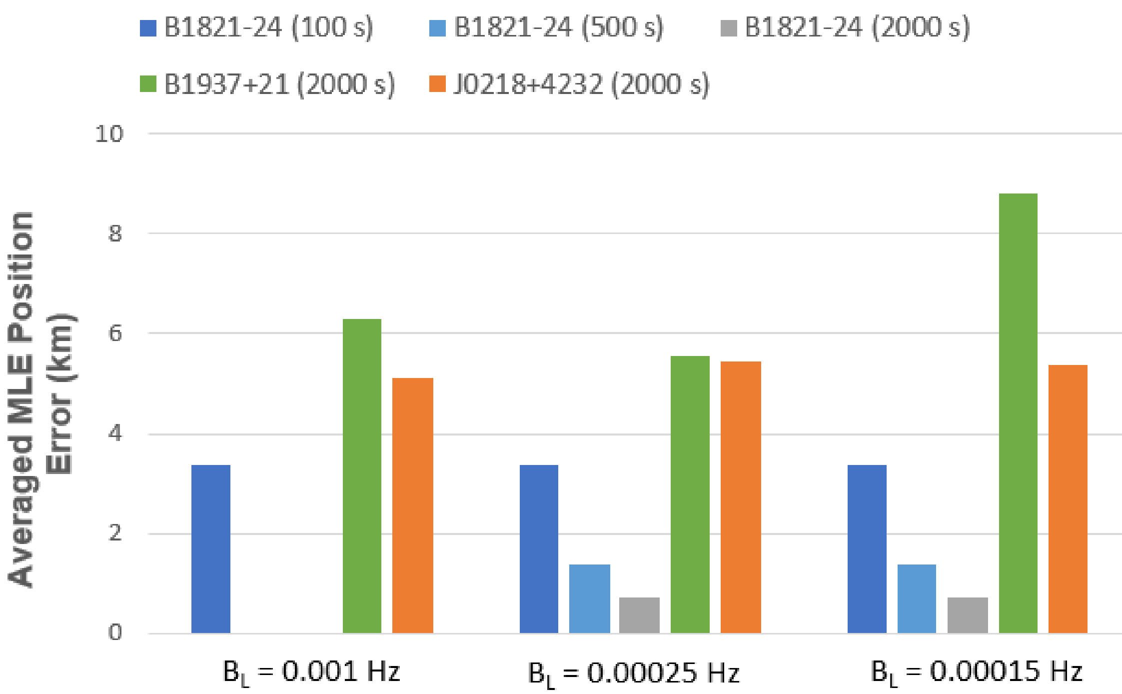

Figure 5.29: Comparison of the average MLE tracking error across the different MSPs with various T and B_L for the constant acceleration trajectory with DSN plus accelerometer level initial condition error. Detector area is 2 m^2. One dimensional results along LOS to pulsar.

position, velocity, and acceleration error plots are similar to those seen for various simulations using the other MSPs considered. There is initial overshoot in position and velocity error and slow settling time for position, velocity, and acceleration error taking nearly the entire simulation duration. The end point position error is 30.79 km, and the velocity end point error is 3.57 m/s. Even with the larger 5 m^2 detector area this performance is significantly worse than that demonstrated for the other MSPs considered: B1821-24, B1937+21, and J0218+4232. This is mostly dependent on J0437-4715 having the lowest SNR of the pulsars considered by a large margin.

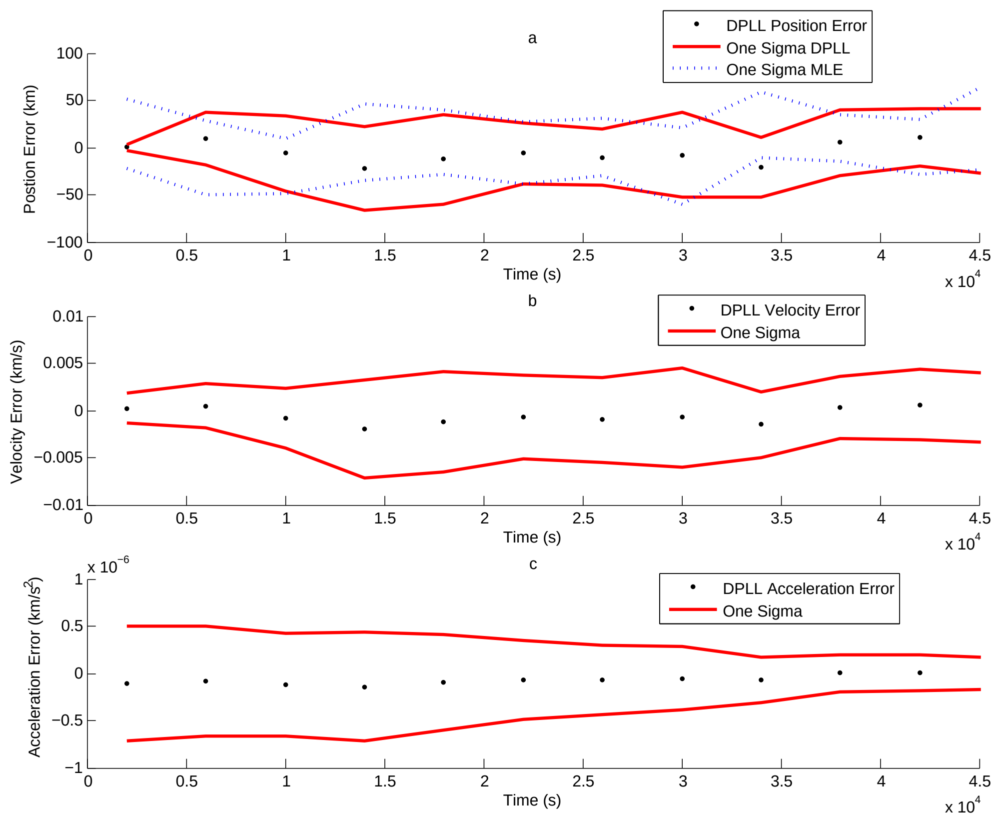

Figure 5.30: Constant acceleration trajectory phase tracking simulation results with DSN plus accelerometer level initial condition error using J0437-4715 with T = 4000 seconds and B_L = 0.0001 Hz. Detector area increased to 5 m^2. One dimensional tracking results along LOS to pulsar.

5.4.2.4 Constant Acceleration Phase Tracking Results with Initial Condition Error Using the Crab Pulsar

Simulations were also performed using the Crab pulsar signal. The much higher source flux of the Crab pulsar provided both some challenges and opportunities with regards to the scenarios considered. The high flux allows for the phase tracking algorithm to be demonstrated with a much smaller detector area that is only viable for the Crab pulsar. A detector area of 1000 cm^2 was used. The sheer number of photons simulated for the Crab pulsar signal necessitated a shorter simulation duration in order to keep the simulation real time processing reasonable. A total observation of 7200 seconds was used for the simulations with the Crab pulsar as opposed to 54000 seconds with the MSPs previously considered. This shorter simulation still allowed for the demonstration of the tracking performance and the visualization of the overall trends and differences based on DPLL parameter choices. The same DSN handoff with an accelerometer was modeled to provide the initial condition errors.

Four simulations were performed with block sizes of T = 10 seconds and T = 100 seconds and loop noise bandwidths of 0.00025 Hz and 0.0005 Hz. The results are summarized in Table 5.12 and compared to the CRLB. The MLE results compare favorably to the CRLB in all four combinations of T and B_L. The MLE phase error decreases as expected from 4.55 km to 1.55 km when T increases from 10 seconds to 100 seconds with B_L = 0.00025 Hz. The end point RMS DPLL position and velocity errors decreased when the loop noise bandwidth increased from 0.00025 Hz to 0.0005 Hz for both T = 10 seconds and T = 100 seconds. For example, for T = 10 seconds the end point RMS DPLL position and velocity errors decreased from 3.92 km and 2.59 m/s with B_L = 0.00025 Hz to 0.72 km and 0.51 m/s with B_L = 0.0005 Hz. This change demonstrates that some other underlying errors are causing an unexpected response to the loop noise bandwidth change. It would be expected that a decrease in B_L would lead to a decrease in the errors, but there is a limit to how small B_L can be made.

The results for the simulation with T = 10 seconds and B_L = 0.0005 Hz are plotted in Figure 5.31. The DPLL position error is able to maintain the level of the initial condition error and outperform the individual errors from the MLE. The velocity error is able to maintain the level corresponding to the initial condition error. The acceleration error is slowly decreasing to correct for the initial error.

It is tough to compare these Crab pulsar results directly with the simulations earlier in this section with the other MSPs due to the change in detector area. The Crab pulsar can produce better phase estimation accuracy if an equivalent 1 to 2 m^2 detector area is used. The Crab pulsar signal does not need to be tracked by the more complicated version of phase tracking developed to deal with the low flux MSPs. It is possible, as demonstrated in Chapter 3, to phase track the Crab using the Golshan and Sheikh method assuming constant velocity per block due to the ability to use smaller block sizes because the Crab pulsar signal flux is multiple orders of magnitude higher than that of the other MSPs conducive to navigation. The Crab pulsar simulation results presented here are included to demonstrate the algorithm performance with another pulsar shape and to show the feasibility of using a smaller detector area with this version of phase tracking and the Crab pulsar signal.

Table 5.12: Results of the Crab Pulsar constant acceleration trajectory simulations with initial condition errors consistent with a DSN handoff. One dimensional tracking results along LOS to pulsar.

T, s	10	10	100	100
B_L, Hz	0.00025	0.0005	0.00025	0.0005
CRLB, km	2.438	2.438	0.771	0.771
Averaged MLE Position Error (km)	4.55	4.55	1.55	1.57
End Point RMS Position Error (km)	3.92	0.72	4.23	0.92
Averaged Position Error (km)	2.22	0.87	2.36	0.96
End Point RMS Velocity Error (m/s)	2.59	0.51	2.66	0.63
Averaged Velocity Error (m/s)	1.97	1.01	1.97	1.04

5.4.2.5 Comparison to Simulations with True Initial State and to Previous Phase Tracking Methods

When comparing the results of the constant acceleration trajectory tracking simulations with initial condition errors corresponding to a DSN hand-off to the simulations with true initial state, the main changes are that a larger loop noise bandwidth needed to be considered and the detector area needed to be doubled for some of the pulsars to achieve similar levels of position error results. With B1821-24, B1937+21, J0218+4232, and the Crab pulsar the position error from the phase tracking outputs was in the same 1 – 10 km range as with the constant acceleration

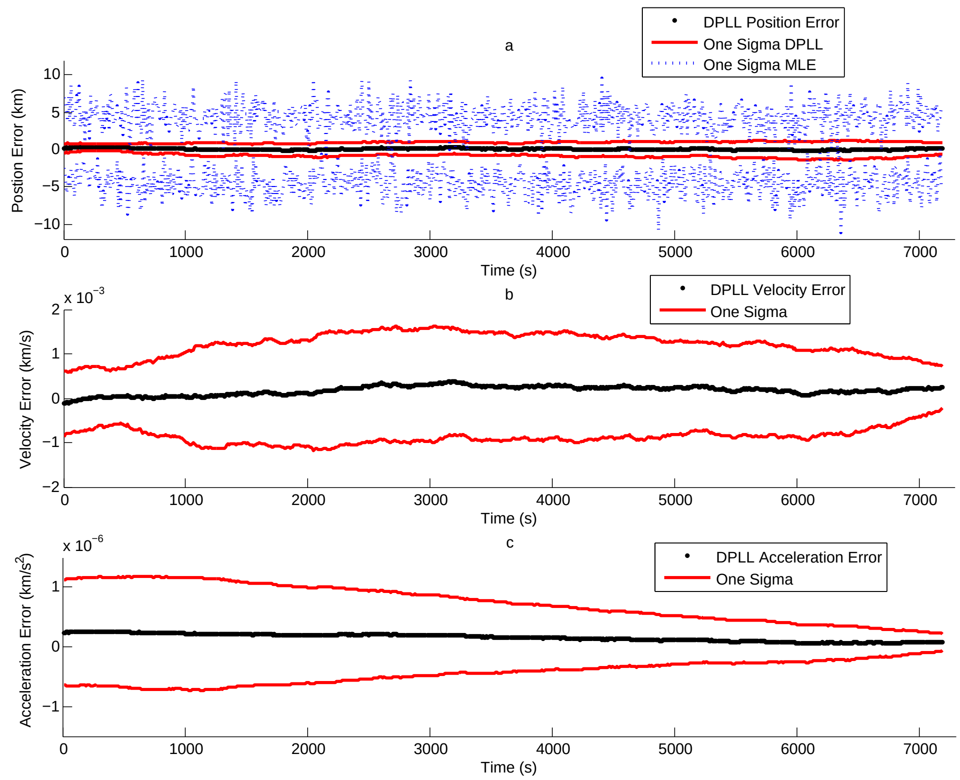

Figure 5.31: Constant acceleration trajectory phase tracking simulation results with DSN plus accelerometer level initial condition error using the Crab Pulsar with T = 10 seconds and B_L = 0.0005 Hz. Detector area decreased to 1000 cm^2. One dimensional tracking results along LOS to pulsar.

trajectories with true initial state. Again, the signal for J0437-4715 was the most difficult to track and the position errors were much worse than the other pulsars considered.

The constant acceleration tracking results with initial condition error also demonstrate major improvements with the new phase tracking algorithm over the previous efforts at phase tracking pulsar signals outlined in Chapter 3. The previous algorithm could only track the PSR B1821-24 signal with detector areas of 25 to 100 m^2, with block sizes under 6 seconds, and the position errors were still on the order of 100 km. As seen in this chapter, the new phase tracking algorithm is able to track the constant acceleration trajectory, with initial condition errors corresponding to a hand-off from the DSN, with detector areas of 1 to 2 m^2 and position errors between $1 - 10$ km.

5.5 Phase Tracking for Earth Orbits and Heliocentric Trajectories

The newly proposed pulsar phase tracking algorithm was tested with realistic orbits and trajectories that exhibit various levels of dynamic stress that could occur on an observed pulsar signal received at a detector on a spacecraft. Two main classes of orbit types were considered: heliocentric transfer orbits and Earth orbits of various altitudes. Two interplanetary trajectories were considered as representative examples of heliocentric transfer orbits. These interplanetary trajectories were portions of the cruise phases of the Mars Science Laboratory (MSL) and Cassini missions on the way to Mars and Saturn, respectively. The portion of the MSL trajectory considered corresponds to 100 days prior to Mars rendezvous. Parameters detailing these two trajectories are contained in Table 5.13. The initial values included for the orbit are all referenced along the line-of-sight to PSR B1821-24 from the SSB as an example. The values are different for each of the other pulsars considered along their lines-of-sight. Heliocentric transfer orbits for interplanetary missions are prime examples for the utility of XNAV to aid in spacecraft navigation to reduce the load on the DSN. They have lower dynamic stress on the observed pulsar signal and need less frequent communications with Earth than spacecraft currently orbiting or in the vicinity of other planetary bodies in the solar system. Thus, simulations of MSL and Cassini were chosen to demonstrate phase tracking performance under these conditions to motivate use for future similar missions.

Three Earth orbits of varying altitudes were considered to provide a range of potential operating conditions on missions in the proximity of the Earth. Example orbits of the International Space Station (ISS) in Low Earth Orbit (LEO), a satellite from the GPS constellation, and a DirecTV satellite in a geostationary orbit were considered. Parameters detailing these three Earth orbit types are contained in Table 5.14, listed in order of lowest to highest altitude orbit of Earth. Again the initial values are all referenced along the line-of-sight to PSR B1821-24 from the SSB as an example. The particular satellites considered are a portion of the GPS BIIA-16 satellite orbit starting on December 6, 2004, a portion of the DirecTV-2 satellite orbit starting on January 2, 2005, and a portion of the ISS orbit starting on December 12, 2013. Figure 5.32 contains plots of the simulated Earth orbits juxtaposed to show the relative altitudes disregarding the discrepancies in the absolute times corresponding to the individual orbits.

As will be seen later, the Earth orbit phase tracking results for some of the pulsars will be poor for the standard detector area and will require the use of potentially much larger detectors. Because of this, the phase tracking performance with a cislunar trajectory was also simulated in order to provide an example with dynamic stress between the Earth orbits and the heliocentric trajectories. This will allow for the investigation of successful phase tracking with a wider range of the MSPs considered. The chosen cislunar orbit is a portion of a transfer trajectory between Earth orbit and the Moon. Parameters detailing this cislunar trajectory are contained in Table 5.14 along with the other Earth orbit values. Figure 5.33 contains a plot demonstrating the cislunar trajectory over one day.

The phase tracking performance was investigated for the same four MSPs simulated with the constant acceleration trajectories: B1821-24, B1937+21, J0218+4232, and J0437-4715. In order to demonstrate another pulsar that works well with Earth orbits, the newly proposed algorithm was tested with the Crab pulsar as well even though its signal could be tracked on these trajectories using previous phase tracking methods, relying on a second-order DPLL. Also, the much higher flux of the Crab pulsar allows for the investigation of using detector areas much smaller than the standard 1 m^2. The phase tracking algorithm provides range information along the LOS to the observed pulsar, which is equivalent to one-dimensional position, velocity, and acceleration. Thus, range, range-rate, and range-rate-rate will be the outputs compared across the various scenario results. This will be used later to form three-dimensional state estimates in Chapter 6.

The simulated pulsar observation data is formed using the same process with XPRESS as with the constant acceleration trajectory simulations. The spacecraft orbit data for each realistic heliocentric or Earth orbit is necessary to generate the NHPP realization that represents a set of photon event times at a detector on the spacecraft. The DPLL update time, T, was taken to be the same as the MLE block length for all simulations and will be referred to as the block update time.

5.5.1 Heliocentric Trajectory Tracking Performance

The phase tracking algorithm was tested with a portion of the cruise trajectory of the MSL mission on route to Mars. The orbit corresponds to 100 days before Mars rendezvous for the MSL. The signals for pulsars B1821-24, B1937+21, and J0218+4232 were tracked with a simulated detector area of 1 m^2, while tracking of

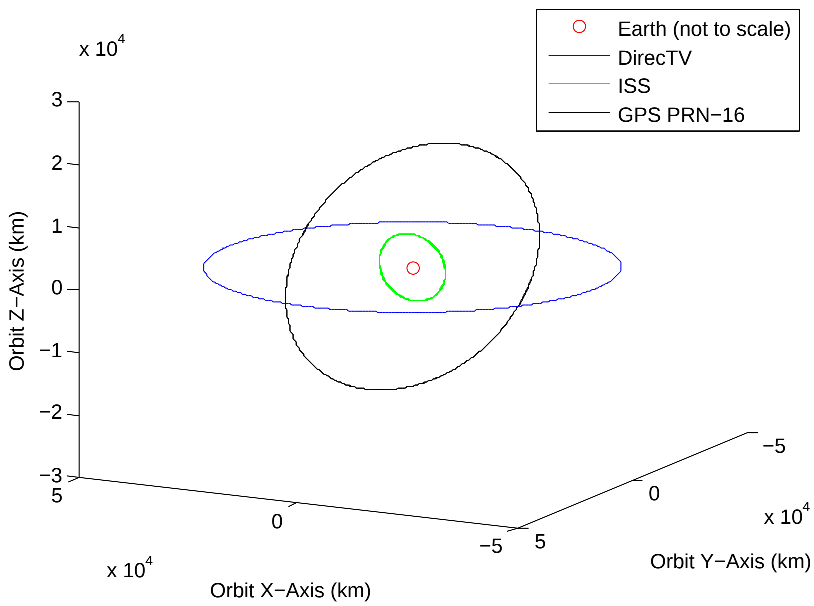

Figure 5.32: Plots of the three simulated Earth orbits used to test the phase tracking algorithm over a range of dynamic stress conditions. Included are a DirecTV satellite in GEO, a GPS satellite, and the ISS in LEO.

Table 5.13: Parameters detailing the interplanetary trajectories simulated. The initial values included are referenced along the line-of-sight to PSR B1821-24 from the SSB.

Parameter	MSL Cruise	Cassini Cruise
Orbit Start Date, yyyy:mm:dd	2012:05:11	2002:10:01
Orbit Start Time, hh:mm:ss	00:24:00	00:00:00
Initial Position, km	39448892	-1044215043
Initial Velocity, km/s	22.41	-5.02
Initial Acceleration, mm/s^2	-0.49	0.089
Initial Phase, cycles	0.77	0.89
Initial Signal Frequency, Hz	327.89	327.86
Observation Time, s	54000	54000

J0437-4715 needed a 5 m^2 detector. Tracking for PSR J0437-4715 was attempted with a 1 m^2 detector to match the other pulsars considered, but a combination of having a lower SNR and worse predicted MLE accuracy given a fixed area-time product led to the need of increasing the size.

The Crab pulsar was also considered for simulations along the MSL trajectory. Due to the much higher flux of the Crab pulsar, various areas and simulation times were considered. The same 1 m^2 (10000 cm^2) detector area as used with the MSPs was simulated with a shorter simulation time of 200 seconds due to computing constraints from the high flux rate. Detector areas of 0.1 m^2 (1000 cm^2) and 0.01 m^2 (100 cm^2) were simulated for 7200 seconds with the Crab pulsar to demonstrate the feasibility with smaller detectors.

The simulations were all performed with the initial conditions having errors corresponding to a hand-off from the DSN. In order to provide the necessary initial

Table 5.14: Parameters detailing the Earth orbits simulated. The initial values included are referenced along the line-of-sight to PSR B1821-24 from the SSB.

Parameter	ISS	GPS	DirecTV	Cislunar
Orbit Start Date, yyyy:mm:dd	2013:12:16	2004:12:07	2005:01:03	2019:06:18
Orbit Start Time, hh:mm:ss	00:00:04	00:00:07.7	00:00:03.559	01:00:00
Initial Position , km	-143850563	-137978938	-145813308	148596334
Initial Velocity , km/s	-0.338	-6.950	1.012	3.50
Initial Acceleration, m/s^2	3.27	-0.188	0.0508	0.000349
Initial Phase, cycles	0.28	0.52	0.53	0.10
Initia Signal Frequency, Hz	327.86	327.86	327.88	327.87
Observation Time, s	54000	54000	54000	54000

acceleration accuracy, an accelerometer is assumed available. This initial accuracy is needed in order for the DPLL to start tracking in-lock from the beginning of the phase tracking using the methods of Section 5.2. The specific initial condition errors were chosen to correspond to those used with the constant acceleration trajectory simulations in Section 5.3.4: 1 km for position, 1 m/s for velocity, and 1 mg or 1 cm/s^2 in acceleration.

Table 5.15 contains a list of examples of the DPLL parameters chosen for tracking the signals of the various pulsars. Specific examples of the DPLL gains K_1, K_2, and K_3 are included as determined by each choice of ζ, T, and B_L. The DPLL update time T was chosen for each pulsar by consulting the empirical MLE versus CRLB plots from Chapter 4. Due to the manageable dynamic stress of the heliocentric orbits, only the lower threshold time, caused by the Poisson statistics of low flux, needs to be considered. The values for T were chosen to have a margin

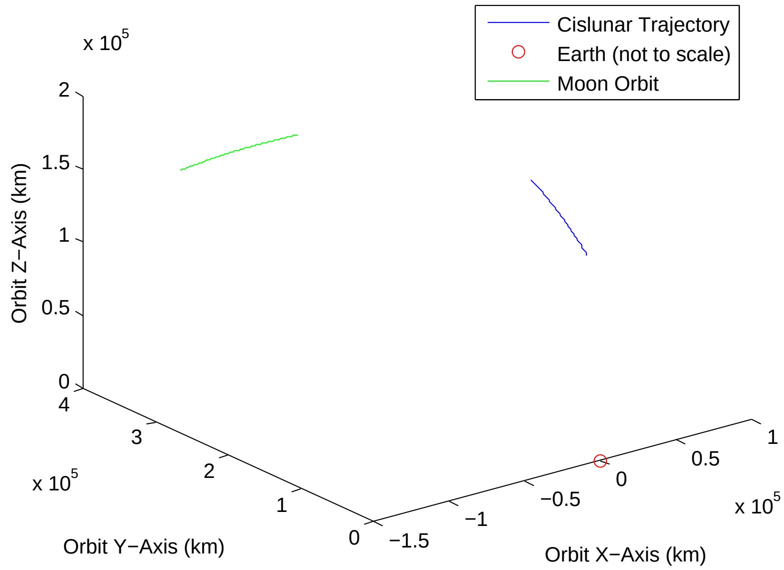

Figure 5.33: Plot of the cislunar transfer trajectory simulated for one day of flight time.

above the threshold in order to further reduce the outlier percentage for the MLE and to increase the anticipated MLE accuracy to more desirable levels. The DPLL noise bandwidth, B_L, was chosen in consideration with the rule-of-thumb for noise bandwidth vs. dynamic stress discussed in Section 5.3.2.

The noise bandwidth, B_L, is directly related to the level of error in the DPLL phase estimates, so B_L is set relatively small as allowed by the low dynamic stress of the MSL cruise trajectory. The specific B_L values were chosen to balance the desire for the DPLL to improve over the MLE accuracy, while not overly damping out the response to changes in the loop filter values. Various combinations of T and B_L were tested and these choices were informed by the performance of the phase tracking of the constant acceleration trajectory in the previous section. A standard choice of $B_L = 0.00025$ Hz was used for each of the pulsars to have a standard comparison. Smaller values for B_L start to over-smooth the DPLL in relation to the MLE outputs. The damping ratio was again chosen to yield an underdamped response with $\zeta = \frac{\sqrt{2}}{2}$ where all loop roots have the same decay rate. The values of the DPLL gains once again come from the tables in [107] for different choices of the $B_L T$ product.

Table 5.15: Settings used for the parameters of the third-order DPLL for the heliocentric cruise trajectory phase tracking simulations.

DPLL Parameter	B1821-24	B1937+21	J0218+4232	J0437-4715	Crab Pulsar
T, s	200	4000	4000	10000	10
B_L, Hz	0.00025	0.00025	0.00025	0.00025	0.00025
ζ	0.707	0.707	0.707	0.707	0.707
K_1	0.1174	0.7829	0.7829	0.9297	0.0065
K_2	0.006445	0.4421	0.4421	0.7544	0.000019
K_3	0.0001355	0.1243	0.1243	0.3802	0.00000002

5.5.1.1 MSL Trajectory Phase Tracking Results

The results from the MSL trajectory tracking simulations are illustrated for B1821-24, B1937+21, and J0218+4232 in Figures 5.34 - 5.37 . Each figure has three subplots that demonstrate (a) position error vs. time, (b) velocity error vs. time, and (c) acceleration error vs. time For PSR B1821-24 two choices for DPLL update time T were considered. First, T = 200 seconds was considered as this is a block update time that is as small as allowed due to the lower bound for convergence to the CRLB with some margin. Second, T = 4000 seconds was considered due to it being the block update time needed for the other MSPs investigated. These two choices together illustrate the benefits provided by the higher flux B1821-24 signal as compared to B1937+21 and J0218+4232. The simulation results are illustrated in Figure 5.34 and Figure 5.35 for T = 200 seconds and T = 4000 seconds, respectively. The loop noise bandwidth for both of these scenarios is set to $B_L = 0.00025$ Hz. Figure 5.36 shows the phase tracking results for B1927+21 with T = 4000 seconds and loop noise bandwidth $B_L = 0.00025$ Hz. Figure 5.37 shows the results for J0218+4232 with T = 4000 seconds and $B_L = 0.00025$ Hz.

The differences in the performance for the phase tracking of the B1821-24 signal for the two choices of block update time T can be seen by comparing Figure 5.34 to Figure 5.35. In both scenarios the simulation results demonstrate that the DPLL is able to maintain the tracking results throughout the simulation duration for position, velocity, and acceleration. One main difference can be seen in the position error plot where in Figure 5.34, with T = 200 seconds, the DPLL position estimate is able to outperform the MLE position estimate after an initial period of overshoot, while in Figure 5.35, with T = 4000 seconds, the overshoot is much larger and the DPLL estimates only approach the accuracy of the MLE outputs by the end of the simulation time. Another main difference is that the overshoots for position, velocity, and acceleration error are much larger and take longer to settle with T = 4000 seconds in Figure 5.35 than with T = 200 seconds in Figure 5.34.

The simulation results for B1937+21 and J0218+4232 are similar to each other as seen in Figure 5.36 and Figure 5.37, respectively, and have more in common with the B1821-24 simulation with T = 4000 seconds. Both the B1937+21 and J0218+4232 simulation results demonstrate the ability to track the signals and maintain the level of position and velocity errors after an initial period of overshoot and settling. As seen in Figure 5.36, the results with B1937+21 show an ability to improve on the initial tracking estimates for position and velocity by the end of the simulation time window, while the results with J0218+4232 in Figure 5.37 show the levels of position and velocity errors are similar at the end of the simulation to the initial condition levels.

Table 5.16 summarizes the MSL tracking results for these three pulsars, including the two T choices considered for B1821-24, and compares them to the results from tracking the Cassini trajectory. The metrics presented and compared in Table 5.16 include the average MLE position error and the end point DPLL position and velocity error. The CRLB for position estimation error is also included for comparison to the theoretical limit. These results will be discussed in more detail later in the section after the Cassini simulations are also presented.

5.5.1.2 Cassini Trajectory Phase Tracking Results

The phase tracking algorithm was also tested with a portion of the cruise trajectory of the Cassini mission on route to Saturn. As with the MSL trajectory, pulsars B1821-24, B1937+21, and J0218+4232 were tracked with a simulated detector area of 1 m^2 while tracking of J0437-4715 used a 5 m^2 detector. Since the dynamic stress of the Cassini trajectory is similar to the MSL, the DPLL parame-

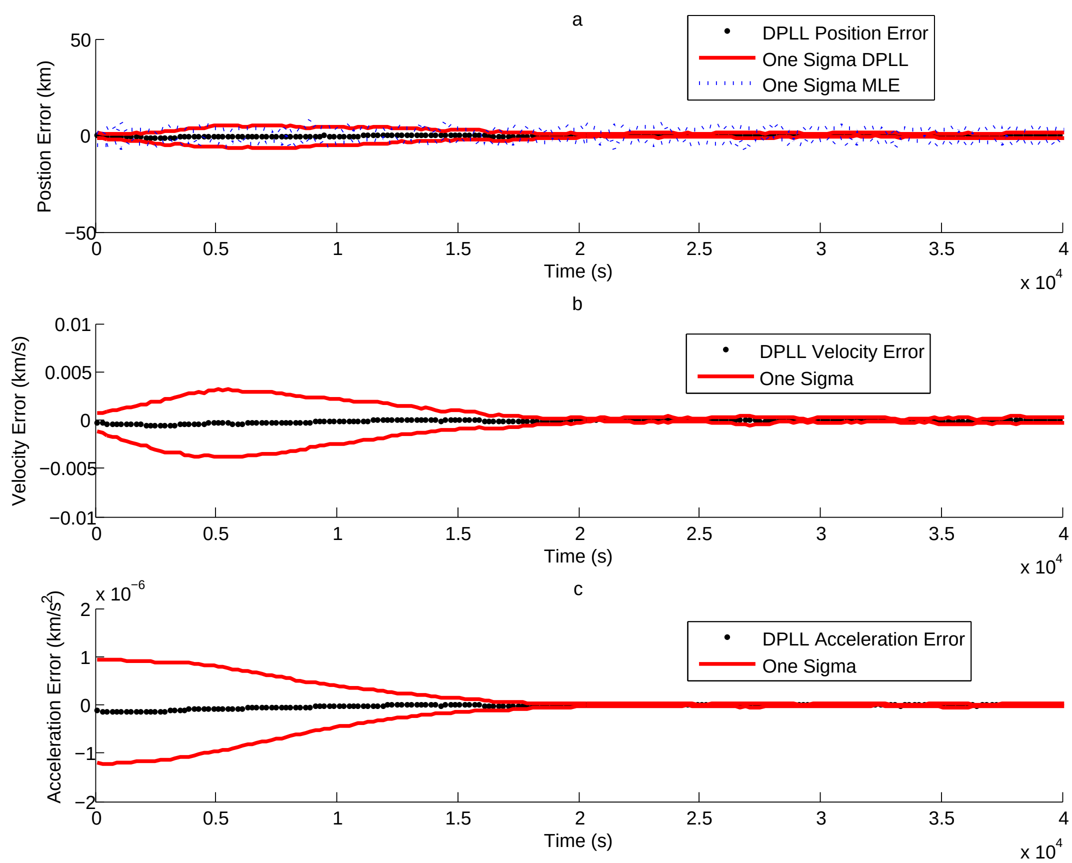

Figure 5.34: MSL cruise trajectory phase tracking simulation results with DSN plus accelerometer initial condition error using B1821-24 with T = 200 seconds and $B_L = 0.00025$ Hz. One dimensional tracking results along LOS to pulsar.

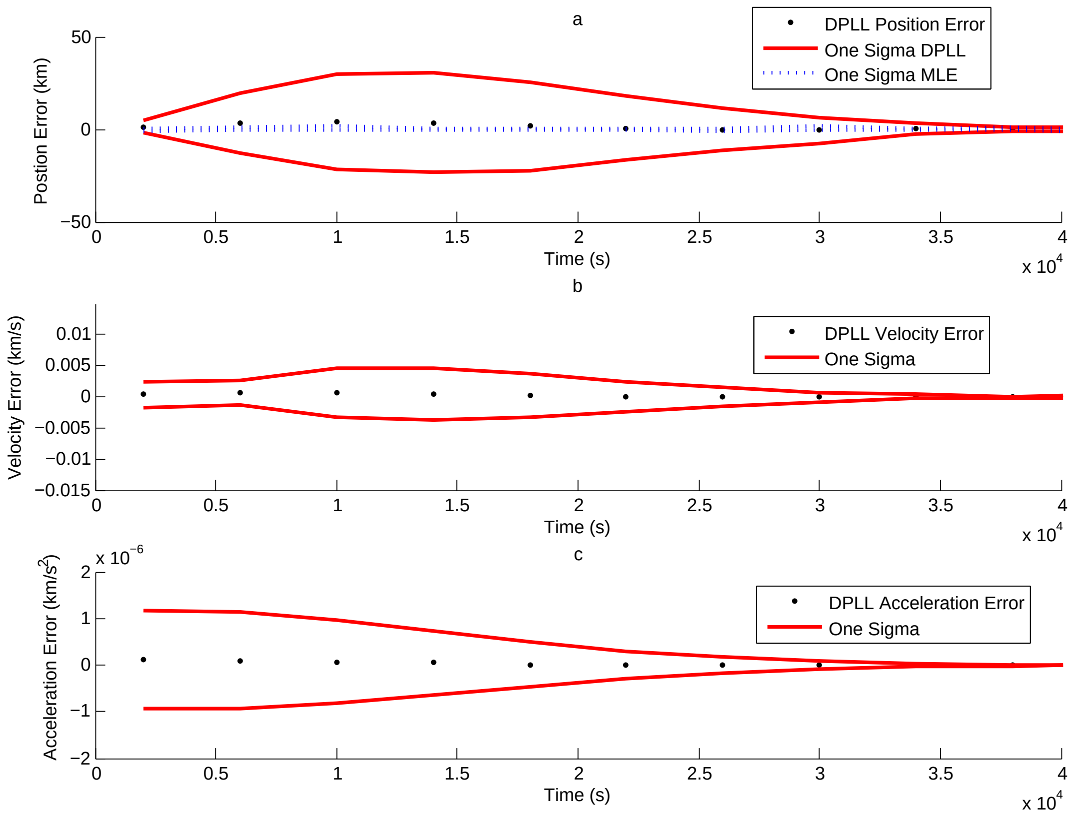

Figure 5.35: MSL cruise trajectory phase tracking simulation results with DSN plus accelerometer initial condition error using B1821-24 with T = 4000 seconds and B_L = 0.00025 Hz. One dimensional tracking results along LOS to pulsar.

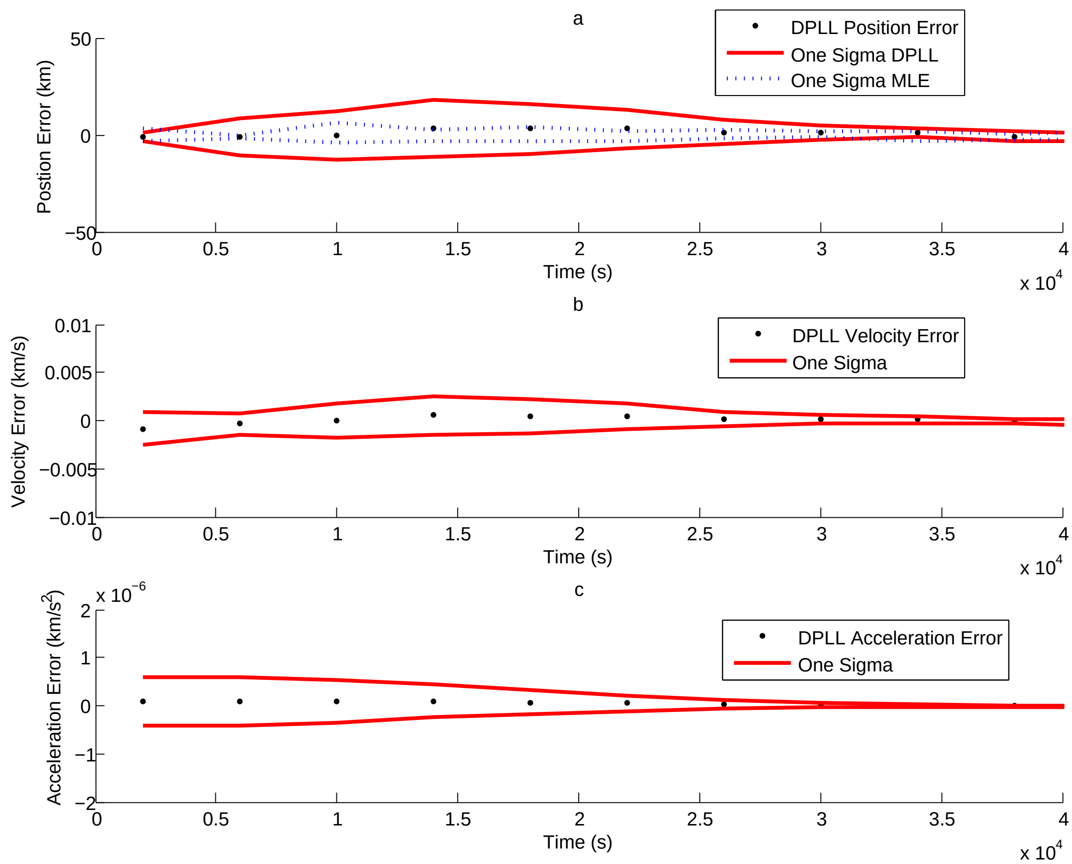

Figure 5.36: MSL cruise trajectory phase tracking simulation results with DSN plus accelerometer initial condition error using B1937+21 with T = 4000 seconds and B_L = 0.00025 Hz. One dimensional tracking results along LOS to pulsar.

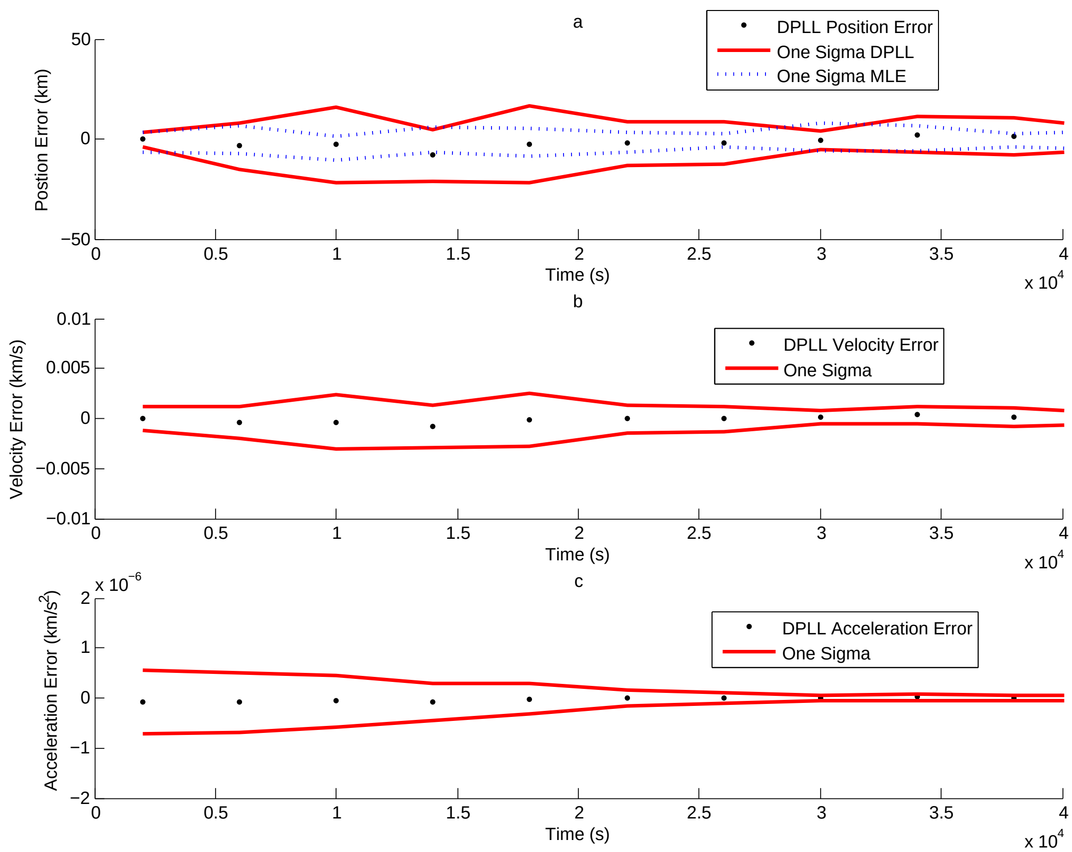

Figure 5.37: MSL cruise trajectory phase tracking simulation results with DSN plus accelerometer initial condition error using J0218+4232 with T = 4000 seconds and $B_L = 0.00025$ Hz. One dimensional tracking results along LOS to pulsar.

ters were set the same as listed in Table 5.15. The results from the simulations are illustrated for B1821-24, B1937+21, and J0218+4232 in Figures 5.38 - 5.41.

As with the MSL trajectory simulations, the performance for the phase tracking of the B1821-24 signal with the Cassini trajectory was tested for two choices of block update time T. Figure 5.38 demonstrates the Cassini tracking performance with B1821-24 and T = 200 seconds and Figure 5.39 demonstrates the performance with T = 4000 seconds. In both scenarios the DPLL is able to maintain the tracking results for position and velocity error throughout the simulation duration. Similar to the MSL simulations, a main difference is that the DPLL position estimate is able to outperform the MLE position estimate after the initial period of overshoot in Figure 5.38 with T = 200 seconds, while the overshoot is much larger in Figure 5.39 with T = 4000 seconds and the DPLL position estimate accuracy only approaches the MLE level by the end of the simulation time. Also, the position, velocity, and acceleration overshoots are larger and take much longer to settle with T = 4000 seconds in Figure 5.39 than with T = 200 seconds in Figure 5.38, similar to the results with the MLE trajectory.

The simulation results for B1937+21 and J0218+4232 are again similar to each other as seen in Figure 5.40 and Figure 5.41, respectively. The simulation results for both B1937+21 and J0218+4232 demonstrate the ability to track the signals and maintain the level of position and velocity errors after an initial period of overshoot and settling. Similar to the results with the MSL trajectory, the simulations with the B1937+21 signal demonstrate the ability to improve on the initial tracking estimates for position and velocity by the end of the Cassini tracking simulation as seen in Figure 5.40, while the simulations for the J0218+4232 signal show the level of position error in Figure 5.41 is similar at the end of the simulation to the initial condition level. The velocity estimation error level is reduced, though, by the end of the simulation for the J0218+4232 signal, which is different than with the MSL trajectory.

Table 5.16 summarizes the Cassini tracking results for these three pulsars and compares them to the MSL tracking results. The metrics included display the average MLE position error and the end point DPLL position error relating to the values at the end of the simulation time. The CRLB is included for comparison to the theoretical limit on the position estimation. Results are included for both choices of loop update time, T, investigated with PSR B1821-24. All of the simulations demonstrate the capability to approach the CRLB with the average MLE performance. The farthest from the CRLB is the B1937+21 results with a 2.53 km average MLE position error compared to a CRLB of 1.02 km. This was expected, though, since the B1937+21 MLE results demonstrated a bias offset from the CRLB in the simulation results in Chapter 4.

For all three pulsars the MSL and Cassini tracking simulations produce similar results as expected due to the similarity in the dynamic stress levels of the orbits. For example, for B1821-24 with T = 200 seconds and $B_L = 0.00025$ Hz the average MLE position error was 3.38 km for the MSL and 3.40 km for Cassini. For the same scenario the end point RMS DPLL position and velocity errors were 1.16 km and 0.24 m/s and 1.00 km and 0.28 m/s for the MSL and Cassini trajectories, respectively.

The B1821-24 results with the two different block update times of 200 and 4000 seconds can be compared in Table 5.16. For example, for the MSL trajectory with T = 200 seconds: the average MLE position error was 3.38 km, the end point RMS DPLL position error was 1.16 km, and the end point RMS DPLL velocity error was 0.24 m/s. With T = 4000 seconds: the average MLE position error was 0.81 km, the end point RMS DPLL position error was 1.04 km, and the end point RMS DPLL velocity error was 0.09 m/s. As expected, the MLE performance improves greatly with the increase in T. The DPLL position and velocity errors show smaller improvements with the increase in T. For T = 4000 seconds the MLE changes to outperforming the DPLL position outputs.

Using Table 5.16 the results for the three pulsars B1821-24, B1937+21, and J0218+4232 can be compared with a standard set of T = 4000 seconds and $B_L =$ 0.00025 Hz. For B1821-24 the average MLE position error is 0.81 km, the end point RMS DPLL position error is 1.04 km, and the end point RMS DPLL velocity error is 0.09 m/s. For B1937+21 the average MLE position error is 2.53 km, the end point RMS DPLL position error is 4.12 km, and the end point RMS DPLL velocity error is 0.41 m/s. For J0218+4232 the average MLE position error is 5.42 km, the end point RMS DPLL position error is 6.45 km, and the end point RMS DPLL velocity error is 0.63 m/s. B1821-24 greatly outperforms the other two pulsars and B1937+21 slightly outperforms J0218+4232.

5.5.1.3 J0437-4715 MSL and Cassini Tracking Results

The MSP J0437-4715 was also investigated with the MSL and Cassini cruise trajectories. Due primarily for the considerably lower SNR than the other MSPs used in simulations, J0437-4715 required a larger detector area to achieve acceptable results. As opposed to the 1 m^2 detector simulated with B1821-24, B1937+21, and J0218+4232, areas of 5 and 10 m^2 were used in simulations with J0437-4715. With smaller detector areas the tracking loses lock and is unable to provide position and velocity estimates with reasonable accuracy or reliability with J0437-4715. Various combinations of T and B_L were simulated and the results are included in Table 5.17. In order to show a greater range of attempts to improve the simulation tracking performance with PSR J0437-4715 more choices of T and B_L are illustrated.

In order to provide a representation of the tracking performance for the J0437-4715 signal two particular simulation results with the MSL trajectory are plotted in Figure 5.42 and Figure 5.43 with detector areas of 5 and 10 m^2, respectively. Figure 5.42 includes plots of the position, velocity, and acceleration errors over time for a MSL cruise trajectory simulation tracking the J0437-4715 signal with T = 10000 seconds, $B_L = 0.00025$ Hz, and a detector area of 5 m^2. Figure 5.43 includes plots of the position, velocity, and acceleration errors over time for a MSL cruise trajectory simulation tracking the J0437-4715 signal with T = 5000 seconds, $B_L = 0.00015$ Hz, and a detector area of 10 m^2. The value of T was halved when the detector area was doubled in order to keep the area-time product constant for comparison. Both J0437-4715 simulations included in the figures are scenarios tracking the MSL trajectory. These were chosen for easier comparison. In general the MSL and Cassini simulations with J0437-4715 performed similarly as seen in the results included in Table 5.17.

The phase tracking simulation results are able to maintain the estimation accuracy for position and velocity using both detector area choices as seen in Figure 5.42 and Figure 5.43 for 5 and 10 m^2, respectively. In both figures, the MLE position estimates outperform the DPLL outputs. In both cases the position and velocity errors are quite large, but remain bounded. The main advantage demonstrated in the simulation with the 10 m^2 detector area are the more frequent estimates allowed by the reduction of DPLL block update time to T = 5000 seconds.

Table 5.17 summarizes the MSL and Cassini phase tracking simulation results with PSR J0437-4715. The metrics included are the average MLE position error and the end point DPLL RMS position and velocity errors. The CRLB values are included for comparison of the position estimates to the theoretical limit. Results for simulations with a range of different T and B_L choices with a 5 m^2 detector area are included along with one set with a 10 m^2 detector area. It can be seen from examining the rows of MLE average position errors for the MSL and Cassini simulations that the performance approaches the CRLB in most scenarios with a wider gap apparent for some of the T and B_L choices. The MSL and Cassini trajectory tracking performances are very similar for all of the different sets of parameters considered as seen by comparing the MLE averages and the DPLL end point position and velocity results. For example, with a detector area of 5 m^2, a loop noise band bandwidth of 0.00025 Hz, and a block update time of 10000 seconds:

the MLE position error average is 20.3 km for the MSL and 20.29 km for Cassini, the DPLL end point RMS position error is 36.19 km for the MSL and 36.05 km for Cassini, and the DPLL end point RMS velocity error is 2.26 m/s for the MSL and 2.24 m/s for Cassini.

Comparing the simulation results in Table 5.17 with a constant detector area of 5 m^2, the effects of the different DPLL parameter choices can be investigated. Changing the block update time for T = 4000 seconds to T = 10000 seconds led to an improvement in the MSL position accuracy and the DPLL position and velocity accuracies, as expected. This can be seen by looking at the MSL tracking results with $B_L = 0.00025$ Hz. With T = 4000 seconds the MLE position error is 36.5 km, the DPLL end point position error is 77.89 km and the DPLL end point velocity error is 7.11 m/s. With T = 10000 seconds the MLE position error is 20.3 km, the DPLL end point position error is 36.19 km and the DPLL end point velocity error is 2.26 m/s. All of these are substantial improvements. Increasing the block size further to T = 20000 seconds did not lead to further improvements, though. This can be seen by looking at the same MSL tracking scenario where the MLE position error stayed similar at 21.65 km, but the end point DPLL position and velocity errors increased to 173.33 km and 3.85 m/s, respectively. This worsening of results comes from the value of T approaching the total simulation time, which reduced the number of estimates performed, and from the required decrease in the loop noised bandwidth to 0.00015 Hz in order to achieve lock with the DPLL. This demonstrates the limits to increasing the block update time to improve the tracking performance.

The changes in performance that result from increasing the detector area from 5 to 10 m^2 are also demonstrated in Table 5.17. This can be seen by directly comparing the simulations with loop noise bandwidth, $B_L = 0.00015$ Hz, held constant. The block update time, T, is halved from 10000 seconds to 5000 seconds when the detector area is doubled in order to keep the area-time product constant, which is the theoretical factor that determines the CRLB for position estimation error. For the Cassini simulations, the MLE position error average stayed relatively similar with 21.38 km and 21.07 km for 5 m^2 and 10 m^2, respectively. This was expected from keeping the area-time product constant. The DPLL end point RMS position error changed from 60.14 km to 25.09 km and the end point RMS velocity error changed from 3.16 m/s to 1.97 m/s for 5 m^2 and 10 m^2, respectively. Thus, the DPLL performance is improved with the increase in the detector area. Part of this comes from the ability to perform more estimates in the same amount of simulation time, while keeping the area-time product the same for the MLE performance. Also, the $T * B_L$ product is decreased, which directly affects the DPLL gain choice and performance.

5.5.1.4 Crab Pulsar MSL and Cassini Tracking Results

The Crab pulsar was also considered for simulations along the MSL and Cassini cruise trajectories. Due to the much higher flux of the Crab pulsar, various areas and simulation times were considered. The same 1 m^2 (10000 cm^2) detector area as used with the MSPs was simulated with a shorter simulation time of 200 seconds due to computing constraints from the high flux rate. Detector areas of 0.1 m^2 (1000 cm^2) and 0.01 m^2 (100 cm^2) were simulated for 7200 seconds with the Crab pulsar to demonstrate the feasibility with smaller detectors. Various combinations of T and B_L were simulated and the results are included in Table 5.18. The different detector area and simulation time, T_{obs}, choices are displayed.

In order to provide a representation of the tracking performance for the Crab pulsar signal four particular simulation results are plotted in Figures 5.44 - 5.47. Figure 5.44 includes plots of the position, velocity, and acceleration errors over time for a Cassini cruise trajectory tracking simulation with a 1 m^2 detector area, a 200 second simulation time, T = 10 seconds, and B_L = 0.00025 Hz. Figure 5.45 includes the results for a MSL cruise trajectory simulation with a 1000 cm^2 detector area, a 7200 second simulation time, T = 10 seconds, and B_L = 0.0005 Hz. Figure 5.46 includes the phase tracking results for the MSL cruise trajectory with a 1000 cm^2 detector area, a 7200 second simulation time, T = 100 seconds, and B_L = 0.0005 Hz. Figure 5.47 includes the MSL cruise trajectory tracking simulation results with a 100 cm^2 detector area, a 7200 second simulation time, T = 100 seconds, and B_L = 0.00025 Hz. The values of T for the 100 cm^2 and 1000 cm^2 detector area simulations were chosen to keep the area-time product constant for ease of comparison of the results. In general the MSL and Cassini simulations with Crab pulsar again performed similarly as seen in the results included in Table 5.18.

The phase tracking simulation results are able to maintain the estimation accuracy for position and velocity in all four scenarios included as seen in Figures 5.44 - 5.47. In all four figures, the DPLL outputs outperform the MLE position estimates.

In Figure 5.44 the tracking results only demonstrate the performance for a 200 second observation due to the computation constraints arising from the high flux Crab pulsar and a 1 m^2 area detector. The results maintain tracking and the error levels remain consistent suggesting that the results would continue to be around the same level if the observation time was increased.

By comparing Figure 5.45 and Figure 5.46 the change in results due to the change in block update time from 10 seconds to 100 seconds can be determined for a detector area of 100 cm^2. For both simulations the velocity and acceleration error tracking profiles are similar. The main difference in the position error plots is a large improvement in the MLE average position error when increasing to T = 100 seconds. In Figure 5.46 the MLE and DPLL position results are much more similar in amplitude.

Comparing Figure 5.45 and Figure 5.47 provides a comparison between simulations with detector area of 1000 cm^2 and 100 cm^2, respecively. The area-time product of the detector area and block update time T is kept constant between these two figures yielding the similar DPLL loop gains and performance. The loop noise bandwidth is changed from 0.0005 Hz to 0.00025 Hz in Figure 5.45 to Figure 5.47, respectively. In the 100 cm^2 simulation in Figure 5.47 the DPLL position estimates are much closer in amplitude to the average MLE values, and the position and velocity estimation errors from the DPLL increase over the initial half of the simulation time and level off toward the end, which is less ideal than the more uniform performance with the 1000 cm^2 detector in Figure 5.45. In all three of these figures the position and velocity estimation errors level off by the end of the 7200 second simulation suggesting that it would be reasonable to extrapolate these results out to similar simulation times as used with the MSPs even though those simulations would be computationally challenging to confirm with the Crab pulsar.

Table 5.18 summarizes the MSL and Cassini phase tracking simulation results with the Crab pulsar. The metrics included are the average MLE position error and the end point DPLL RMS position and velocity errors. The CRLB values are included for comparison of the position estimates to the theoretical limit. Results for 7200 second long simulations with a range of different T and B_L choices with detector areas of 0.1 m^2 and 0.01 m^2 are included along with one set for a 200 second long simulation with a 1 m^2 detector area. It can be seen from examining the rows of MLE average position errors for the MSL and Cassini simulations that the performance approaches the CRLB in most scenarios with a wider gap apparent for some of the T and B_L choices. The MSL and Cassini trajectory tracking performances are very similar for all of the different sets of parameters considered as seen by comparing the MLE averages and the DPLL end point position and velocity results. For example, with a detector area of 0.1 m^2, a loop noise band bandwidth of 0.00025 Hz, and a block update time of 10 seconds: the MLE position error average is 4.53 km for the MSL and 4.54 km for Cassini, the DPLL end point RMS position error is 3.92 km for the MSL and 3.93 km for Cassini, and the DPLL end point RMS velocity error is 2.59 m/s for the MSL and 2.59 m/s for Cassini.

The results of the various simulations using a 0.1 m^2 detector can be compared in Table 5.18. For example, the changes due to block update time can be seen by comparing the MSL results with a 0.1 m^2 detector and a loop noise bandwidth of

0.0005 Hz. With a block update time of T = 10 seconds: the average MLE position error is 4.53 km, the end point DPLL position error is 0.72 km, and the end point DPLL velocity error is 0.51 m/s. With a block update time of T = 100 seconds: the average MLE position error is 1.56 km, the end point DPLL position error is 0.94 km, and the end point DPLL velocity error is 0.64 m/s. The MLE position error decreases when the block size is increased, as expected, and the DPLL error results stay relatively the same.

The affect of changing the loop noise bandwidth with a detector area of 0.1 m^2 can be seen in Table 5.18. This can be seen by looking at the MSL results with a block update time of 10 seconds. With a loop noise bandwidth of 0.00025 Hz: the average MLE position error is 4.53 km, the end point DPLL position error is 3.92 km, and the end point DPLL velocity error is 2.59 m/s. With a loop noise bandwidth of 0.0005 Hz: the average MLE position error is 4.53 km, the end point DPLL position error is 0.72 km, and the end point DPLL velocity error is 0.51 m/s. The MLE position error stays the same, as expected with the constant block size, and the DPLL position and velocity errors decrease with the increase in the loop noise bandwidth. This change in DPLL performance is contrary to expectations based on the theoretical filter model and suggest that there is a more complicated link between loop noise bandwidth and steady-state position error for this scenario. There are limitations due to various factors including pulsar signal physics and orbit dynamic stress that constraining the range of choices for T and B_L that cause the expected changes in DPLL performance. This bounds the improvement in tracking errors due solely to changes in the DPLL and simulation parameters.

Table 5.18 can be used to compare the phase tracking simulation results across the three different detector areas tested. For example, the results of the MSL simulations with a loop noise bandwidth of 0.00025 Hz and a constant area-time product can be compared. With a detector area of 1 m^2 and T = 10 seconds: the average MLE position error is 1.46 km, the end point DPLL position error is 0.61 km, and the end point DPLL velocity error is 0.53 m/s. With a detector area of 0.1 m^2 and T = 100 seconds: the average MLE position error is 1.55 km, the end point DPLL position error is 4.21 km, and the end point DPLL velocity error is 2.66 m/s. With a detector area of 0.01 m^2 and T = 1000 seconds: the average MLE position error is 1.52 km, the end point DPLL position error is 5.13 km, and the end point DPLL velocity error is 2.23 m/s. The MLE position errors are similar across all of the detector areas, as expected due to the constant area-time product. The DPLL position and velocity errors increase with the decrease in detector area due to a reduction in the number of estimates per simulation window as well as an increase in the B_L*T product affecting the DPLL gains.

5.5.1.5 Comparison to the Constant Acceleration Results and the Previous Phase Tracking Methods

The results for phase tracking the MSL and Cassini interplanetary trajectories compare favorably to the results from the more idealized case of the last section with a constant acceleration trajectory. Even though the dynamic stress is slightly larger than the idealized case of the constant acceleration trajectory, the tracking results

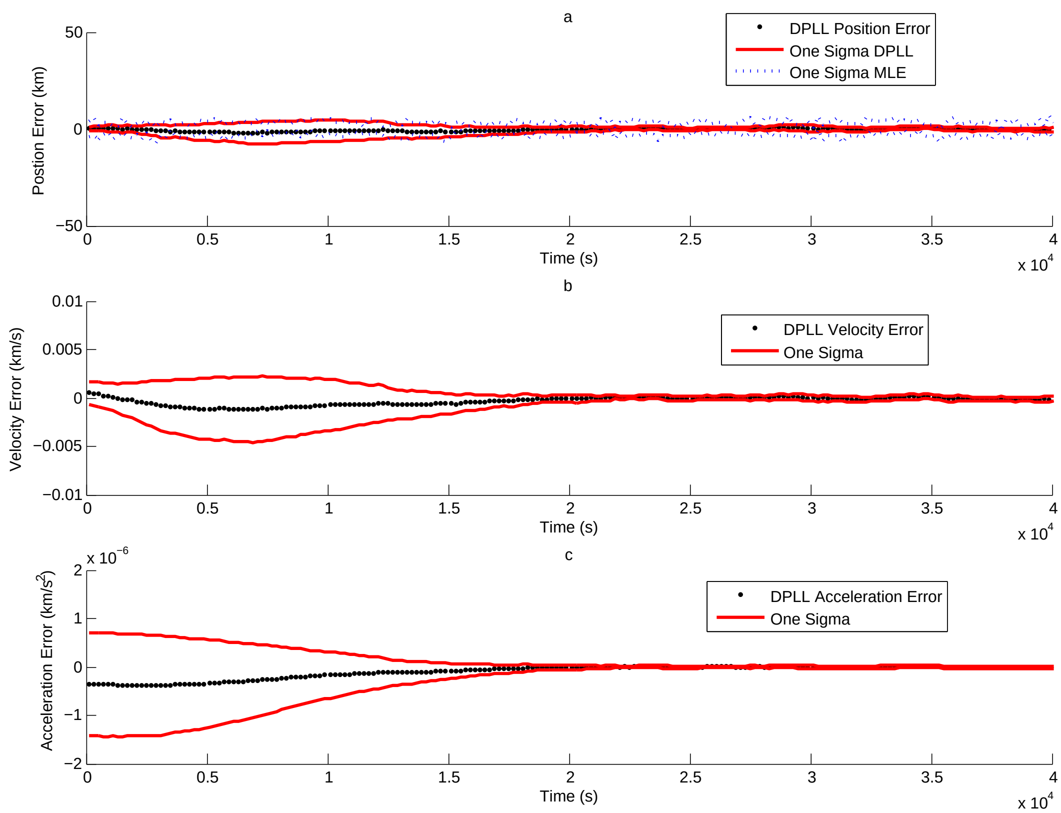

Figure 5.38: Cassini cruise trajectory phase tracking simulation results with DSN plus accelerometer initial condition error using B1821-24 with T = 200 seconds and $B_L = 0.00025$ Hz. One dimensional tracking results along LOS to pulsar.

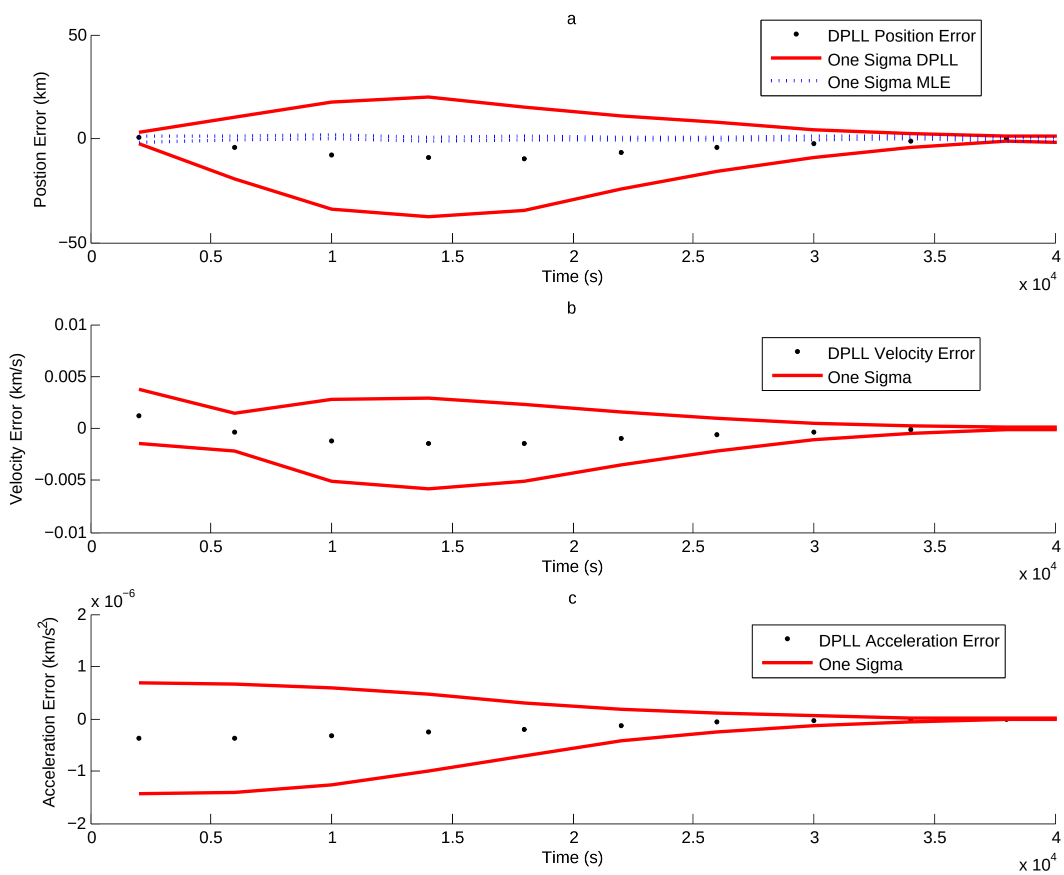

Figure 5.39: Cassini cruise trajectory phase tracking simulation results with DSN plus accelerometer initial condition error using B1821-24 with T = 4000 seconds and B_L = 0.00025 Hz. One dimensional tracking results along LOS to pulsar.

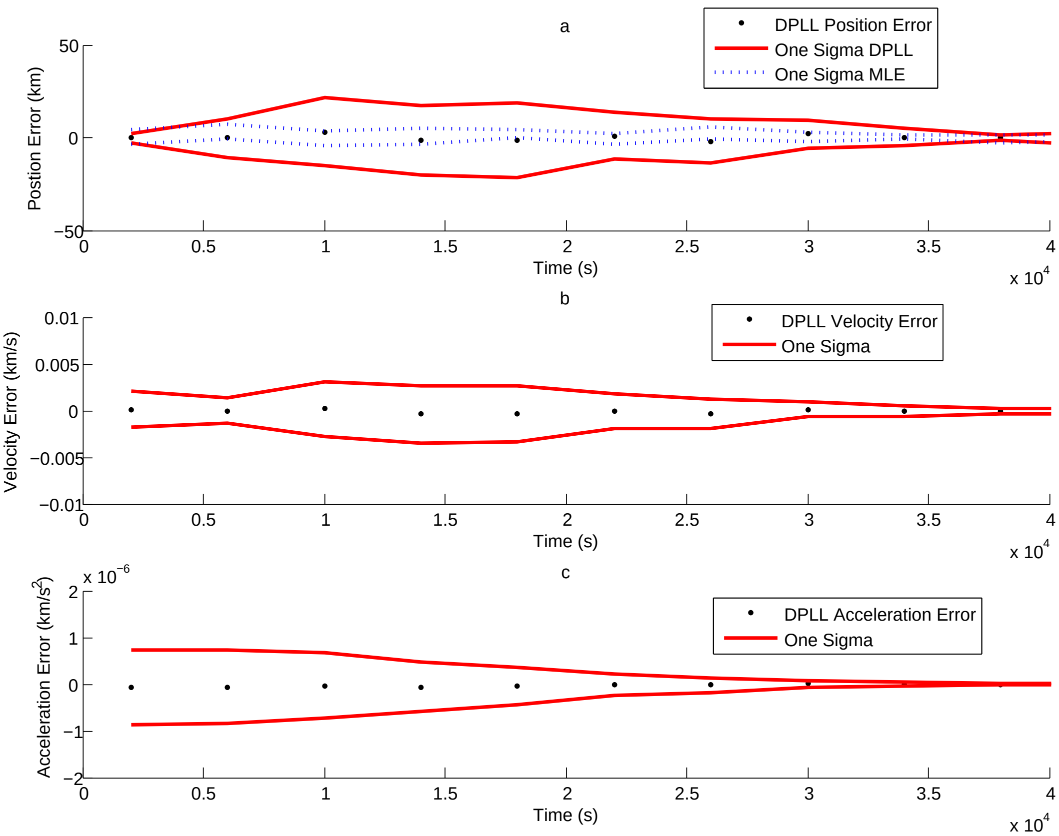

Figure 5.40: Cassini cruise trajectory phase tracking simulation results with DSN plus accelerometer initial condition error using B1937+21 with T = 4000 seconds and B_L = 0.00025 Hz. One dimensional tracking results along LOS to pulsar.

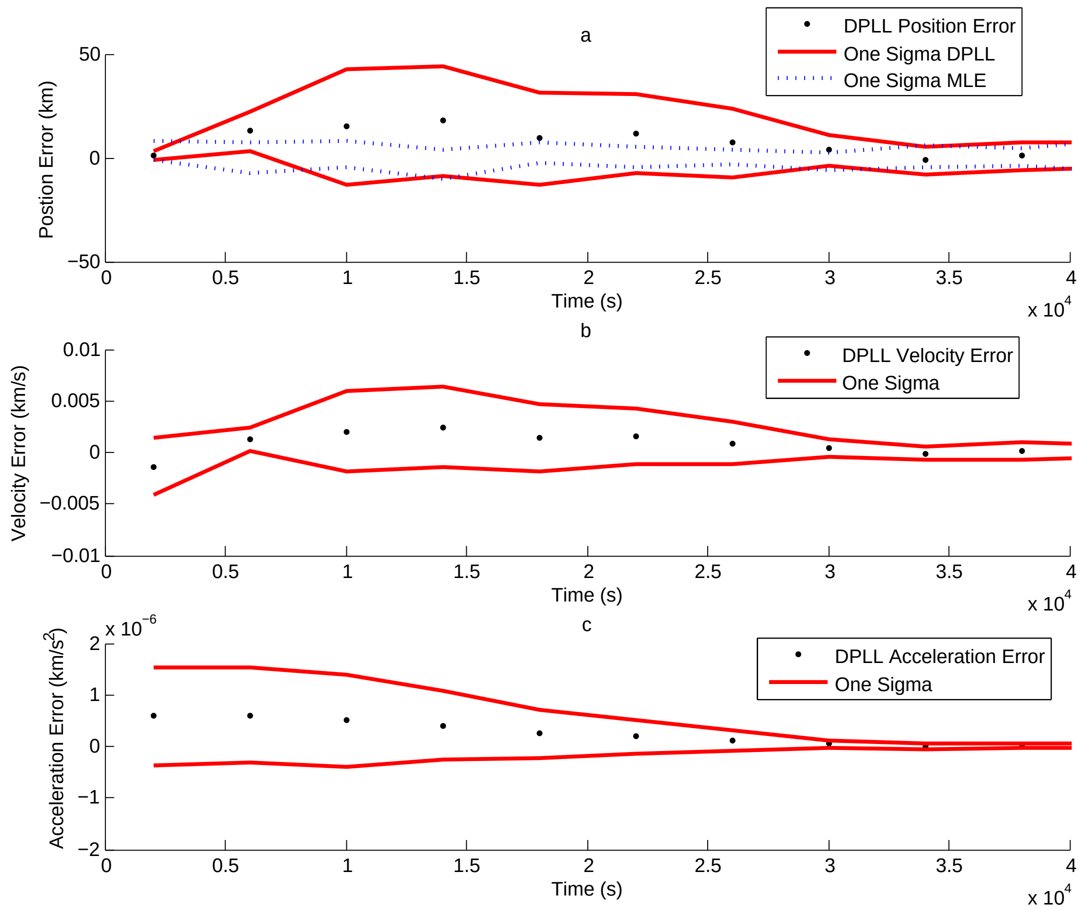

Figure 5.41: Cassini cruise trajectory phase tracking simulation results with DSN level initial condition error using J0218+4232 with T = 4000 seconds and $B_L = 0.00025$ Hz. One dimensional tracking results along LOS to pulsar.

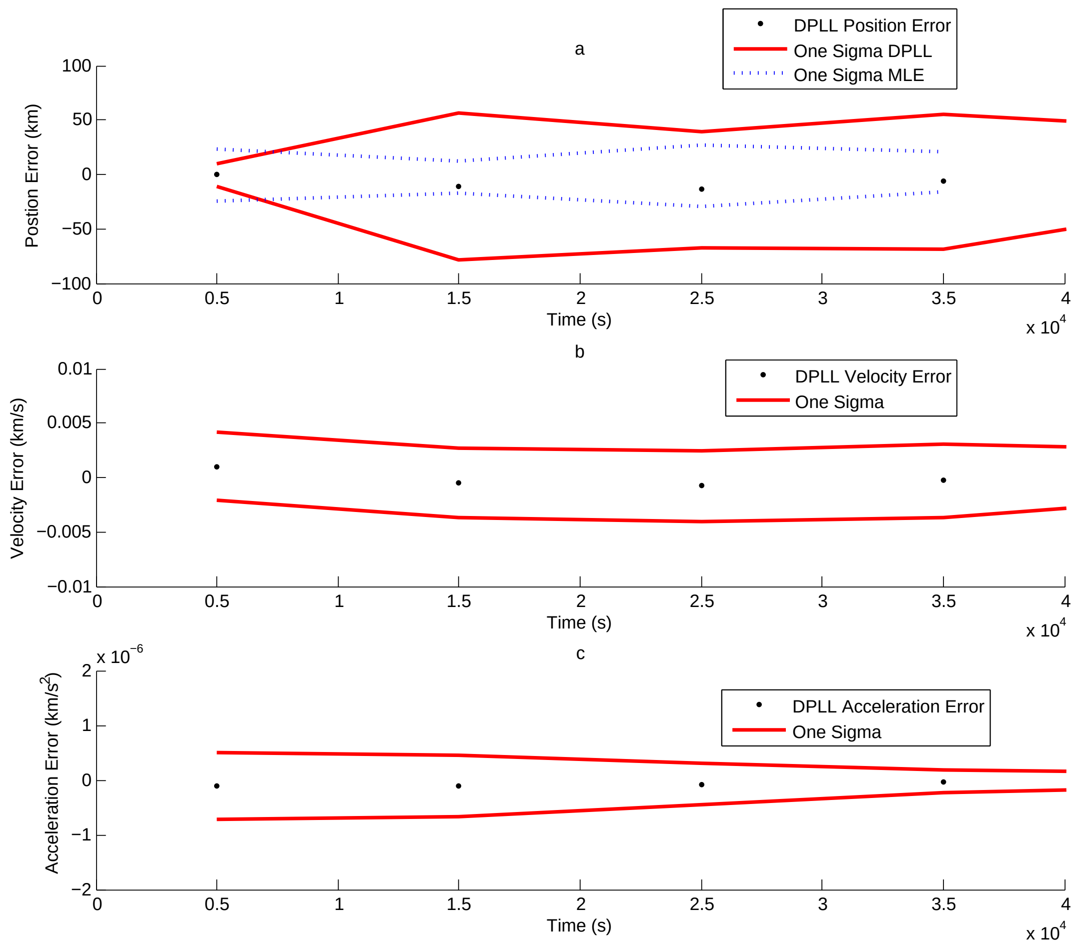

Figure 5.42: MSL cruise trajectory phase tracking simulation results with DSN plus accelerometer initial condition error using J0437-4715 with T = 10000 seconds and B_L = 0.00025 Hz. The simulated detector area is 5 m^2. One dimensional tracking results along LOS to pulsar.

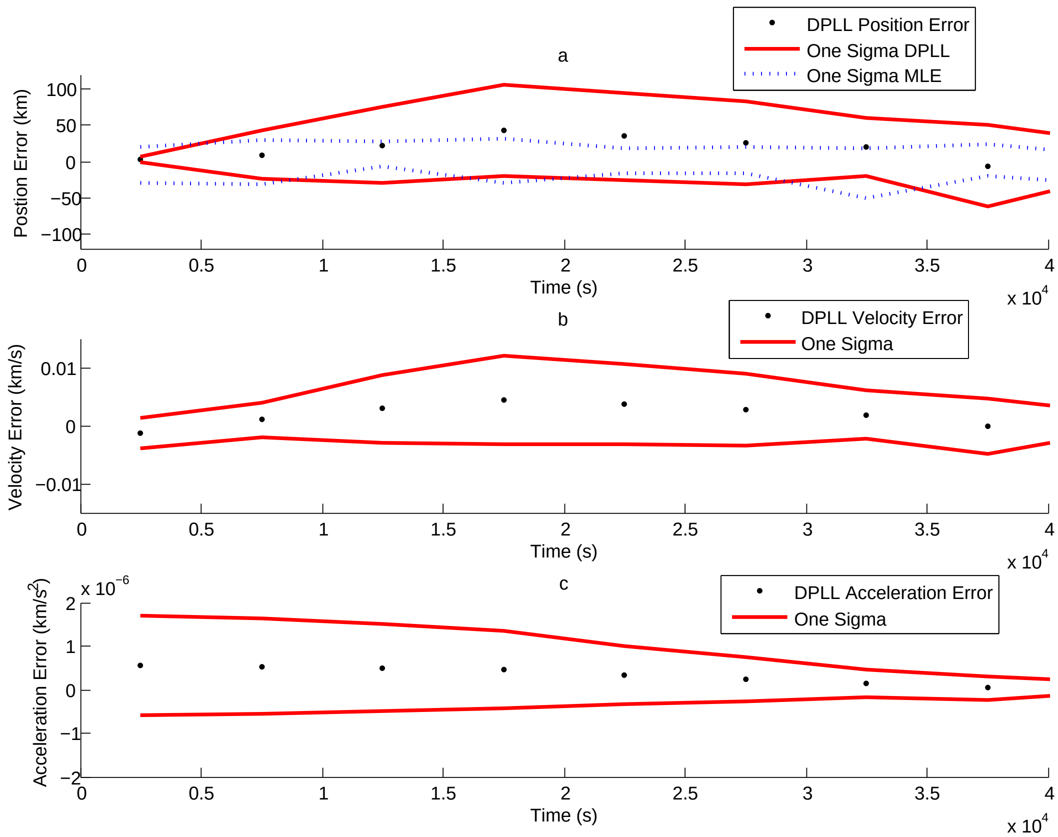

Figure 5.43: MSL cruise trajectory phase tracking simulation results with DSN plus accelerometer initial condition error using J0437-4715 with T = 5000 seconds and B_L = 0.00015 Hz. The simulated detector area is 10 m^2. One dimensional tracking results along LOS to pulsar.

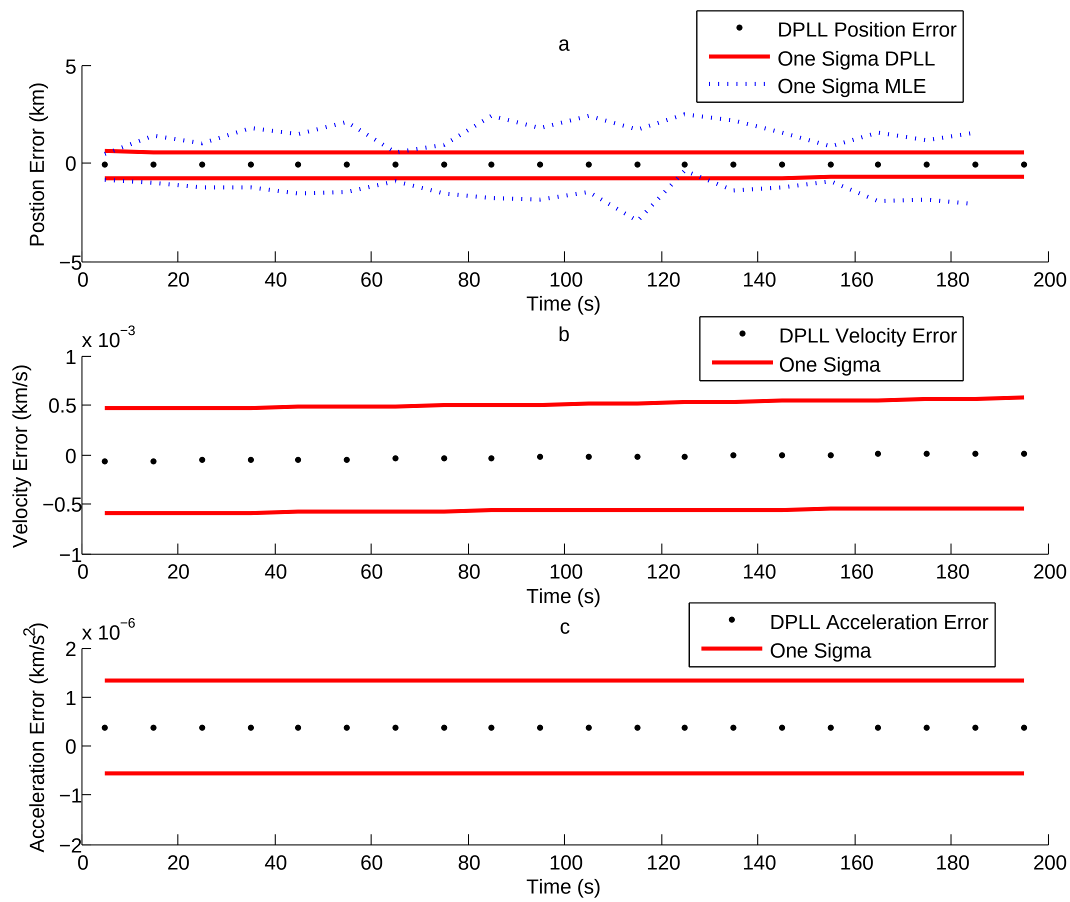

Figure 5.44: Cassini cruise trajectory phase tracking simulation results with DSN plus accelerometer initial condition error using the Crab Pulsar with T = 10 seconds and $B_L = 0.00025$ Hz. The simulated detector area is 1 m^2. One dimensional tracking results along LOS to pulsar.

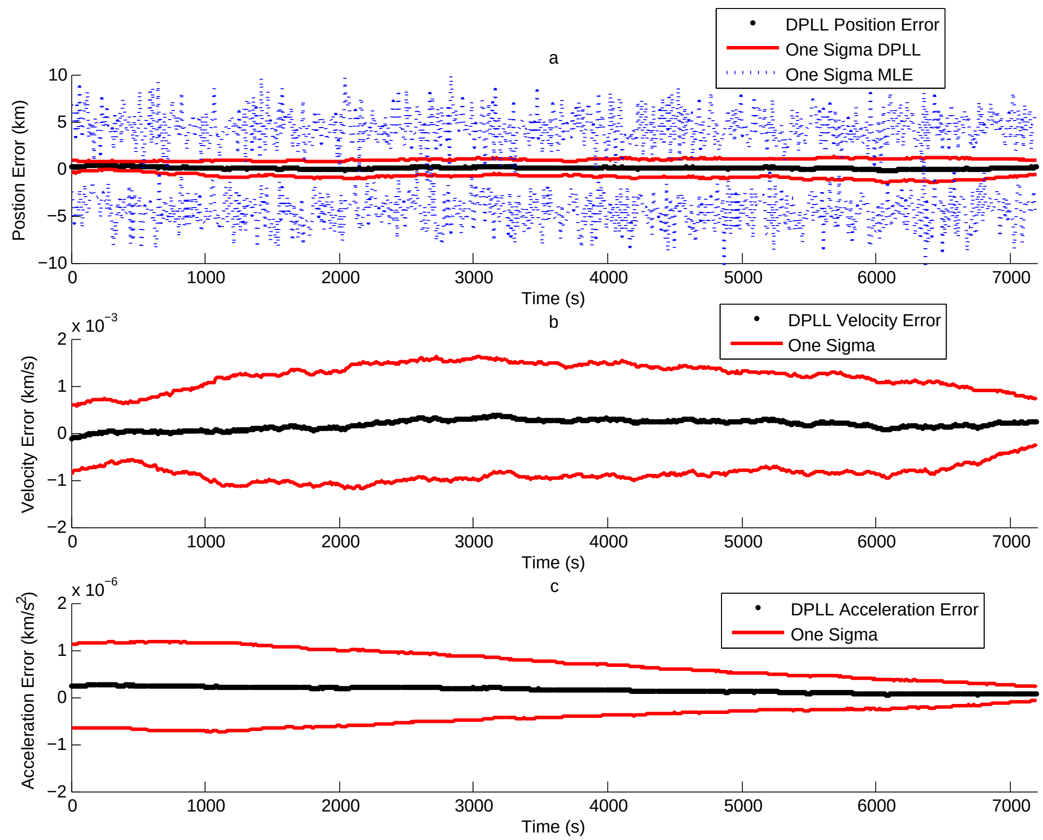

Figure 5.45: MSL cruise trajectory phase tracking simulation results with DSN plus accelerometer initial condition error using the Crab Pulsar with T = 10 seconds and $B_L = 0.0005$ Hz. The simulated detector area is 1000 cm^2. One dimensional tracking results along LOS to pulsar.

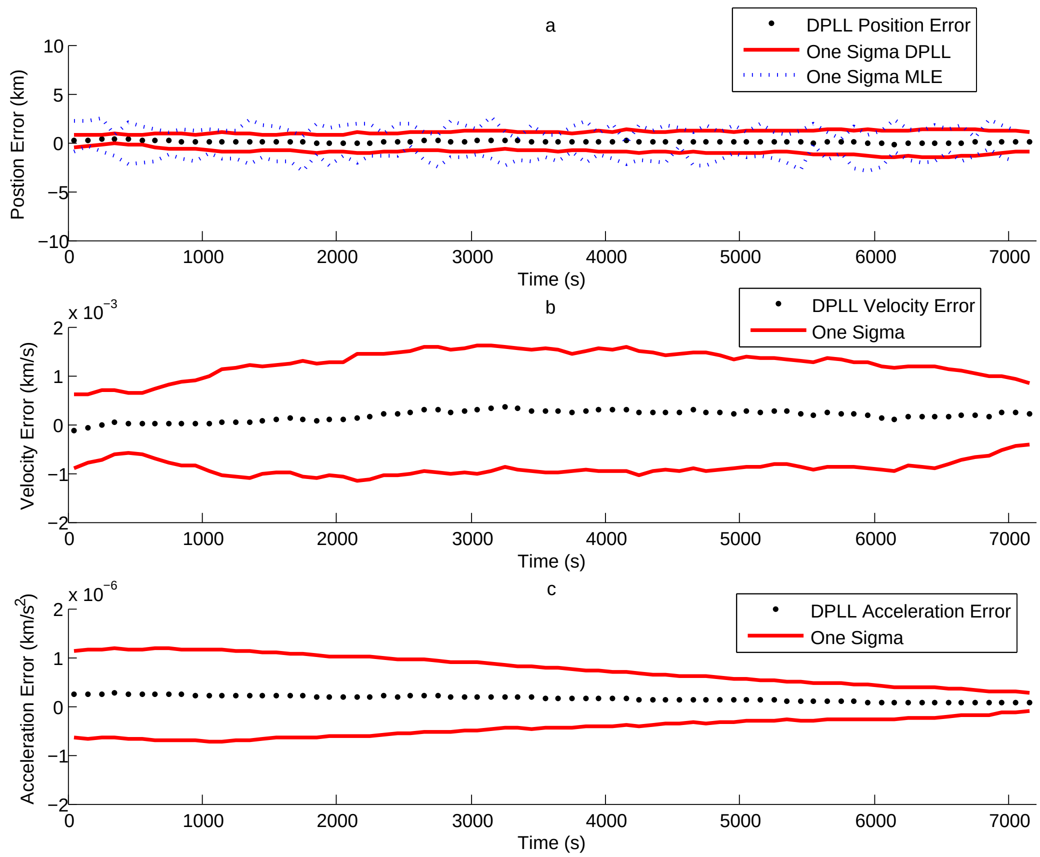

Figure 5.46: MSL cruise trajectory phase tracking simulation results with DSN plus accelerometer initial condition error using the Crab Pulsar with T = 100 seconds and $B_L = 0.0005$ Hz. The simulated detector area is 1000 cm^2. One dimensional tracking results along LOS to pulsar.

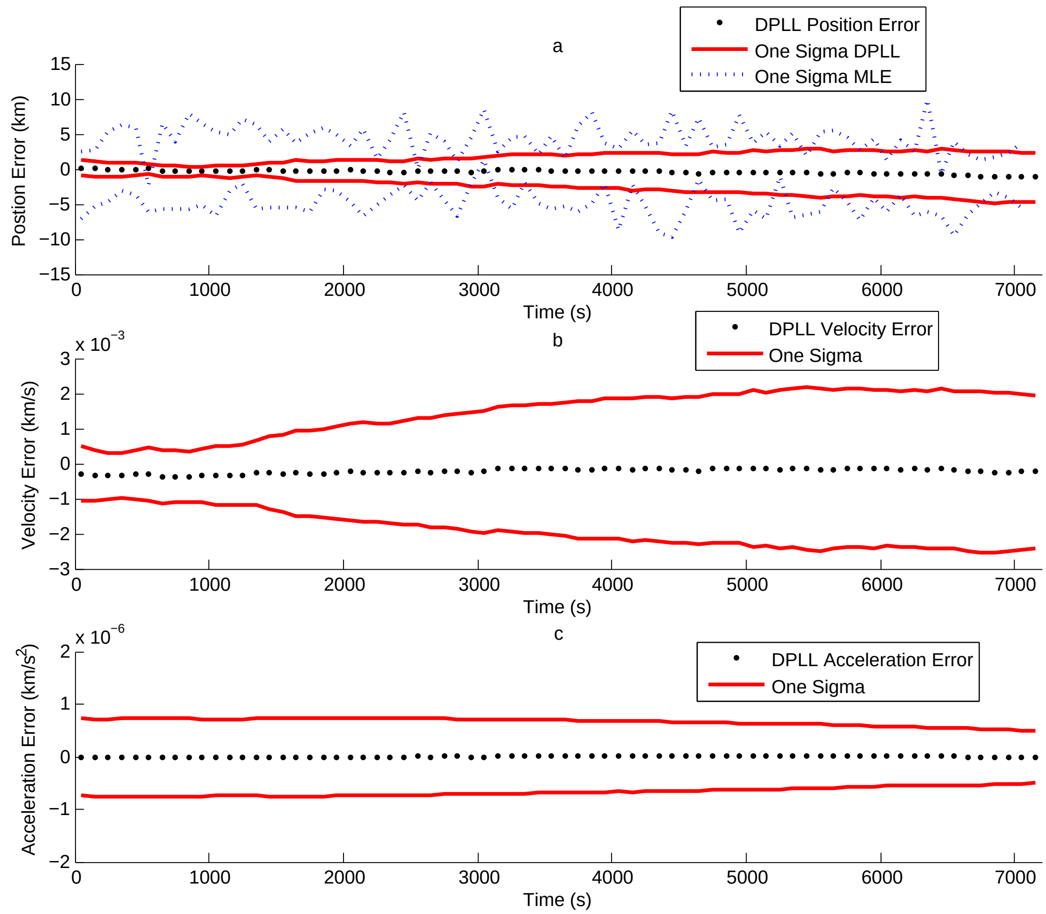

Figure 5.47: MSL cruise trajectory phase tracking simulation results with DSN plus accelerometer initial condition error using the Crab Pulsar with T = 100 seconds and $B_L = 0.00025$ Hz. The simulated detector area is 100 cm^2. One dimensional tracking results along LOS to pulsar.

Table 5.16: Cassini and MSL cruise trajectory simulation results for range of MSPs with initialization from DSN and an accelerometer and a detector area of 1 m^2. One dimensional tracking results along LOS to pulsar.

	B1821-24	B1821-24	B1937+21	J0218+4232
T, s	200	4000	4000	4000
B_L, Hz	0.00025	0.00025	0.00025	0.00025
CRLB, km	3.07	0.69	1.02	4.19
MSL Averaged MLE Position Error (km)	3.38	0.81	2.53	5.42
Cassini Averaged MLE Position Error (km)	3.40	0.90	2.95	5.64
MSL End Point RMS Position Error (km)	1.16	1.04	4.12	6.45
Cassini End Point RMS Position Error (km)	1.00	1.11	2.43	10.35
MSL End Point RMS Velocity Error (m/s)	0.24	0.09	0.41	0.63
Cassini End Point RMS Velocity Error (m/s)	0.28	0.11	0.22	1.00

are very promising for B1821-24, B1937+21, J0218+4232, and the Crab pulsar. The position errors from the phase tracking outputs are in the same 1 – 10 km range. The J0437-4715 signal again has the most difficulty with the phase tracking due to having the smallest SNR.

The MSL tracking results with PSR B1821-24 also demonstrate major improvements with the new phase tracking algorithm over the previous efforts at phase tracking pulsar signals outlined in Chapter 3. The previous algorithm could only track the PSR B1821-24 signal with detector areas of 25 to 100 m^2, with block sizes under 6 seconds, and the position errors were still on the order of 100 km. As seen in

Table 5.17: Cassini and MSL cruise trajectory simulation results for PSR J0437-4715 with initialization from DSN and an accelerometer. One dimensional tracking results along LOS to pulsar.

T, s	4000	10000	10000	10000	20000	5000
B_L, Hz	0.00025	0.0001	0.00015	0.00025	0.00015	0.00015
Area, m^2	5	5	5	5	5	10
CRLB, km	29.24	18.49	18.49	18.49	13.07	18.49
MSL Averaged MLE Position Error (km)	36.50	21.76	20.43	20.30	21.65	23.54
Cassini Averaged MLE Position Error (km)	36.45	21.55	21.38	20.29	21.67	21.07
MSL End Point RMS Position Error (km)	77.89	68.19	40.19	36.19	173.33	25.74
Cassini End Point RMS Position Error (km)	77.08	69.36	60.14	36.05	173.3	25.09
MSL End Point RMS Velocity Error (m/s)	7.11	3.97	2.48	2.26	3.85	1.87
Cassini End Point RMS Velocity Error (m/s)	7.06	4.01	3.16	2.24	3.84	1.97

this chapter, the new phase tracking algorithm is able to track the MSL trajectory with a detector area of 1 m^2 and a position error of 3.38 km.

Table 5.18: Results of the Crab Pulsar MSL and Cassini cruise trajectory simulations with initial condition errors consistent with a DSN handoff. One dimensional tracking results along LOS to pulsar.

T, s	10	10	10	100	100	100	1000
B_L, Hz	0.00025	0.00025	0.0005	0.00025	0.0005	0.00025	0.00025
Area, m^2	1	0.1	0.1	0.1	0.1	0.01	0.01
T_{obs}, s	200	7200	7200	7200	7200	7200	7200
CRLB, km	1.22	3.86	3.86	1.22	1.22	3.86	1.22
MSL Averaged MLE Position Error (km)	1.46	4.53	4.53	1.55	1.56	4.74	1.52
Cassini Averaged MLE Position Error (km)	1.47	4.54	4.54	1.55	1.56	4.58	1.43
MSL End Point RMS Position Error (km)	0.61	3.92	0.72	4.21	0.94	3.46	5.13
Cassini End Point RMS Position Error (km)	0.61	3.93	0.73	4.22	0.95	7.05	11.37
MSL End Point RMS Velocity Error (m/s)	0.53	2.59	0.51	2.66	0.64	2.08	2.23
Cassini End Point RMS Velocity Error (m/s)	0.53	2.59	0.52	2.66	0.64	4.59	5.03

5.5.2 Earth Orbit Tracking Performance

The phase tracking algorithm was also tested with various Earth orbits. The orbits tested include examples of ISS, GPS, and DirecTV satellite orbits to give a range of different altitudes and Earth orbital environments. As seen earlier, the pulsars considered have a range of different signal characteristics and SNRs. The Crab pulsar has a signal strength multiple orders of magnitude higher than the MSPs. PSR B1821-24 has the highest SNR of the MSPs considered, B1937+21 and J0218+4232 have similar SNRs, and J0437-4715 has the lowest as seen in Tables 5.1 and 5.2.

A wide range of detector areas and DPLL parameter choices were tested to get tracking results for the various pulsars. First a standard 1 m^2 detector was tested for all of the MSPs and each of the Earth orbits. For B1821-24 this was a feasible choice for the detector area for the DirecTV and GPS orbits, but a larger 2 m^2 detector area was needed for the ISS. With B1937+21 and J0218+4232 much larger detector areas were needed to track the DirecTV and GPS orbits and no feasible choice of detector area was found to work with the ISS orbit. The SNR for J0437-4715 was low enough that attempts to phase track this pulsar signal did not track at all for the Earth orbits considered. Smaller areas and shorter simulation times were considered for the Crab pulsar due to its significantly higher signal strength. All of these scenarios will be addressed in more detail in the following subsections.

The simulations were all performed with the initial condition errors corresponding to a hand-off from an Earth-based range tracking system, not necessarily the DSN like with the interplanetary examples. An accelerometer is again assumed available in order to provide the necessary initial acceleration accuracy for the DPLL to start tracking in-lock. The specific initial condition errors were: 10 m for position, 10 cm/s for velocity, and 1 mm/s^2. The simulations were idealized to assume that there are no interruptions from occlusions of the pulsars during the phase tracking. This is obviously not possible in real Earth orbit situations due to blockage of the pulsar by the Earth and will need to be addressed in further study, but for an initial analysis of the feasibility of the phase tracking algorithm for various combinations of pulsar signals and Earth orbit dynamics it is sufficient. As with the constant acceleration and interplanetary trajectory phase tracking simulations, for each scenario ten runs are performed using different random number seeds and then the results are averaged.

The DPLL parameters chosen for tracking the various pulsars are included in Table 5.19, Table 5.20, and Table 5.21 for B1821-24, B1937+21 and J0218+4232, and the Crab pulsar, respectively. The DPLL update time T was chosen for each pulsar by consulting the empirical MLE versus CRLB plots from Chapter 4. Many factors and experimentation went into the process of settling on these choices of DPLL parameters that lead lead to tracking for each pulsar and orbit. Various combinations of loop bandwidth and detector areas were simulated. Some sets of parameters led to lock being lost early in the orbit, some failed to track at all, and there was not much room to adjust the parameters for better tracking accuracy. The DPLL noise bandwidth, B_L, was chosen in each case using a trade-off between being large enough to account for dynamic stress errors from the Earth orbit physics and being small enough for better steady state tracking error. The damping ratio was again chosen to yield the standard underdamped response with $\zeta = \frac{\sqrt{2}}{2}$. The values of the DPLL gains once again come from the tables in [107] for different choices of the $B_L T$ product.

Table 5.19: Settings used for the parameters of the third-order DPLL for the Earth orbit simulations with PSR B1821-24.

Orbit Type	DirecTV	GPS	ISS	ISS
T, s	150	150	100	120
B_L, Hz	0.005	0.005	0.05	0.05
ζ	0.707	0.707	0.707	0.707
K_1	0.7156	0.7156	0.9798	0.9870
K_2	0.3463	0.3463	0.9267	0.9573
K_3	0.0791	0.0791	0.6760	0.7635

Table 5.20: Settings used for the parameters of the third-order DPLL for the Earth orbit simulations with B1937+21 and J0218+4232.

Orbit Type	DirecTV	GPS
T, s	700	500
B_L, Hz	0.05	0.05
ζ	0.707	0.707
K_1	0.9592	0.9297
K_2	0.8485	0.7544
K_3	0.5151	0.3802

Table 5.21: Settings used for the parameters of the third-order DPLL for the Earth orbit simulations with the Crab Pulsar.

Orbit Type	DirecTV	DirecTV	GPS	GPS	ISS	ISS
T, s	10	100	10	100	10	100
B_L, Hz	0.005	0.005	0.005	0.005	0.05	0.05
ζ	0.707	0.707	0.707	0.707	0.707	0.707
K_1	0.1174	0.6085	0.1174	0.6085	0.6085	0.9798
K_2	0.0064	0.2294	0.0064	0.2294	0.2294	0.9267
K_3	0.0001	0.0384	0.0001	0.2294	0.0384	0.6760

5.5.2.1 Dynamic Stress of Earth Orbits

The Earth orbits have different levels of dynamic stress proportional to their altitudes. This will lead to the phase tracking problem being more difficult for the lower altitude ISS orbit than the higher altitude GPS and DirecTV orbits. Pulsars with lower flux, and thus longer necessary block times, will be affected more due to the buildup up in dynamic stress caused by the difference in the orbit from a constant acceleration trajectory over time.

Table 5.22 contains information capturing the dynamic stress for the various Earth orbits that will be simulated. The values for the interplanetary MSL and Cassini trajectories of the previous section and the cislunar trajectory of the next section are included for comparison. Since the internal phase dynamic model for the MLE is a second-order Taylor polynomial that corresponds to a constant acceleration parabolic trajectory, the amount of change in the acceleration over the orbit is a way to capture the dynamic stress. This is represented by the maximum jerk in the range to the pulsar over the observation window. This jerk value is what is compared in Table 5.22. It can be seen that the ISS orbit has the highest maximum range jerk by two orders of magnitude over the GPS orbit. The GPS and DirecTV orbit have similar levels of dynamic stress with the GPS slightly higher as expected.

When comparing the Earth orbit examples to the other trajectories it can be seen that the cislunar orbit has two orders of magnitude lower maximum range jerk than the DirecTV orbit, the MSL dynamic stress is one order of magnitude smaller than the cislunar trajectory, and the Cassini trajectory has the smallest by far at five orders of magnitude smaller than the MSL. The consequences of these differences in levels of dynamic stress will be seen in the range of effectiveness and difficulties with the phase tracking algorithm with the various Earth orbits in the simulations presented in the rest of this section.

Table 5.22: Levels of dynamic stress for the various orbits simulated in this chapter.

Orbit Type	Maximum Range Jerk, mm/s^3
ISS	8.021
GPS	0.0812
DirecTV	0.0156
Cislunar	0.000127
MSL	0.0000137
Cassini	0.000000000691

A visual comparison of the different levels of dynamic stress can be seen by comparing a few of the range acceleration plots for the orbits and trajectories considered. Figures 5.48 - 5.50 contain plots of the range acceleration of the GPS orbit,

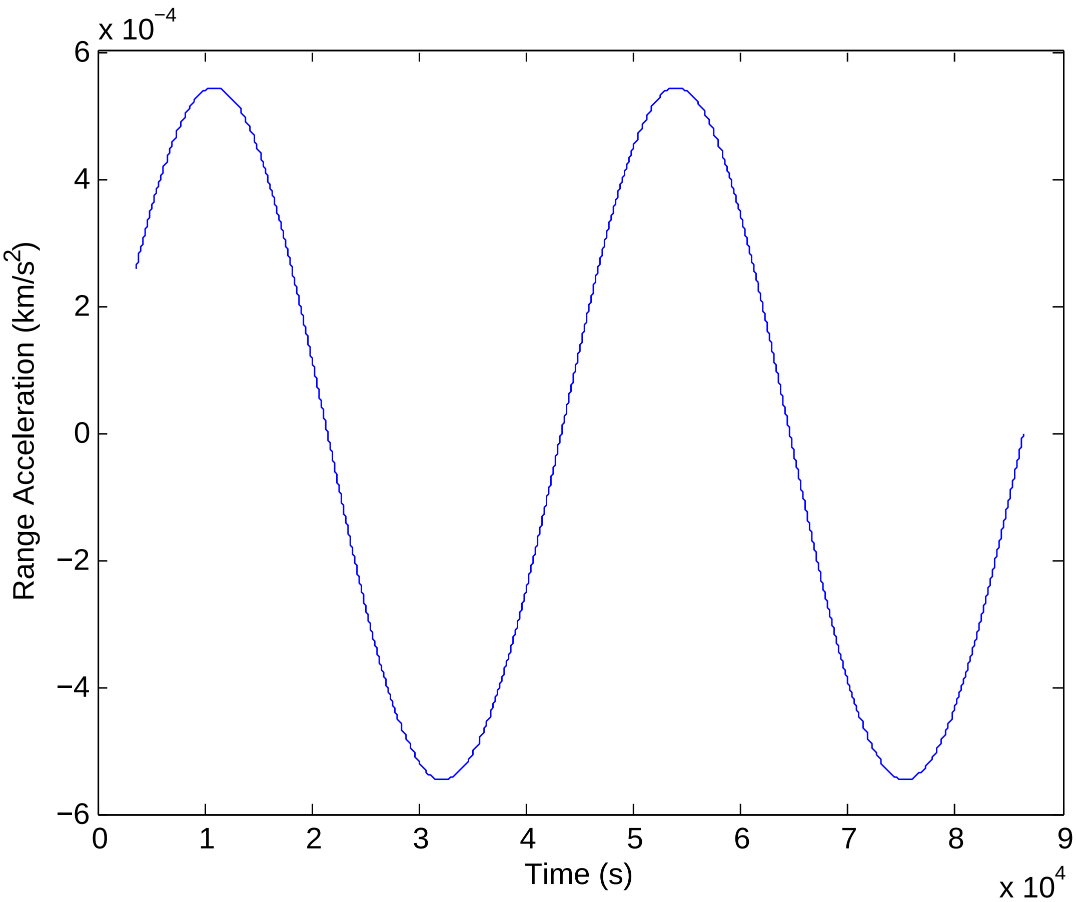

Figure 5.48: The range acceleration for the GPS orbit over the observation window for the phase tracking simulations.

cislunar trajectory, and MSL trajectory, respectively, over the observation windows for the phase tracking simulations. Figure 5.49 and Figure 5.50 are plotted with similar y-axis scaling in order to demonstrate that the MSL trajectory range acceleration is closer to a line with slope zero that corresponds to being closer to constant acceleration and thus lower dynamic stress.

A diagram illustrating the different detector areas necessary to phase track each pulsar with the different dynamic stress conditions represented by the different

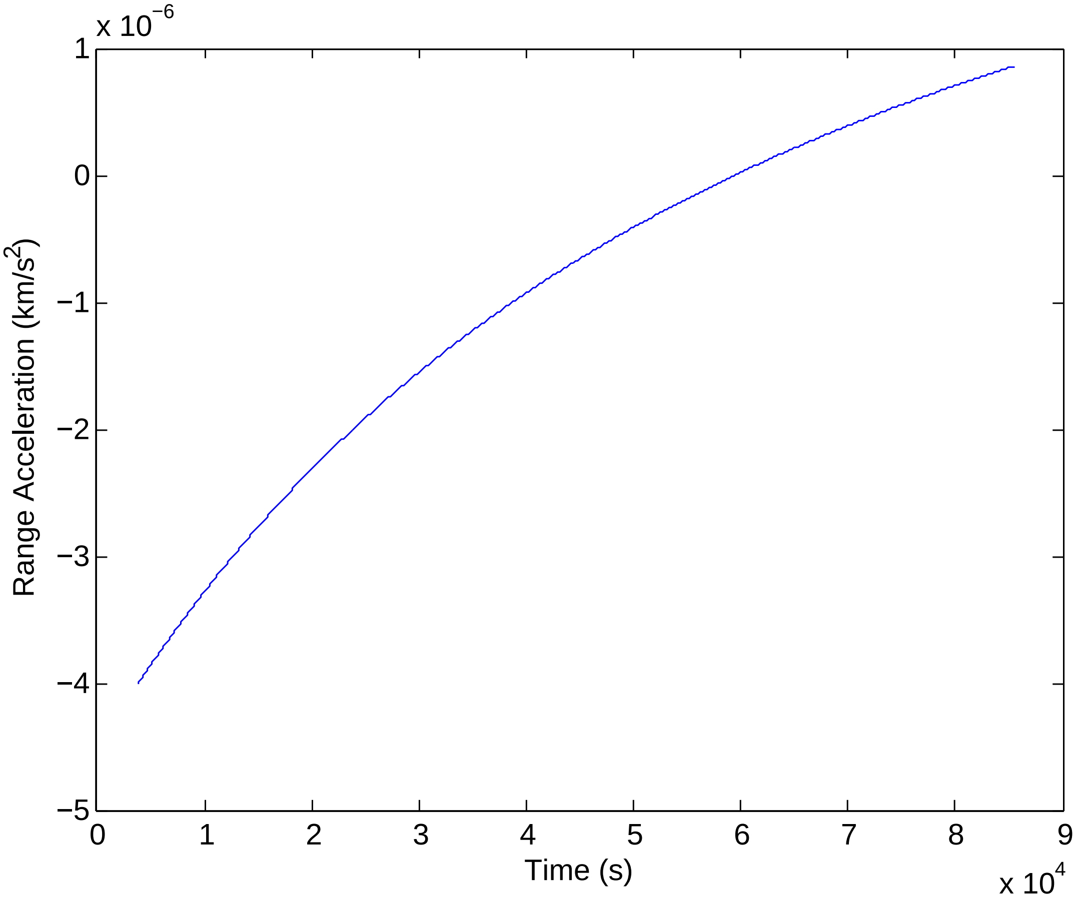

Figure 5.49: The range acceleration for the cislunar trajectory over the observation window for the phase tracking simulations.

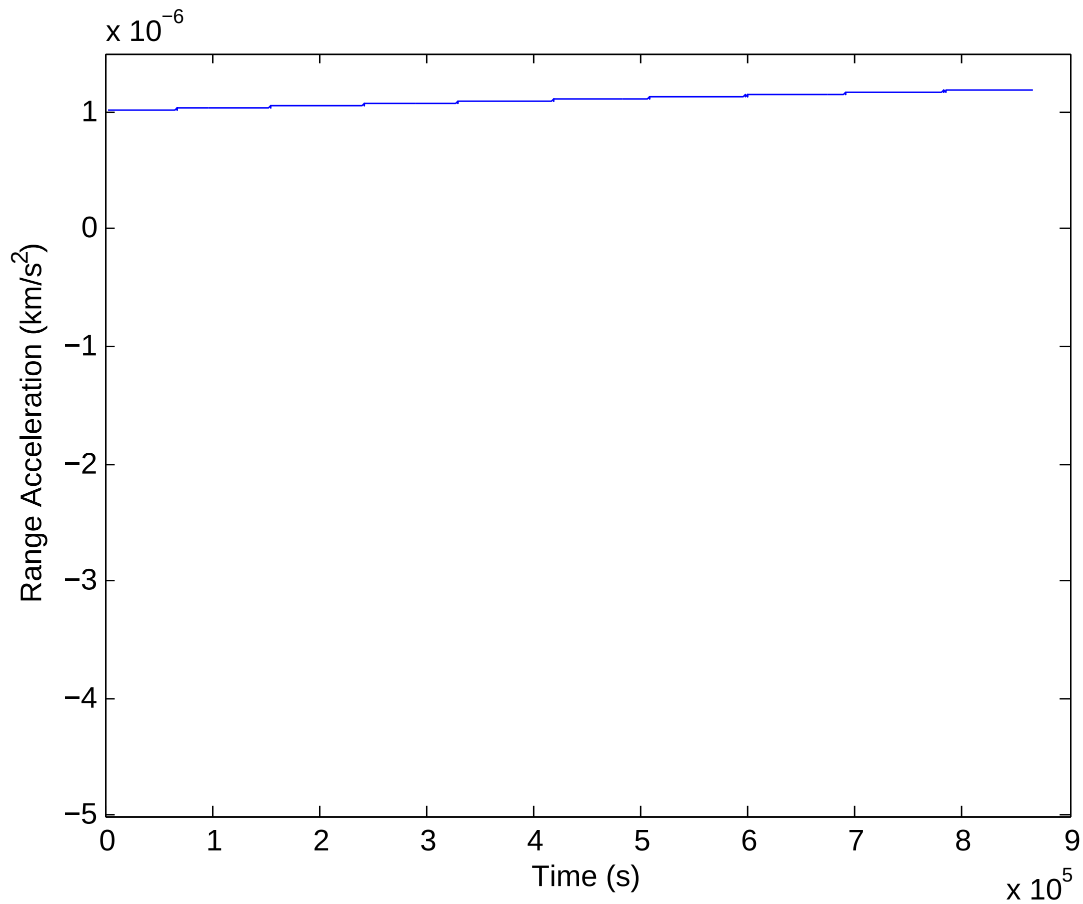

Figure 5.50: The range acceleration for the MSL trajectory over the observation window for the phase tracking simulations.

orbits is included in Figure 5.51. This plot is to help visualize the performance conditions where the phase tracking algorithm works well. The plot contains plotted points for each pulsar, represented by different colors, that correspond to each detector area and orbit combination that allow for phase tracking the signal.

PSR J0437+4715 was only shown to be able to phase track the Cassini and MSL orbits with an area of 5 m^2. For the ISS orbit, only B1821-24 with an area of 2 m^2 and the Crab pulsar with an area of at least 10000 cm^2, were able to acquire a phase tracking solution. With both B1937+21 and J0218+4232, phase tracking was possible with detector areas of: 10 m^2 for the GPS orbit, 8 m^2 for the DirecTV orbit, and 1 m^2 for the cislunar, MSL, and Cassini trajectories.

5.5.2.2 Earth Orbit Phase Tracking Results with PSR B1821-24

Earth orbit phase tracking simulations were performed using the PSR B1821-24 signal. For the DirecTV and GPS orbit tracking simulations a detector area of 1 m^2 was used. For the ISS orbit tracking simulations a detector area of 2 m^2 was needed to achieve similar position and velocity error levels with PSR B1821-24. With simulations that attempted to use a 1 m^2 detector with the ISS orbit there consistently was loss-of-lock before the completion of the simulation window. The results for the B1821-24 tracking Earth orbit simulations are summarized in Table 5.23. Metrics to illustrate the phase tracking results include: the averaged MLE position error, the DPLL end point RMS position and velocity errors, and the average DPLL position and velocity errors over the simulation time. The CRLB is

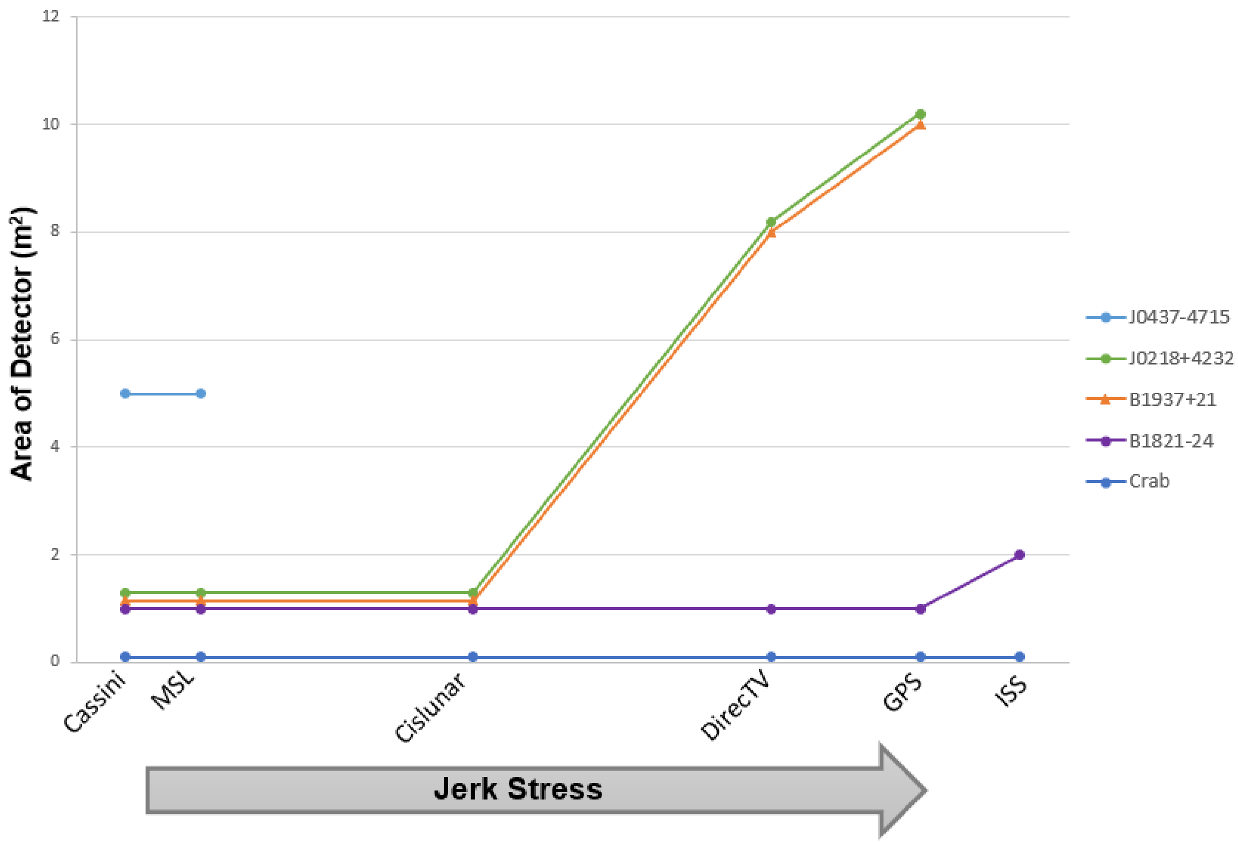

Figure 5.51: Qualitative representation of the detector areas needed to phase track each pulsar signal for the different dynamic stress conditions of the orbits.

included to provide a comparison to the theoretical limit achievable by the MLE for position estimation.

The DPLL parameter choices used in the B1821-24 simulations in this section that led to the best Earth orbit tracking results are included in Table 5.19. For the DirecTV and GPS orbits a loop noise bandwidth of 0.005 Hz was used, while for the ISS orbit $B_L = 0.05$ Hz. The difference was required due to the dynamic stress levels. These are both much larger than the loop noise bandwidths that were allowable for both the interplanetary and constant acceleration trajectories of the previous sections. The block sizes used were 150 seconds for the DirecTV and GPS orbits and both 100 and 120 seconds with the ISS orbit. These were chosen to correspond with the 1 and 2 m^2 detectors. Two different block length times were included in simulations to demonstrate a small portion of the different parameter choices considered to find the DPLL settings that yielded the best phase tracking results in each orbit scenario.

For the higher altitude orbits, the DirecTV and GPS, the same DPLL parameters were used to compare the B1821-24 phase tracking results. A block update time of T = 150 seconds was used along with a loop noise bandwidth of $B_L = 0.005$ Hz and a detector area of 1 m^2. For the ISS orbit, the higher dynamic stress of the lower orbit altitude required a larger loop noise bandwidth and a larger 2 m^2 detector area. Simulations were performed with $B_L = 0.05$ Hz and two choices of block update time, 100 and 120 seconds. The phase tracking simulation results for B1821-24 are compared in Figure 5.52 and Figure 5.53 for the DirecTV and GPS orbits, respectively. The ISS tracking results for the different block update time used with B1821-24 are included in Figure 5.54 and Figure 5.55 for T = 100 seconds and T = 120 seconds, respectively. Each figure contains three subplots detailing the position, velocity, and acceleration errors over the simulation time. The DPLL and MLE outputs are included in the position error plot.

Figure 5.52 includes the phase tracking results of the B1821-24 signal with the DirecTV orbit. The block update time is 150 seconds, the loop noise bandwidth is 0.005 Hz, and the detector area is 1 m^2. It can be seen that the position, velocity, and acceleration errors stay bounded for the entire simulation time. This demonstrates that the algorithm is tracking the phase and staying consistently in-lock. In the position error plot, the MLE error level is similar to the DPLL output error level.

The B1821-24 phase tracking results for the GPS orbit are included in Figure 5.53. For this simulation the DPLL parameters were kept the same as for the DirecTV orbit for comparison. The block update time is 150 seconds, the loop noise bandwidth is 0.005 Hz, and the detector area is 1 m^2. It can be seen that the tracking is achieving bounded position, velocity, and acceleration errors. The performance levels and shapes of the error plots are similar to those seen with the DirecTV orbit. Again the MLE error is similar to the DPLL error level is the position error plot.Oscillations start to show up in the velocity error plot and most notably in the acceleration error plot. These oscillations seem to have a period similar to the GPS orbital period. These oscillations were unable to be removed through DPLL parameter choices while also attempting to optimize the tracking performance and account for the dynamic stress.

Figure 5.54 contains the phase tracking results of the B1821-24 signal with the ISS orbit, a block update time of 100 seconds, a loop noise bandwidth of 0.05 Hz, and a detector area of 2 m^2. Figure 5.55 illustrates the ISS phase tracking results for B1821-24 with the block update time changed to 120 seconds. The loop noise bandwidth remained 0.05 Hz and the detector area was kept 2 m^2. Both of these figures demonstrate the ability to track within bounds the navigational state of the ISS orbit using the B1821-24 signal. The errors are higher than with the DirecTV and GPS orbit examples. This is due to the higher dynamic stress and the increase in the loop noise bandwidth from 0.005 Hz to 0.05 Hz. Even with double the detector area the tracking has higher errors. The MLE is outperforming the DPLL in position error, and this is slightly more pronounced in the scenario with T = 120 seconds. There are large oscillations apparent in the position, velocity, and acceleration error plots with periodicity similar to the ISS orbital period. The position error oscillation amplitude is larger in the scenario with T = 120 seconds.

The Earth orbit simulation results with PSR B1821-24 are summarized in Table 5.23. The average MLE position error for each of the orbit scenarios is reasonably close to the theoretical limit of the CRLB. Comparing the DirecTV and GPS orbit results, it can be seen that the position and velocity errors are similar, but slightly larger for the GPS orbit as expected due to dynamic stress. The DPLL RMS end point position and velocity errors are 2.47 km and 6.25 m/s and 3.49 km and 8.54 m/s for the DirecTV and GPS orbits, respectively.

For both scenarios with the ISS orbit the position and velocity errors are much larger. For example the DPLL RMS end point position and velocity errors are 18.61 km and 103.85 m/s for the scenario with T = 100 seconds. For these ISS results, the position error is high from the DPLL output, but the individual MLE results are usable as long as the phase-locked loop remains in lock. The average MLE position error is 3.61 km for the scenario with T = 100 seconds. This is better than the MLE results for the DirecTV and GPS simulations due to the larger detector area, but worse than the DPLL position error results for the DirecTV and GPS. Of the MSPs considered, B1821-24 was the only signal trackable on the ISS orbit. The Crab pulsar signal also works because its signal strength is a large outlier compared to the MSPs.

Table 5.23: Earth orbit simulation results for PSR B1821-24 with initial condition errors consistent with a DSN handoff and an accelerometer. One dimensional tracking results along LOS to pulsar.

Orbit	DirecTV	GPS	ISS	ISS
Area (m^2)	1	1	2	2
T, s	150	150	100	120
B_L, Hz	0.005	0.005	0.05	0.05
CRLB, km	3.55	3.55	3.07	2.80
Averaged MLE Position Error (km)	3.93	3.98	3.61	3.54
End Point RMS Position Error (km)	2.47	3.49	18.61	20.76
Averaged Position Error (km)	4.82	5.33	13.67	16.37
End Point RMS Velocity Error (m/s)	6.25	8.54	103.85	83.72
Averaged Velocity Error (m/s)	11.88	14.12	74.04	70.30

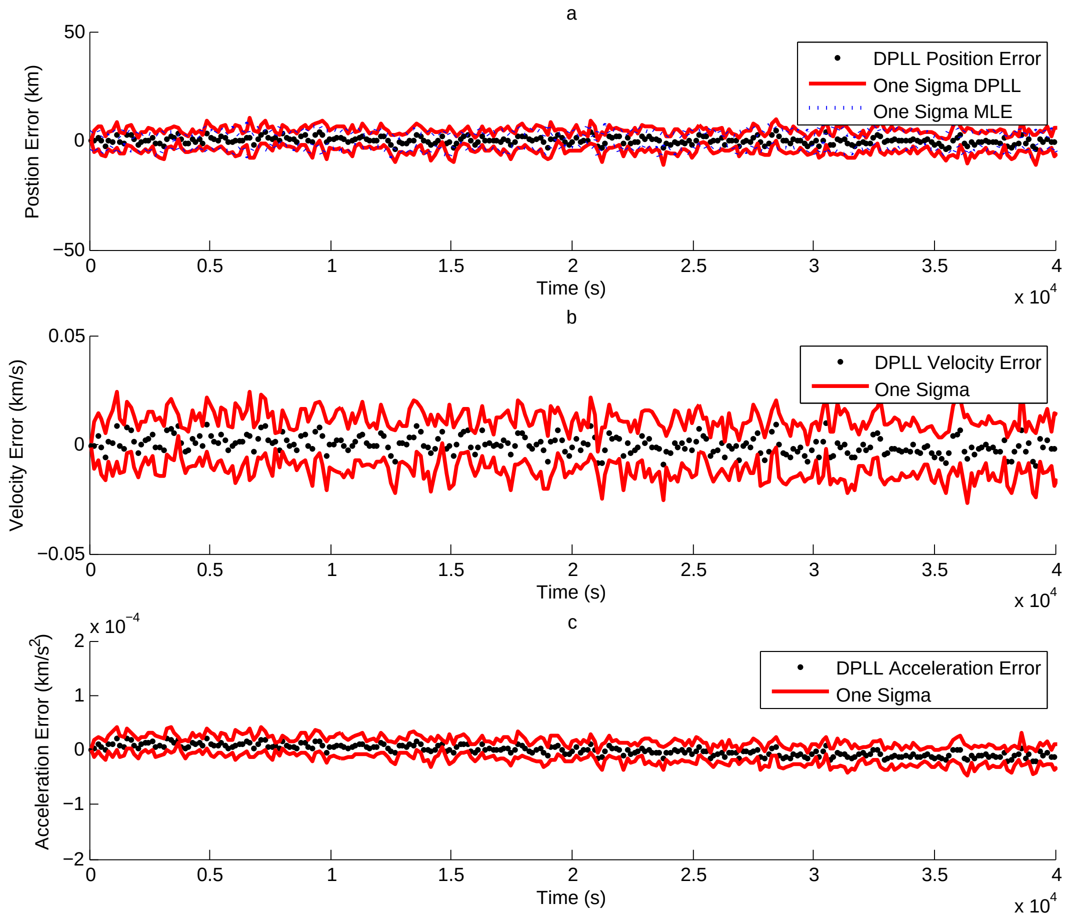

Figure 5.52: DirecTV satellite orbit phase tracking simulation results for PSR B1821-24 with T = 150 seconds and B_L = 0.005 Hz. One dimensional tracking results along LOS to pulsar.

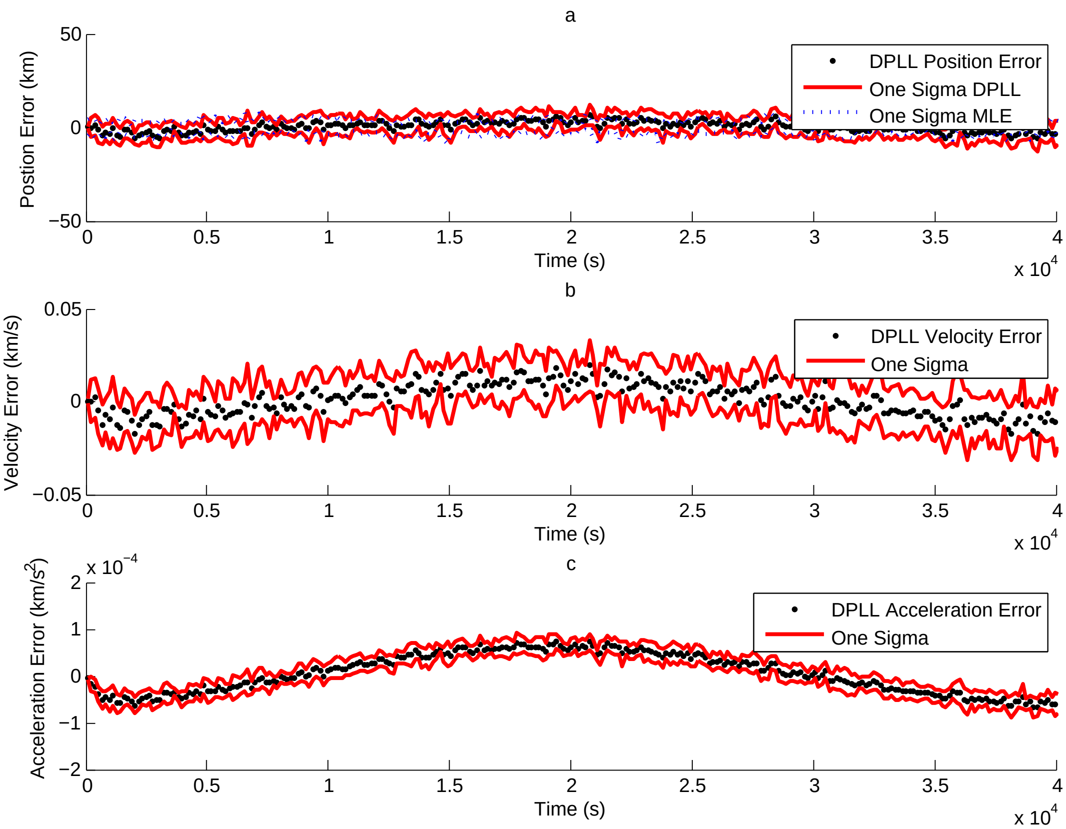

Figure 5.53: GPS satellite orbit phase tracking simulation results for PSR B1821-24 with T = 150 seconds and B_L = 0.005 Hz. One dimensional tracking results along LOS to pulsar.

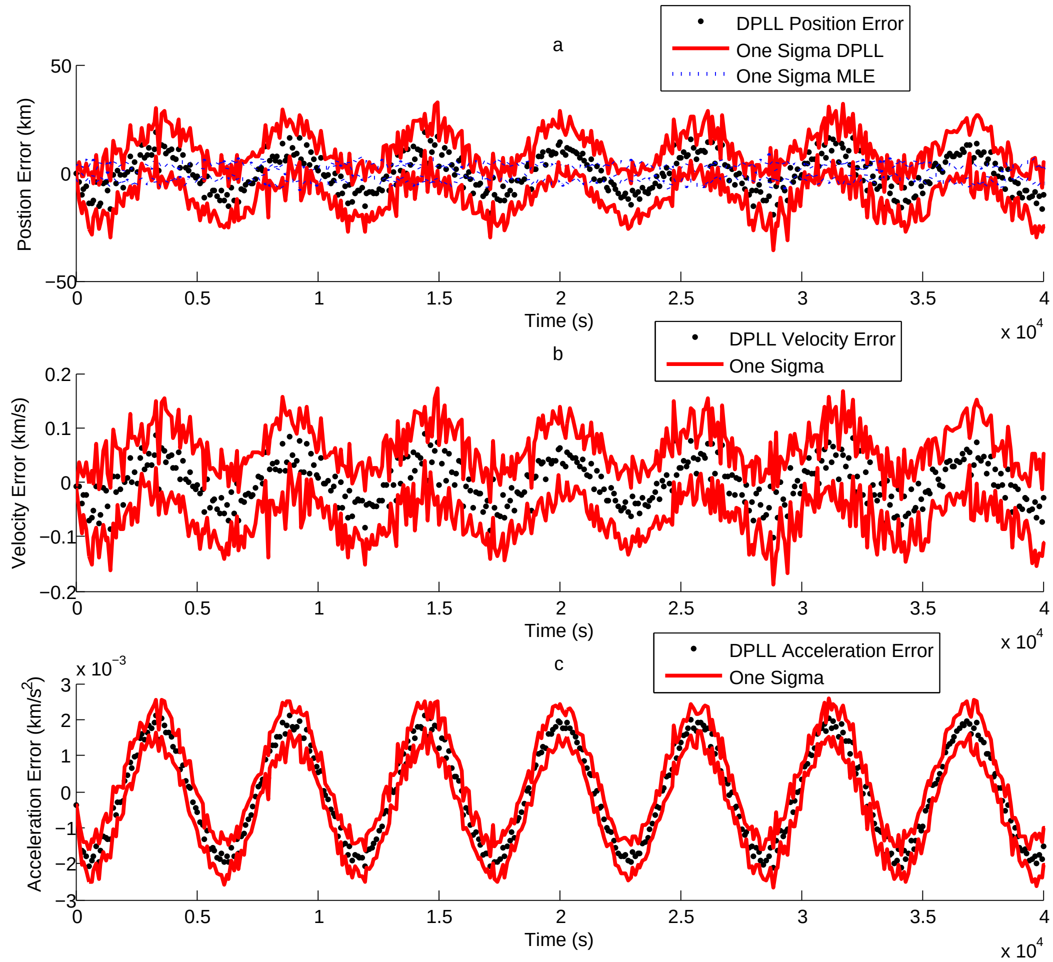

Figure 5.54: ISS orbit phase tracking simulation results for PSR B1821-24 with T = 100 seconds, B_L = 0.05 Hz, and a detector area of 2 m^2. One dimensional tracking results along LOS to pulsar.

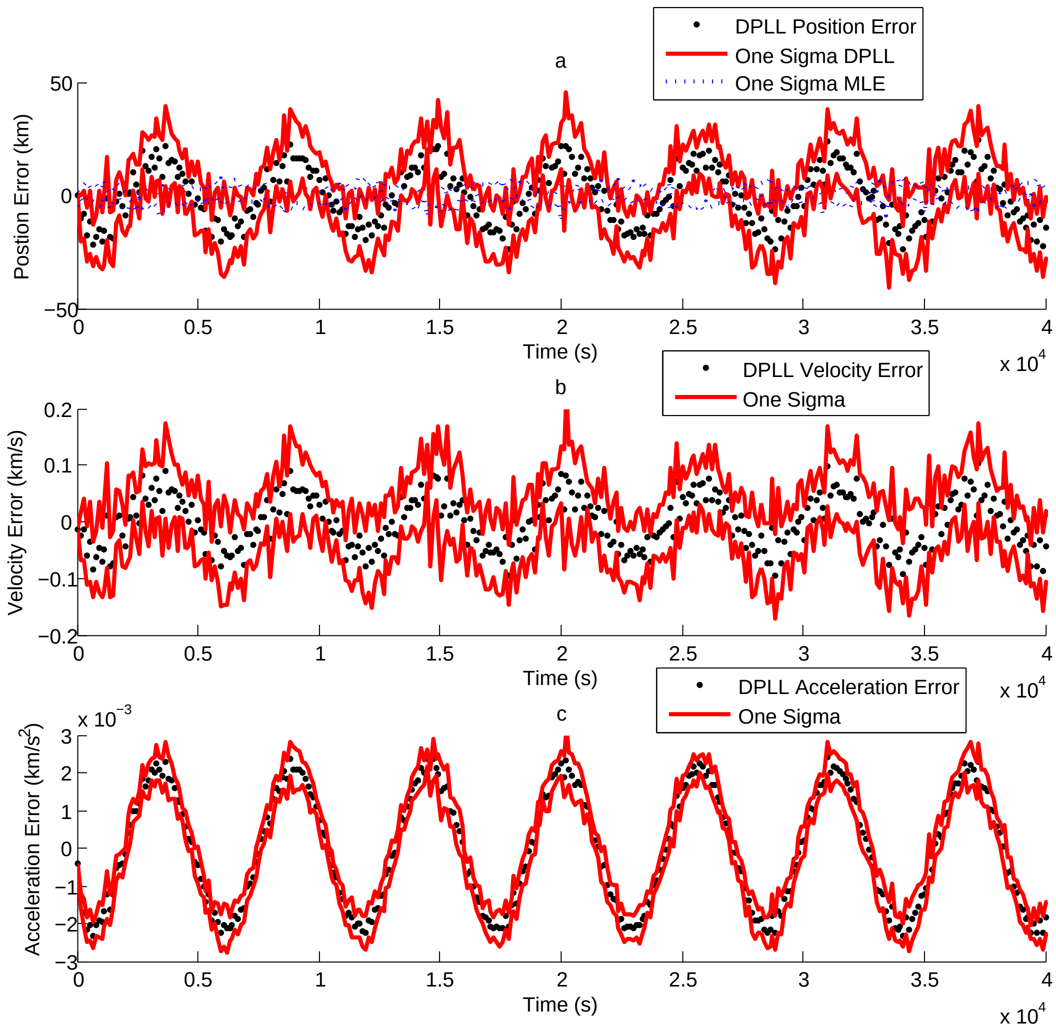

Figure 5.55: ISS orbit phase tracking simulation results for PSR B1821-24 with T = 120 seconds, B_L = 0.05 Hz, and a detector area of 2 m^2. One dimensional tracking results along LOS to pulsar.

5.5.2.3 Earth Orbit Results for B1937+21 and J0218+4232

Earth orbit phase tracking simulations were also performed using the MSPs B1937+21 and J0218+4232. Due to the high dynamic stress of the Earth orbits and the low source fluxes of these MSPs a much larger detector area was needed in order to find a set of DPLL parameters that allowed for consistent tracking of the DirecTV and GPS orbits. An 8 m^2 detector and 10 m^2 detector were found to be necessary for tracking the DirecTV and GPS orbits, respectively. No detector areas was found to pair with DPLL parameter choices that would allow tracking the ISS orbit. The results for B1937+21 and J0218+4232 Earth orbit simulations are summarized in Table 5.24. Metrics to illustrate the phase tracking results include: the averaged MLE position error, the DPLL end point RMS position and velocity errors, and the average DPLL position and velocity errors over the simulation time. The CRLB is included to provide a comparison to the theoretical limit achievable by the MLE for position estimation.

The DPLL parameter choices that led to tracking for both B1937+21 and J0218+4232 in the simulations of the DirecTV and GPS orbits are included in Table 5.20. For both orbits a loop noise bandwidth of 0.05 Hz was used. This is a larger B_L than was used for these orbits with the B1821-24 signal. It is also much larger than the loop noise bandwidth that was allowable for both the interplanetary and constant acceleration trajectories of the previous sections. The block sizes used were 700 seconds and 500 seconds for the DirecTV and GPS orbits, respectively. These were chosen to correspond with the 8 and 10 m^2 detectors.

The phase tracking simulation results for B1937+21 and J0218+4232 are compared in Figure 5.56 and Figure 5.58 for the DirecTV orbit and in Figure 5.57 and Figure 5.59 for the GPS orbit. Each figure contains three subplots detailing the position, velocity, and acceleration errors over the simulation time. The DPLL and MLE outputs are included in the position error plot.

Figure 5.56 includes the phase tracking results of the B1937+21 signal with the DirecTV orbit. The block update time is 700 seconds, the loop noise bandwidth is 0.05 Hz, and the detector area is 8 m^2. Similar to the B1821-24 results, it can be seen that the position, velocity, and acceleration errors stay bounded for the entire simulation time. This demonstrates that the algorithm is tracking the phase and staying consistently in-lock. In the position error plot, the MLE error level is similar to the DPLL output error level, but there are some portions of the simulation where the DPLL error level is larger than the MLE. Also, there appears to be some bias that might be from oscillatory behavior in the DPLL error results.

The B1937+21 phase tracking results for the GPS orbit are included in Figure 5.57. The block update time is 500 seconds, the loop noise bandwidth is 0.05 Hz, and the detector area is 10 m^2. It can be seen that the tracking is achieving bounded position, velocity, and acceleration errors. The performance levels and shapes of the error plots are similar to those seen with the DirecTV orbit. The oscillations are more apparent than with the DirecTV orbit and follow the orbital period of the GPS orbit. There are again portions of the DPLL position output error that are larger than the individual MLE position error averages. This appears to be due to the oscillatory behavior.

Figure 5.58 includes the phase tracking results of the J0218+4232 signal with the DirecTV orbit. The DPLL parameters were able to be kept the same as for the B1937+21 pulsar signal for comparison.The block update time is 700 seconds, the loop noise bandwidth is 0.05 Hz, and the detector area is 8 m^2. This figure again illustrates bounded phase tracking errors for the entire simulation. The DPLL errors appear to be larger in magnitude than in the corresponding simulation with B1937+21. The same oscillatory behavior and relationship between the DPLL and MLE position estimates are present.

The J0218+4232 phase tracking results for the GPS orbit are included in Figure 5.59. The block update time is 500 seconds, the loop noise bandwidth is 0.05 Hz, and the detector area is 10 m^2. This demonstrates bounded phase tracking performance, but with larger errors than with B1937+21. This figure also contains must larger amplitude oscillations with this orbit scenario and pulsar choice. There are greater discrepancies between the DPLL and MLE position estimates than were present with the DirecTV orbit with J0218+4232 and with both B1937+21 simulation scenarios.

The Earth orbit simulation results with B1937+21 and J0218+4232 are summarized in Table 5.24. The average MLE position error for each of the orbit scenarios is reasonably close to the theoretical limit of the CRLB. For both orbits, B1937+21 has a larger discrepancy with the CRLB, which matches with the bias offset that was found in the MLE simulations in Chapter 4. For both orbits and both pulsars the average MLE position estimates outperform the DPLL outputs. For the DirecTV orbit the average MLE position error is 2.91 km and 4.72 km for B1937+21 and

J0218+4232, respectively. For the GPS orbit the average MLE position error is 2.74 km and 5.26 km for B1937+21 and J0218+4232, respectively. In both cases, the MLE results for B1937+21 outperform those for J0218+4232, and they are similar across both orbits.

Comparing the DirecTV and GPS orbit results, it can be seen that for B1937+21 the GPS tracking results are better than those for the DirecTV orbit, while for J0218+4232 the opposite is true. For example for B1937+21, the DPLL RMS end point position and velocity errors are 13.03 km and 9.62 m/s and 7.29 km and 7.33 m/s for the DirecTV and GPS orbits, respectively. For J0218+4232, the DPLL RMS end point position and velocity errors are 7.42 km and 6.41 m/s and 15.98 km and 16.57 m/s for the DirecTV and GPS orbits, respectively. This might be caused by the use of the same set of DPLL parameters for B1937+21 and J0218+4232. For the DirecTV orbit the set of parameters might be better optimized for J0218+4232 and for the GPS orbit the set of parameters might be better for B1937+21.

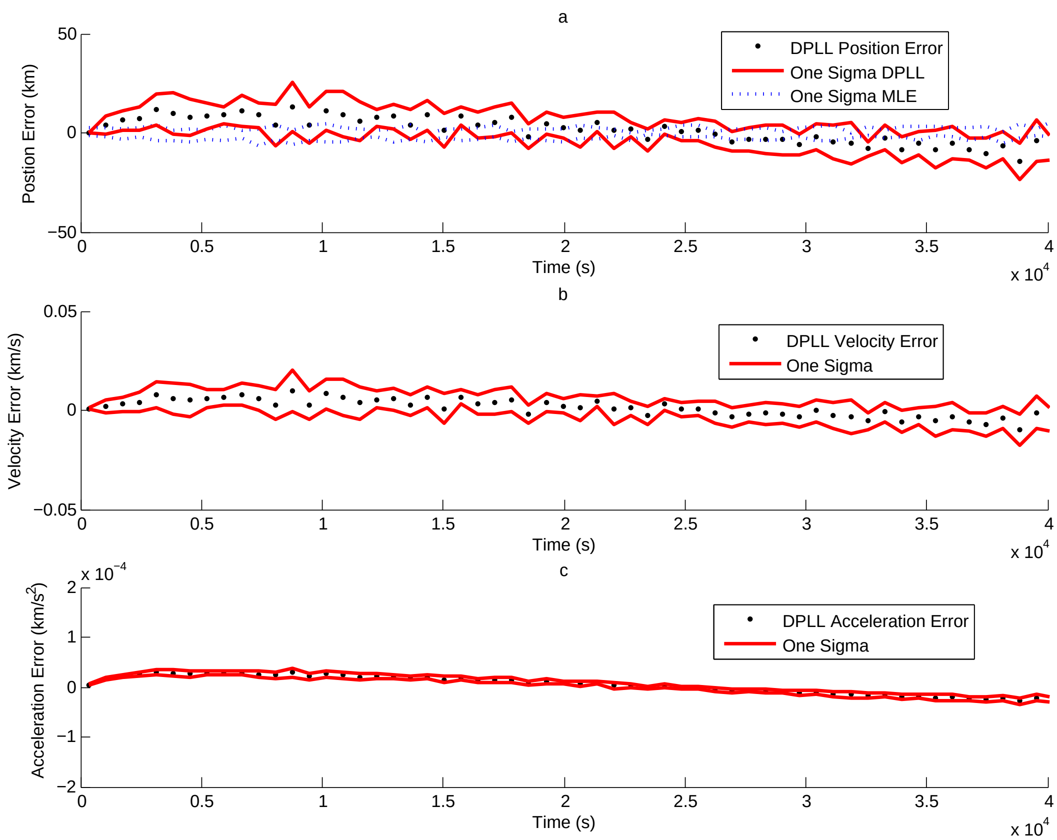

Figure 5.56: DirecTV satellite orbit phase tracking simulation results for PSR B1937+21 with T = 700 seconds and B_L = 0.05 Hz. The detector area is increased to 8 m^2. One dimensional tracking results along LOS to pulsar.

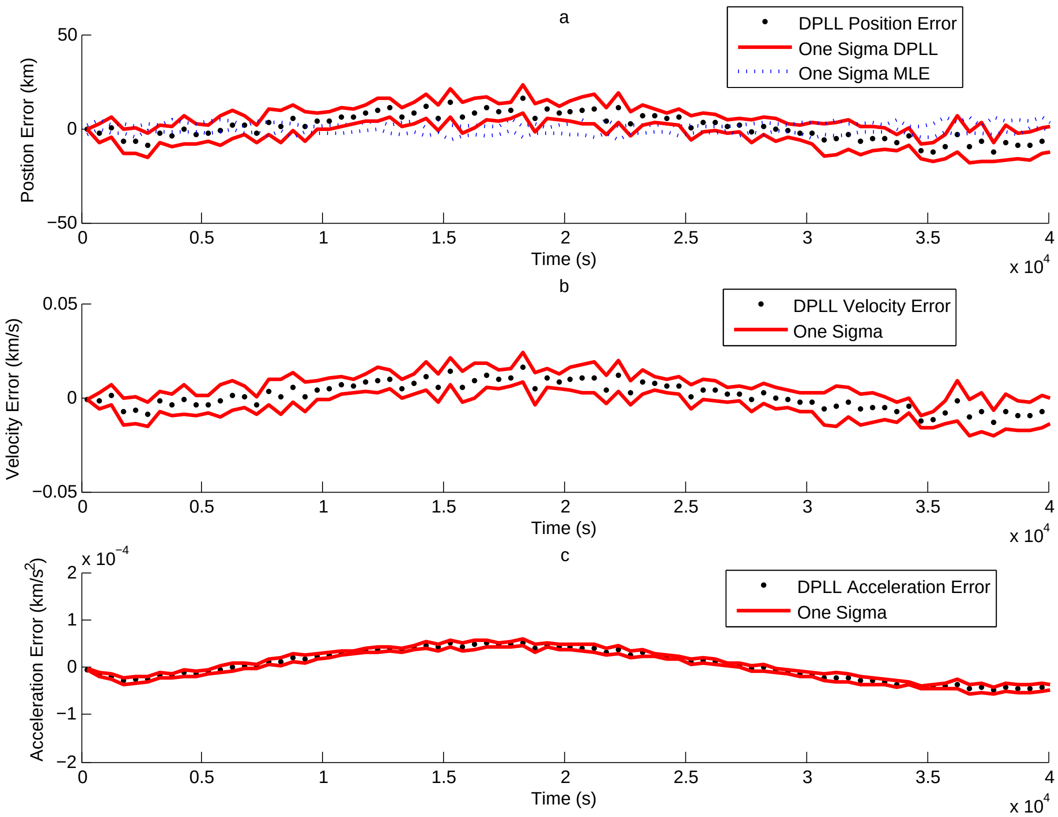

Figure 5.57: GPS satellite orbit phase tracking simulation results for PSR B1937+21 with T = 500 seconds and $B_L = 0.05$ Hz. The detector area is increased to 10 m^2. One dimensional tracking results along LOS to pulsar.

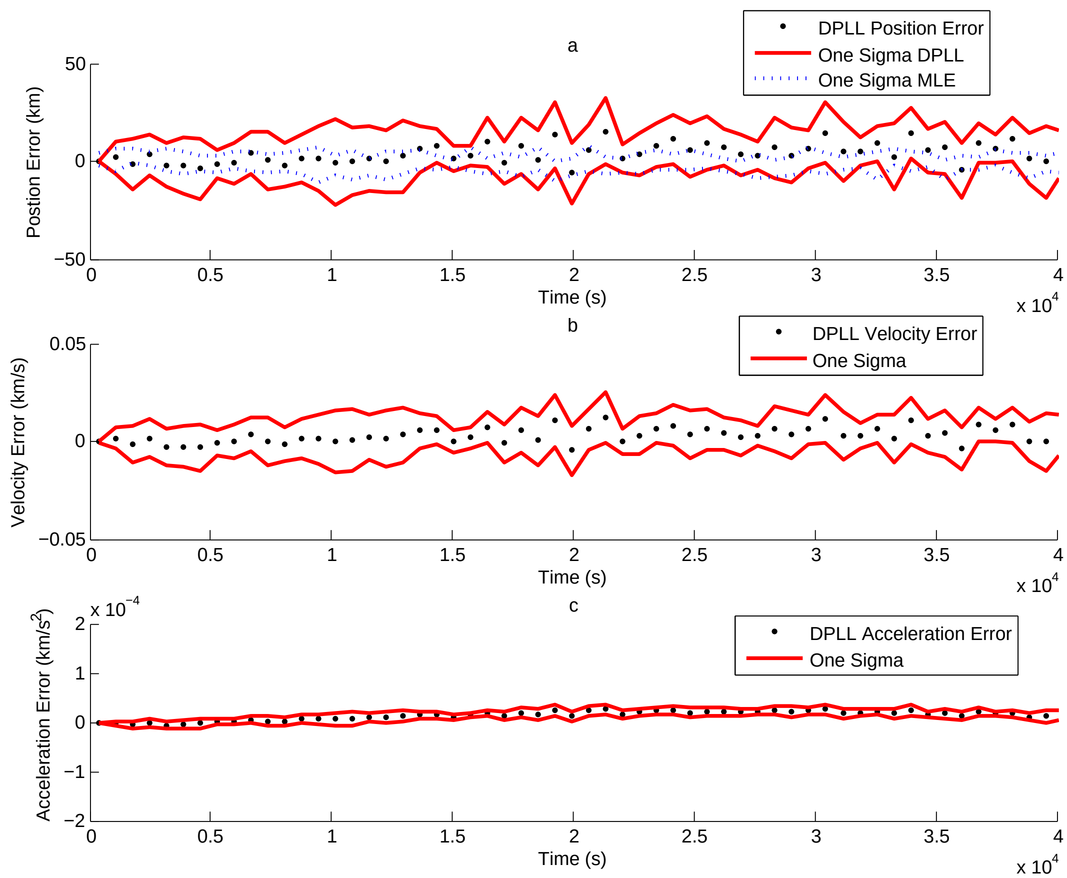

Figure 5.58: DirecTV satellite orbit phase tracking simulation results for PSR J0218+4232 with T = 700 seconds and $B_L = 0.05$ Hz. The detector area is increased to 8 m^2. One dimensional tracking results along LOS to pulsar.

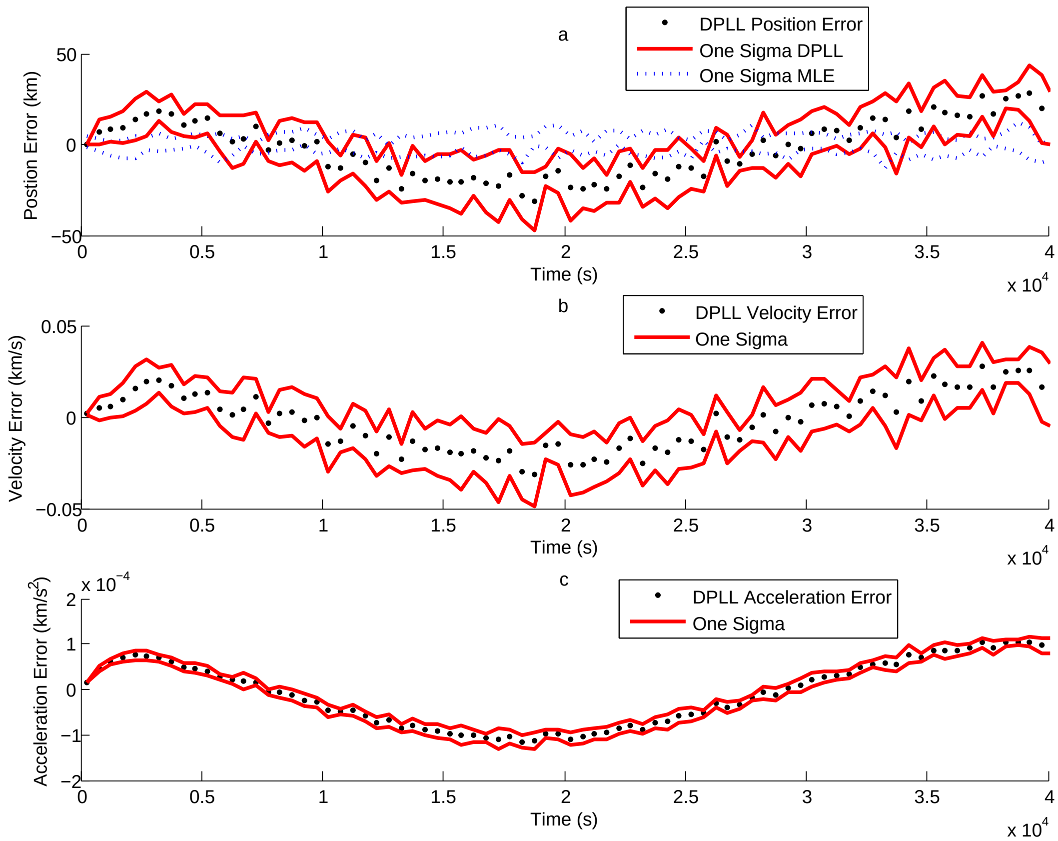

Figure 5.59: GPS satellite orbit phase tracking simulation results for PSR J0218+4232 with T = 500 seconds and $B_L = 0.05$ Hz. The detector area is increased to 10 m^2. One dimensional tracking results along LOS to pulsar.

Table 5.24: GPS and DirecTV orbit simulation results for PSR B1937+21 and PSR J0218+4232 with initial condition errors consistent with a DSN handoff and an accelerometer. One dimensional tracking results along LOS to pulsar.

Pulsar	B1937+21	J0218+4232	B1937+21	J0218+4232
Orbit	DirecTV	DirecTV	GPS	GPS
Area (m^2)	8	8	10	10
T, s	700	700	500	500
B_L, Hz	0.005	0.005	0.005	0.005
CRLB, km	0.86	3.54	0.91	3.75
Averaged MLE Position Error (km)	2.91	4.72	2.74	5.26
End Point RMS Position Error (km)	13.03	7.42	7.29	15.98
Averaged Position Error (km)	10.26	12.72	8.50	18.17
End Point RMS Velocity Error (m/s)	9.62	6.41	7.33	16.47
Averaged Velocity Error (m/s)	7.59	10.23	8.95	18.79

5.5.2.4 Earth Orbit Results for the Crab Pulsar

Earth orbit phase tracking simulations were also performed using the Crab pulsar. Due to the multiple orders of magnitude higher flux of the Crab pulsar, various areas and simulation times were considered. Similar to the interplanetary orbit simulations, a 1 m^2 (10000 cm^2) detector was simulated with a shorter simulation time of 200 seconds and a smaller 0.1 m^2 (1000 cm^2) detector was simulated for 7200 seconds. The shorter simulation times were necessary due to the high flux rate, but tracking results that stay in-lock can be extrapolated to the times used for the MSP Earth orbit simulations. The results for the Crab pulsar Earth orbit simulations are summarized in Table 5.25 and Table 5.26 for detector areas of 1 m^2 and 1000 cm^2, respectively. Metrics to illustrate the phase tracking results include: the averaged MLE position error, the DPLL end point RMS position and velocity errors, and the average DPLL position and velocity errors over the simulation time. The CRLB is included to provide a comparison to the theoretical limit achievable by the MLE for position estimation.

The DPLL parameter choices for tracking the Crab pulsar signal are included in Table 5.21. For the DirecTV and GPS orbits a loop noise bandwidth of 0.005 Hz was used. For the ISS orbit a loop noise bandwidth of 0.05 Hz was used. These are the same B_L values that were used with the B1821-24 signal. It is much larger than the loop noise bandwidth that was allowable for both the interplanetary and constant acceleration trajectories of the previous sections. A block size of 10 seconds was used for all of the Earth orbit simulations with the Crab pulsar. A block size of 100 seconds was also considered with the 1000 cm^2 detector. This added block size was considered in order to have a comparison that keeps the area-time product constant between the 1 m^2 and 1000 cm^2 detector scenarios.

The phase tracking simulation results for the Crab pulsar with a 1 m^2 (10000 cm^2) detector and 200 second simulation time are compared in Figure 5.60, Figure 5.61, and Figure 5.62 for the DirecTV, GPS, and ISS orbits, respectively. The phase tracking simulation results for the Crab pulsar with a 0.1 m^2 (1000 cm^2) detector and 7200 second simulation time are compared in Figure 5.63, Figure 5.64, and Figure 5.65 for the DirecTV, GPS, and ISS orbits, respectively. All of the figures include the simulation results with a block size choice of T = 10 seconds. Each figure contains three subplots detailing the position, velocity, and acceleration errors over the simulation time. The DPLL and MLE outputs are included in the position error plot. It is hard to compare the phase tracking results for the 1 m^2 detector to those for the 1000 cm^2 detector solely using these figures due to the difference in simulation time from 200 to 7200 seconds, respectively.

Figure 5.60 includes the phase tracking results of the Crab pulsar signal with the DirecTV orbit with a detector area of 1 m^2. The block update time is 10 seconds and the loop noise bandwidth is 0.005 Hz. Similar to the various MSP results, it can be seen that the position, velocity, and acceleration errors stay bounded for the entire simulation time. This demonstrates that, as with the other pulsars, the algorithm is tracking the phase and staying consistently in-lock. In the position error plot, the DPLL position error is outperforming the MLE outputs.

The Crab pulsar phase tracking results for the GPS orbit with a detector area of 1 m^2 are included in Figure 5.61. The block update time is 10 seconds and the loop noise bandwidth is 0.005 Hz. The tracking is achieving bounded position, velocity, and acceleration errors. The performance levels and shapes of the error plots are similar to those seen with the DirecTV orbit. The DPLL position error is again outperforming the MLE outputs. There is a bias in the acceleration error plot near the end of the simulation time. This might be the start of the oscillatory behavior seen with the other pulsars. These oscillations are otherwise not present due to the shorter simulation times used with the Crab pulsar that is less than the orbital period.

The phase tracking results for the Crab pulsar with the ISS and a detector area of 1 m^2 are included in Figure 5.62. The block update time is 10 seconds and the loop noise bandwidth is 0.05 Hz. The scaling is zoomed out in the velocity and acceleration error plots compared to the DirecTV and GPS results. The tracking performance is bounded for position, velocity, and acceleration. The MLE and DPLL position error levels are similar on average. The oscillations that are seen with the tracking of the B1821-24 signal are not detectable due to the short simulation time of 200 seconds compared to the ISS orbital period.

Figure 5.63 includes the phase tracking results of the Crab pulsar signal with the DirecTV orbit with a detector area of 1000 cm^2. The block update time is 10 seconds and the loop noise bandwidth is 0.005 Hz. The tracking performance is bounded for the entire simulation time. The DPLL is outperforming the MLE position errors by a larger margin than with the 1 m^2 detector, which is directly due to the smaller area.

The Crab pulsar phase tracking results for the GPS orbit with a detector area of 1000 cm^2 are included in Figure 5.64. The block update time is 10 seconds and the loop noise bandwidth is 0.005 Hz. The tracking performance is bounded for position, velocity, and acceleration with similar levels of error as with the DirecTV orbit simulations. Again the DPLL position error is outperforming the MLE. There is maybe a little oscillatory behavior apparent in the acceleration error, which is visible due to the longer simulation time.

The phase tracking results for the Crab pulsar with the ISS and a detector area of 1000 cm^2 are included in Figure 5.65. The block update time is 10 seconds and the loop noise bandwidth is 0.05 Hz. As with all of the Crab pulsar Earth orbit simulations, the tracking performance is bounded for position, velocity, and acceleration. The error levels are higher, though. The scaling is zoomed out in the velocity and acceleration error plots compared to the DirecTV and GPS results. The position errors for the DPLL outputs are larger and unlike with the DirecTV and GPS orbits, the MLE and DPLL position error levels are similar on average. Oscillatory behavior can be seen in the acceleration error plot. It is following the orbital period of the ISS.

The Crab pulsar Earth orbit simulation results are summarized in Table 5.25 and Table 5.26 for detector areas of 1 m^2 and 1000 cm^2, respectively. The average MLE position error for each of the orbit scenarios is reasonably close to the theoretical limit of the CRLB. For the scenarios with 1 m^2 the MLE average is closer to the CRLB than with the 1000 cm^2 simulations. For example with the DirecTV orbit and a block size of 10 seconds the CRLB is 1.22 km and the MLE average position error is 1.46 km with the 1 m^2 detector while the CRLB is 2.44 km and the MLE average position error is 4.55 km with the 1000 cm^2 detector.

Looking at Table 5.25 it can be seen that with a detector area of 1 m^2 the position and velocity errors are similar for the DirecTV and GPS orbits and they are larger for the ISS orbit. The end point RMS DPLL position errors are 0.47 km, 0.47 km, and 1.68 km for the DirecTV, GPS, and ISS orbit simulations, respectively. The end point RMS DPLL velocity errors are 2.08 m/s, 2.24 m/s, and 51.08 m/s for the DirecTV, GPS, and ISS orbit simulations, respectively. For the DirecTV and GPS orbits the DPLL end point RMS position error outperforms the average MLE error. For example with the DirecTV orbit the MLE average error is 1.46 km and the DPLL end point RMS position error is 0.47 km. For the ISS orbit the MLE slightly outperforms the DPLL end point RMS position error 1.45 km to 1.68 km.

In Table 5.26 it can be seen that with a detector area of 1000 cm^2, and for both T = 10 seconds and T = 1000 seconds, the position and velocity errors increase as the orbit altitude is decreased from the DirecTV to the GPS to the ISS orbit. For example, with T = 10 seconds the end point RMS DPLL position errors are 1.16 km, 1.19 km, and 5.43 km for the DirecTV, GPS, and ISS orbit simulations, respectively. This trend matches the differences in dynamic stress between these orbits. For T = 10 seconds, the end point RMS DPLL position error outperforms the MLE average error with the DirecTV and GPS orbits, but the opposite is true for the ISS orbit. For T = 100 seconds, MLE average error outperforms the DPLL for all three of the orbits.

When comparing the simulation results with block sizes of 10 seconds and 100 seconds, with the 1000 cm^2 detector, it can be seen that the MLE average error decreases, the DPLL end point RMS position error increases, and the DPLL end point RMS velocity error decreases when changing from T = 10 seconds to T = 100 seconds. For example, with the DirecTV orbit and T = 10 seconds the average MLE position error is 4.55 km, the DPLL end point RMS position error is 1.16 km, and the DPLL end point RMS velocity error is 5.03 m/s, and with T = 100 seconds the average MLE position error is 1.55 km, the DPLL end point RMS position error is 1.67 km, and the DPLL end point RMS velocity error is 4.88 m/s.

Even with large differences in the simulation times general comparisons can be made between the results with a 1 m^2 detector and those with a 1000 cm^2 detector. For all three orbit scenarios considered the results are better for the larger detector, as expected due to the number of photons available for each estimate. This is true even for the scenarios where the block size was set at 100 seconds in order to match the area-time product from the simulations with the 1 m^2 detector. The MLE results with T = 100 seconds and a detector area of 1000 cm^2 are similar to the results with T = 10 seconds and a detector area of 1 m^2, but the DPLL results are greatly improved with the larger detector area. This is due to the change in the TB_L product affecting the DPLL gains detrimentally for error performance when the value of T is increased.

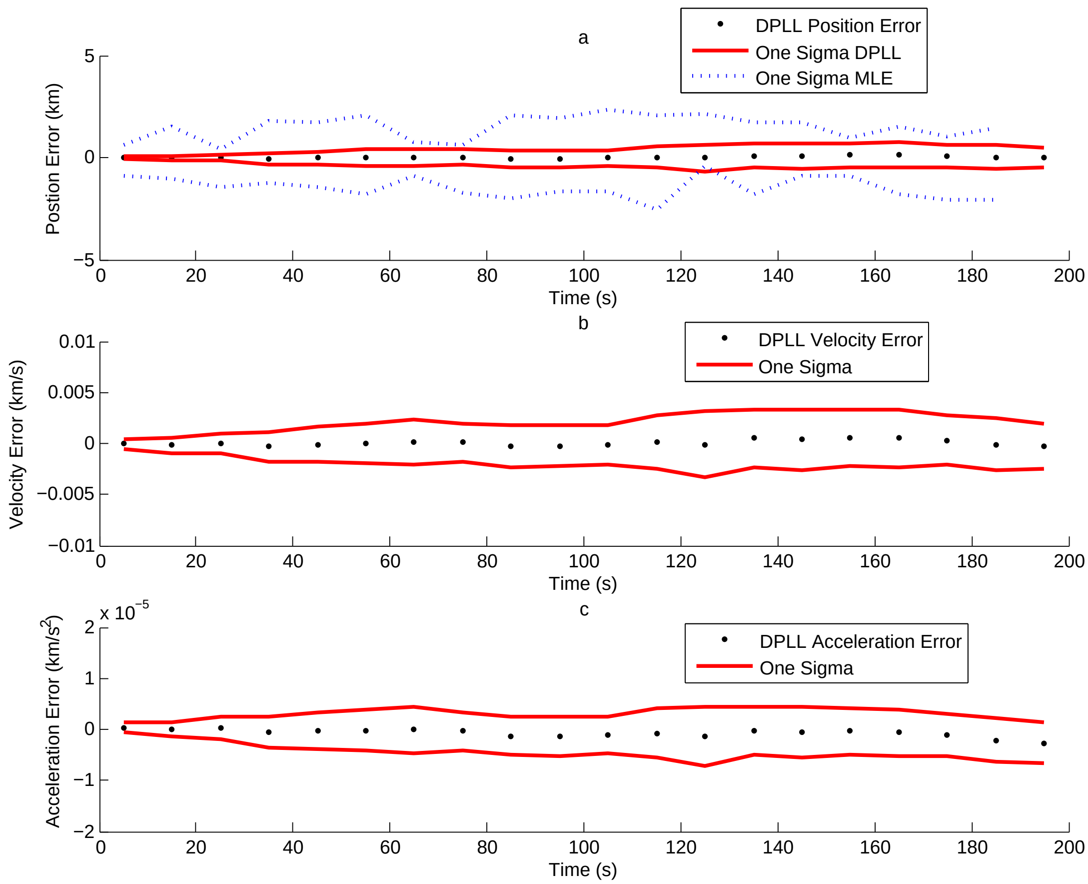

Figure 5.60: DirecTV orbit phase tracking simulation results for the Crab pulsar with T = 10 seconds, $B_L = 0.005$ Hz, and a detector area of 1 m^2. One dimensional tracking results along LOS to pulsar.

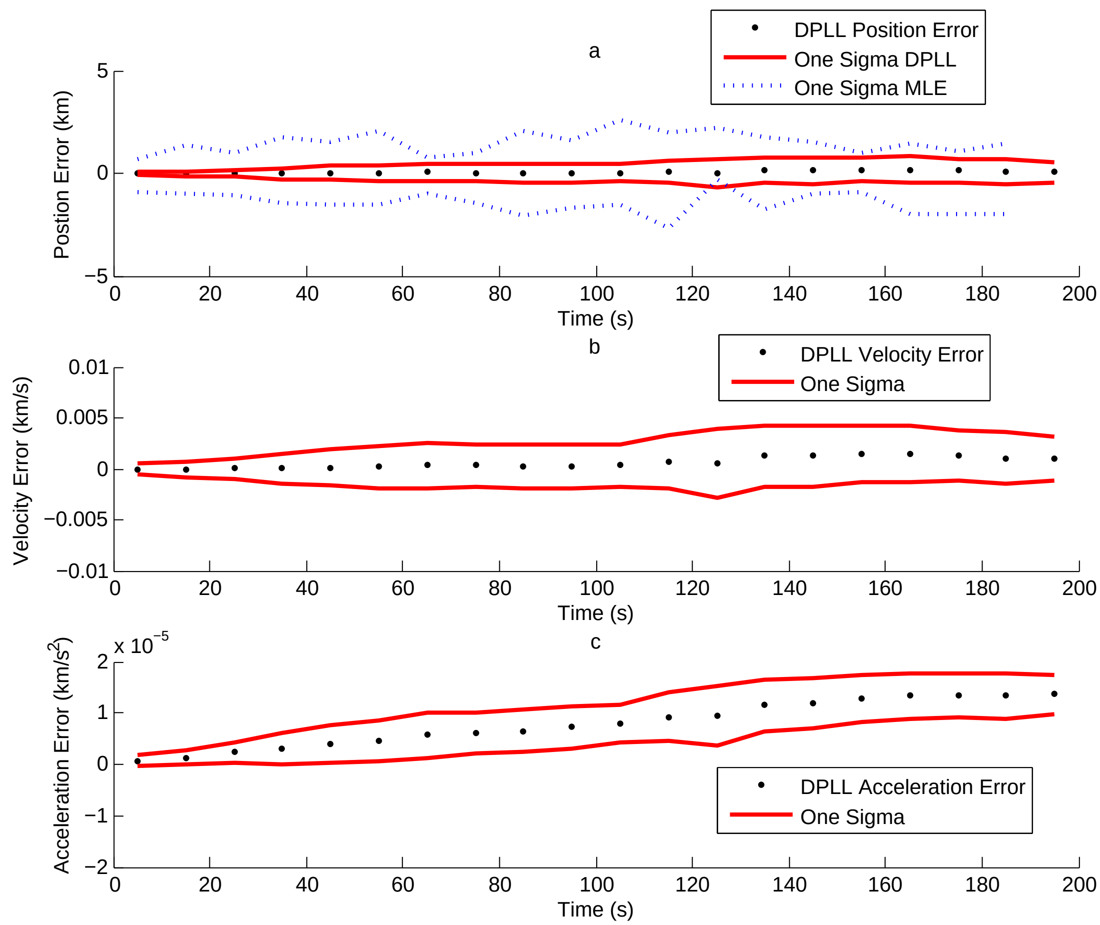

Figure 5.61: GPS orbit phase tracking simulation results for the Crab pulsar with T = 10 seconds, B_L = 0.005 Hz, and a detector area of 1 m^2. One dimensional tracking results along LOS to pulsar.

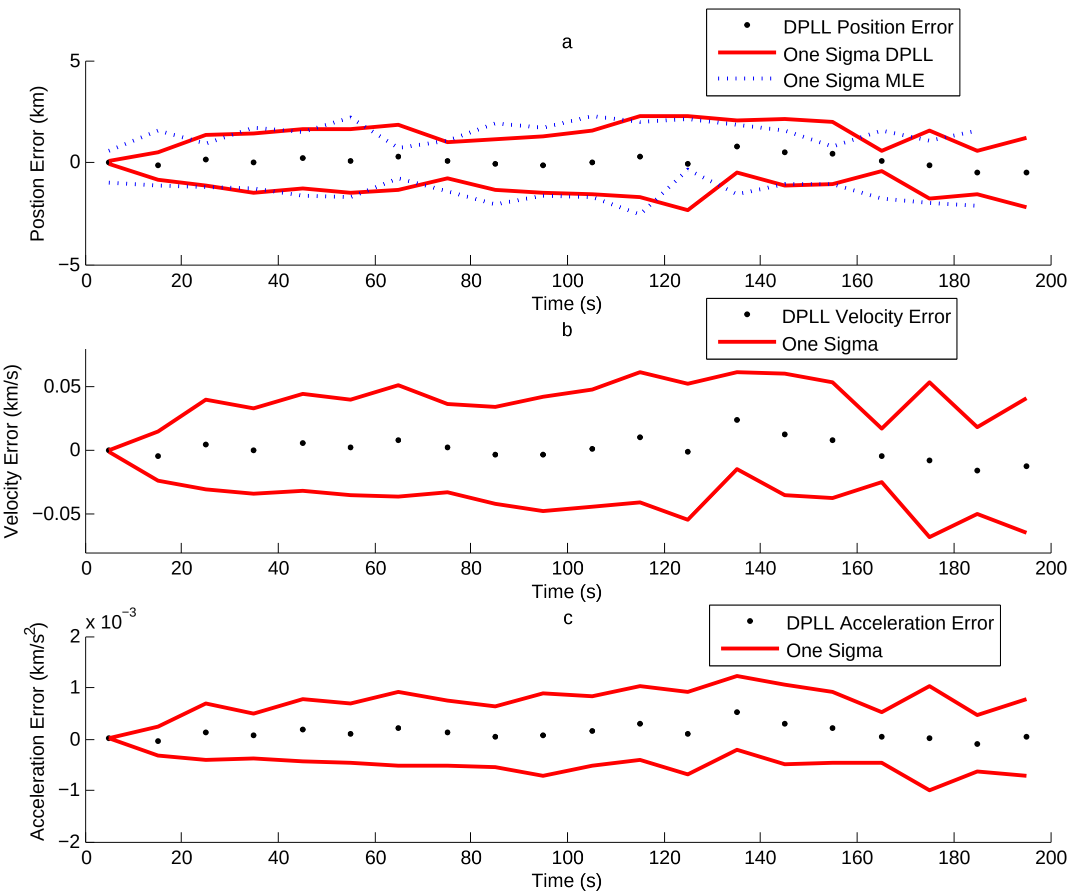

Figure 5.62: ISS orbit phase tracking simulation results for the Crab pulsar with T = 10 seconds, $B_L = 0.05$ Hz, and a detector area of 1 m^2. One dimensional tracking results along LOS to pulsar.

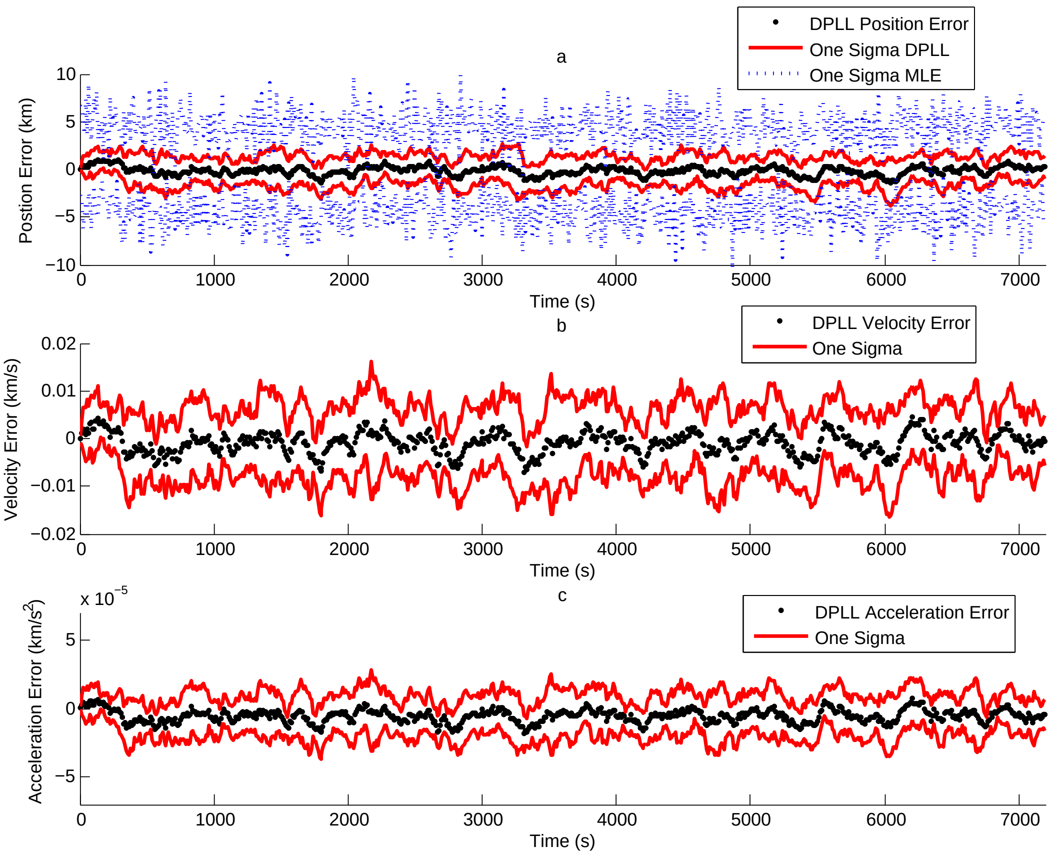

Figure 5.63: DirecTV orbit phase tracking simulation results for the Crab pulsar with T = 10 seconds, B_L = 0.005 Hz, and a detector area of 1000 cm^2. One dimensional tracking results along LOS to pulsar.

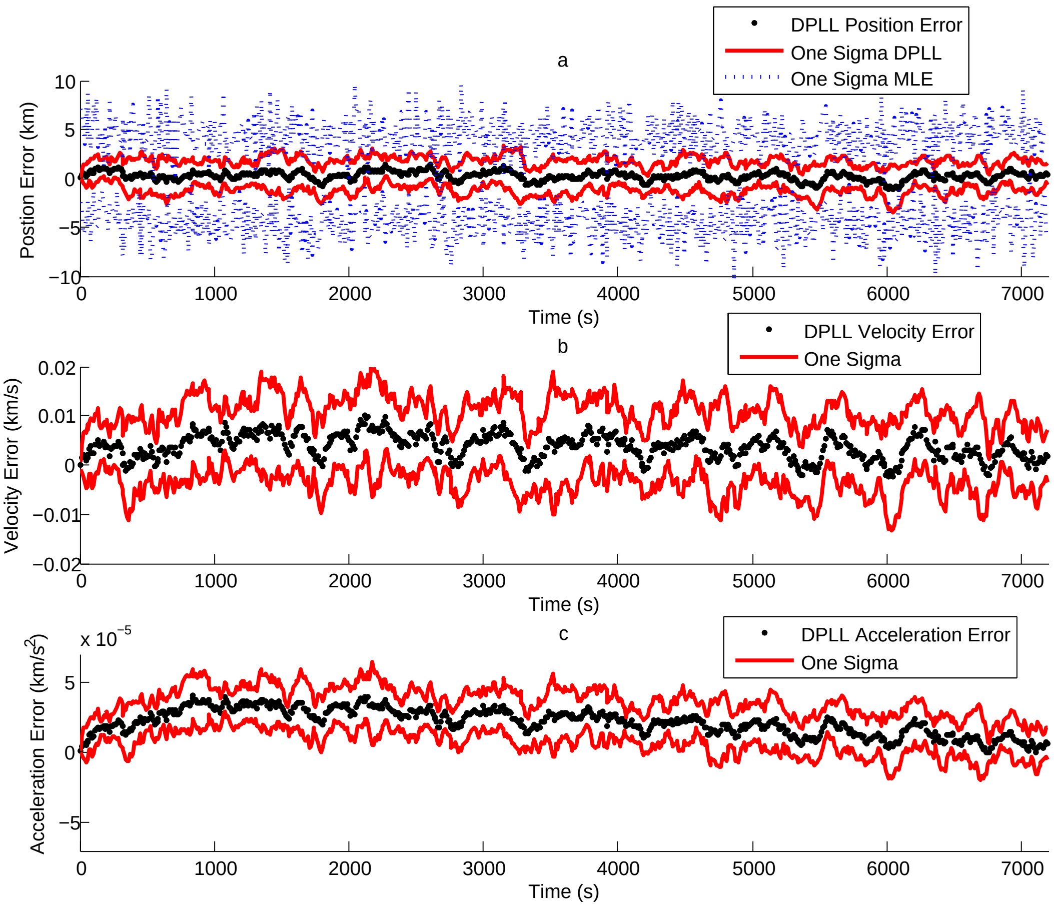

Figure 5.64: GPS orbit phase tracking simulation results for the Crab pulsar with T = 10 seconds, $B_L = 0.005$ Hz, and a detector area of 1000 cm^2. One dimensional tracking results along LOS to pulsar.

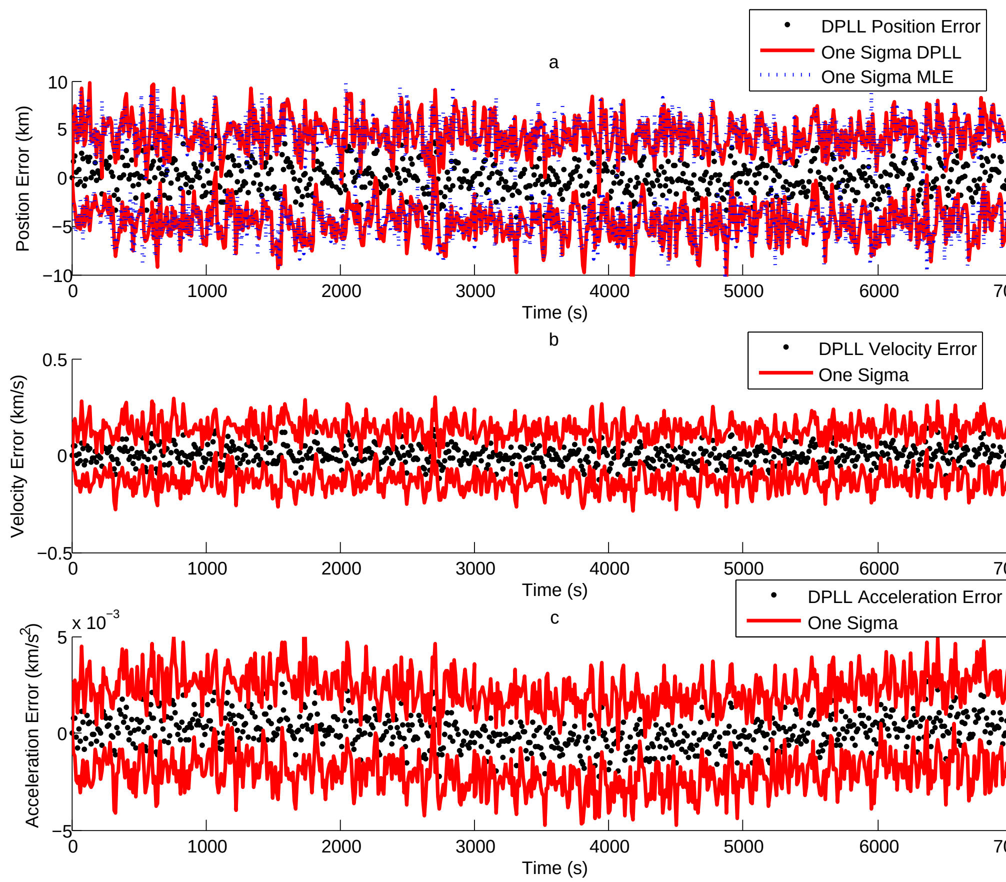

Figure 5.65: ISS orbit phase tracking simulation results for the Crab pulsar with T = 10 seconds, B_L = 0.05 Hz, and a detector area of 1000 cm^2. One dimensional tracking results along LOS to pulsar.

Table 5.25: Earth orbit simulation results for the Crab pulsar with a detector area of 1 m^2 and initial condition errors consistent with a DSN handoff and an accelerometer. One dimensional tracking results along LOS to pulsar.

Orbit	DirecTV	GPS	ISS
T, s	10	10	10
B_L, Hz	0.005	0.005	0.05
CRLB, km	1.22	1.22	1.22
Averaged MLE Position Error (km)	1.46	1.45	1.45
End Point RMS Position Error (km)	0.47	0.47	1.68
Averaged Position Error (km)	0.43	0.45	1.36
End Point RMS Velocity Error (m/s)	2.08	2.24	51.08
Averaged Velocity Error (m/s)	2.08	2.24	39.73

5.5.2.5 Main Takeaways from the Earth Orbit Results

In general, the phase tracking algorithm has more difficulty with the Earth orbits than previously with the interplanetary trajectories. This is as expected due to the significantly larger dynamic stress and divergence from the constant acceleration assumption over long block times with the Earth orbits. There are still many positive takeaways from the performance with PSR B1821-24 in particular, but PSR J0437-4715 doesn't track for any of the area and DPLL parameter combinations simulated for the Earth orbits considered due to having the lowest SNR of the pulsars investigated. This was not surprising since it already had the worst results for

Table 5.26: Earth orbit simulation results for the Crab pulsar with a detector area of 1000 cm^2 and initial condition errors consistent with a DSN handoff and an accelerometer. One dimensional tracking results along LOS to pulsar.

Orbit	DirecTV	DirecTV	GPS	GPS	ISS	ISS
T, s	10	100	10	100	10	100
B_L, Hz	0.005	0.005	0.005	0.005	0.05	0.05
CRLB, km	2.44	0.77	2.44	0.77	2.44	0.77
Averaged MLE Position Error (km)	4.55	1.55	4.54	1.54	4.55	1.61
End Point RMS Position Error (km)	1.16	1.67	1.19	1.74	5.43	10.80
Averaged Position Error (km)	1.54	1.61	1.55	1.90	4.56	8.83
End Point RMS Velocity Error (m/s)	5.03	4.88	5.27	4.77	166.71	49.06
Averaged Velocity Error (m/s)	7.39	4.80	8.26	7.28	135.10	42.16

the constant acceleration and interplanetary trajectory simulations in the previous sections.

PSR B1821-24 and the Crab are the only pulsars considered that were able to track the ISS orbit with the phase tracking algorithm. Both B1937+21 and J0218+4232 required large areas to track the DirecTV and GPS orbits with 8 and 10 m^2, respectively. The relative performance with the various pulsars simulated and the abilities to track the Earth orbits with their various dynamic stress conditions were related to the various pulsar signal parameters. The Crab pulsar has the highest flux by multiple orders of magnitude, B1821-24 has the largest flux and SNR of the MSPs considered, B1937+21 and J0218+4232 have similar flux and SNR levels and thus have similar performance with the Earth orbits, and J0437-4715 has the lowest SNR of the MSPs considered due to a small pulse fraction and this contributes to the difficulty with tracking this pulsar signal in high dynamic stress conditions.

In comparison to the interplanetary simulations with the MSL and Cassini trajectories and the constant acceleration simulations, the Earth orbit simulations have poorer estimation accuracy results. With PSR B1821-24 position accuracy under 4 km error is achievable with each of the Earth orbits which is not much worse than the interplanetary trajectory simulations. Also, the Crab pulsar can achieve position accuracies under a few kilometers. Pulsars B1937+21 and J0218+4232 can achieve similar position accuracies to the interplanetary simulations with the DirecTV and GPS orbits, but only with much larger detector areas. The tracking difficulty increases and the estimation accuracy decreases as the altitude of the Earth orbits decrease from the DirecTV orbit to the GPS orbit to the ISS orbit. This is directly related to the dynamic stress constraints from the physics of orbits.

These results imply that phase tracking pulsar signals to navigate Earth orbits will be difficult. The set of pulsars available for tracking will be small compared to interplanetary trajectories and other lower dynamic stress environments. The feasibility will be constrained by the detector area that is available for use and also on whether there are ways to offset the navigational constraints of only having a few pulsars to provide estimates from. This will limit the geometric diversity of the estimates and might prevent the filter from tracking components of the navigational state. This method is still usable in those cases if there is some sort of a hybrid model to offset the drawbacks of only having a few pulsars to track.

To get more pulsar signals that allow for phase tracking with Earth orbits specific parameter changes could be made to either adjust these pulsars for greater usability or search for desirable other pulsar signals with good Earth orbit tracking characteristics. Specific changes that might be achievable through advances in detector technology include larger collection areas, lower background photon rates, and better rejection of nonpulsed photons from the source. Other more intrinsic changes to the pulsar physics include signals with greater SNR from either higher pulse fraction or higher raw source photon flux. Basically, the ability to overcome the high dynamic stress environment of the Earth orbits to allow tracking relies on getting more source photons in a shorter period of time to allow for estimation over a smaller observation window with less time for the offset from constant acceleration to buildup.

5.5.3 Cislunar Trajectory Tracking Performance

In order to test the phase tracking performance on a scenario with dynamic stress between that of the Earth orbits and heliocentric trajectories tested, a cislunar trajectory was simulated. An intermediate level of dynamic stress was desired to get a better sense of the of the capabilities and limitations of the phase tracking algorithm. With the Earth orbits, only the Crab pulsar and B1821-24 provided desirable results with a reasonably sized detector. With both interplanetary cruise trajectories, tracking performed well for all of the pulsars besides J0437-4715. The tests with the cislunar orbit were designed to determine if the phase tracking performance is closer to the outcomes with the interplanetary trajectories or the Earth orbits and if this provides a greater range of potential use scenarios for the algorithm.

The chosen cislunar orbit is a portion of a transfer trajectory between the Earth and Moon orbit. A plot of the trajectory is included in Figure 5.33 along with the Earth and Moon for reference. In this section the results of phase tracking simulations for various pulsars along this cislunar trajectory will be presented.

A detector area of 1 m^2 was simulated for each pulsar in order to compare to the Earth orbit and interplanetary results of the previous sections. Pulsars B1821-24, B1937+21, J0218+4232, and the Crab were each individually phase tracked to estimate the cislunar trajectory. J0437-4715 was not considered due to its poor performance with the interplanetary MSL and Cassini trajectories. The DPLL and other simulation parameters were chosen similar to the interplanetary trajectory simulations. As with the previous sections, the Crab pulsar simulations are run for

200 seconds instead of the 54000 seconds used with the other pulsars due to the difference in flux rates. Two different loop noise bandwidths were tested, $B_L = 0.001$ Hz and $B_L = 0.00025$ Hz.

The initial condition errors were assumed to be the same as with the MSL and Cassini trajectories. These values were: 1 km for position, 1 m/s for velocity, and 1 mg or 1 cm/s^2 in acceleration. This corresponds to a hand-off from the DSN or other Earth-based tracking system. An accelerometer is assumed available to provide the necessary initial acceleration estimation accuracy. This again allows the DPLL to start tracking in-lock from the beginning of the phase tracking. Simulations were also performed using PSR B1821-24 with a higher initial position error of 10 km to test the ability to correct for more initial error. As with the previous simulation scenarios, each combination of simulation and DPLL parameter choices are tested ten times and the results are averaged to produce the results that are included in the tables and figures that follow.

Two different choices for loop noise bandwidth were tested for the cislunar trajectory. The results for simulations using $B_L = 0.00025$ Hz are included in Table 5.27, and results using $B_L = 0.0001$ Hz are included in Table 5.28. The Crab pulsar was only tested with $B_L = 0.00025$ Hz, while the three MSPs were tested with both values.

The results for the cislunar trajectory phase tracking simulation using PSR B1821-24 with T = 200 seconds and $B_L = 0.00025$ Hz are included in Figure 5.66. It can be seen in the figure that the phase tracking successfully stays in-lock for the entire simulation time and the position, velocity, and acceleration tracking results all settle after an initial period of higher error. The DPLL position error is biased compared to the MLE position error outputs. This causes a scew in the comparison with the one-sigma MLE bound, but it is settling out toward the end of the 12 hour simulation window. It is unclear what is causing this bias. It might be related to the underlying dynamic stress of the orbit.

The results for B1821-24 with T = 200 seconds and B_L = 0.001 Hz using a higher initial position error of 10 km are included in Figure 5.67. The phase tracking results stay in-lock for the entire simulation time and the DPLL position error can be seen to outperform the equivalent MLE position estimates. The increased initial error caused by the position error shows up in the position, velocity, and acceleration tracking results, but settle out in the first few thousand seconds. The bias is not apparent in the position tracking results that were seen in Figure 5.66. This is probably due to the increase of the loop noise bandwidth to B_L = 0.001 Hz leading to a better ability to accommodate dynamic stress in the phase model.

The phase tracking results using PSR B1937+21 with T = 4000 seconds and B_L = 0.00025 Hz are included in Figure 5.68. The results for B1937+21 with T = 4000 and B_L = 0.001 Hz are included in Figure 5.69. Both figures demonstrate that the phase tracking algorithm is able to track the cislunar trajectory in-lock with the B1937+21 signal. The differences between the results due to the change in loop noise bandwidth are minor and difficult to see in the figures. The largest difference is a small bias that again appears in the position error plot with B_L = 0.00025 Hz and is removed with B_L = 0.001 Hz, but this is less pronounced than with the equivalent B1821-24 results. It might be more difficult to see due to the relative lack of estimation updates in the simulation due to the change in block time to T = 4000 seconds from T = 200 seconds, with B1821-24.

Figure 5.70 demonstrates the results for phase tracking the cislunar trajectory with PSR J0218+4232 with T = 4000 seconds and $B_L = 0.001$ Hz. Again, it can be seen that the DPLL stays in-lock for the simulation window and the phase tracking algorithm is able to track the cislunar trajectory with the J0218+4232 signal. The results are similar to those in Figure 5.69 B1937+21 with $B_L = 0.001$ Hz., but the position errors are larger. Also, for J0218+4232, the MLE updates now outperform the DPLL estimates and should be the values given to the underlying navigation EKF.

Figure 5.71 contains the simulation results for tracking the cislunar trajectory using the Crab pulsar signal for a simulation time of 200 seconds with T = 10 seconds and $B_L = 0.00025$ Hz. It can be seen that the phase tracking algorithm successfully tracks the cislunar trajectory. There is not a bias apparent in the DPLL position estimates even with the smaller loop noise bandwidth of $B_L = 0.00025$ being used. This is due to the much smaller loop update time of T = 10 seconds reducing the buildup of the dynamic stress error. The DPLL position estimates are outperforming the MLE outputs. The velocity and acceleration errors are bounded, but it is difficult to tell if they are improving over the length of the simulation. It is harder to see any general longer term trends in the phase tracking results due to the limitation of the 200 second simulation length.

Overall, from the figures containing the cislunar trajectory tracking results, it can be seen that the cislunar trajectory can be successfully navigated using the signals of all the pulsars simulated: B1821-24, B1937+21, J0218+4232, and the Crab pulsar. With the smaller loop noise bandwidth choice of $B_L = 0.00025$ Hz. there is an apparent bias in the position error plots relative to the MLE outputs for some of the pulsars potentially due to the dynamic stress. For PSR B1821-24 and the Crab pulsar the DPLL position estimates outperform the MLE outputs and should be fed to the navigation EKF, and for B1937+21 and J0218+4232 the opposite is true.

Table 5.27: Simulation results for tracking the example cislunar trajectory with a detector area of 1 m^2 and a loop noise bandwidth of $B_L = 0.00025$. The simulation time with the Crab pulsar is 200 seconds compared to 54000 seconds with the other pulsars. One dimensional tracking results along LOS to pulsar.

Pulsar	B1821-24	B1937+21	J0218+4232	Crab
T, s	200	4000	4000	10
CRLB, km	3.07	1.02	4.19	1.22
Averaged MLE Position Error (km)	3.36	3.44	5.95	1.44
End Point RMS Position Error (km)	3.49	11.79	24.9	0.61
Averaged Position Error (km)	4.43	13.91	29.67	0.63
End Point RMS Velocity Error (m/s)	1.59	1.52	3.60	0.53
Averaged Velocity Error (m/s)	2.50	1.79	4.21	0.51

A compilation of the cislunar phase tracking results with $B_L = 0.00025$ Hz is included in Table 5.27. All four pulsars were simulated with this loop noise bandwidth. The table contains the DPLL parameters T and B_L along with average

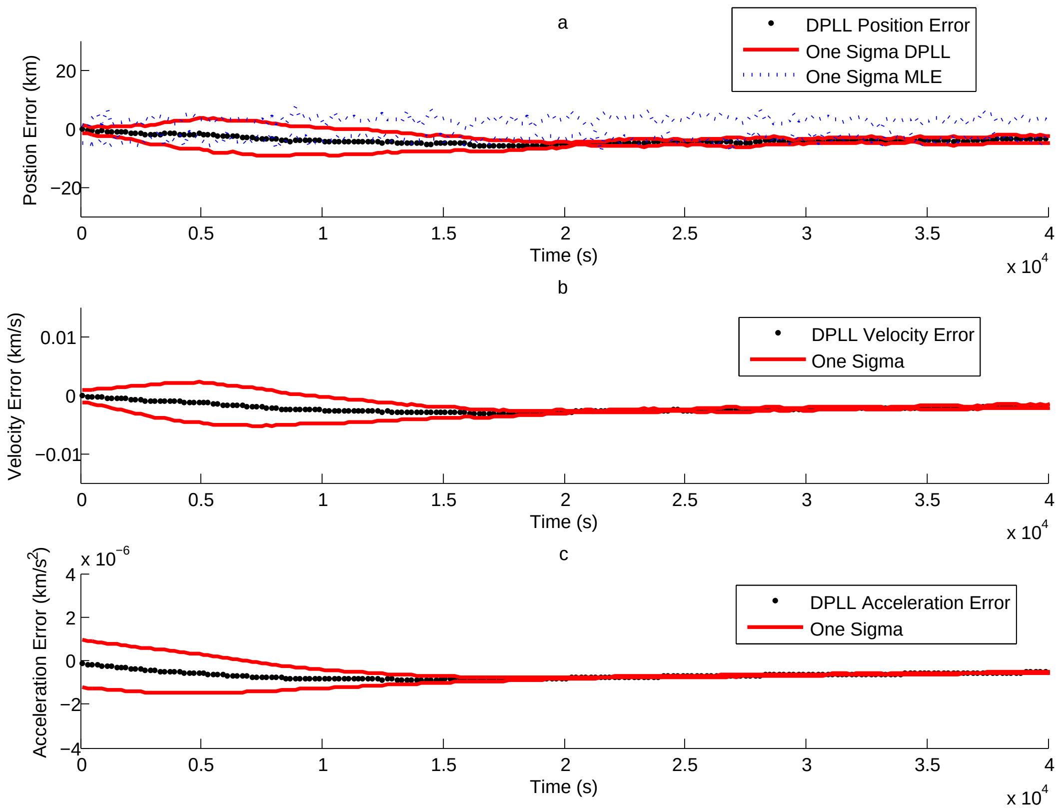

Figure 5.66: Phase tracking simulation results for the sample cislunar trajectory using PSR B1821-24 with T = 200 seconds, B_L = 0.00025 Hz, and a detector area of 1 m ^{2}. One dimensional tracking results along LOS to pulsar.

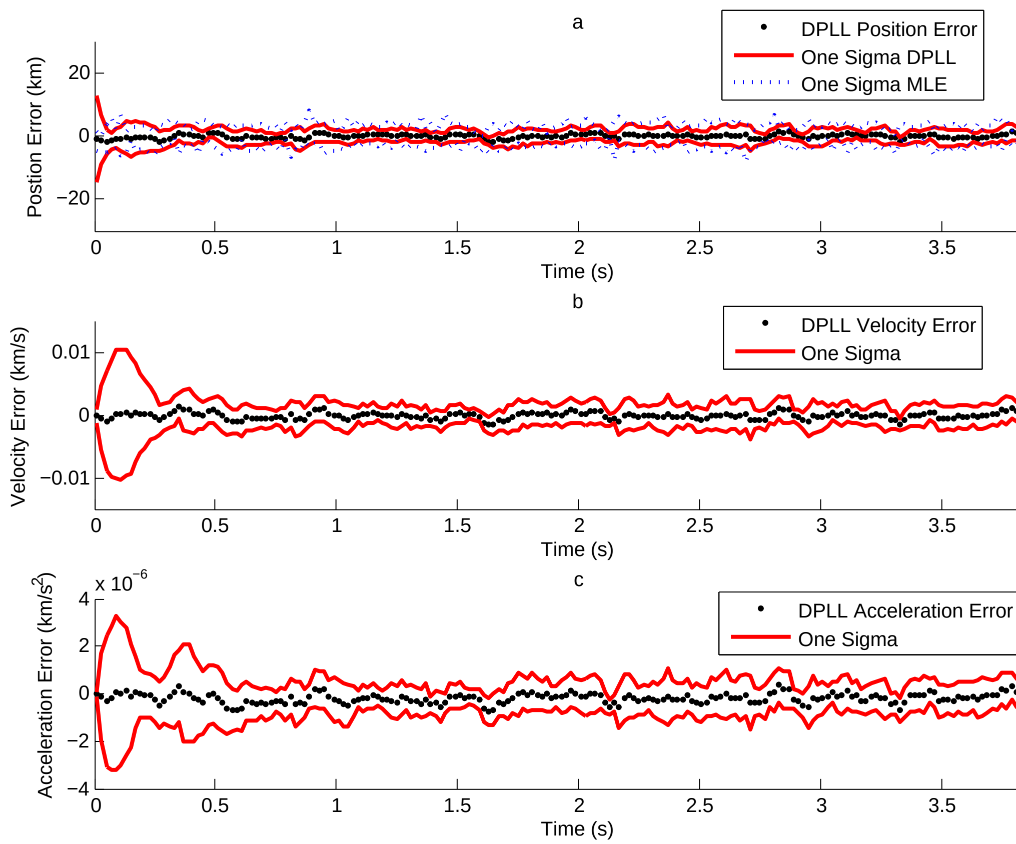

Figure 5.67: Phase tracking simulation results for the sample cislunar trajectory using PSR B1821-24 with T = 200 seconds, $B_L = 0.001$ Hz, a detector area of 1 m ^{2}, and a higher position initial condition error level. One dimensional tracking results along LOS to pulsar.

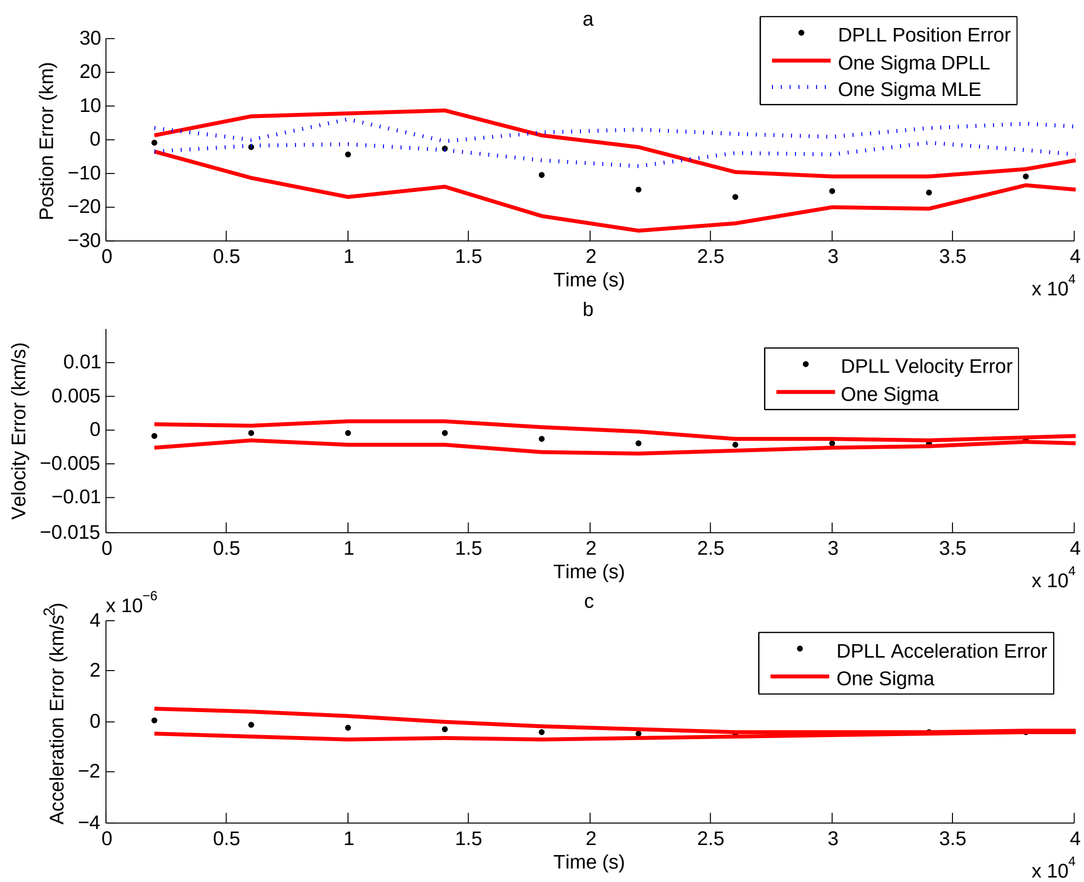

Figure 5.68: Phase tracking simulation results for the sample cislunar trajectory using PSR B1937+21 with T = 4000 seconds, B_L = 0.00025 Hz, and a detector area of 1 m ^{2}. One dimensional tracking results along LOS to pulsar.

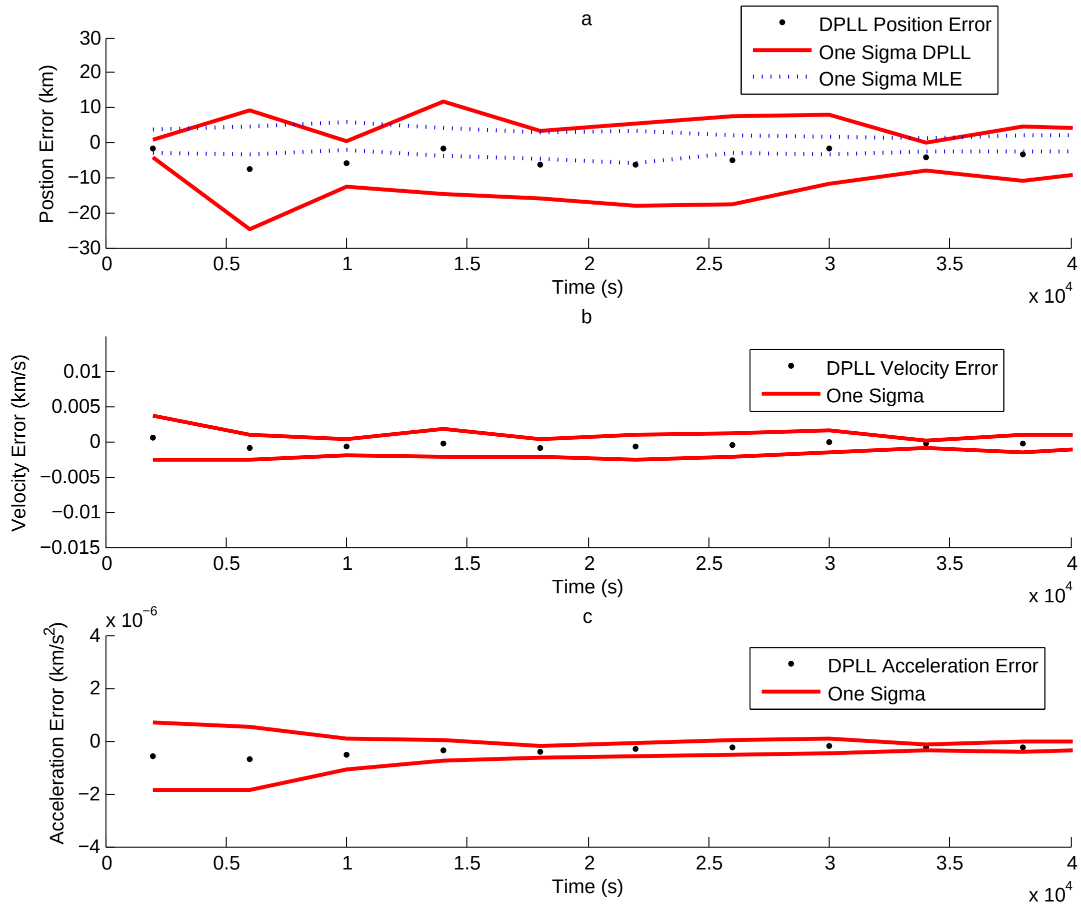

Figure 5.69: Phase tracking simulation results for the sample cislunar trajectory using PSR B1937+21 with T = 4000 seconds, $B_L = 0.001$ Hz, and a detector area of 1 m ^{2}. One dimensional tracking results along LOS to pulsar.

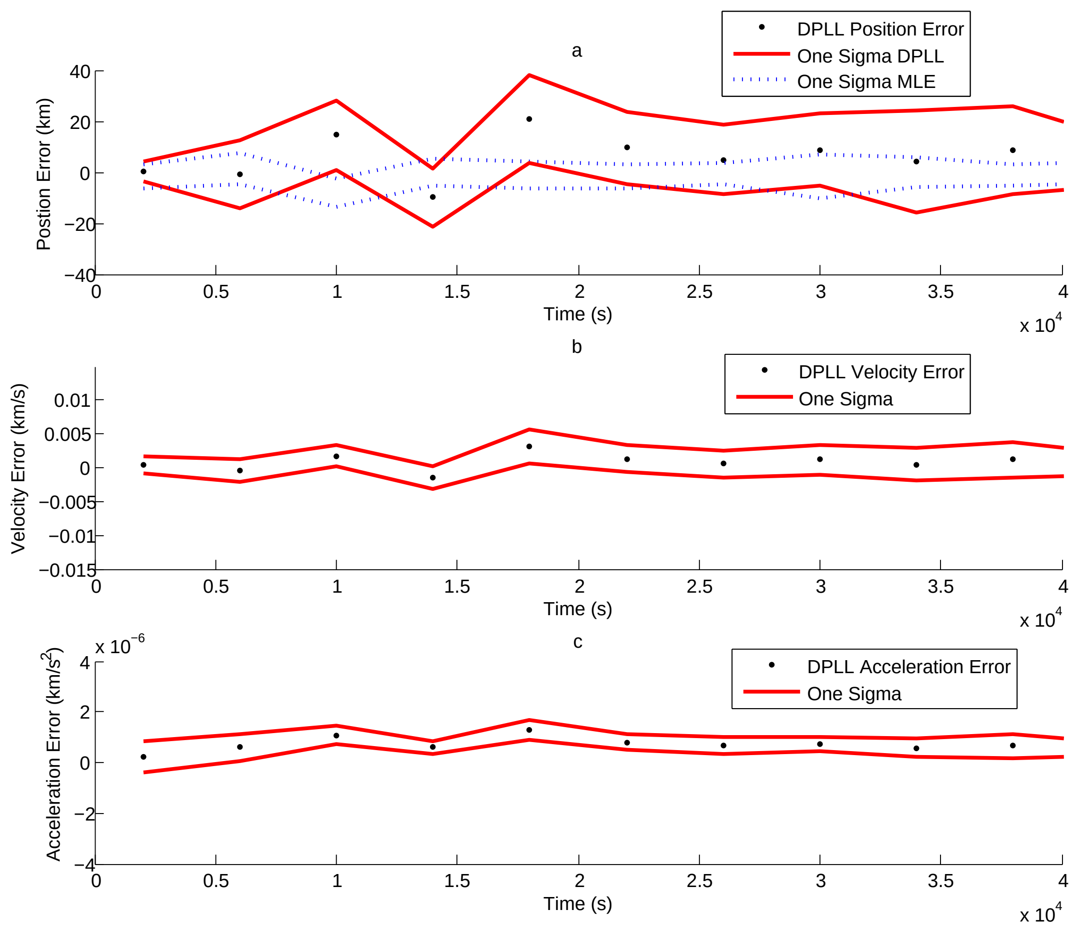

Figure 5.70: Phase tracking simulation results for the sample cislunar trajectory using PSR J0218+4232 with T = 4000 seconds, $B_L = 0.001$ Hz, and a detector area of 1 m ^{2}. One dimensional tracking results along LOS to pulsar.

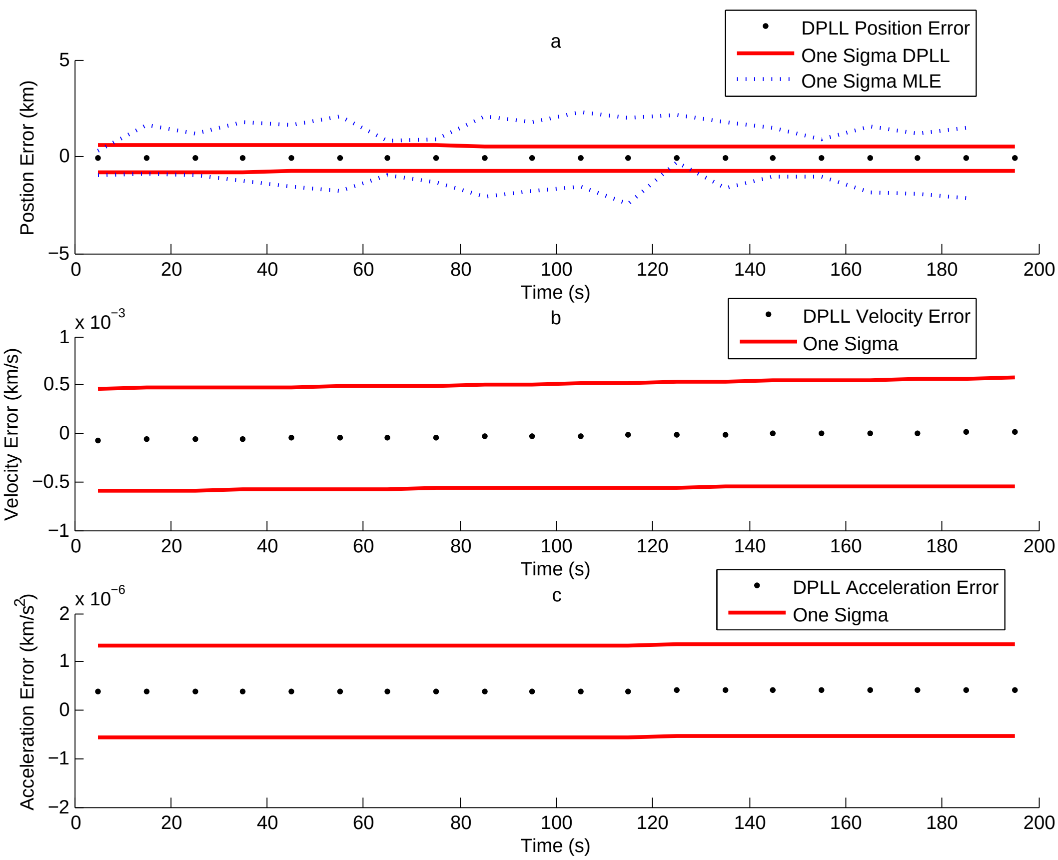

Figure 5.71: Phase tracking simulation results for the sample cislunar trajectory using the Crab pulsar with T = 10 seconds, B_L = 0.00025 Hz, and a detector area of 1 m ^{2}. One dimensional tracking results along LOS to pulsar.

Table 5.28: Simulation results for tracking the example cislunar trajectory with a detector area of 1 m^2 and a loop noise bandwidth of $B_L = 0.001$. One dimensional tracking results along LOS to pulsar.

Pulsar	B1821-24	B1937+21	J0218+4232
T, s	200	4000	4000
CRLB, km	3.07	1.02	4.19
Averaged MLE Position Error (km)	3.37	3.07	5.49
End Point RMS Position Error (km)	2.60	4.22	11.14
Averaged Position Error (km)	2.26	9.76	15.82
End Point RMS Velocity Error (m/s)	2.09	0.46	1.48
Averaged Velocity Error (m/s)	2.02	1.33	2.20

MLE position error, the end point and average DPLL position errors, and the end point and average DPLL velocity errors. For all of the pulsars the MLE position results compare favorably to the CRLB. PSR B1937+21 has a larger offset than the other pulsars, as has been seen with all of the other simulation scenarios. The end point and average RMS DPLL position errors are outperformed by the MLE for B1821-24, B1937+21, and J0218+4232, but as explained previously this is not a problem because the MLE would not be able to run as formulated without feedback of frequency and frequency derivative from the DPLL. The achievable position error to feed to the navigation EKF is the better of the DPLL and MLE position errors depending on the pulsar and it ranges from 0.62 km for the Crab pulsar to 5.95 km for J0218+4232. The end point and average RMS position and velocity errors are relatively similar for all of the pulsars. This indicates that there is not much long term settling in the DPLL outputs.

Table 5.28 contains the cislunar results with $B_L = 0.001$ Hz. The three MSPs were simulated with this loop noise bandwidth, but not the Crab pulsar. Again, the table contains the DPLL parameters T and B_L along with average MLE position error, the end point and average DPLL position errors, and the end point and average DPLL velocity errors. All of the MLE position error values compare well to the CRLB with B1937+21 having the largest offset. For PSR B1821-24 the end point RMS DPLL position error is smaller the MLE average value. The end point and average RMS DPLL position errors are outperformed by the MLE for B1937+21 and J0218+4232. The achievable position error to feed to the EKF ranges from 2.60 km for B1821-24 to 5.49 km for J0218+4232. The end point and average RMS position and velocity errors are again similar for all three pulsars.

Comparing the results in Table 5.27 to those in Table 5.28 demonstrates the difference in the simulations resulting from the change in loop noise bandwidth from $B_L = 0.00025$ Hz to $B_L = 0.001$ Hz. The position error estimation accuracies are slightly improved with $B_L = 0.001$ Hz for B1937+21 and J0218+4232 and are improved from 3.36 km to 2.60 km for B1821-24. This improved accuracy combined with the lack of a bias in position error in the plots for the simulations $B_L = 0.001$ Hz. demonstrates that this is the better choice for loop noise bandwidth for this cislunar trajectory. Theoretically, the smaller bandwidth of $B_L = 0.00025$ Hz. should allow for better position estimation accuracy, while the larger $B_L = 0.001$ Hz. accounts better for model errors due to the dynamic stress. The dynamic stress model errors must be large enough in this scenario to offset the ability of decreasing the bandwidth to improving steady state accuracy.

As expected, the cislunar trajectory phase tracking results provide an intermediate example to the performance with the simulated Earth orbits and heliocentric trajectories. For B1821-24, B1937+21, J0218+4232, and the Crab pulsar the phase tracking algorithm is able to track the cislunar trajectory with position accuracies ranging from under a kilometer for the Crab and between 2 km and 6 km for the other three pulsars. This performance is similar to the heliocentric trajectory results seen in the previous sections. These results demonstrate that the cislunar trajectory is another example of an orbit situation where there are many usable pulsars for phase tracking to go along with the MSL and Cassini trajectories as opposed to the Earth orbits where only PSR B1821-24 and the Crab pulsar were usable with reasonable detector area choices.

5.6 Summary

In this chapter, the proposed new phase tracking algorithm to extend capabilities to tracking millisecond period pulsars that are attractive for use in navigation was presented and tested in comprehensive detail. This algorithm built on the previous phase tracking work, but overcomes the major drawbacks seen before. The algorithm consists of a higher order Taylor expansion in the maximum likelihood estimator for phase along with feedback of frequency and frequency derivative from a third-order phase-locked loop. This allowed for the relaxation of the signal model assumptions to assume constant acceleration along the line-of-sight to the source. This led to the possibility to use longer block lengths for the phase estimation and smaller detector areas.

A range of simulated orbits with a variety of dynamic stress conditions were simulated in order to test the capabilities and limits of the proposed phase tracking algorithm. The pulsars considered included the Crab pulsar and four millisecond period pulsars: B1821-24, B1937+21, J0218+4232, and J0437+4715. The spacecraft trajectories included the low dynamic stress examples of a constant acceleration trajectory and interplanetary cruise trajectories from Cassini and MSL. An in between level of dynamic stress was considered with a cislunar transfer trajectory. High levels of dynamic stress were investigated with Earth orbits including: DirecTV, GPS, and ISS orbits.

For the constant acceleration trajectory, tracking was demonstrated with all of the pulsars considering both an initial state with perfect knowledge and also initial condition errors that corresponded with a handoff from the DSN. Phase tracking was also shown for all of the pulsars with the two interplanetary trajectories. For each of these trajectories PSR J0437+4715 had the highest position tracking errors even when considering a larger detector area. This pulsar was not as conducive to use for phase tracking as the others due to its much lower SNR.

The rest of the pulsars were all shown to track the cislunar trajectory with position errors under 6 km. For the Earth tracking results, only the Crab pulsar and B1821-24 were able to track the ISS orbit. PSRs B1937+21 and J0218+4232 needed larger areas of 8 m^2 and 10 m^2 to track the DirecTV and GPS orbits, respectively. A trade-study was compared to determine for each pulsar the detector areas required to track the dynamic stress conditions represented by each orbit.

In general the choices of loop noise bandwidth B_L and block update time T were constrained by the dynamic environment in each scenario and were directly related to the achievable performance. The smaller B_L the smaller the steady state error, but the higher the dynamic stress the higher B_L needs to be to compensate.

The phase tracking algorithm was shown to work well in general for a wide range of pulsar and orbit conditions. The pulsars most suitable for tracking in each situation were determined and unsurprisingly it was the ones with the higher SNRs. The phase tracking algorithm had the most difficulty in the high dynamic stress environments of the Earth orbits. For the interplanetary and cislunar trajectories the algorithm worked well and showed the potential to produce position estimates with errors under 6 to 7 km for all of the pulsars besides J0437-4715 using a reasonably sized 1 m^2 area detector.

Chapter 6: Three-Dimensional Combined Navigation

6.1 Overview

The phase tracking algorithm presented in Chapter 5 provides range measurements of a spacecraft along the LOS to a pulsar. This chapter introduces and analyzes the performance of a navigation filter that processes phase-tracking estimates from multiple different pulsars to track three-dimensional spacecraft position and velocity. Two different detector configurations are considered to provide a range of performance conditions to test the use of the navigation filter to process phase tracking estimates in various ways. Spacecraft were simulated with either a single gimbaled detector to observe pulsars in a scheduled sequence or with three separate gimbaled detectors that can track up to three pulsars simultaneously.

Section 6.2 introduces the navigation filter including a description of the three-dimensional combined navigation concept incorporating an Extended Kalman Filter (EKF) to process the phase tracking results from multiple pulsars to determine the spacecraft state. Previous EKF work with x-ray pulsar-based spacecraft navigation is referenced and adapted to the particular problem of incorporating pulsar phase tracking measurements. Different elements of the EKF processing are discussed including the state transition matrix, the covariance matrix, and the specific measurement model that corresponds to incorporating pulsar range measurements via phase tracking estimation.

Section 6.3 provides an overview of the simulation structure. The various orbit and pulsar scenarios and parameters for the phase tracking algorithm and the EKF are detailed. The setup and operation for the three detector and single detector filtering environments are discussed. The way the EKF processes the DPLL/MLE results from the phase tracking loop is introduced. The pulsar visibility on the orbits is investigated and used to determine scheduling for the pulsar phase tracking measurements to feed to the EKF.

The simulation results are presented in Section 6.4. Various three-dimensional orbital state estimation scenarios are considered. The results for the three and single detector setups are outlined and compared. The performance with the each pulsar schedule choice is detailed. A general discussion comparing the performance across the different orbit and detector scenarios concludes the chapter.

6.2 Navigation Filter

Kalman filtering as discussed in [122] is used to blend spacecraft dynamics and pulsar phase tracking range measurements. Specifically, the nonlinear extension known as the Extended Kalman Filter (EKF) was used. The EKF is built upon the framework of [1] – [98] and [72] for x-ray pulsars and gamma ray sources, respectively. In particular, the EKF developed by Dr. Suneel Sheikh to produce results for filtering range measurements generated from pulse time of arrival estimates in [1] was instrumental as an initial framework that was built upon and expanded to produce the EKF used here with pulsar phase tracking range measurements.

The navigation filter used to simulate three-dimensional combined navigation consists of a standard EKF that recursively incorporates phase tracking range measurements with an estimate of the orbital state. The orbital state estimates are provided using a numerically propagated position and velocity solution. This numerical propagation is computed based on the methods of [98], [123], [124], [125], and [126]. Inputs to the EKF are based on the expected accuracy of the phase tracking algorithm for the scenario considered taking into account the trajectory and pulsar. The blending together of phase tracking estimates from multiple pulsars in different directions will improve the position and velocity estimation results that were available using the DPLL and MLE alone for individual pulsars.

Most of the EKF processing is standard based on the above cited filtering references, but enough detail will be provided in the following subsections to introduce the changes and particulars relevant to the problem of Kalman filtering x-ray pulsar phase tracking measurements. The general framework of [98] is followed.

6.2.1 State Dynamics

The three-dimensional position and velocity, referenced to an inertial central body, are used as the states to describe spacecraft motion. The state vector, $\mathbf{x}$, has six elements and is made up of a combination of the three dimensional position and velocity vectors, $\mathbf{r}$ and $\mathbf{v}$, respectively as follows:

$$\mathbf{x} = \begin{bmatrix} \mathbf{r} \\ \mathbf{v} \end{bmatrix}. \tag{6.1}$$

This state vector can be used to define the dynamics of a nonlinear system as follow:

$$\dot{\mathbf{x}}(t) = \begin{bmatrix} \mathbf{v} \\ \mathbf{a} \end{bmatrix} = \mathbf{f}(\mathbf{x}(t), t) + \eta(t), \tag{6.2}$$

where $\mathbf{f}$ is a nonlinear function of the state vector, η represents the noise from the unmodeled state dynamics, and $\mathbf{a}$ is the spacecraft acceleration. An initial condition known at time t_0 can be represented as

$$\mathbf{x}_0 = \mathbf{x}(t_0) = \begin{bmatrix} \mathbf{r}(t_0) \\ \mathbf{v}(t_0) \end{bmatrix}. \tag{6.3}$$

The following acceleration effects are modeled in order to represent the spacecraft orbit dynamics: two-body acceleration with the central body, $\mathbf{a}_{two-body}$; effects from a non-spherical gravitational potential for the central body, $\mathbf{a}_{non-spherical}$; drag effects from the atmosphere of the central body, $\mathbf{a}_{drag}$; any third-body gravitational effects, $\mathbf{a}_{third-body}$; and any higher-order effects that are left unmodeled and considered negligible, $\mathbf{a}_{H.O.T.}$. The total spacecraft acceleration is the sum of these effects:

$$\mathbf{a}_{Total} = \mathbf{a}_{two-body} + \mathbf{a}_{non-spherical} + \mathbf{a}_{drag} + \mathbf{a}_{third-body} + \mathbf{a}_{H.O.T.}. \tag{6.4}$$

The modeling of these effects in the processing of the EKF followed the methods presented in [125] and [126].

6.2.2 State Transition and Covariance Matrices

The states of the navigation EKF are the errors in the state vector, $\delta\mathbf{x}$. The error states are the difference of the true states and the estimates of the state, $\tilde{\mathbf{x}}$:

$$\mathbf{x} = \tilde{\mathbf{x}} + \delta\mathbf{x}. \tag{6.5}$$

The state transition matrix is used to determine the error state at a future time t as follows:

$$\delta\mathbf{x} = \mathbf{\Phi}(t, t_0)\delta\mathbf{x}_0 \tag{6.6}$$

The following equations can be solved to find the state transition matrix:

$$\mathbf{\Phi}(t, t_0) = \mathbf{F}(t)\mathbf{\Phi}(t, t_0) \tag{6.7}$$

$$\mathbf{\Phi}(t_0, t_0) = \mathbf{I}, \tag{6.8}$$

where $\mathbf{I}$ is the identity matrix and $\mathbf{F}(t)$ is the Jacobian matrix, defined as the derivative of the state dynamics with respect to each state. The Jacobian is represented as:

$$\mathbf{F}(t) = \begin{bmatrix} \frac{\delta\mathbf{v}}{\delta\mathbf{r}} & \frac{\delta\mathbf{v}}{\delta\mathbf{v}} \\ \frac{\delta\mathbf{a}}{\delta\mathbf{r}} & \frac{\delta\mathbf{a}}{\delta\mathbf{v}} \end{bmatrix} = \begin{bmatrix} \mathbf{0} & \mathbf{I} \\ \frac{\delta\mathbf{a}}{\delta\mathbf{r}} & \frac{\delta\mathbf{a}}{\delta\mathbf{v}} \end{bmatrix}, \tag{6.9}$$

where $\mathbf{0}$ is a properly sized matrix of all 0 entries. The second row of the Jacobian is computed by differentiating the model of the spacecraft acceleration expressed in Eq. (6.4).

The covariance matrix is a measure of the statistical uncertainty in the error states, $\delta\mathbf{x}$, and can be expressed for the kth step in a discrete system as follows [122]:

$$\mathbf{P}_k = \ \mathrm{E}[\delta \mathbf{x}_k \delta \mathbf{x}_k^T]. \tag{6.10}$$

The process noise matrix describes the uncertainty in the state variable dynamics and can be expressed for the kth step in a discrete system as:

$$\mathbf{Q}_k = \ \mathrm{E}[\delta \omega_k \delta \omega_k^T]. \tag{6.11}$$

The individual error state noise, ω, is assumed to be uncorrelated with respect to the states, $\mathrm{E}[\delta \mathbf{x}_k \omega_k^T] = \mathbf{0}$, and white noise, i.e., uncorrelated with respect to time.

The dynamics of the covariance matrix can be represented in discrete form using [122]

$$\mathbf{P}_{k+1}^- = \mathbf{\Phi}_k \mathbf{P}_k \mathbf{\Phi}_k^T + \mathbf{\Gamma}_k \mathbf{Q}_k \mathbf{\Gamma}_k^T. \tag{6.12}$$

The matrix $\mathbf{\Gamma}$ is an identity matrix due to the system state dynamics expressed in Eq. (6.2). The a priori time update of the EKF is generated using Eqs. (6.6) and (6.12) [122].

The observations also have a nonlinear relationship with respect to the states. These observations can be modeled as a measurement, $\mathbf{y}$, which is represented as follows:

$$\mathbf{y}(t) = \mathbf{h}(\mathbf{x}(t), t) + \nu(t), \tag{6.13}$$

where $\mathbf{h}$ is a nonlinear function of the state vector and time and ν is the measurement noise with each observation. The measurement residual $\mathbf{z}(t)$ is defined in order to relate the observations to the error-states of the EKF by comparing the measurement to the estimated value given in Eq. (6.13) [122]. The measurement residual can be expressed to first order as:

$$\mathbf{z}(t) = \mathbf{y} - \mathbf{h}(\tilde{\mathbf{x}}) = \frac{\delta \mathbf{h}(\tilde{\mathbf{x}})}{\delta \mathbf{x}} \delta \mathbf{x} + \nu(t) = \mathbf{H}(\tilde{\mathbf{x}}) \delta \mathbf{x} + \nu(t), \tag{6.14}$$

where $\mathbf{H}$ is the measurement matrix and it is defined to have its elements as the partial derivatives of the measurement with respect to the states. The discrete form of the measurement residual is as follows [122]:

$$\mathbf{z}_{k+1} = \mathbf{H}_{k+1} \delta \mathbf{x}_{k+1} + \nu_{k+1}. \tag{6.15}$$

The optimal Kalman gain, $\mathbf{K}_{opt}$, for the EKF can be computed using [122]

$$\mathbf{K}_{k+1_{opt}} = \mathbf{P}^{-}_{k+1} \mathbf{H}^{T}_{k+1} (\mathbf{H}_{k+1} \mathbf{P}^{-}_{k+1} \mathbf{H}^{T}_{k+1} + \mathbf{R}_{k+1})^{-1}, \tag{6.16}$$

where the expectation of the measurement noise is represented as $\mathbf{R} = \mathrm{E}[\nu \nu^T]$. The a posteriori measurement update of the state estimates and covariance matrix can by computed using the optimal Kalman gain from Eq. (6.16) as follows [122] [127]:

$$\tilde{\mathbf{x}}^{+}_{k+1} = \tilde{\mathbf{x}}^{-}_{k+1} + \mathbf{K}_{k+1_{opt}} \mathbf{z}_{k+1} \tag{6.17}$$

$$\mathbf{P}^{+}_{k+1} = (\mathbf{I} - \mathbf{K}_{k+1_{opt}} \mathbf{H}_{k+1}) \mathbf{P}^{-}_{k+1}. \tag{6.18}$$

A measurement residual test was used to remove any pulsar-based measurements that have improperly low measurement noise in order to reduce the impacts on the filter performance. This allowed the filter to ignore outlier measurements that were much larger than the performance estimate of the EKF. This residual test was based on the innovations of the EKF, which are calculated in the optimal

Kalman gain equation in Eq. (6.16) [122]. The discrete form of the innovation, α, is defined for a nonlinear system as

$$\alpha_{k+1} = \mathbf{H}_{k+1}\mathbf{P}^{-}_{k+1}\mathbf{H}^{T}_{k+1} + \mathbf{R}_{k+1}. \tag{6.19}$$

The residual for an individual scalar measurement from Eq. (6.15) can be computed as

$$z_i = \mathbf{w}_i \delta\mathbf{x}, \tag{6.20}$$

where $\mathbf{w}_i$ is the ith row of $\mathbf{H}$ and N is the number of states. The innovation that corresponds to this measurement is defined as the ith diagonal element of α_{k+1} in Eq. (6.19) and will be written as $\alpha_i = \alpha_{k+1}(i,i)$. The residual test for this individual measurement can be written as [98]

$$z_i \leq m\alpha_i, \tag{6.21}$$

where m is a scalar value chosen to be the acceptable proportional value of the innovation for the test. This results in the processing of the measurement as long as it is less than or equal to m-times the innovations of the EKF. For the EKF designed for the simulations presented in the following sections m was chosen to be 2 or 5 depending on the scenario and the initial filter covariance chosen.

6.2.3 EKF Measurement Model for X-ray Pulsar Phase Tracking

The EKF was designed to utilize measurements from phase tracking x-ray pulsars as defined and simulated in Chapter 5. The phase tracking algorithm is used to provide a measurement of the spacecraft's relative range along the LOS to the pulsar tracked. Each output is a measurement of the range referenced to the previous estimate, which removes any cycle ambiguity issues in the phase measurements when the update time of the DPLL is small enough. As long as the range the spacecraft travels between measurements is smaller than the wavelength of the source pulsar, $\frac{c}{f}$, there is no problem with ambiguity.

A phase tracking measurement can be written in the form of the Kalman filter measurement equation, Eq. (6.14), by computing the difference between the range measurement and the estimated range using the Kalman filter error states. This is represented as follows:

$$\mathbf{z} = \mathbf{y} - \mathbf{h}(\tilde{\mathbf{x}}) = \mathbf{r}_{DPLL} - \hat{\mathbf{n}} \cdot \delta\mathbf{x} \tag{6.22}$$

where $\mathbf{r}_{DPLL}$ is the range measurement from the phase tracking algorithm and $\hat{\mathbf{n}}$ is the unit vector in the direction of the pulsar. The EKF measurement matrix can be written as

$$\mathbf{H} = [\hat{\mathbf{n}}^T \ 0 \ 0 \ 0]. \tag{6.23}$$

6.3 Simulation Structure

Two different detector configurations were considered to investigate the performance of the navigation filter supported by phase tracking estimates. A spacecraft with three x-ray detectors was simulated to test the ideal case of being able to track up to three pulsars simultaneously. A more realistic scenario, in the near term, was modeled using a spacecraft with a single x-ray detector that observes various pulsars in a scheduled sequence. In both cases, the detectors are assumed to be gimbaled to allow for them to rotate to track various pulsars in the sky. The time necessary to rotate the single detector from tracking one to another was not modeled. In order to model this in the future, a set amount of time could be determined to let the filter states evolve without any measurements to account for the time necessary to change the spacecraft or detector orientation and lock on to the next pulsar in the observation sequence.

An area of 1 m^2 was considered with both the single detector and three detector setups. This area was chosen to match the simulations performed in the previous chapter. This was found to be a large enough area for tracking the set of pulsars considered, which are the set of five used in Chapters 4 and 5 to investigate the performance of the MLE and phase tracking algorithm, respectively. One of these five, PSR J0437-4715, was seen in Chapter 5 to have less than ideal phase tracking results and will not be used in the filter scheduling. The other four pulsars: B1821-24, B1937+21, J0218+4232, and the Crab will be considered in various configurations.

6.3.1 EKF and DPLL Setup and Parameters

Table 6.1 contains the necessary information obtained from the simulations in Chapters 4 and 5 that are needed as parameters to set in the processing of the EKF. This includes the observation time necessary for the RMS phase error from the MLE to converge to the CRLB and the expected phase estimation accuracy when using the DPLL-MLE parameters considered for phase tracking in Chapter 5 as listed in Table 5.15 and Table 5.19 for the heliocentric trajectories and Earth orbits, respectively.

In Table 6.1 the MLE-DPLL position accuracy corresponds to the achievable position accuracy from the phase tracking algorithm where the better output from either the MLE or DPLL position estimates are taken depending on the simulations in Chapter 5 for each pulsar, orbit, and DPLL parameter combination. As discussed earlier, in certain dynamic stress environments the MLE outputs outperform the DPLL position estimates and in some cases the DPLL is able to improve on the MLE values depending on the DPLL noise bandwidth. For the phase tracking algorithm both the MLE and DPLL outputs are necessary in tandem and the better estimate can be fed to the EKF if simulations are done to determine the performance for a given orbit and DPLL parameter set. T is the block time in seconds used in the phase tracking algorithm for each pulsar and orbit combination. B_L is the settling of the loop noise bandwidth that was used in the simulations to achieve the given position accuracy.

Three of the different orbit examples investigated in Chapter 5 will be considered for three-dimensional tracking with the navigation EKF: the portion of the MSL cruise trajectory, the cislunar transfer trajectory, and the DirecTV orbit. This gives a range of the different dynamic stress environments addressed in Chapter 5. The MSL and cislunar trajectories had good phase tracking results with a detector area of 1 m^2 with all four pulsars: B1821-24, B1937+21, J0218+4232, and the Crab. For these trajectories, since there are enough available pulsars, both the three detector and single detector configurations will be tested. With a 1 m^2 detector the phase tracking algorithm only produced results for the DirecTV orbit with PSR B1821-24

Table 6.1: Settings used for the parameters of the third-order DPLL for the Earth orbit and interplanetary trajectory phase tracking simulations.

Orbit	Pulsar	MLE-DPLL Position Accuracy, km	T, s	B_L, Hz
MSL	Crab Pulsar	0.61	10	0.00025
MSL	B1821-24	1.16	200	0.00025
MSL	B1937+21	2.53	4000	0.00025
MSL	J0218+4232	5.42	4000	0.00025
Cislunar	Crab Pulsar	0.61	10	0.00025
Cislunar	B1821-24	3.36	200	0.00025
Cislunar	B1937+21	3.44	4000	0.00025
Cislunar	J0218+4232	5.95	4000	0.00025
DirecTV	Crab Pulsar	0.47	10	0.005
DirecTV	B1821-24	2.47	150	0.005

and the Crab pulsar, so only there two pulsars will be considered in the observations for this orbit. Due to the lack of available pulsars, only the single detector configuration will be tested for the DirecTV orbit. Table 6.2 contains descriptions of the different scenarios tested with the navigation EKF. The information includes the orbit type, number of detectors, the pulsars considered, and the area of the detectors.

For the simulations in this chapter, the phase tracking estimates are not performed in real time with the processing of the EKF. At each block update, the EKF is fed an estimate of position equivalent to what the phase tracking simulation results suggested was possible for a DPLL in lock. The achievable position estimation error level from the phase tracking algorithm, included in Table 6.1, is used to generate a random representative measurement for the EKF. This is done due to

Table 6.2: Description of the different orbit and detector scenarios tested.

Orbit	Number of Detectors	Pulsars	Area, m^2
MSL	3	Crab, B1821-24, B1937+21, J0218+4232	1
MSL	1	Crab, B1821-24, B1937+21, J0218+4232	1
Cislunar	3	Crab, B1821-24, B1937+21, J0218+4232	1
Cislunar	1	Crab, B1821-24, B1937+21, J0218+4232	1
DirecTV	1	Crab, B1821-24	1

the computational difficulty of running a photon level phase tracking simulation in real time with the EKF. This will allow for a first level look at the feasibility and capabilities of using an EKF to incorporate phase tracking estimates from multiple pulsars in sequence.

If the DPLL loses lock, the state value in the EKF can be used to reacquire tracking using the transient-free acquisition techniques discussed in Chapter 5. The loop filter accumulators are preset with the best values for position, velocity, and acceleration from the EKF in a similar manner to the process with the initial conditions from the DSN handoff. If the EKF state has a similar covariance to the DSN handoff then this reacquisition can be performed without waiting for another communication from the DSN. For these simulations an idealized case where the DPLL is always in-lock will be considered.

Table 6.3 contains the settings and assumptions for the EKF model and scenario. The coordinate frame is J2000. The time step for the EKF, dt, is 10 seconds. The initial position error is set as 2 km in each component direction and the initial velocity error is 20 cm/s in each component. The initial covariance matrix for the EKF is $P_0 = \text{diag}([1\ 1\ 1\ 0.0003^2\ 0.0003^2\ 0.0003^2])$. The length of each simulation is three days or 259200 seconds. Each simulation scenario was run ten times with different random number generator seeds and the results were averaged.

Table 6.3: EKF settings and assumptions.

EKF Parameter	Value
Coordinate Frame	J2000
dt, s	10
Initial Position Error, km	[2, 2 , 2]
Initial Velocity Error, cm/s	[20, 20, 20]
P_0	$\text{diag}([1\ 1\ 1\ 0.0003^2\ 0.0003^2\ 0.0003^2])$
Simulation Length, days	3

6.3.2 Pulsar Visibility and Scheduling

The visibility of the pulsars determines their availability for scheduling in the navigation algorithm. Each orbit has its own environment that effects the visibility. Only line-of-sight blockages to the pulsars by various solar system bodies will be considered for determining the visibility in the simulations. Each orbit has different solar system bodies that are the most likely to block pulsar availability. For the DirecTV orbit, the Earth will block the Crab pulsar and B1821-24 for a large percentage of each orbit. For the cislunar orbit, the Earth and moon will occasionally block each of the pulsars considered. The MSL trajectory is a heliocentric orbit in interplanetary space and thus does not have many visibility blockages.

For each of the orbits, the pulsar visibility was modeled and plotted in order to determine the possible scheduling with the navigation filter simulations. A margin around the elevation angles that represent the locations of the solar system bodies was used to designate when a pulsar is blocked. The pulsar visibility plots are contained in Figures 6.1, 6.3, and 6.4 for the DirecTV orbit, the cislunar trajectory, and the MSL trajectory, respectively. These figures plot the elevation angles of the various pulsars over each orbit. The elevations are computed as the angle between the LOS to the pulsar and the unit direction of the central body for the orbit, either the Earth or the Sun. When the elevation angles are below a threshold of 10°, they are considered blocked and not visible. For the DirecTV orbit and the cislunar trajectory it is the Earth that is the greatest potential for blocking visibility, and for the MSL trajectory it is the sun. For the DirecTV orbit a three-dimensional plot overlaying the pulsar visibility on the trajectory around the Earth is included in Figure 6.2.

In Figures 6.1 and 6.2 it can be seen that the visibilities for the Crab pulsar and PSR B1821-24 do not overlap much for the DirecTV orbit. Each pulsar is visible when the spacecraft is on one side of the Earth during its orbit. There is a small window where neither pulsar is available, but generally an observation schedule could be built on tracking the two pulsars alternately over 12 hour time periods. The DirecTV orbital period is 24 hours due to being a geosynchronous orbit. In Figure 6.3 and Figure 6.4 it can be seen that all four pulsars have visibility throughout the simulated portion of each trajectory. This is as expected due to the trajectories being far enough away from any orbital bodies to reduce the risk

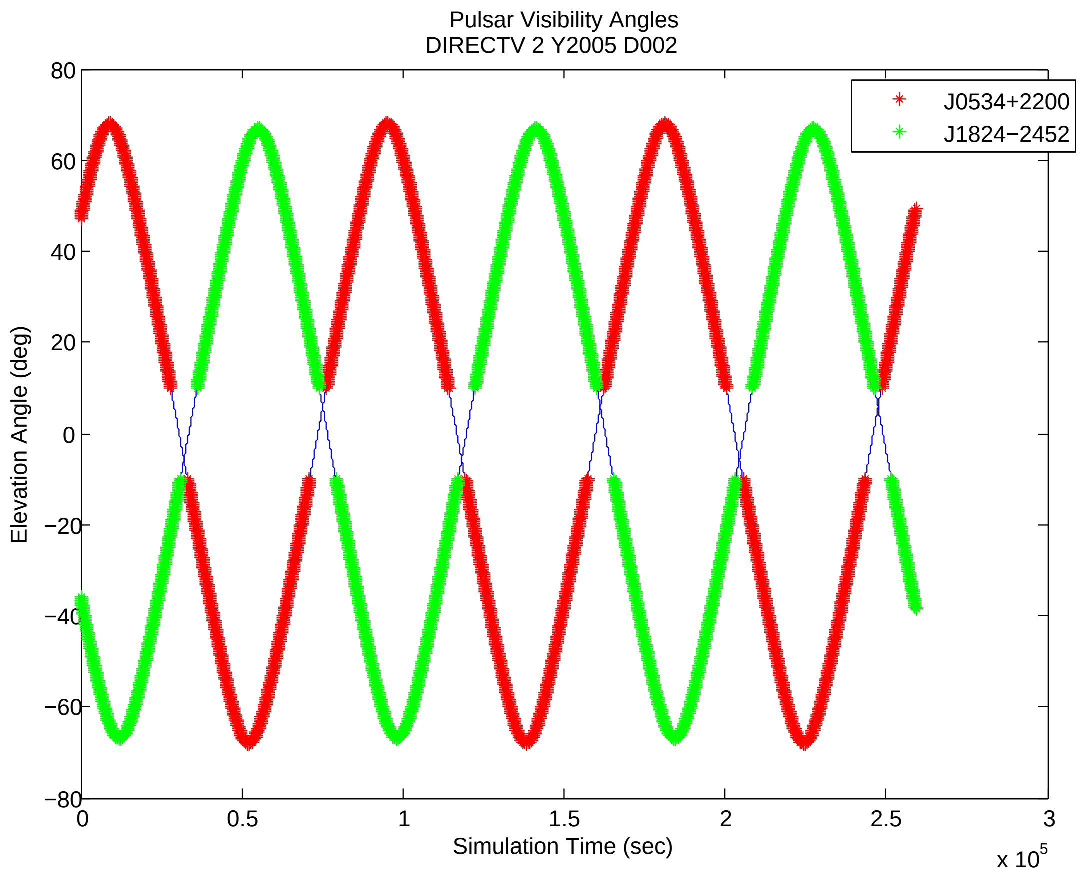

Figure 6.1: Plot of pulsar visibility for the DirecTV orbit. The elevation angles are plotted for B1821-24 and the Crab pulsar. A pulsar is considered visible when the angle between the LOS to the pulsar and the unit direction to the Earth is larger than 10° [98].

of occlusion. Thus, pulsar phase tracking schedules can be designed for these two trajectories without having to worry about visibility. For both the MSL and cislunar trajectories, pulsar blockages do not last long, due to the geometry relative to various solar system bodies, and can be planned around in the observation scheduling.

Observation schedules can be defined for each of the orbits using the visibility information. First, for the three detector case only the cislunar and MSL trajectories

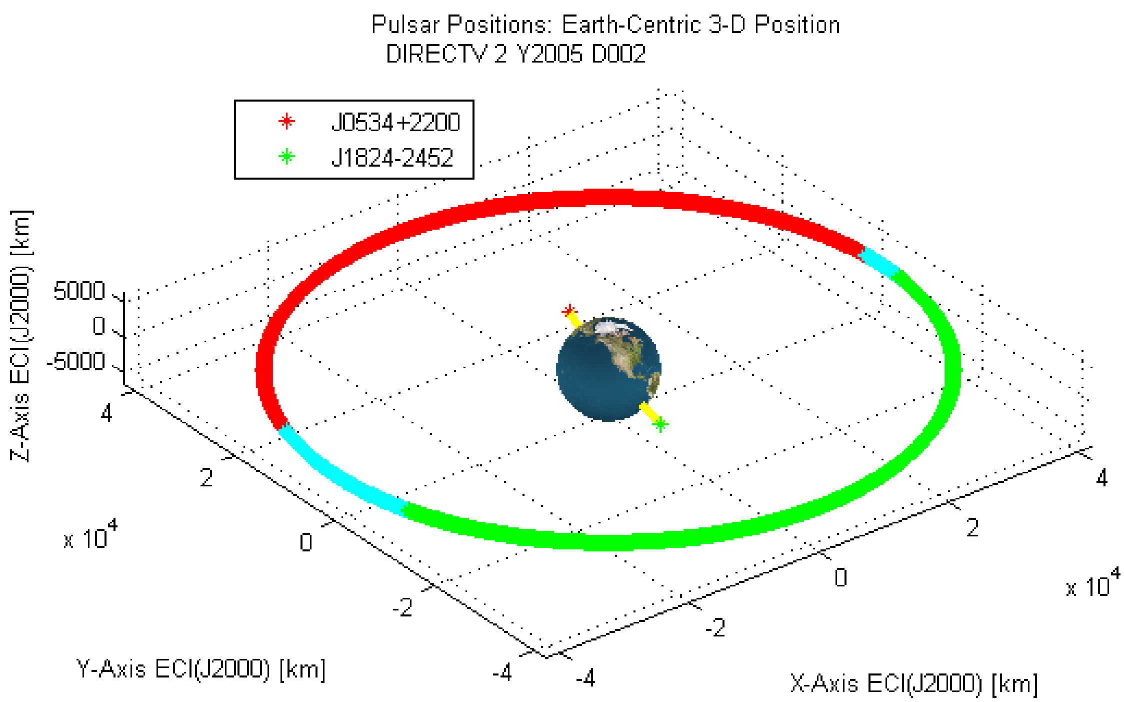

Figure 6.2: Three dimensional plot of pulsar visibility for the DirecTV orbit. The portion of the orbit where the Crab pulsar is visible is colored red, the portion where B1821-24 is visible is colored green, and the portion where neither are visible is light blue.

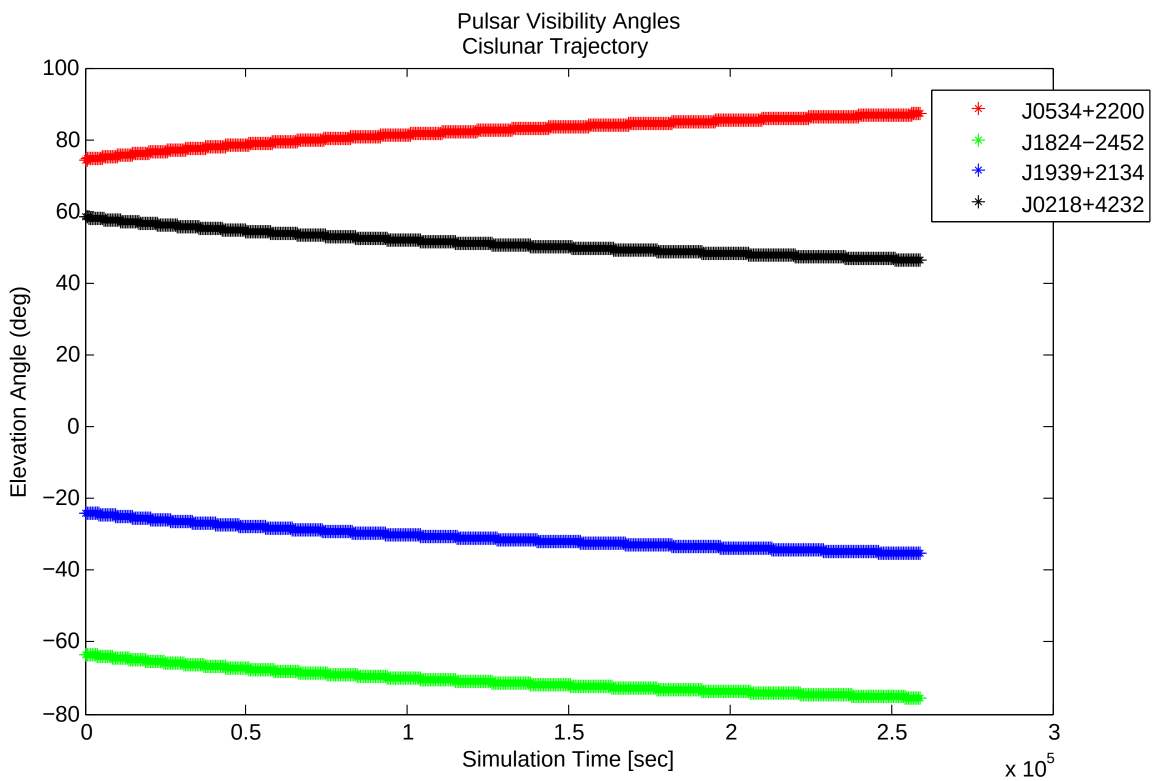

Figure 6.3: Plot of pulsar visibility for the cislunar trajectory. The elevation angles are plotted for B1821-24, B1937+21, J0218+4232, and the Crab pulsar. A pulsar is considered visible when the angle between the LOS to the pulsar and the unit direction to the Earth is larger than 10°.

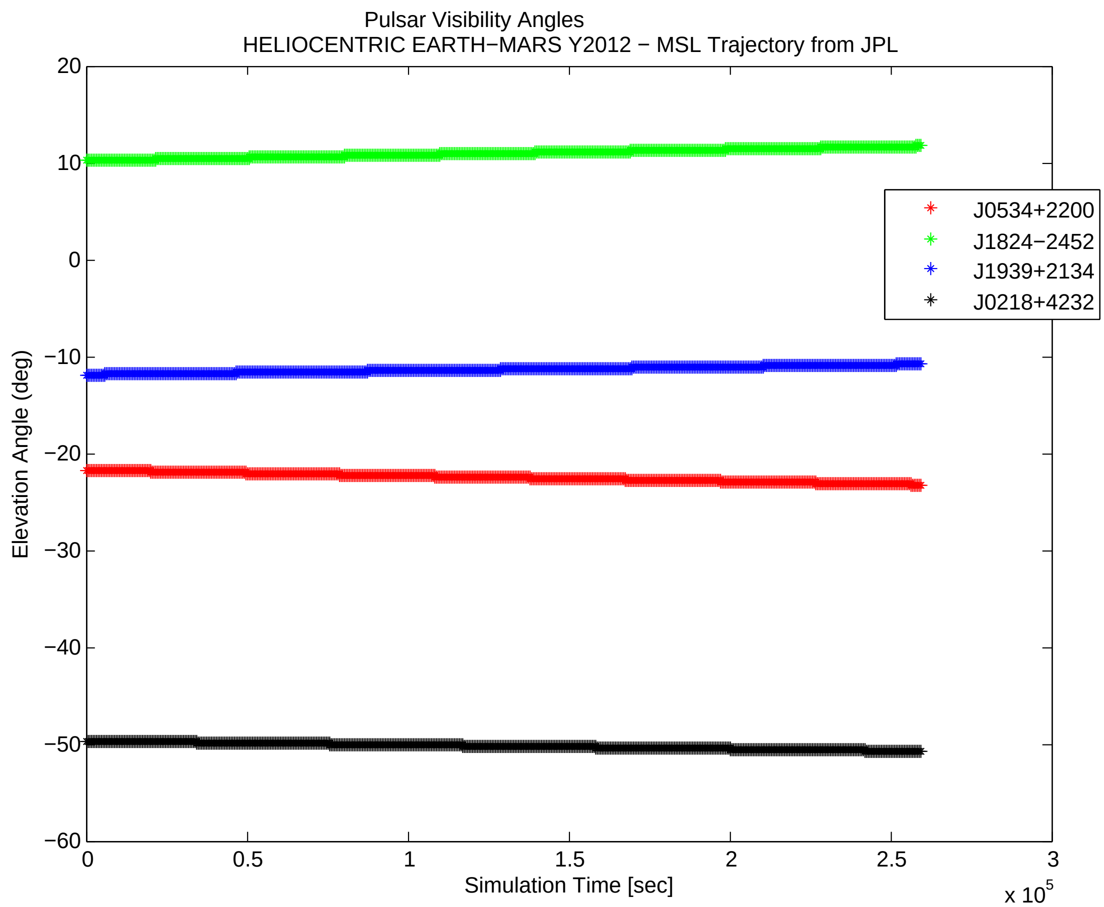

Figure 6.4: Plot of pulsar visibility for the MSL trajectory. The elevation angles are plotted for B1821-24, B1937+21, J0218+4232, and the Crab pulsar. The angles are computed between the LOS to the pulsars and the unit direction of the Sun.

were simulated due to the number of pulsars available. As seen above, there are no visibility limitations for these trajectories for the portions of the orbits simulated. Two different methods will be tested with three detectors: taking a subset of three of the pulsars and phase tracking each of them for the whole three day simulation or using all four pulsars in a rotation where three are phase tracked for the first 12000 seconds and then every 12000 seconds one of the pulsars is switched out to add in the one not currently being observed. Table 6.4 contains the descriptions of the pulsar observation schedules for the five three-detector scenarios considered for both the cislunar and MSL trajectories. When there is not rotation of the detectors, the three pulsars are tracked for the entire three day simulation time. There is an offset added between the starts of the three pulsar observations since the EKF processes the measurements sequentially and can not add two at the same filter time step. If two pulsar measurements line up at the same time step, the one that is less frequent is incorporated into the EKF and the other is skipped.

For the single detector simulations there are visibility constraints with the DirecTV orbit, but again none for the cislunar and MSL trajectories. Table 6.5 contains the descriptions of the pulsar observation schedules for the single detector scenarios. For the DirecTV orbit, the visibility worked out to allow the scheduling to alternate every 12 hours between tracking the Crab pulsar and PSR B1821-24. For the cislunar and MSL trajectory the four pulsars were observed and phase tracked in sequence for periods of 12000 seconds each. The order of the pulsars was B1821-24, B1937+21, the Crab pulsar, and then J0218+4232. This order was chosen to spread out the best two pulsars for position estimation error levels, B1821-24 and the Crab pulsar, in order to not have a long window where only the less useful pulsars are being tracked.

Table 6.4: Pulsar observation schedules for three detectors.

Scenario Number	Pulsars Tracked	Rotation of Detectors
1	Crab, B1821-24, B1937+21	No
2	Crab, B1821-24, J0218+4232	No
3	Crab, B1937+21, J0218+4232	No
4	B1821-24, B1937+21, J0218+4232	No
5	Crab, B1821-24, B1937+21, J0218+4232	Yes

Table 6.5: Pulsar observation schedules for a single detector.

Orbit	Pulsar Order	Time per Pulsar, s
MSL	B1821-24, B1937+21, Crab, J0218+4232	12000
Cislunar	B1821-24, B1937+21, Crab, J0218+4232	12000
DirecTV	Crab, B1821-24	43200

6.4 Results

In this section the EKF simulation results are displayed for each of the sets of combinations of pulsars and trajectories as detailed above. First the results for the three detector configuration tracking the MSL and cislunar trajectories will be displayed. Then the single detector simulation results for the DirecTV orbit and MSL and cislunar trajectories will be discussed. Each simulation scenario was run ten times with different random number generator seeds and the results were averaged to obtain the outputs in the tables and figures that follow.

6.4.1 Three Detector Case

First, simulations were performed assuming that the spacecraft had three separate gimbaled 1 m^2 detectors that can each phase track pulsars independently. This scenario was only used to perform simulations to estimate the cislunar and MSL trajectories due to the number of pulsars that are available for tracking. The simulation and EKF settings were defined above in Tables 6.1 - 6.3. The observation schedules considered were detailed above in Table 6.4.

The three dimensional navigation EKF results for the cislunar trajectory with three detectors phase tracking the Crab pulsar, B1821-24, and B1937+21 are presented in Figures 6.5 – 6.8. The position errors and one sigma bounds, split up into individual coordinates, are plotted in Figure 6.5. The average position error stays inside the bounds for all of the components and the error level is maintained. Figure 6.6 contains the velocity component errors with their one sigma bounds.

The velocity errors remain within the bounds and the level of error is reduced over the simulation. Improvements in different component position and velocity errors can be seen periodically over the simulation. This is because different pulsar measurements are incorporated by the EKF at different times, and each pulsar's phase tracking measurements improve the errors in different components depending on the geometry of the source orientations in the sky.

Figures 6.7 and 6.8 contain plots comparing the total EKF position and velocity accuracies to the uncorrected state errors of a filter evolving without measurements, respectively. The position and velocity error magnitudes settle and maintain a level of accuracy over the entire simulation window. By the end of the three day MSL trajectory simulation, the EKF with phase tracking measurements from three detectors outperforms the uncorrected filter error in both position and velocity.

The three dimensional navigation EKF results for the MSL trajectory with three detectors phase tracking the Crab pulsar, B1821-24, and B1937+21 are presented in Figures 6.9 – 6.12. In Figure 6.9 the component position errors and sigma bounds are plotted. The average position errors stay bounded by the one sigma values after an initial settling period. Figure 6.10 contains plots of the velocity errors and one sigma bounds split up by components. The velocity errors also are bounded by the one sigma values after an initial settling period, particularly in the x-component. The improvements in different components of the position and velocity errors at different times is again due to the pulsar source orientation and observation scheduling.

Figures 6.11 and 6.12 show the total EKF position and velocity errors plotted

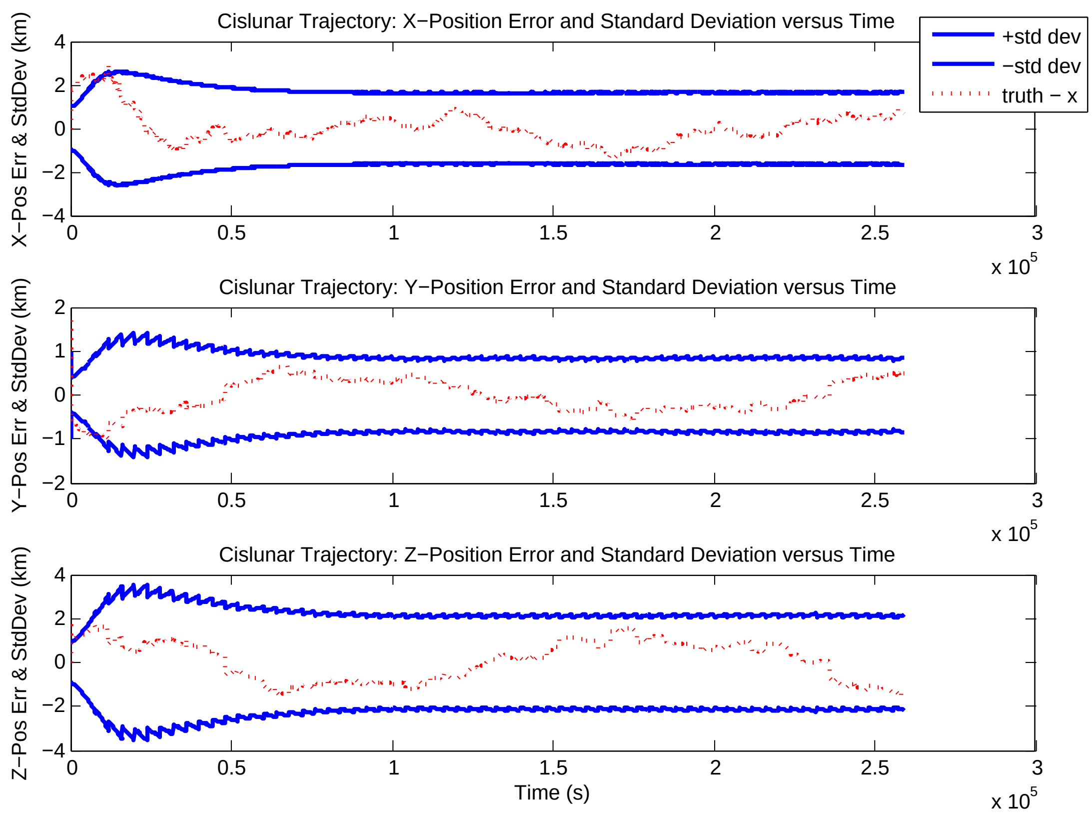

Figure 6.5: Position errors and one sigma bounds for the cislunar trajectory EKF simulation with three 1 m^2 detectors. The detectors are tracking the Crab pulsar, B1821-24, and B1937+21.

against those of an uncorrected filter evolving without measurements, respectively. The position error level is maintained and the velocity error level settles and stays bounded. The EKF with phase tracking measurements from three detectors outperforms the uncorrected filter error in both position and velocity for the cislunar trajectory as well. The position and velocity performance plots are similar in general shape between the cislunar and MSL trajectories due to the similar dynamic environment.

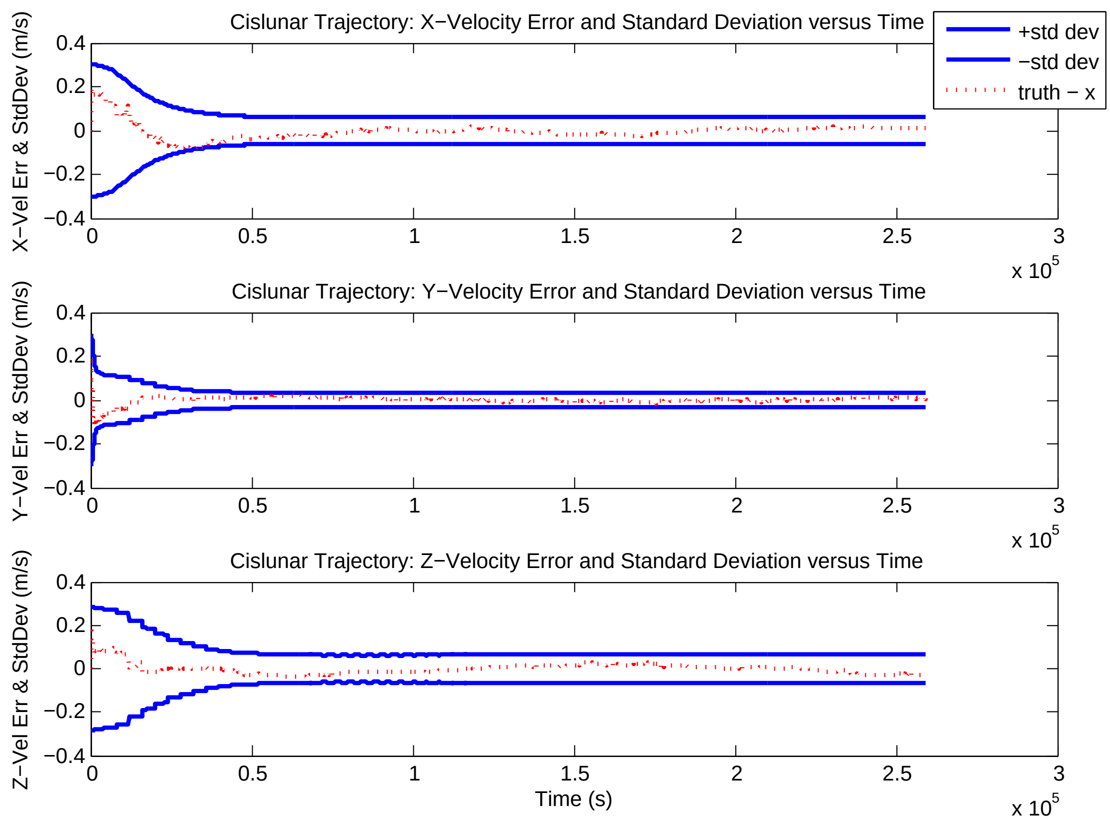

Figure 6.6: Velocity errors and one sigma bounds for the cislunar trajectory EKF simulation with three 1 m^2 detectors. The detectors are tracking the Crab pulsar, B1821-24, and B1937+21.

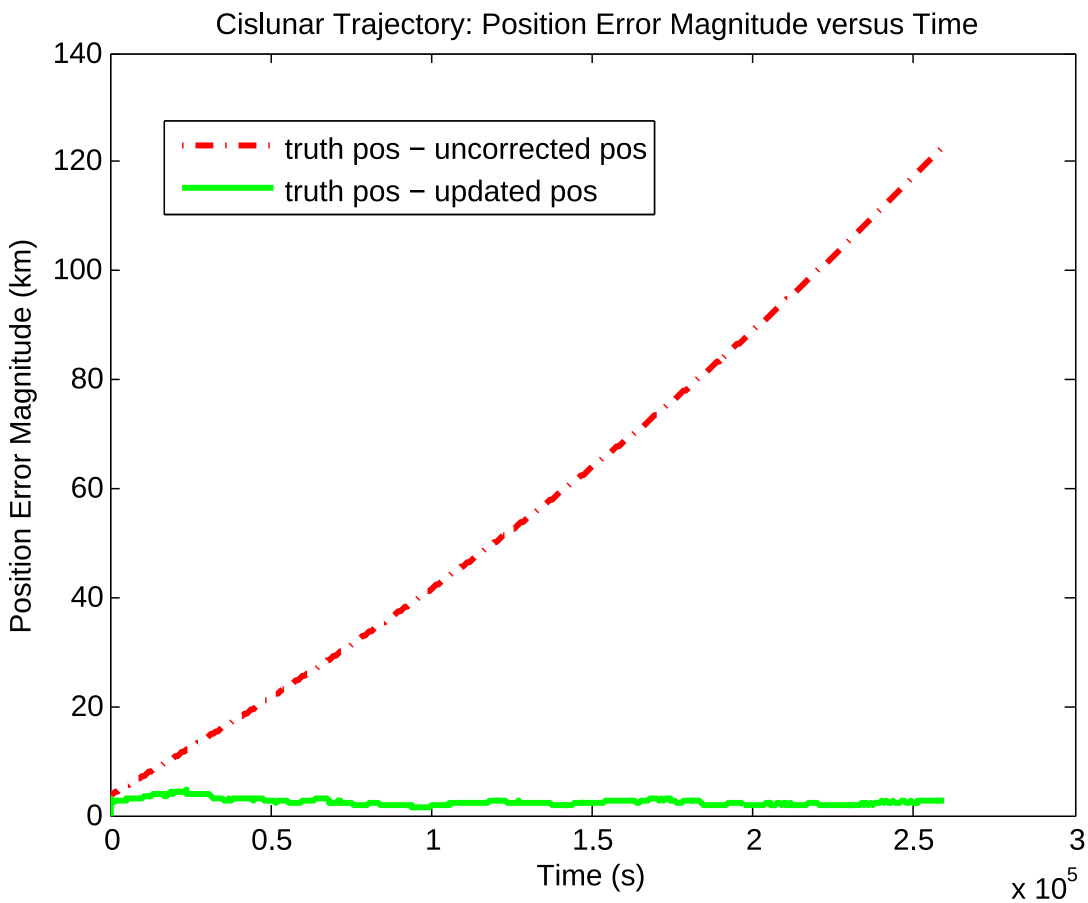

Figure 6.7: EKF position accuracy versus the uncorrected state accuracy for the cislunar trajectory with three 1 m^2 detectors. The detectors are tracking the Crab pulsar, B1821-24, and B1937+21.

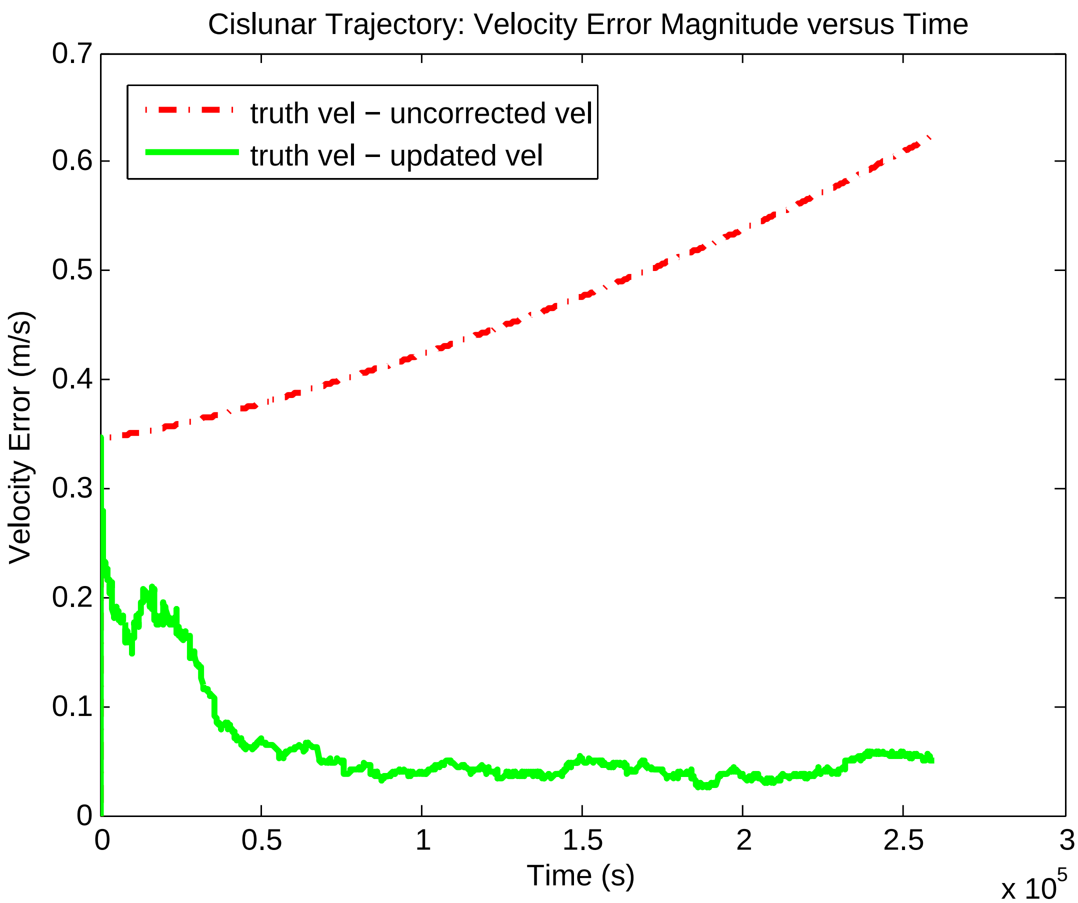

Figure 6.8: EKF position accuracy versus the uncorrected state accuracy for the cislunar trajectory with three 1 m^2 detectors. The detectors are tracking the Crab pulsar, B1821-24, and B1937+21.

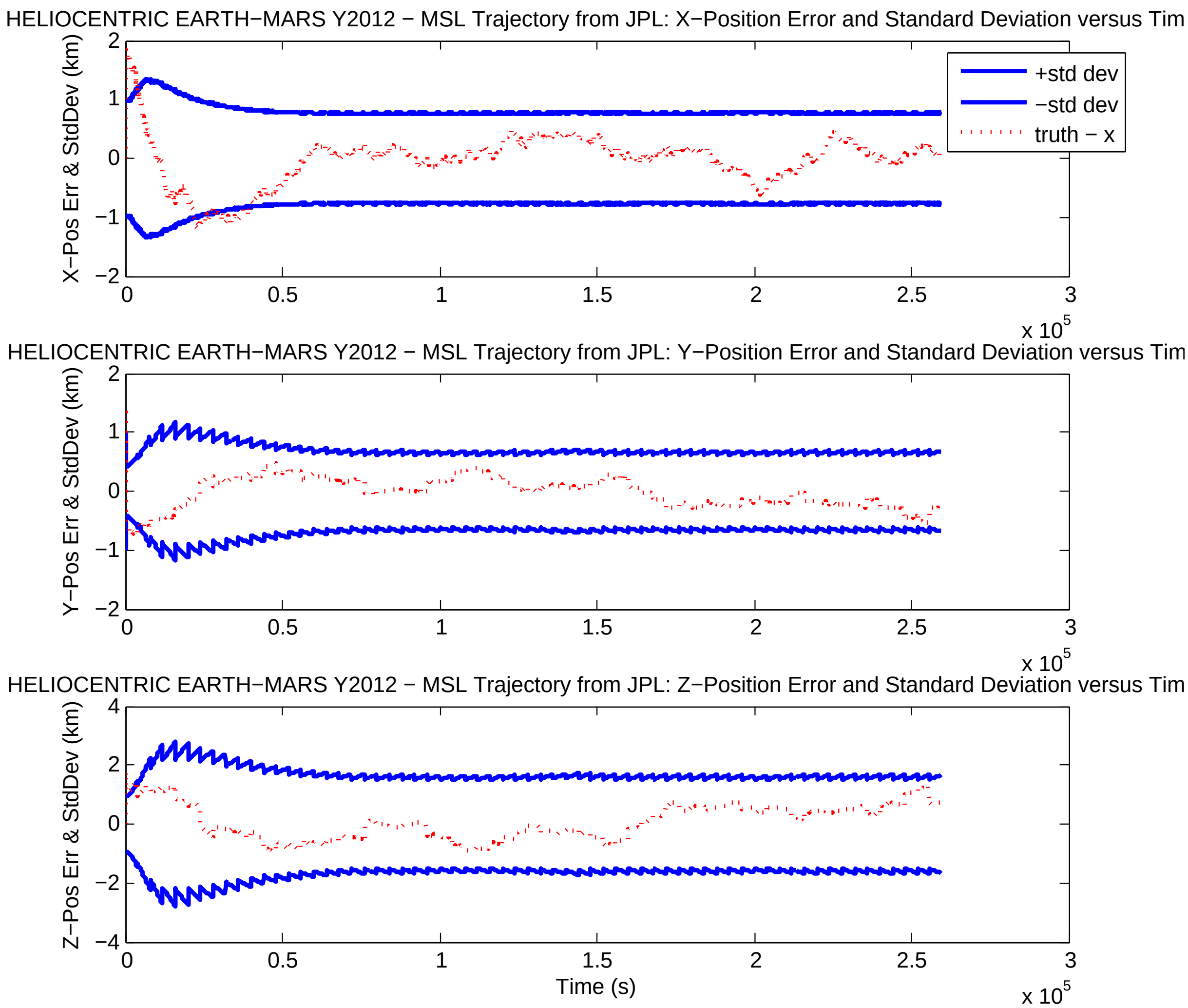

Figure 6.9: Position errors and one sigma bounds for the MSL trajectory EKF simulation with three 1 m^2 detectors. The detectors are tracking the Crab pulsar, B1821-24, and B1937+21.

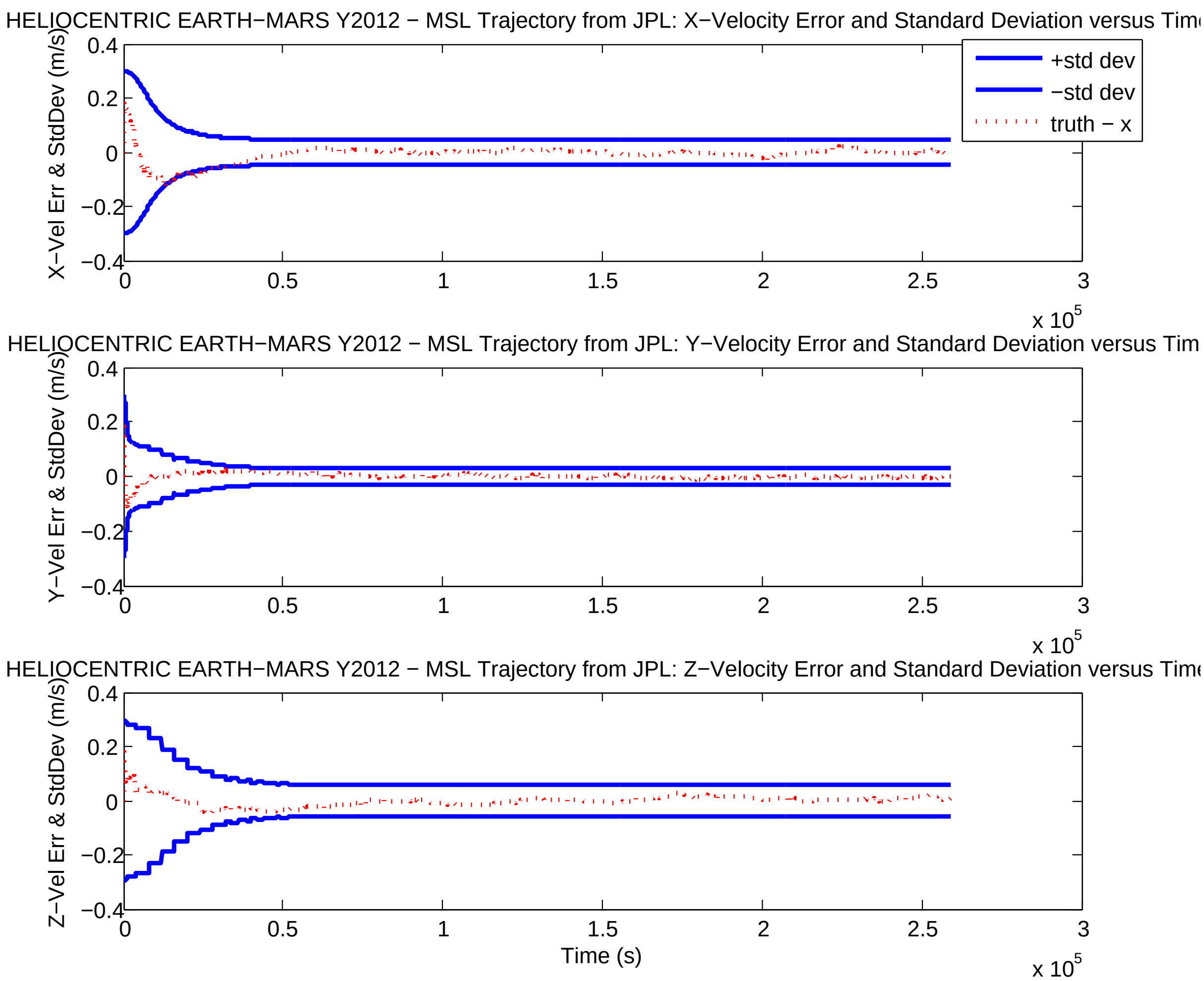

Figure 6.10: Velocity errors and one sigma bounds for the MSL trajectory EKF simulation with three 1 m^2 detectors. The detectors are tracking the Crab pulsar, B1821-24, and B1937+21.

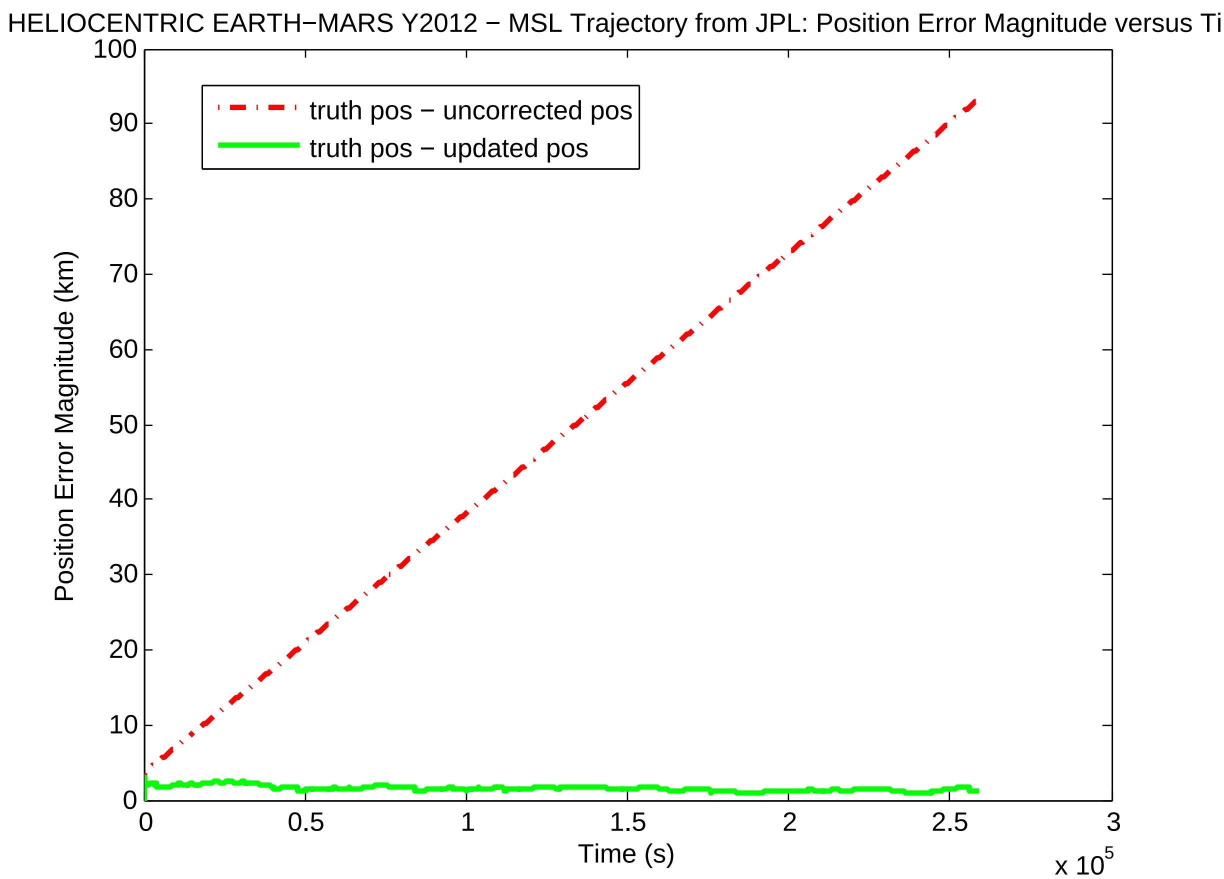

Figure 6.11: EKF position accuracy versus the uncorrected state accuracy for the MSL trajectory with three 1 m^2 detectors. The detectors are tracking the Crab pulsar, B1821-24, and B1937+21.

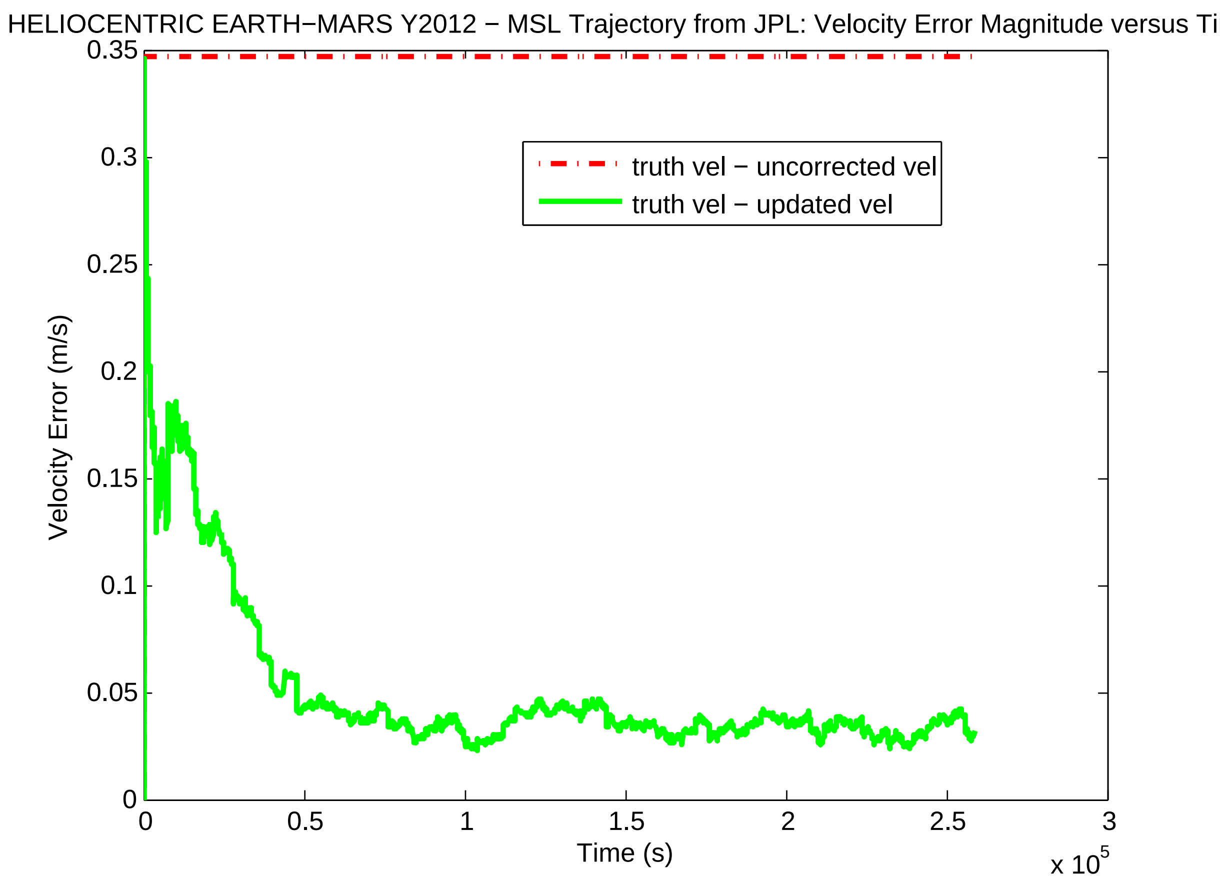

Figure 6.12: EKF position accuracy versus the uncorrected state accuracy for the MSL trajectory with three 1 m^2 detectors. The detectors are tracking the Crab pulsar, B1821-24, and B1937+21.

Next, the other combinations of pulsars to track with the three detectors are investigated. Figure 6.13 contains the position errors and one sigma bounds for the scenario tracking the Crab pulsar, B1821-24, and J0218+4232 with the three detectors. Figure 6.14 contains the position errors and one sigma bounds with the three detectors tracking the Crab pulsar, B1937+21, and J0218+4232. Figure 6.15 has the plot of the position errors and one sigma bounds for tracking B1821-24, B1937+21, and J0218+4232. The general shapes of the plots in all components of the position errors are similar across the different pulsars considered. The position errors are bounded by the one sigma values in all cases.

The overall error level is highest for the case tracking the Crab pulsar, B1937+21, and J0218+4232 and lowest for the case tracking the Crab pulsar, B1821-24, and B1937+21. The scenarios that do not track B1821-24 perform the worst, and the ones that incorporate only one of B1937+21 or J0218+4232 perform the best. This is for a variety of reasons including the accuracy, geometric diversity, and frequency of the various pulsar phase tracking measurements.

Next, the scenario considers a pulsar observation schedule rotating the three detectors through phase tracking the four pulsars. One pulsar is switched out from the set being tracked every 12000 seconds. Figures 6.16 and 6.17 contain plots of the position component errors and one sigma bound values for the MSL and cislunar trajectories, respectively. The performance is similar between the two trajectories, with the errors slightly higher for the cislunar trajectory. For both cases, the average position errors stay bounded by the one sigma values after initial settling. The changes in pulsar observations can clearly be seen with the different patterns

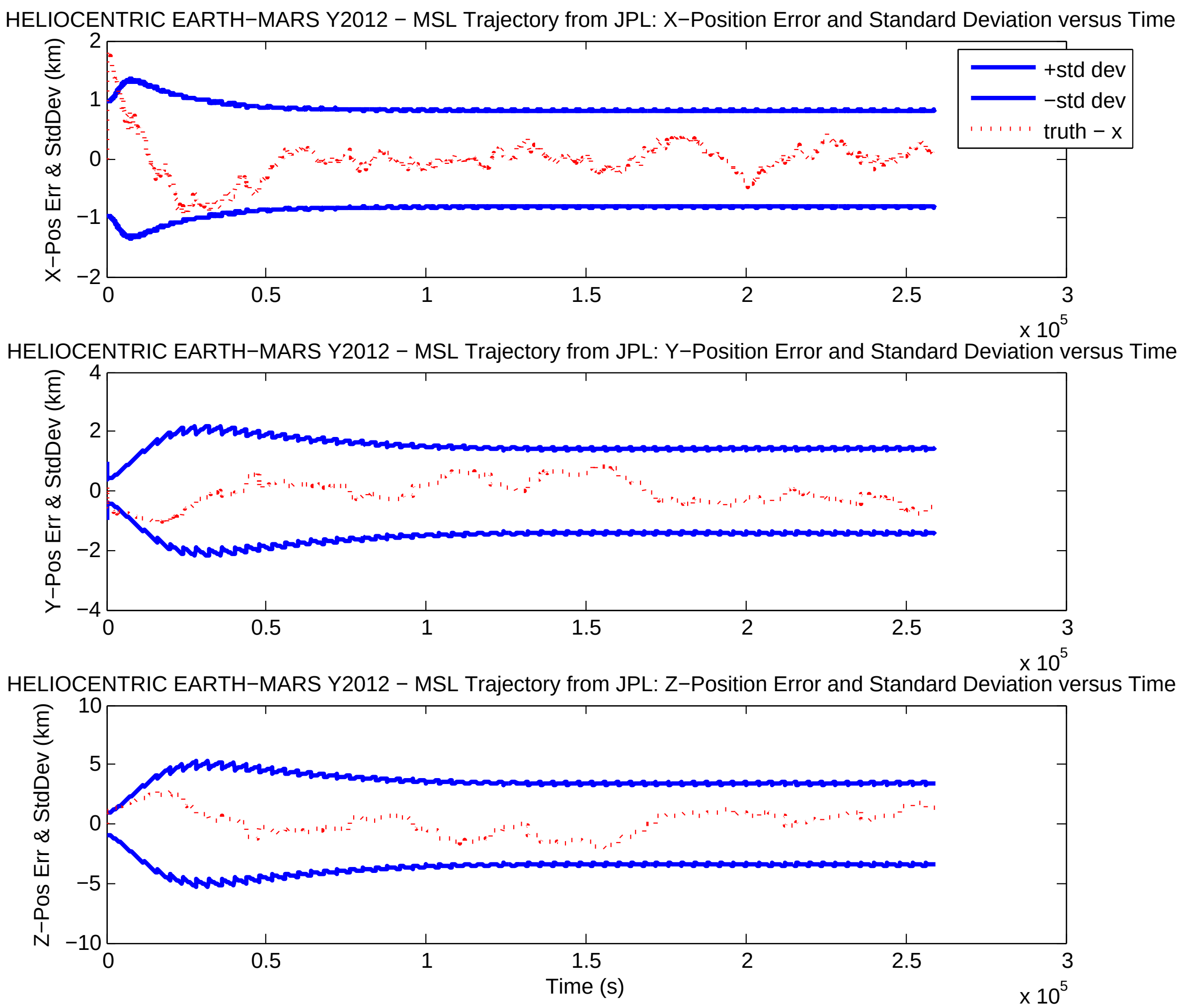

Figure 6.13: Position errors and one sigma bounds for the MSL trajectory EKF simulation with three 1 m^2 detectors. The detectors are tracking the Crab pulsar, B1821-24, and J0218+4232.

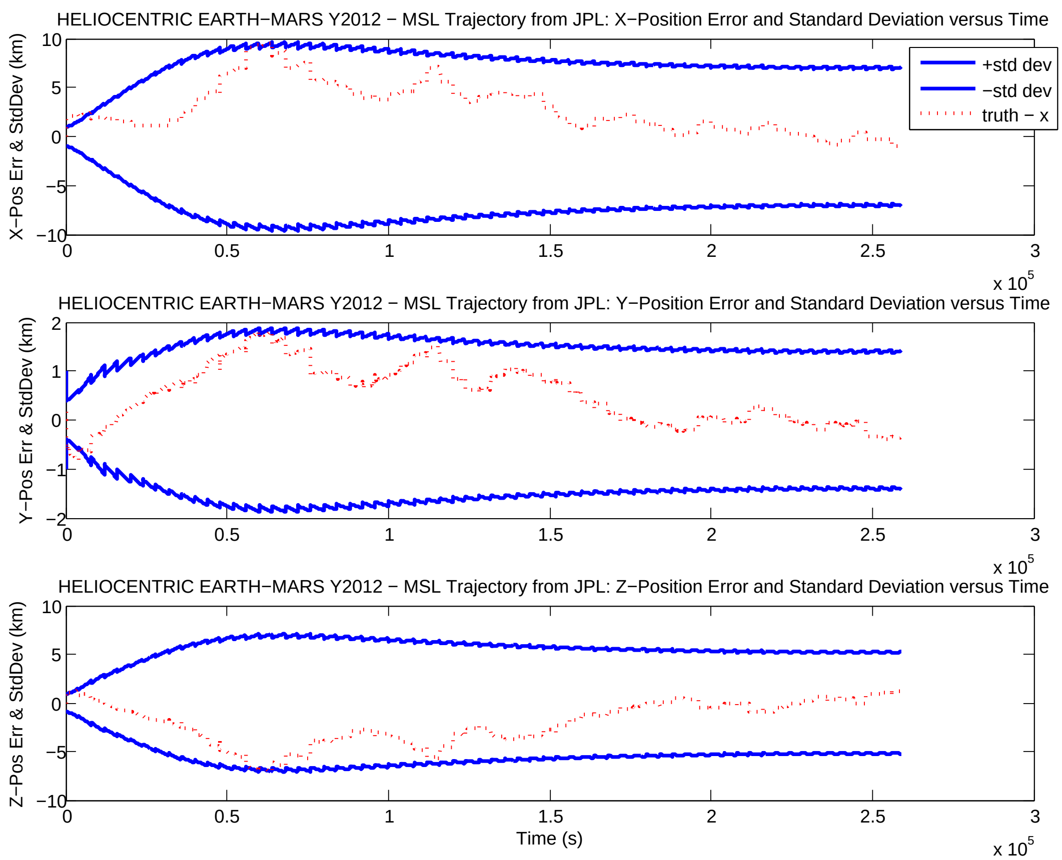

Figure 6.14: Position errors and one sigma bounds for the MSL trajectory EKF simulation with three 1 m^2 detectors. The detectors are tracking the Crab pulsar, B1937+21 and J0218+4232.

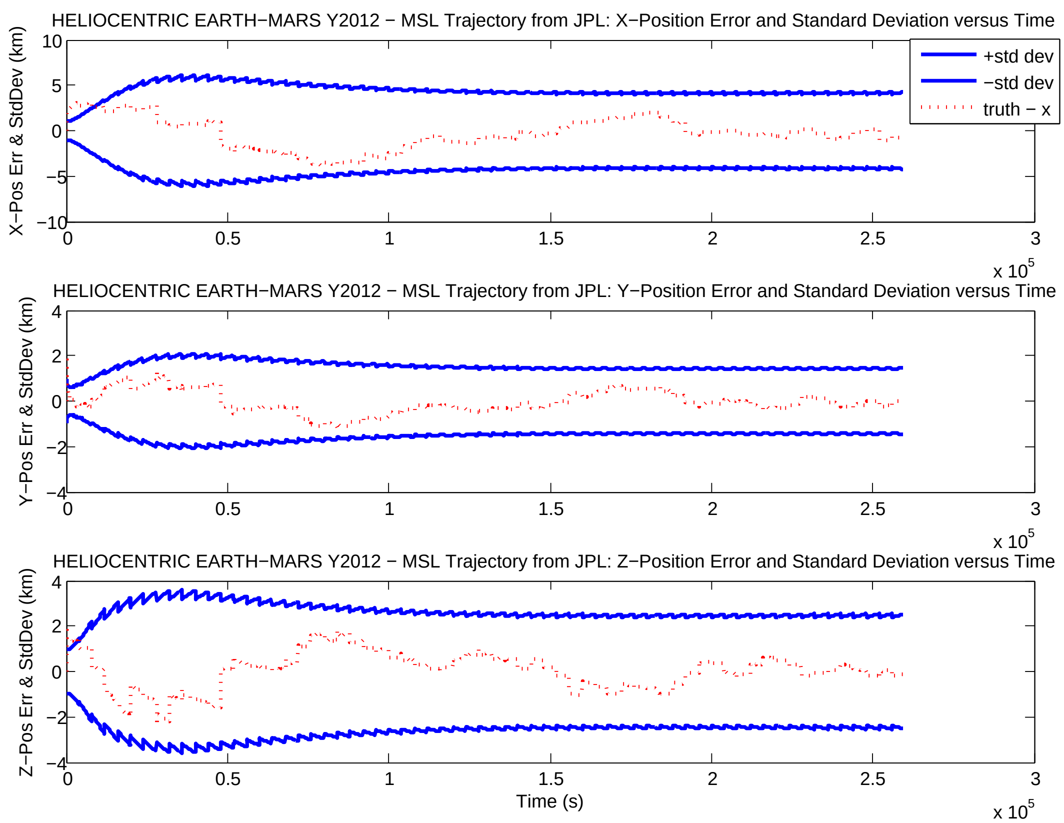

Figure 6.15: Position errors and one sigma bounds for the MSL trajectory EKF simulation with three 1 m^2 detectors. The detectors are tracking B1821-24, B1937+21, and J0218+4232.

of improvement in the components of the position error over the simulation. The performance is similar to the scenarios above tracking sets of three pulsars over the entire simulation. The one-sigma bounds are tighter and have better error performance than any of the cases that only tracked three of the pulsars. The geometric diversity outweighs the incorporation of more of the lower quality measurements from B1937+21 and J0218+4232.

A compilation of the three dimensional navigation EKF results with a single detector is included in Table 6.6. The results for tracking both the MSL and cislunar trajectories, with all of the pulsar observation combinations considered, are displayed. The position and velocity error levels are both quantified by reporting the RMS error from the end of the simulation as well as through an average position and velocity metric. The average metric is computed over the last 48000 seconds of the simulation duration in order to capture the performance over a time after the filter has settled. The RMS is computed at each time step across the ten iterations of the simulations for each orbit and pulsar schedule scenario.

It can be seen from the results in Table 6.6 that the EKF with phase tracking measurements maintains position error levels under 6 km and velocity error levels below 6 cm/s for all of the pulsar combinations and both trajectories. In most cases, the end point position and velocity errors are similar to the averages computed over the later stages of the simulation. This demonstrates that the settling time has been reached by the filter by the time the averages are computed. For some cases, the averages were larger than the end point values. For the cislunar trajectory tracking the Crab pulsar, B1821-24, and B1937+21, the average position error was 9.29 km

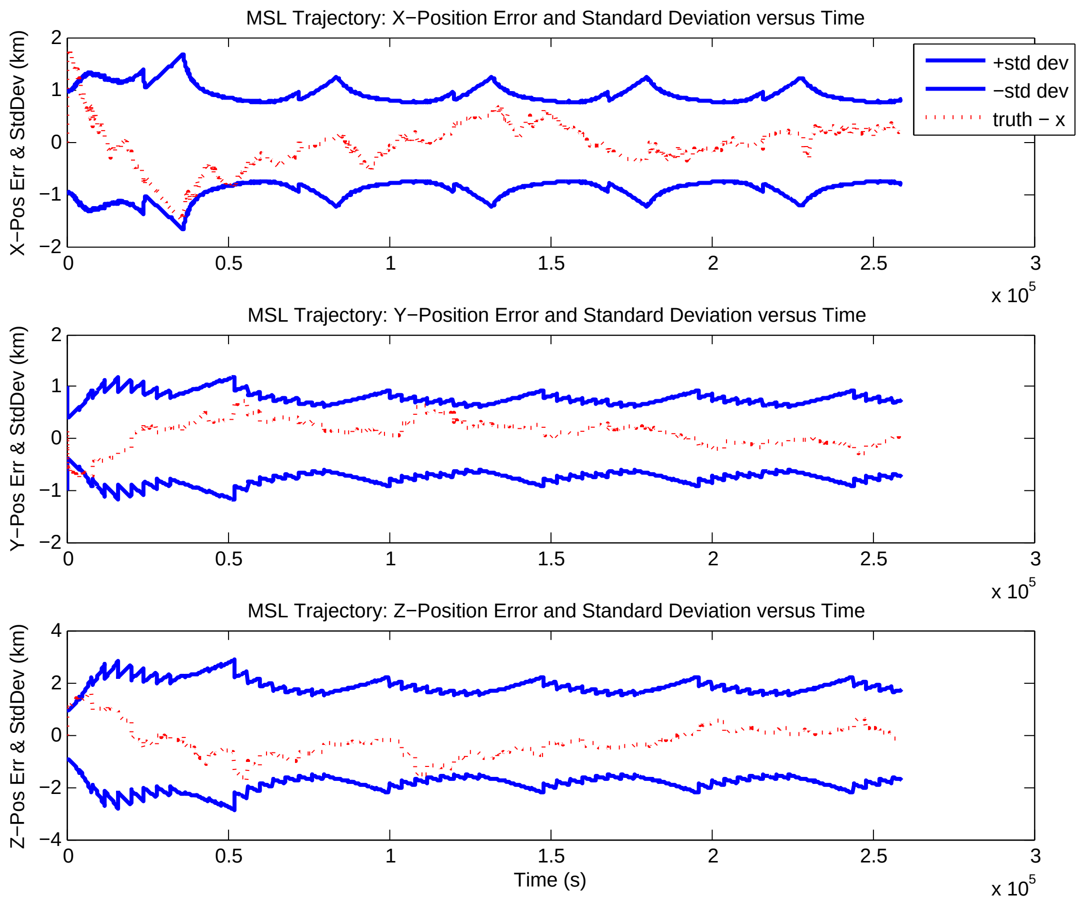

Figure 6.16: Position errors and one sigma bounds for the MSL trajectory EKF simulation with three 1 m^2 detectors. The detectors are rotating through tracking the Crab pulsar, B1821-24, B1937+21, and J0218+4232.

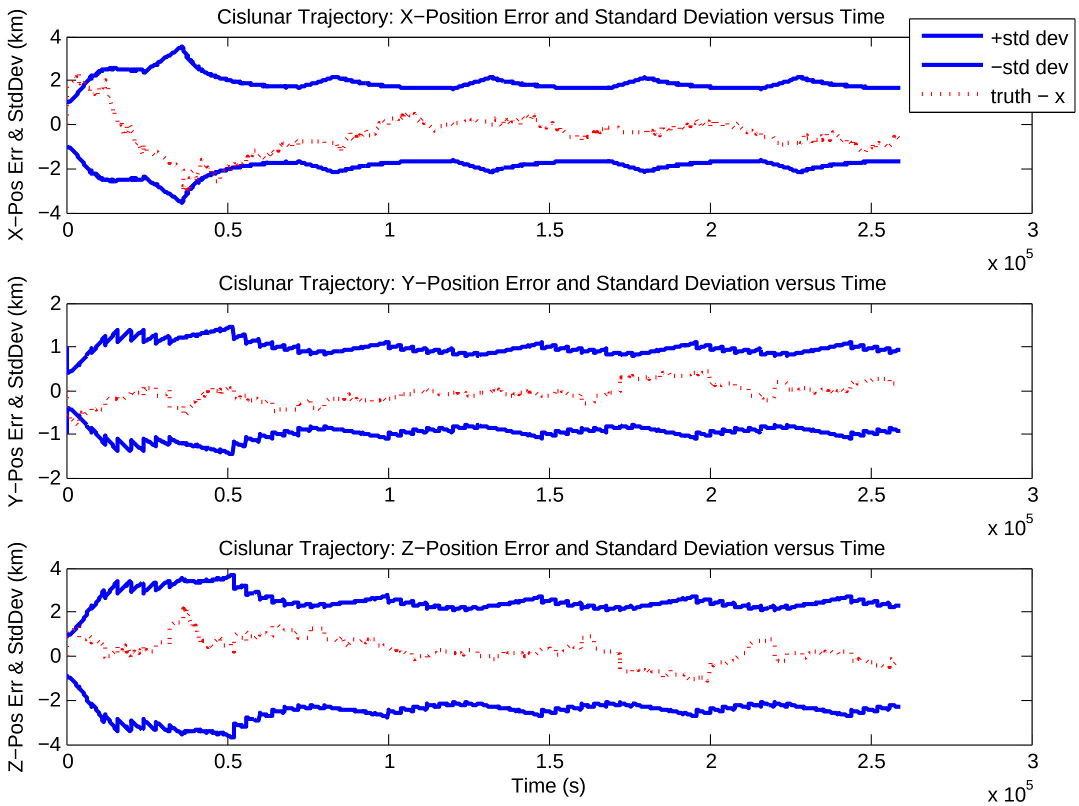

Figure 6.17: Position errors and one sigma bounds for the cislunar trajectory EKF simulation with three 1 m^2 detectors. The detectors are rotating through tracking the Crab pulsar, B1821-24, B1937+21, and J0218+4232.

and the end point RMS position error was 5.47 km. This increase can be attributed to slow settling of the filter after incorporating multiple high variance measurements.

The position and velocity results are similar across the various pulsar combinations considered for both the MSL and cislunar trajectories. For example with the MSL trajectory, the endpoint RMS position error varies from 1.21 km for observations of the Crab pulsar, B1821-24, and B1937+21 to 5.85 km for observations of the Crab pulsar, B1937+21, and J0218+4232. For the cislunar trajectory, the endpoint RMS position error varies from 2.74 km for observations of the Crab pulsar, B1821-24, and B1937+21 to 5.47 km for observations of the Crab pulsar, B1937+21, and J0218+4232. The scenarios that include observations of B1937+21 and J0218+4232 have the worst results as expected due to their higher phase tracking errors as seen in Chapter 5.

When comparing the results for the MSL and cislunar trajectories, the position estimation results are similar and each trajectory outperforms the other for some of the combinations of pulsars tracked. This is due to how the geometries of the pulsar directions in the sky relate to the path of each trajectory and how this interacts with the EKF. For the case observing the Crab pulsar, B1821-24, and B1937+21, the end point RMS position error is 1.21 km for the MSL trajectory and 2.74 km for the cislunar trajectory. For the case observing B1821-24, B1937+21, and J0218+4232, the end point RMS position error is 4.25 km for the MSL trajectory and 3.32 km for the cislunar trajectory.

For the case where the four pulsars are rotated through the three detectors, the position tracking outperforms the cases where three pulsars are tracked for the full simulation. For the MSL trajectory, the end point RMS position error is 1.16 km. For the cislunar trajectory, the end point RMS position error is 2.62 km. Both of these are better than any of the three pulsar combination results. Overall, good three-dimensional tracking was demonstrated with the three detector model for the EKF, using phase tracking measurements, for both trajectories.

Table 6.6: Results for the combined navigation EKF simulations using three detectors each with an area of 1 m^2. The pulsar names are abbreviated when listing the scheduling. The fifth scenario rotates the four pulsars through the three detectors.

Pulsars Observed	Crab, B1821, B1937	Crab, B1821, J0218	Crab, B1937, J0218	B1821, B1937, J0218	Crab, B1821, B1937, J0218 Rotated
MSL End Point RMS Position Error (km)	1.21	2.29	5.85	4.25	1.16
MSL Averaged Position Error (km)	1.24	2.32	4.74	4.28	1.61
MSL End Point RMS Velocity Error (cm/s)	3.16	2.94	4.90	5.37	3.31
MSL Averaged Velocity Error (cm/s)	3.32	4.35	5.00	5.79	3.72
Cislunar End Point RMS Position Error (km)	2.74	4.06	5.47	3.32	2.62
Cislunar Averaged Position Error (km)	1.98	3.30	9.29	4.32	2.52
Cislunar End Point RMS Velocity Error (cm/s)	5.01	4.89	4.36	4.99	4.19
Cislunar Averaged Velocity Error (cm/s)	5.79	4.31	5.18	5.58	4.31

6.4.2 Single Detector Case

Next, simulations were performed assuming the spacecraft has a single gimbaled 1 m^2 detector to phase track pulsars. This configuration was tested for the DirecTV orbit, cislunar trajectory, and MSL trajectory to consider a range of dynamic stress levels and pulsar availabilities. The simulation and EKF settings were defined above in Tables 6.1 – 6.3. The observation schedules considered were detailed above in Table 6.5.

The three dimensional navigation EKF results for the MSL trajectory are presented in Figures 6.18 – 6.21. The pulsars B1821-24, B1937+21, the Crab, and J0218+4232 were observed in sequence for 12000 seconds each over a simulation time of three days. Figure 6.18 contains the position errors and one sigma bounds split up into individual coordinates. It can be seen that the average position error is remaining within the one sigma bounds in each of the components and the error level is maintained over the entire simulation window. Figure 6.19 contains the velocity errors and one sigma bounds split up into individual coordinates. The average velocity error also remains within the one sigma bounds. The error levels for the velocity components are reduced from the initial values. In both the position and velocity error plots it can be seen that different pulsar measurements are improving the error bounds in different components as a result of the geometric dispersion of the pulsars.

Figures 6.20 and 6.21 contain the total magnitude of the EKF position and velocity accuracies, respectively, plotted against the uncorrected state errors of a

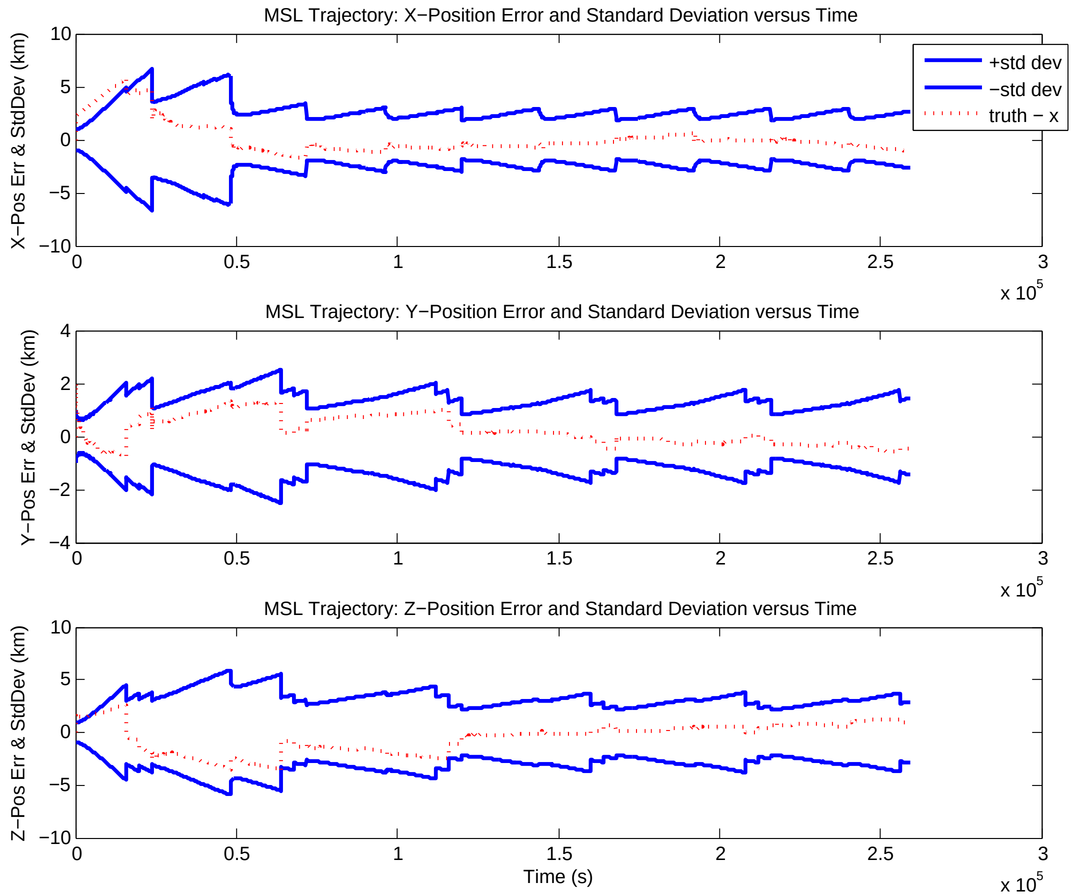

Figure 6.18: Position errors and one sigma bounds for the MSL trajectory EKF simulation with a single 1 m^2 detector.

hypothetical filter that is allowed to evolve without incorporating any measurements. For both the position and velocity it can be seen that the error magnitude reduces and settles after initially following the uncorrected state errors. By the end of the three day simulation time the EKF with phase tracking measurements is greatly outperforming the uncorrected filter error.

The three dimensional navigation EKF results for the cislunar trajectory are

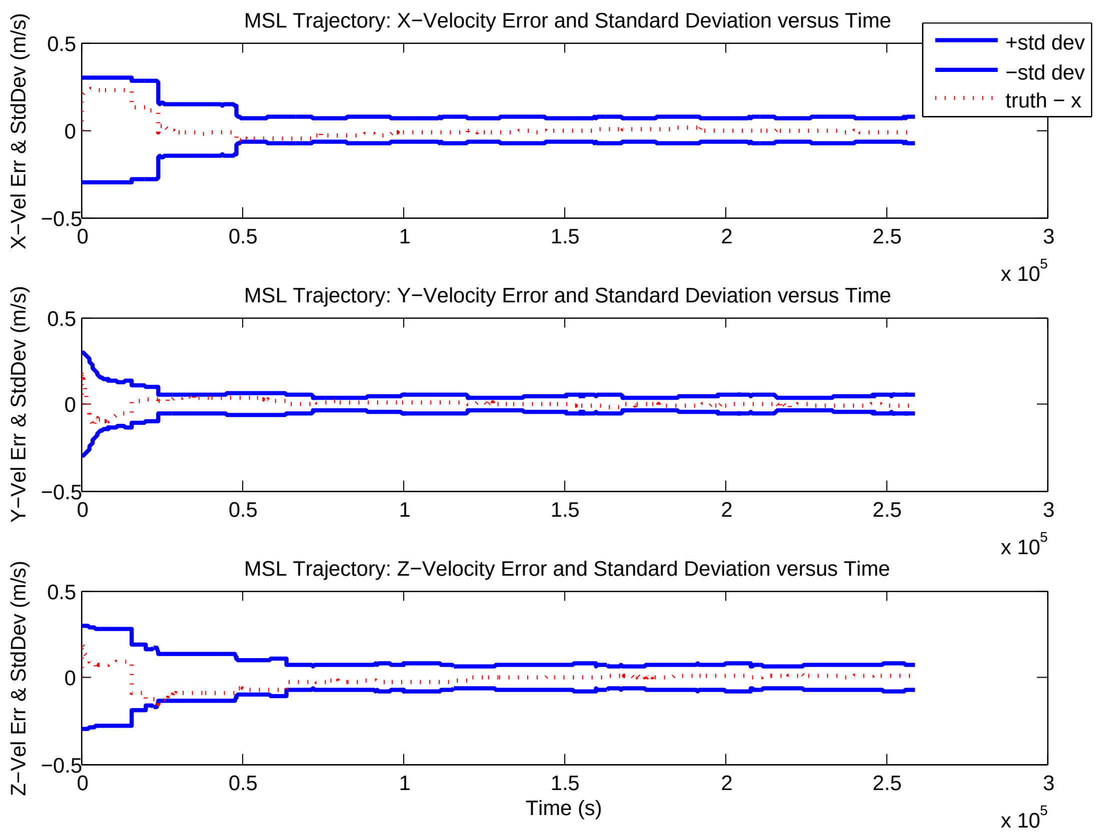

Figure 6.19: Velocity errors and one sigma bounds for the MSL trajectory EKF simulation with a single 1 m^2 detector.

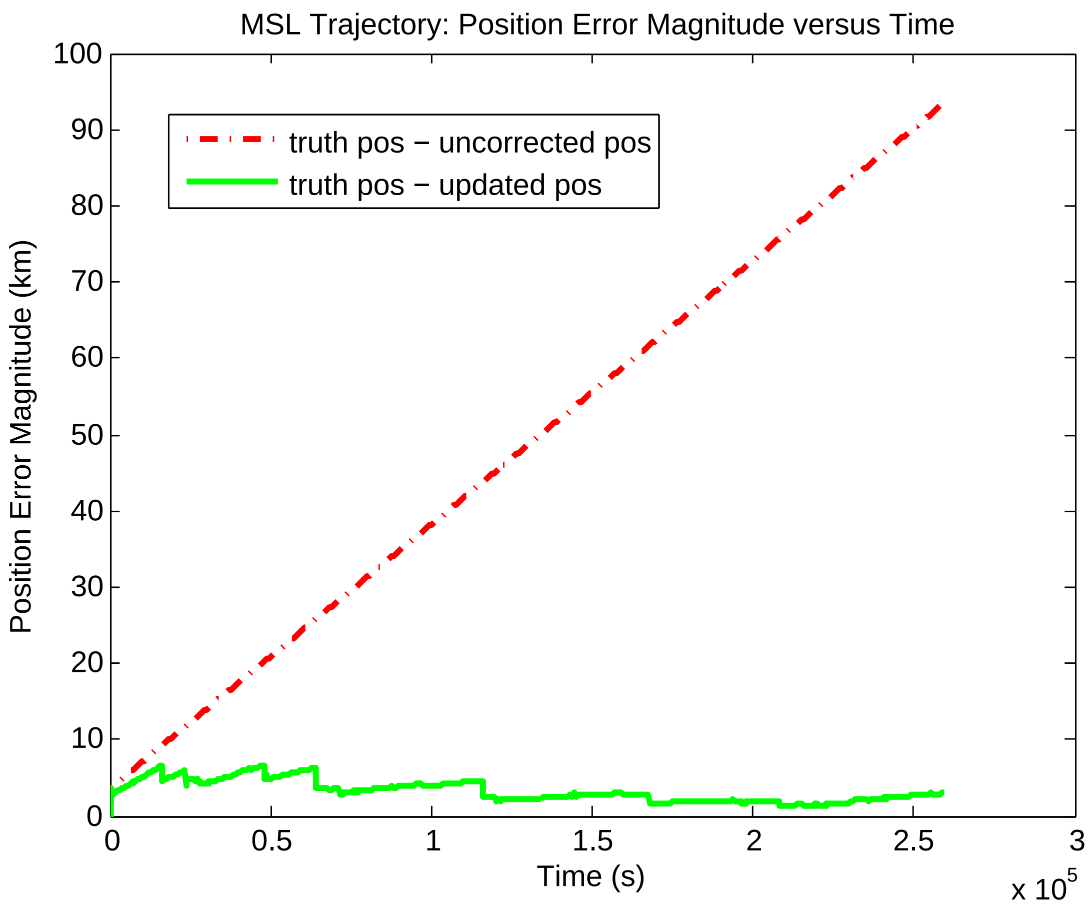

Figure 6.20: EKF position accuracy versus the uncorrected state accuracy for the MSL trajectory with a single 1 m^2 detector.

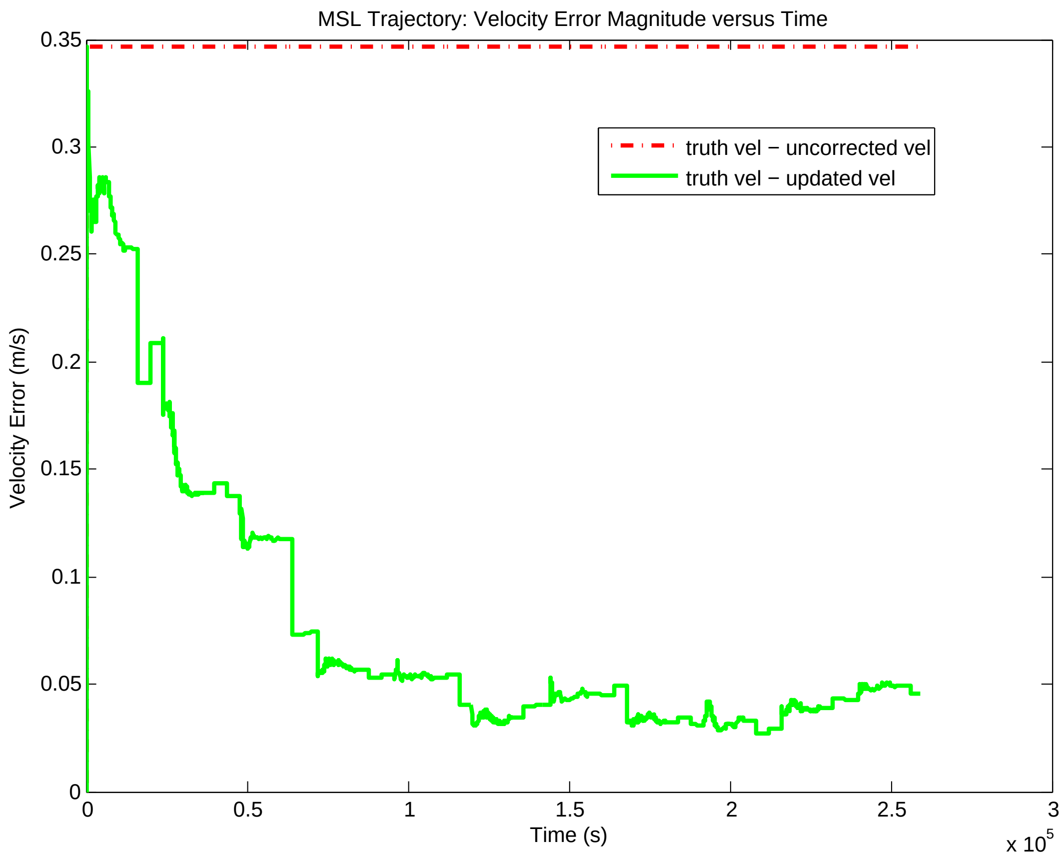

Figure 6.21: EKF velocity accuracy versus the uncorrected state accuracy for the MSL trajectory with a single 1 m^2 detector.

presented in Figures 6.22 – 6.25. The pulsars B1821-24, B1937+21, the Crab, and J0218+4232 were observed in sequence for 12000 seconds each over a simulation time of three days. Figure 6.22 contains the position errors and one sigma bounds split up into individual coordinates. The average position error is bounded by the sigma bounds in all components and the error level is maintained over the entire simulation window. Figure 6.23 contains the velocity errors and one sigma bounds split up into individual coordinates. The velocity errors stay bounded and decrease over the course of the simulation. These position and velocity error plots for the cislunar trajectory are very similar to the ones above for the MSL trajectory. This demonstrates that these trajectories are very similar environments for phase tracking pulsars.

Figures 6.24 and 6.25 contain the total magnitude of the EKF position and velocity accuracies, respectively, plotted against the uncorrected state errors of a hypothetical filter that is allowed to evolve without incorporating any measurements. Both the position and velocity total magnitude errors settle to a bounded level over the simulation time. There is large improvement over the unbounded growth of the uncorrected state errors from the filter with no measurements. The slight curve in the uncorrected filter error due to the dynamics of the cislunar trajectory can be seen as opposed to the relatively linear growth with the MSL trajectory.

The three dimensional navigation EKF results for the DirecTV orbit are presented in Figures 6.26 – 6.29. The Crab pulsar and B1821-24 were observed in sequence for 12 hours each over a simulation time of three days. Figure 6.26 and Figure 6.27 contain the position errors and velocity errors, respectively, along with

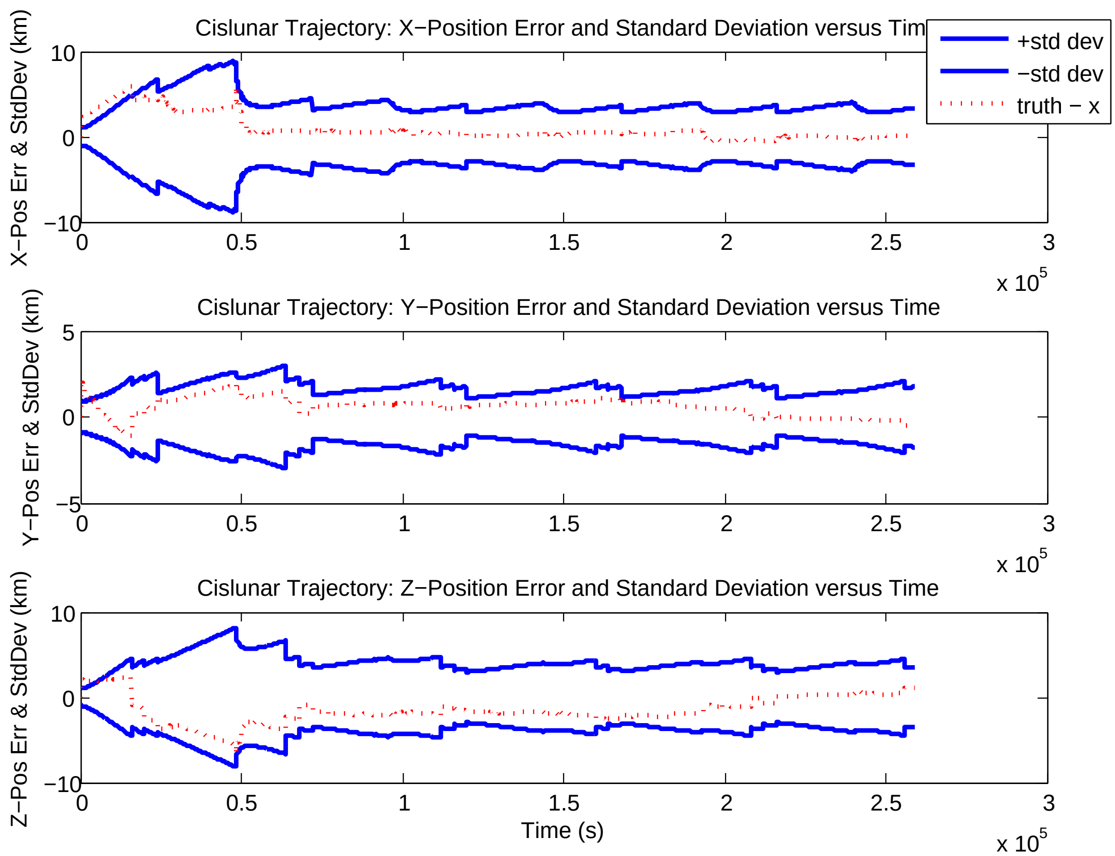

Figure 6.22: Position errors and one sigma bounds for the cislunar trajectory EKF simulation with a single 1 m^2 detector.

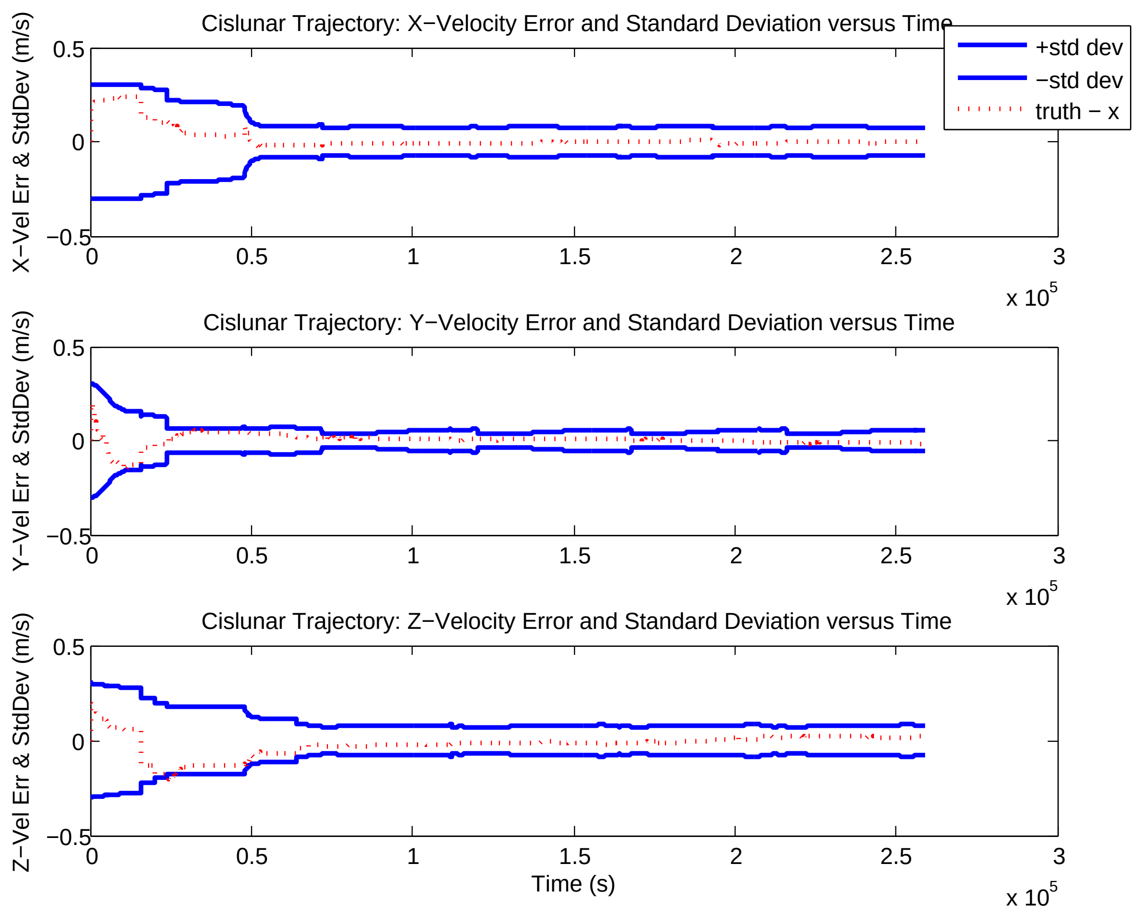

Figure 6.23: Velocity errors and one sigma bounds for the cislunar trajectory EKF simulation with a single 1 m^2 detector.

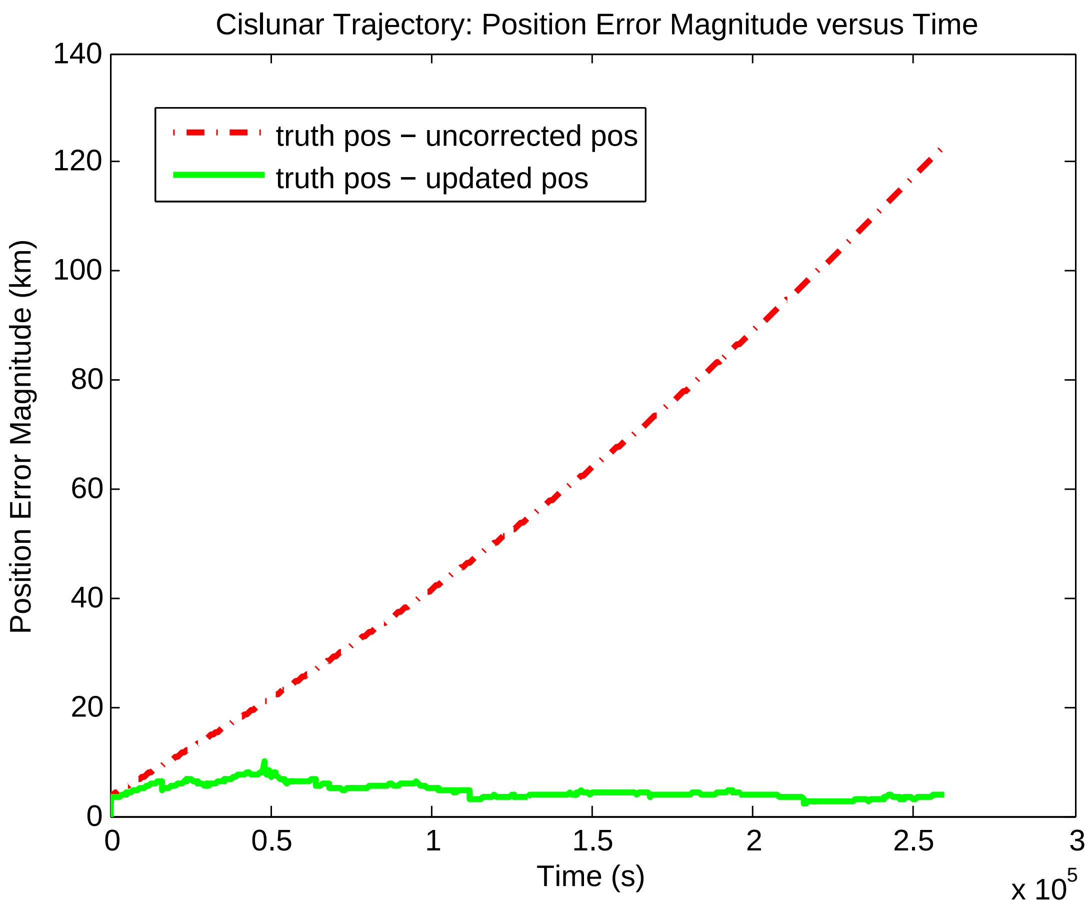

Figure 6.24: EKF position accuracy versus the uncorrected state accuracy for the cislunar trajectory with a single 1 m^2 detector.

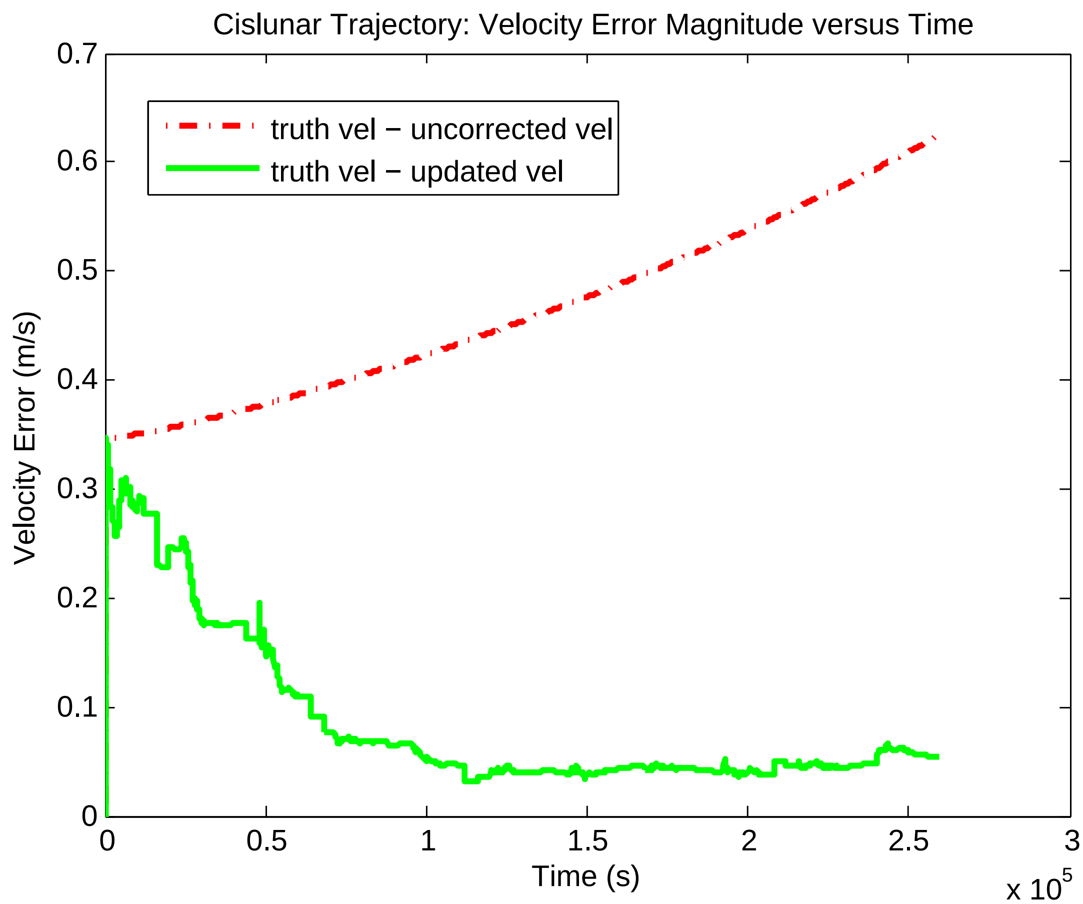

Figure 6.25: EKF velocity accuracy versus the uncorrected state accuracy for the cislunar trajectory with a single 1 m^2 detector.

the corresponding one sigma bounds split up into individual coordinates. The average position and velocity errors stay bounded in all components by the one sigma bound over the entire simulation window.

The effects caused by the greater dynamics of the DirecTV orbit, as compared to the cislunar and MSL trajectories, can be seen through the cyclical nature of the one sigma bounds and average position and velocity errors in each component. The three orbital periods of the DirecTV orbit that are contained within the simulation can be seen. Again, different pulsars improve the position and velocity error more in some component directions than in others. This yields a cyclical effect related to the pulsar observation schedule. Every 12 hours the pulsar phase tracked is alternated. There is enough geometric diversity, along with the changing LOS to each pulsar, to maintain the error levels using only the Crab pulsar and B1821-24.

Figures 6.28 and 6.29 contain the total magnitude of the EKF position and velocity accuracies, respectively, plotted against the uncorrected state errors of a hypothetical filter that is allowed to evolve without incorporating any measurements. The position and velocity errors are maintained over the simulation duration and greatly outperform the uncorrected filter state errors. Again, it is shown that adequate three dimensional tracking results can be maintained for the DirecTV orbit using phase tracking measurements only from the Crab pulsar and B1821-24. This might not be capable in other orbits depending on the geometry and physics of the individual scenarios and the pulsars available to phase track.

A compilation of the three dimensional navigation EKF results with a single detector is included in Table 6.7. The results for tracking the MSL and cislunar

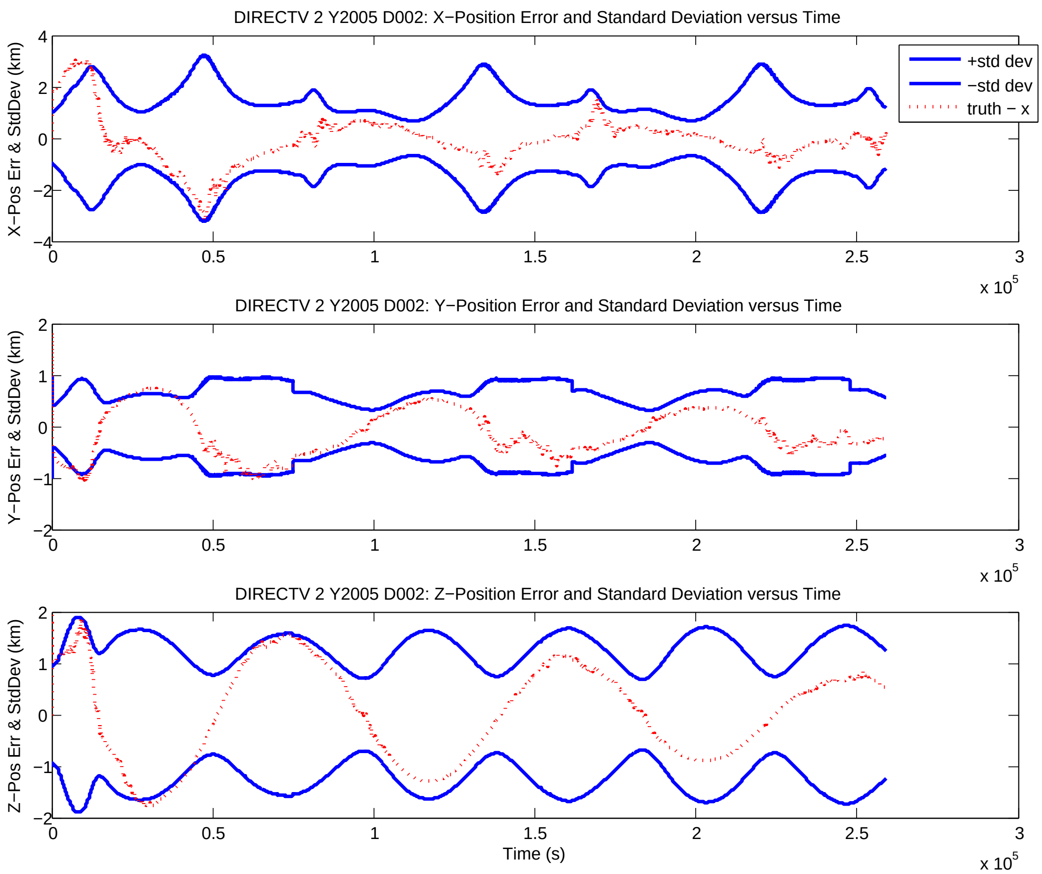

Figure 6.26: Position errors and one sigma bounds for the DirecTV orbit EKF simulation with a single 1 m^2 detector.

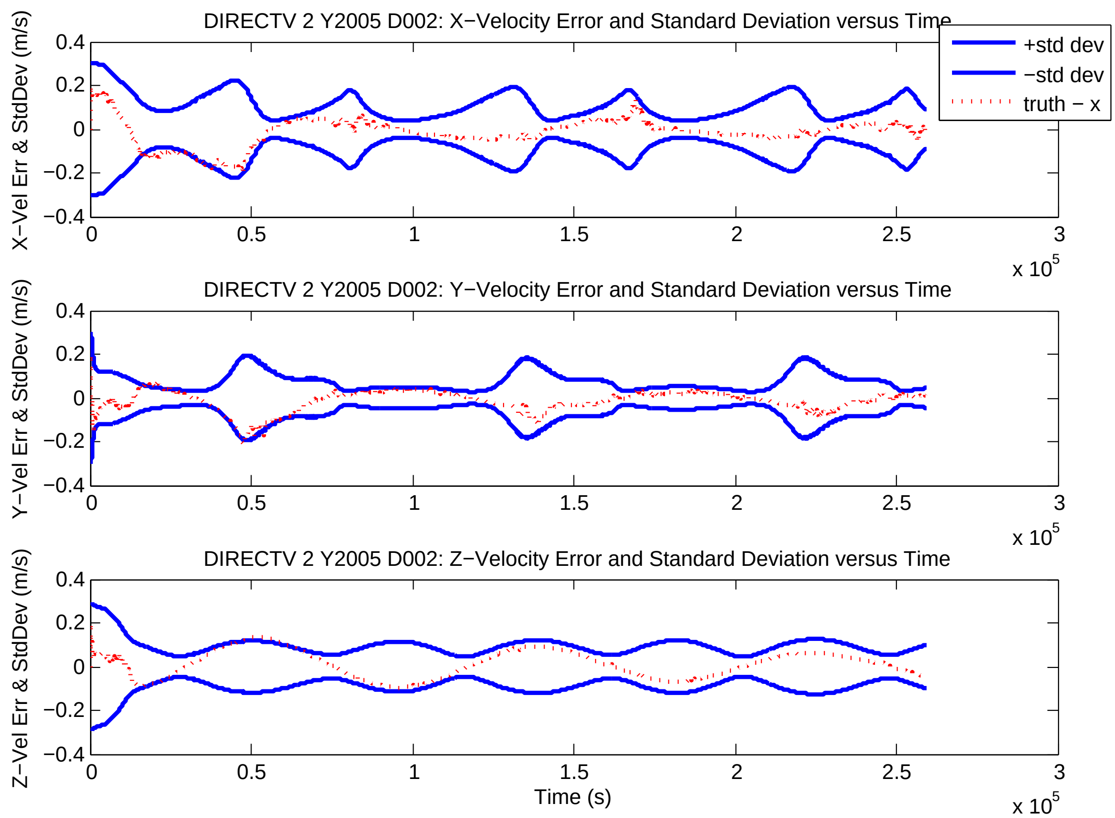

Figure 6.27: Velocity errors and one sigma bounds for the DirecTV orbit EKF simulation with a single 1 m^2 detector.

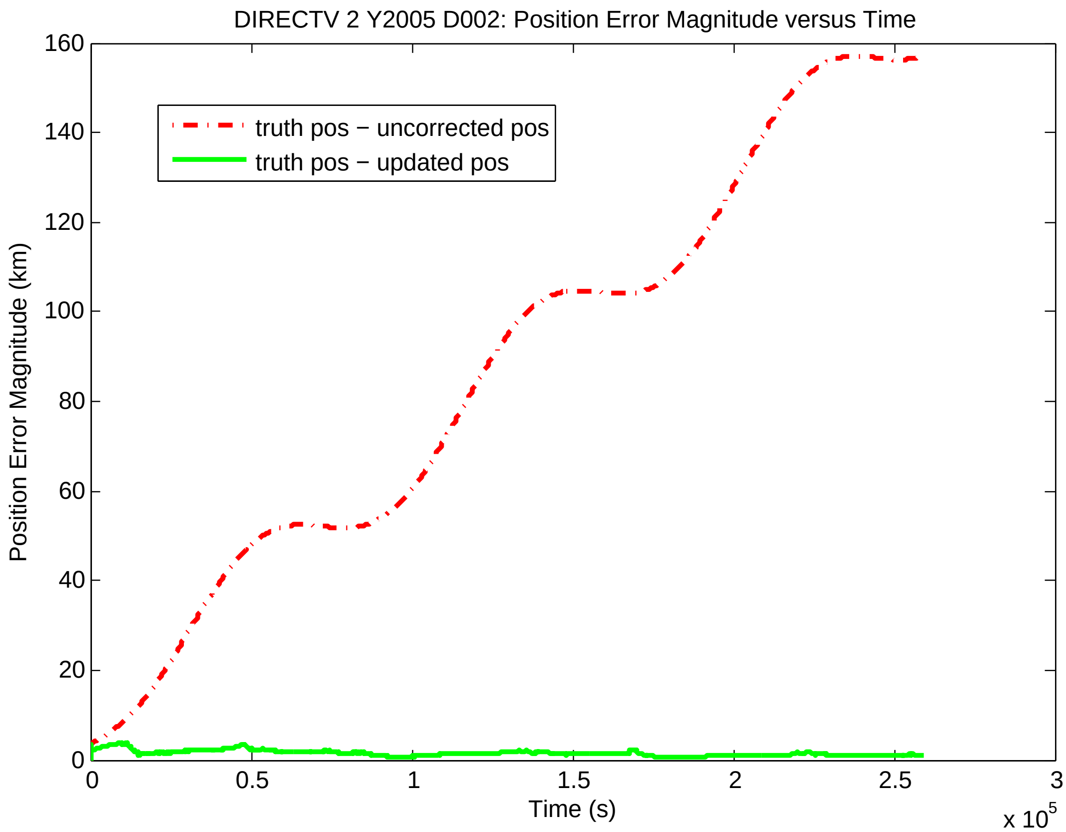

Figure 6.28: EKF position accuracy versus the uncorrected state accuracy for the DirecTV orbit with a single 1 m^2 detector.

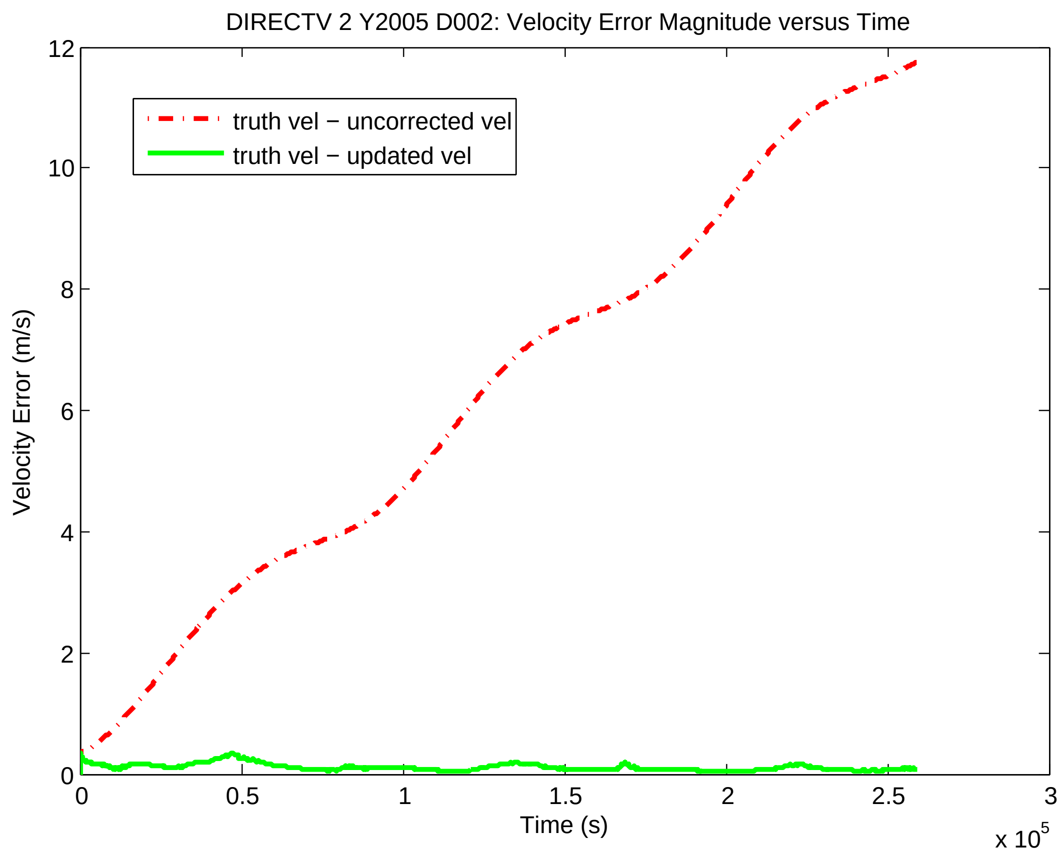

Figure 6.29: EKF velocity accuracy versus the uncorrected state accuracy for the DirecTV orbit with a single 1 m^2 detector.

trajectories and the DirecTV orbit are all displayed. The position and velocity error levels are both quantified by reporting the RMS error from the end of the simulation as well as through an average position and velocity metric. The average metric is computed over the last 48000 seconds of the simulation duration for the cislunar and MSL trajectories in order to capture the performance over an entire time through the pulsar schedule sequence: B1821-24, B1937+21, Crab pulsar, and J0218+4232. For the DirecTV orbit the averages are computed over the last orbit, 24 hours, of the simulation. These averages were used to provide a measure of the performance after the initial settling time of the filter. The RMS is computed at each time step across the ten iterations of the simulations for each orbit and pulsar schedule scenario.

It can be seen from the results in Table 6.7 that the EKF with phase tracking measurement input is able to maintain position error levels under 4 km and velocity error levels below 8 cm/s for all of the trajectories considered. There is a clear increasing trend in the velocity errors when the dynamic stress increases. The MSL trajectory has 4.8 cm/s, the cislunar trajectory has 5.49 cm/s, and the DirecTV orbit has 7.28 cm/s for RMS velocity error at the end of the simulations. In all cases the end point position and velocity errors are similar to the averages computed over the later stages of the simulation. This demonstrates that the settling time has been reached by the filter by the time the averages are computed.

The average position error varies from 1.71 km for the MSL trajectory to 3.27 km for the cislunar trajectory to 1.00 km for the DirecTV orbit. It is interesting that the position estimation results are the best for the DirecTV orbit even with its elevated dynamic environment. The Crab pulsar and B1821-24 are the two best pulsars demonstrated for phase tracking in this dissertation and these are the sources available for the DirecTV orbit, but they are also available for the other trajectories considered. Overall, good three-dimensional tracking was demonstrated with the single detector model for the EKF, using phase tracking measurements, for all of the trajectories considered.

Table 6.7: Results for the combined navigation EKF simulations using a single detector with an area of 1 m^2. The key for the pulsar numbering in the schedule is as follows: 1 = Crab Pulsar, 2 = B1821-24, 3 = B1937+21, and 4 = J0218+4232.

	MSL Trajectory	Cislunar Trajectory	DirecTV Orbit
Pulsar Schedule	2, 3, 1, 4	2, 3, 1, 4	1, 2
End Point RMS Position Error (km)	2.94	3.93	0.82
Averaged Position Error (km)	1.71	3.27	1.00
End Point RMS Velocity Error (cm/s)	4.58	5.49	7.28
Averaged Velocity Error (cm/s)	3.57	4.44	7.45

The results for the simulations with a single detector in Table 6.7can be compared against the three detector results in Table 6.6. For the MSL trajectory, the end point RMS position error was 2.94 km with a single detector and 1.16 km with three detectors cycling through the four pulsars. For the cislunar trajectory, the end point RMS position error was 3.93 km with a single detector and 2.62 km with three detectors cycling through the four pulsars. For both trajectories, the three detector simulations have better position tracking errors as expected. Both the three and single detector configurations yield good position and velocity determination results with the EKF using x-ray pulsar phase tracking measurements, for all of the trajectories simulated.

6.5 Summary

In this chapter an extended Kalman filter was used to incorporate phase tracking measurements from multiple pulsars in order to produce a three-dimensional navigation solution. This builds upon the individual range measurements along the line-of-sight to a pulsar that were generated through the phase tracking methods developed and simulated in Chapter 5. Each of these individual phase tracking measurements is unable to give accurate estimates of the entire three-dimensional position and velocity of the spacecraft. When incorporated into the extended Kalman filter, good tracking performance of the overall navigation state was achievable.

The measurements incorporated into the EKF used the accuracy levels demonstrated for the phase tracking simulations in Chapter 5 to generate representative estimates of the range error. Two different detector configurations were simulated. One with three independent, 1 m^2 detectors each tracking different pulsars, and another with a single 1 m^2 detector that looks at pulsars in sequence. Different sets of pulsars and observation schedules were considered for each detector scenario.

Simulations were performed to show the EKF performance with the MSL trajectory, cislunar trajectory, and DirecTV orbit considered in Chapter 5. For the MSL and Cassini trajectories, B1821-24, B1937+21, J0218+4232, and the Crab pulsar were considered. For the DirecTV orbit, only B1821-24 and the Crab pulsar were considered due to the detector area limitations of phase tracking the other pulsars. Only the single detector setup was simulated for the DirecTV orbit due to the observation schedule.

For the three detector case the best results were shown with the scenario cycling through all four pulsars. A position error of 1.16 km and velocity error of 3.31 cm/s was demonstrated. The geometric diversity outweighed the incorporation of more of the lower quality measurements from B1937+21 and J0218+4232. For all of the single detector scenarios simulated, a position error under 4 km and a velocity error under 8 cm/s was achievable. The DirecTV orbit had the best position estimation error of 0.82 km and the largest velocity error of 7.28 cm/s. This was due to both the optimal observation scheduling using only the Crab pulsar and B1821-24, but also the highest dynamic environment.

Chapter 7: Conclusions and Future Work

7.1 Overview

This dissertation has presented new methods for phase tracking x-ray pulsar signals. X-ray pulsars have many desirable characteristics for navigation such as unique, reliable, and repeatable signals. Pulsars exist in a wide range of directions in the sky and their vast distances allow them to provide signal coverage for spacecraft in various operational environments throughout the solar system. There are challenges that make their use more difficult such as their weak signal strengths, but their potential outweighs the difficulties. In this Dissertation, the specific navigation method of phase tracking x-ray pulsars is investigated in depth.

Previous x-ray pulsar phase tracking methods, introduced by Golshan and Sheikh in [64], were presented and validated using an x-ray pulsar emulator at NASA Goddard. This x-ray testbed allowed for phase tracking to be performed with x-ray photon generation and detection in a controlled lab environment. This method was demonstrated to work well with the Crab pulsar, but is unusable with any of the other pulsar signals that are desirable for navigation due to their much lower signal fluxes. This motivated the investigation into changes to the phase tracking algorithm that would allow for the use of millisecond period pulsars with a reasonably sized x-ray detector.

An extension to the MLE algorithm for signal phase was developed to allow the signal frequency to vary over an observation at an assumed constant rate. This update over previous phase tracking methods, that required the signal frequency to be constant, allowed the use of longer observations per estimate. This expanded the set of usable pulsars to include low flux millisecond period pulsars that are attractive for navigation.

Empirical tests were performed to determine the performance of the MLE and compare it to the theoretical Cramer-Rao lower bound using B1821-24, B1937+21, J0218+4232, J0437-4715, and the Crab pulsar. These tests covered a range of trajectory dynamic conditions including an MSL interplanetary trajectory and DirecTV, GPS, and ISS Earth orbits. Lower and upper thresholds on observation time were determined for convergence to the Cramer-Rao bound for each pulsar and orbit combination. These thresholds resulted from the effects of Poisson statistics and trajectory dynamic stress.

A method for analytically predicting the lower threshold observation time for the MLE was created to provide a quick means of approximating the necessary observation time for convergence of the MLE to the Cramer-Rao bound without having to perform extensive and time consuming empirical tests. This analytical prediction performed well for the three pulsars with the smaller pulse widths, but provided very conservative estimates for the two pulsars with larger pulse width. It was demonstrated using artificial pulse profiles that the analytical threshold observation time prediction provides good results for pulse widths below 0.15 cycles.

The proposed new phase tracking algorithm, using a higher order Taylor expansion in the maximum likelihood estimator for phase along with feedback of frequency and frequency derivative from a third-order phase-locked loop, was tested throughout various spacecraft trajectories. The same set of pulsars from the empirical MLE tests were simulated. Phase tracking was tested with low dynamic stress examples including interplanetary cruise trajectories from Cassini and MSL, an intermediate dynamic stress environment with a cislunar trajectory, and high dynamic stress Earth orbits including DirecTV, GPS, and ISS orbits.

PSR J0437+4715 was shown to be less conducive to use for phase tracking due to its much lower SNR, but for all the other pulsars with the interplanetary and cislunar trajectories the phase tracking algorithm worked well and showed the potential to produce position estimates with errors under 6 to 7 km using a reasonably sized 1 m^2 area detector.

For the Earth tracking results, only the Crab pulsar and B1821-24 were able to track the ISS orbit. PSRs B1937+21 and J0218+4232 needed larger areas of 8 m^2 and 10 m^2 to track the DirecTV and GPS orbits, respectively. A trade-study was compared to determine for each pulsar the detector areas required to track the dynamic stress conditions represented by each orbit. The choices of loop noise bandwidth B_L and block update time T were constrained by the dynamic environment in each scenario and were directly related to the achievable performance.

An extended Kalman filter was used to incorporate phase tracking measurements from multiple pulsars in order to produce a three-dimensional navigation solution. This built upon the capability of the phase tracking algorithm to provide one-dimensional range measurements along the line-of-sight to the source pulsar. Simulations were performed using three detectors or a single detector using the Crab pulsar, B1821-24, B1937+21, and J0218+4232 to track the cislunar and MSL trajectories and the Crab pulsar and B1821-24 to track the DirecTV orbit. Various observation schedules were considered and results under 4 km position error and 8 cm/s velocity error were obtained for all of the orbits.

7.2 Summary of Contributions

Through the work demonstrated in the various chapters, the goals set forth in Chapter 1 have been achieved. The major contributions of this work include:

- Validate previous phase tracking with NASA Goddard X-ray Laboratory Testbed (Chapter 3)

  The Golshan and Sheikh phase tracking method was demonstrated for the Crab pulsar using the tabletop pulsar emulator at NASA Goddard. This tested the algorithm under conditions that included x-ray photon generation and detection. The drawbacks of this method were clearly demonstrated for any pulsar with a lower flux than the Crab pulsar, which is all current other x-ray pulsars for navigation. This previous phase tracking method can not track any pulsar, other than the Crab pulsar, with a x-ray detector area under 25 to 100 m^2 depending on the orbit.

- Characterization of the position maximum likelihood estimator performance for 4 millisecond period pulsars and the Crab pulsar (Chapter 4)

A new form of a x-ray pulsar phase maximum likelihood estimator was presented with a second-order Taylor polynomial internal phase model in order to allow for phase-tracking of a wide range of low flux pulsars. The threshold lower bound observation times for convergence to the Cramer-Rao lower bound were empirically determined. Upper bounds on observation time for convergence to the Cramer-Rao bound were empirically determined due to the dynamic stress conditions of the orbits. These lower and upper bounds were determined for B1821-24, B1937+21, J0218+4232, J0437-4715, and the Crab pulsar for various Earth orbits and interplanetary trajectories. Optimal observation times were determined for each pulsar that fit between the lower and upper bounds for use with the phase tracking algorithm.

- Generated a method to analytically predict the threshold observation time for a given pulsar (Chapter 4)

  An analytical method to estimate the threshold observation time for convergence to the Cramer-Rao bound was presented and tested. This method provides a first order supplement to the time and computation intensive process of creating new maximum likelihood estimator performance plots. This allows for a quick way to start up phase tracking with a new pulsar and orbit combination by providing a rough initial block update time to determine if further analysis seems profitable.

- Extension of phase tracking to low flux pulsars (Chapter 5)

  A new phase tracking algorithm is presented and tested that allows for the inclusion of a set of much lower flux pulsars than previously possible including a large number of the ones deemed to have signal characteristics most suitable for navigation. This relied on the relaxation of the assumption that the signal frequency is constant over the time considered for each estimate, that was present for previous attempts at phase tracking x-ray pulsars. This was accomplished using a second-order Taylor polynomial phase model with a third-order digital phase-locked loop. The performance was demonstrated with simulations for four millisecond period pulsars and the Crab pulsar over a variety of different orbital environments: the MSL and Cassini cruise trajectories; a cislunar trajectory; and the DirecTV, GPS, and ISS orbits.

- Simulated a three-dimensional navigation extended Kalman filter to integrate phase tracking measurements from various pulsars (Chapter 6)

  An extended Kalman filter was used to incorporate one-dimensional range measurements from the phase tracking algorithm from multiple pulsars to produce a three-dimensional navigation solution. Three detector and single detector spacecraft scenarios were simulated for the MSL trajectory, the cislunar trajectory, and the DirecTV orbit using the B1821-24, B1937+21, J0218+4232, and Crab pulsar signals. Different pulsar observation scheduling choices were investigated. This is the first work to combine phase tracking pulsar estimates into a three-dimensional filtering model.

7.3 Future Research Recommendations

Although this dissertation presents a great improvement to the capabilities of phase tracking x-ray pulsar signals there are many areas of inquiry left open. To assist future research in phase tracking pulsar signals and in celestial object signal of opportunity navigation in general, several ideas for areas of further study are listed below:

- Develop a two parameter maximum likelihood estimator for phase and frequency

  The algorithm for the computation of the maximum likelihood estimator could be expanded to also include a search through potential frequencies to provide a Doppler estimate along with the phase estimate already provided. This would allow both a range and range-rate measurement from the phase tracking algorithm to be used in the navigation filter. This could potentially reduce the initial condition requirements.

- Investigate other internal phase models for the maximum likelihood estimator that might work better with Earth orbits based on orbital elements

  The phase tracking algorithm as designed has the most trouble tracking Earth orbits due to their higher dynamic environment. Other potential internal phase models beyond the Taylor polynomial model could be investigated to use other parameters specific to the orbit such as the Keplerian elements.

- Perform photon level simulations with the three-dimensional navigation filter

A simulation that generates the phase tracking range measurements from a photon level simulation in real time with the extended Kalman filter processing would be the most complete way to test the simulated capability of the phase tracking algorithm. This is computationally intensive and ways to work around that would need to be addressed.

- Investigate types of x-ray detectors or other instruments that work best for phase tracking

  This investigation of detector types would include determining the parameters necessary for good phase tracking performance. Specific detector characteristics that need to be looked at include good source direction pointing, good background rejection, and a large detection area.

- Launch a CubeSat to test x-ray pulsar phase tracking methods in cislunar or interplanetary space

  In order to test x-ray pulsar phase tracking algorithms outside of simulations it would be desirable to launch a CubeSat into a cislunar or interplanetary trajectory carrying a x-ray detector capable of use for navigation. X-ray signals do not pass through the Earth's atmosphere, so it is necessary to go to space to test XNAV in an experimental setting. Orbits that have lower dynamic stress would be desirable due to the limitations of phase tracking most x-ray pulsar signals in higher dynamic environments.

- Investigate other periodic celestial sources for phase tracking such as radio pulsars

There are other possible periodic celestial sources that can be looked at for their suitability for phase tracking. The most promising is radio pulsars, depending on the availability of a spacecraft-based radio dish that can provide adequate signal strength.

- Investigate other potentially usable celestial sources for navigation such as fast radio bursts and gamma ray bursts

  There are other celestial sources that are promising for use in a spacecraft navigation algorithm. Some of these are potentially repeatable, like fast radio bursts, and others are one-time events that could be used for relative navigation, like gamma ray bursts.

- Look into ways to combine measurements from multiple different types of celestial sources together for improved performance

  Each celestial source has its own capabilities and limitations for use in spacecraft navigation methods. A system that incorporates navigation measurements from a wide range of these source types might have greater performance and durability than a system considering only one type alone.

- Look into advancements in phase tracking methods that could potentially lead to single photon measurement updates

  The ideal use of a x-ray pulsar signal for navigation would be in a method that can provide measurements from single photons since this would minimize the loss of data when combining multiple photon events into an estimate. Potential nonlinear filtering methods should be considered to work toward this goal.

7.4 Concluding Summary

X-ray pulsars provide the potential for use as aids to spacecraft navigation due to their unique, stable, and repeatable signals. Challenges exist due to their low source fluxes that make signal detection difficult. There have been many promising results, including this dissertation, that show the potential for XNAV to be used as a compliment to existing systems such as the DSN, in the near future. Limitations with detector physics need to be overcome, but progress is being made.

Phase tracking is a method that is an improvement on the state of the art in XNAV measurement processing. It provides a greater number of measurements than previous methods that relied on the comparison of pulse time of arrival measurements. Phase tracking provides the potential for range and range rate measurements. It also has greater durability to catch potential errors in the measurements due to naturally occurring signal glitches or instrument errors. This dissertation has provided a foundation for future research into the use of phase tracking by expanding capability and demonstrating performance with a wide range of usable pulsar signals and spacecraft orbit environments.

Appendix A: NHPP Simulation Methods

This appendix provides background on the methods for simulating realizations of a nonhomogeneous Poisson process (NHPP). In particular the inversion method of non-uniform random variable generation will be described. This is the method used by [64] to generate sets of simulated photon arrival times in previous pulsar phase tracking research. The X-ray Photons and Relativistic Effects Simulation System (XPRESS), developed by ASTER Labs, Inc and collaborators, uses this method to generate simulated photon event times for different pulsar observation scenarios.

This formulation follows the framework from [108]. The general principle comes from an extension of the inversion method for continuous random variable generation. We want to simulate the times of events, T_i, given in increasing order as $0 < T_1 < T_2 < \cdots < T_N$, of a NHPP with rate $\lambda(t)$. First, define the integral of the rate function, which will take the role of the distribution function from the continuous case:

$$\Lambda(t) = \int_0^t \lambda(u)du. \tag{A.1}$$

Now note that given $T_n = t$, $T_{n+1} - T_n$ has the following distribution function

$$F(x) = 1 - e^{-(\Lambda(t+z)-\Lambda(t))} \text{ for } x \geq 0 \tag{A.2}$$

as long as $\lim_{t\to\infty} \Lambda(t) = \infty$, which corresponds to $\int_0^\infty \lambda(t)dt = \infty$. This follows from the following:

$$
\begin{aligned}
F(x) &= P(T_{n+1} - T_n > x | T_n = t) \\
&= P(N(t, t + x) = 0 | T_n = t) \\
&= e^{-(\Lambda(t+z) - \Lambda(t))} \text{ for } x \geq 0
\end{aligned} \tag{A.3}
$$

This tells us that T_{n+1} is distributed as $T_n + F^{-1}(U)$ where U is a uniform random variable on [0 , 1]. Now write U as $1-e^{-E}$ where E is an exponential random variable. Then it can be seen that T_{n+1} is also distributed as $\Lambda^{-1}(E + \Lambda(T_n))$. Thus, we need to invert Λ. Now we can follow the following algorithm proposed by [103] and used in [67] to invert the integrated rate function, Λ, to obtain a realization of the NHPP.

Algorithm for Inversion Method to generate a NHPP Realization [108]:

- L = 0 (Set L as an auxiliary variable)
- k = 0 (Set k as a counter)
- while $T_k \leq T_f$
  - Generate E as a random variable with parameter $\lambda_e = 1$
  - Update k to k + 1
  - Set $L = L + \Lambda^{-1}(E + \Lambda(L))$
  - Set T_k = L

This algorithm will continue generating values, T_k, until the chosen end time, T_f, is reached. This output is the desired realization of the NHPP.

Appendix B: X-ray Detectors

This Appendix will provide an overview of various types of x-ray detectors that are available for spacecraft missions. [1] and [128] provide the background for x-ray detector types and their applicability to the XNAV application.

When an x-ray is received by an x-ray detector it interacts with the detector's medium and leverages the photoelectric effect at low energies (< 100 keV) to generate a signal output. The energy released is directly proportional to the number of x-ray photons detected. Broadly, x-ray detectors are classified by the material with which the soft x-rays (photon energy of 1-15 keV) interact. There are four primary classes of x-ray detectors: proportional counters, scintillator detectors, microchannel plates, and semiconductor detectors.

Proportional counters use an inert gas as the interaction medium. When an x-ray photon arrives, the gas is ionized, the positively charged ions move to the anode and the negatively charged electrons move to the cathode within the chamber. This creates a strong output signal via the avalanche effect. However, proportional counters have a high risk of leaking in space and are typically too large for spacecraft of interest. A diagram showing the setup of a proportional counter style detector is included in Figure B.1.

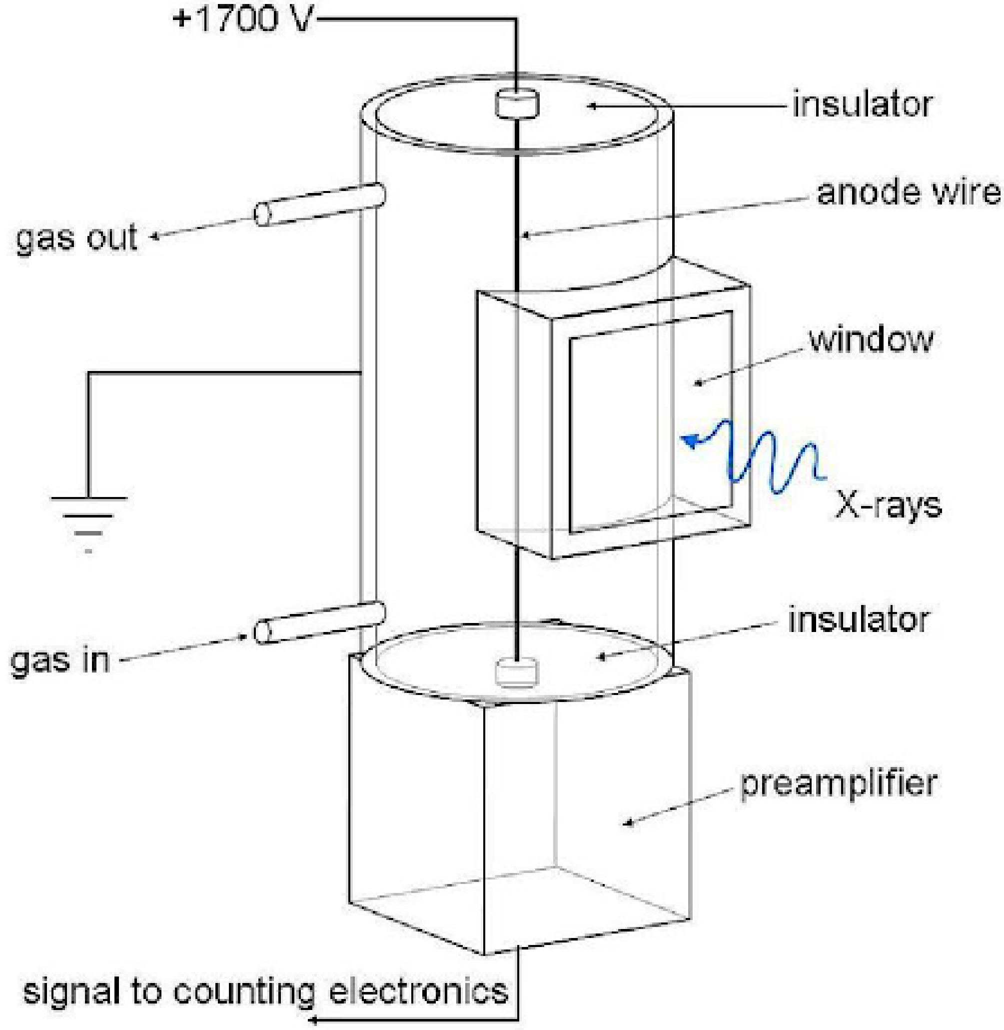

Figure B.1: Diagram of a x-ray proportional counter detector [128]

Figure B.2: Diagram of a x-ray scintillator detector [128]

Scintillator detectors use photomultiplier tubes to amplify the light and scintillators as the detection medium. Scintillators are transparent materials that emit light when acted upon by ionizing radiation, including x-rays [128]. This optic signal is amplified by the photomultiplier tubes similar to the avalanche effect with the proportional count style detectors.

Like proportional counters, scintillator detectors are not viable for space applications though their detection efficiency is higher than that of most proportional counters. Unfortunately, the most common scintillators are NaI and CsI which are prone to deliquescence in space. A diagram showing the setup of a scintillator style detector is included in Figure B.2.

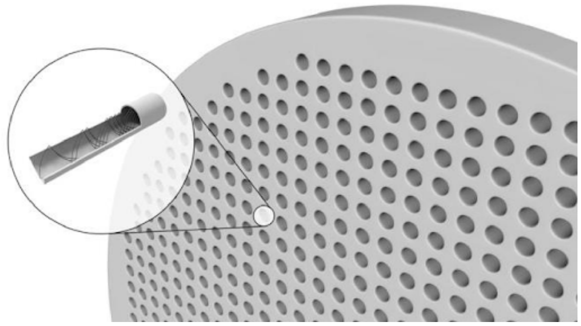

Figure B.3: Diagram of a x-ray microchannel plate detector [128]

Microchannel plates (MCPs) are composed of 1-10 million tightly packed microchannels that function like photomultiplier tubes as the x-rays emit electrons when they interact with the coated tubes. The microchannels function as both the detection medium and the amplifier for the avalanche effect. MCPs may be serviceable for XNAV applications dependent upon the material coating the tubes and the overall energy resolution. A diagram showing the setup of an MCP x-ray detector is included in Figure B.3.

Semiconductor detectors typically use silicon or germanium as the detection medium. As the x-ray photons interact with the semiconductor, electron hole pairs are produced and move to the anode where they are amplified, and a voltage signal is generated. Included in this class of detectors are charge-coupled devices (CCD) which use an array of micro-semiconductors and silicon drift detectors (SDD). For space applications, this class of x-ray detectors is the most common and viable type. Semiconductor detectors have high position and temporal resolution [128].

The X-ray Flux Monitor (XFM) detector is a new, more advanced SDD launch-ing on the ESA Lagrange mission to monitor space weather. The XFM is designed to measure x-ray flux with one second time resolution in the 1.55 keV to 24.8 keV energy range [129].

Appendix C: Maximum Likelihood Estimation

This appendix provides an introductory background for maximum likelihood estimation including a basic example to illustrate the concept. The maximum likelihood estimator (MLE) is a frequently employed classical method of parameter estimation developed by R.A. Fisher in the early 20th century [130]. This estimation technique does not assume the complete probability distribution function, but instead obtains parameter estimates by maximizing the joint distribution over the parameter space. This joint distribution of the sample together with the parameters of interest form the likelihood function. Thus, MLEs are based on the observed data not a priori model assumptions.

Typically, the natural logarithm of the likelihood function is used to determine the parameter value(s) that maximize the likelihood function. The MLE is an unbiased estimator (i.e., the expectation of the sample mean is the true mean) with very low variance. In fact, the MLE achieves the Cramer Rao Lower Bound (CRLB) and is therefore a minimum variance unbiased estimator (MVUE) [130].

To define the MLE we need to first define the likelihood function. Let $X_1, X_2, \ldots, X_n$ be independent, identically distributed random variables and

$$f(x_1, x_2, \ldots, x_n; \lambda_1, \ldots, \lambda_k)$$

be the joint probability distribution (mass) function of our random variables and unknown parameters $\lambda_1, \ldots, \lambda_k$.

The likelihood function is the probability distribution (mass) function over $\lambda_1, \ldots, \lambda_k$ for a fixed sample $x_1, x_2, \ldots, x_n$, and the maximum likelihood estimates $\hat{\lambda}_1, \ldots, \hat{\lambda}_k$ are the set of parameter values that maximize f.

Consider the following simple scenario. A bag contains 3 balls each of which is red or white, but we don't know how many of those 3 are red (or white). Suppose there are r red balls, then the probability of blindly drawing a red ball from the bag would be $\frac{r}{3}$. If we continue to draw from the bag with replacement four additional times, we can express our joint probability mass function as

$$f(x_1, x_2, x_3, x_4; r)$$

where $X_1, \ldots, X_4$ are dichotomous random variables and the probability of drawing a white ball on the 3rd draw can be expressed as $P(X_3 = white) = 1 - \frac{r}{3}$.

We perform this experiment once and obtain the sample $\{red, red, white, red\}$. Therefore our likelihood function is:

$$f(red, red, white, red; r) = \frac{r}{3}\frac{r}{3}(1 - \frac{r}{3})\frac{r}{3} = \frac{-r^3(r-3)}{81} \tag{C.1}$$

Since this is discrete, to determine the maximum likelihood estimates we evaluate f at each of the possible values for r:

$$f(red, red, white, red; 0) = 0$$

$$f(red, red, white, red; 1) = 0.0247$$

$$f(red, red, white, red; 2) = 0.0988$$

$$f(red, red, white, red; 3) = 0$$

The parameter value $r = 2$ yields the maximal value for the likelihood function. Therefore the MLE is $\hat{r} = 2$.

Appendix D: Accelerometer Performance in Space

This appendix provides a general overview of accelerometers that are available for use on spacecraft. An accelerometer was assumed available for the phase tracking algorithm in order to provide an initial estimate of acceleration to help initialize the DPLL. The level of acceleration accuracy required was 1 mg or 1 cm/s^2. There are many aspects of the space environment that make accelerometer performance difficult.

A wide range of accelerometers have been developed for space conditions and flown over the years. Table D.1 contains an overview of accelerometers available for use on spacecraft including their achievable accuracies. The listed accelerometers all possess the necessary accuracy required to seed the phase tracking algorithm. Most of the accelerometers for space listed are electrostatic and developed for use in gravitational wave detection.

The STAR ultra-sensitive space accelerometer was flown on the CHAMP satellite and had an accuracy of 10e-10 m/s^2 over a 1 Hz bandwidth [131]. It has the potential for an accuracy of 10e-12 m/s^2 and was developed by ONERA in France.

The Capteur Accelerometrique Triaxial Ultra Sensible (CACTUS) was an electrostatic accelerometer that was developed for satellite testing in the early

Table D.1: Spacecraft Accelerometer Missions and Accuracies

Name	Mission/Organization	Accuracy and notes
STAR ultra-sensitive	CHAMP Satellite	10e-10 m/s^2 over 1 Hz bandwidth
CACTUS	Satellite testing	10e-9 m/s^2
HUST Electrostateic	Tianzhou-1	10e-10 m/s^2/hz$^{1/2}$
X-servo	Huygen's Probe	10e-4 to 10e-1 with 1 Hz bandwidth
ASTRE	ESA	10e-8 m/s^2 DC to 1 Hz
GRADIO	ESA	4e-13 m/s^2/hz$^(1/2)$

1970s [132]. It has an achievable accuracy of 10e-9 m/s^2.

The HUST Electrostatic Accelerometer flew on the Tianzhou-1 mission [133]. It has an accuracy of 10e-10 m/s^2/Hz$^{1/2}$. This was an electrostatic accelerometer and is developed for use with space gravitational wave detection missions.

The X-servo accelerometer flew on the Huygen's probe with the Cassini mission to Saturn and landed on the moon Titan [134]. It had an accuracy of 0.3 mg to 0.3 μg or 10e-4 to 10e-1 with a 1 Hz bandwidth.

The ASTRE and GRADIO accelerometers were developed by ESA and are both electrostatic accelerometers [135]. The ASTRE accelerometer flew on the GRACE mission. The GRADIO accelerometer flew on the CHAMP mission in 2000, the GRACE mission in 2002, and the GOCE mission 2009. The ASTRE accelerometer can provide full scale range to 10e-2 m/s^2 with a resolution exceeding 10e-8 m/s^2 from DC to 1 Hz. The GRADIO accelerometer has a resolution of 4e-13 m/s^2/hz$^{1/2}$ with a frequency bandwidth of 5e-3 to 0.1 Hz.

Bibliography

[1] Sheikh, S. I., *The Use of Variable Celestial X-ray Sources for Spacecraft Navigation*, Ph.D. Thesis, University of Maryland, 2005, URL: https://drum.umd.edu/dspace/handle/1903/2856.

[2] Melbourne, W. G., "Navigation Between the Planets," *Scientific American*, Vol. 234, No. 6, 1976, pp. 58-74.

[3] Battin, R. H., *An Introduction to the Mathematics and Methods of Astrodynamics*, Revised ed., American Insitute of Aeronautics and Astronautics, Washington, DC, 1999.

[4] Gounley, R., White, R., and Gai, E., "Autonomous Satellite Navigation by Stellar Refraction," *Journal of Guidance, Control, and Dynamics*, Vol. 7, No. 2, 1984, pp. 129-134.

[5] Jordan, J. F., "Navigation of Spacecraft on Deep Space Missions," *Journal of Navigation*, Vol. 40, January 1987, pp. 19-29.

[6] Wertz, J. R., *Spacecraft Attitude Determination and Control*, Kluwer Academic Publishers, Boston, MA, 1978.

[7] Bate, R. R., Mueller, D. D., and White, J. E., *Fundamentals of Astrodynamics*, Dover Publications Inc., New York, 1971.

[8] Weeks, C. J. and Bowers, M. J., "Analytical Models of Doppler Data Signatures," *Journal of Guidance, Control, and Dynamics*, Vol. 18, No. 6, 1995, pp. 1287-1291.

[9] Jet Propulsion Laboratory, "About The Deep Space Network," [online], California Insitute of Technology, NASA, 2017 URL: https://deepspace.jpl.nasa.gov/ [cited 8 Oct 2017].

[10] Sheikh, S. I., Hanson, J. E., Collins, J., and Graven P., "Deep Space Navigation Augmentation Using Variable Celestial X-ray Sources," *Proceedings of the 2009 International Technical Meeting of The Institute of Navigation*, Anaheim, CA, January 2009, pp. 34-48.

[11] Mudgway, D. J., *Uplink-Downlink, A History of the Deep Space Network 1957-1997*, National Aeronautics and Space Administration, Washington, DC, 2001.

[12] Thornton, C. L. and Border, J. S., *Radiometric Tracking Techniques for Deep Space Navigation*, John Wiley & Sons, Hoboken, NJ, 2003.

[13] Moyer, T. D., *Formulation for Observed and Computed Values of Deep Space Network Data Types for Navigation*, John Wiley & Sons, Inc., Hoboken, NJ, 2003.

[14] Lanyi, G., Bagri, D. S., and Border, J. S., "Angular Position Determination by Spacecraft by Radio Interferometry," *Proceedings of the IEEE*, Vol. 95, No. 11, IEEE, November 2007.

[15] Bhaskaran, S., "The Application of Noncoherent Doppler Data Types for Deep Space Navigation," Jet Propulsion Laboratory, Pasadena, CA, The Telecommunications and Data Acquisition Progress Report 42-121, May 15, 1995.

[16] Folta, D. C., Gramlin, C. J., Long, A. C., Leung, D. S. P., and Belur, S. V., "Autonomous Navigation Using Celstial Objects," *American Astronomical Society (AAS) Astrodynamics Specialist Conference*, AAS Paper 99-439, August 1999, pp. 2161-2177.

[17] Larson, W. J. and Wertz, J. R. Eds., *Space Mission Analysis and Design*, 3rd Edition, Space Technology Series. Microcosm Press and Kluwer Academic Publishers (Jointly), Boston, MA, 1999.

[18] Parkinson, B. W. and Spilker, J. J. J. Eds., *Global Positioning System: Theory and Applications, Volume I*, American Institute of Aeronautics and Astronautics, Washington, DC, 1996.

[19] Parkinson, B. W. and Spilker, J. J. J. Eds., *Global Positioning System: Theory and Applications, Volume II*, American Institute of Aeronautics and Astronautics, Washington, DC, 1996.

[20] Steffes, S. R. and Barton, G. H., "Deep Space Autonomous Navigation Options for Future Missions," AIAA SPACE and Astronautics Forum and Exposition, Orlando, FL, September 2017.

[21] Christian J. A. and Lightsey, E. G., "Onboard Image-Processing Algorithm for a Spacecraft Optical Navigation Sensor System," *Journal of Spacecraft and Rockets*, Vol. 49, No. 2, March - April 2012, pp. 337-352.

[22] Bader, N. A., "Autonomous Vision Navigation of Spacecraft in Lunar Orbit," Master's Thesis, Rice University, 2016, URL: http://hdl.handle.net/1911/96609.

[23] Singh, L. and Lim, S., "On Lunar On-Orbit Vision-Based Navigation: Terrain Mapping, Feature Tracking Driven EKF," *AIAA Guidance, Navigation and Control Conference and Exhibit*, AIAA 2008-6834, Honolulu, Hi, August 2008.

[24] Woffinden, D., Robinson, S., Spehar, P., and Pedrotty, S., "The Development and Testing of Vision Navigation for Proximity Operations and Docking Using the ISS Selfie," *Advances in the Astronautical Sciences Guidance, Navigation and Control*, Vol. 159, No. AAS 17-076, 2017.

[25] Frommert, H., and Kronberg, C., "The First Known Variable Stars," [online database], URL: https://www.spider.seds.org/spider/Vars/vars.html.

[26] Halley, E., "A Short History of several New-Stars that have apper'd within these 150 Years; with an Account of the Return of that in Collo Cygni, and of its Continuance observed this Year 1715," *Phil. Trans.*, Vol. 29, 1715, pp. 354-356

[27] AAVSO, "Types of Variable Stars," [online database], The American Association of Variable Star Observers, URL: https://www.aavso.org/types-variables [cited 6 Oct 2017].

[28] Seward, F. D. and Charles, P. A., *Exploring the X-ray Universe*, Second Edition, Cambridge University Press, Cambridge UK, 2010.

[29] Hewish, A., Bell, S. J., Pilkington, J. D., Scott, P. F., and Collins, R. A., "Observation of a Rapidly Pulsating Radio Source," *Nature*, Vol. 217, 1968, pp. 709-713.

[30] Lyne, A. and Graham-Smith, F., *Pulsar Astronomy*, Third Edition, Cambridge University Press, Cambridge UK, 2005.

[31] Manchester, R. N. and Taylor, J. H., *Pulsars*, W. H. Freeman and Company, San Francisco, 1977.

[32] Baade, W. and Zwicky, F., "On Super-Novae," *Proceedings of the National Academy of Science*, Vol. 20, No. 5, 1934, pp. 254-259.

[33] Oppenheimer, J. R. and Volkoff, G. M., "On Massive Neutron Cores," *Physical Review*, Vol. 55, 1939, pp. 374-381.

[34] Sheikh, S. I., Hanson, J. E., Graven, P. H., and Pines, D. J., "Spacecraft Navigation and Timing Using X-ray Pulsars," *Navigation: Journal of The Institute of Navigation* Vol. 58, No. 2, Summer 2011.

[35] Taylor, J. H., "Millisecond Pulsars: Nature's Most Stable Clocks," *Proceedings of the IEEE*, Vol. 79, No. 7, 1991, pp. 1054-1062.

[36] Kaspi, V. M., Tayor, J. H., and Ryba, M. F., "High-Precision Timing of Millisecond Pulsars. III: Long-Term Monitoring of PSRs B1855+09 and B1937+21," *Astrophysical Journal*, Vol. 428, 1994.

[37] Matsakis, D. N., Taylor, J. H. and Eubanks, T. M., "A Statistic for Describing Pulsar and Clock Stabilities," *Astronomy and Astrophysics*, Vol. 326, 1997, pp. 924-928.

[38] Buist, P. J., Engelen, S., Noroozi, A., Sundaramoorthy, P., Verhagen, S., and Verhoeven, C., "Overview of Pulsar Navigation: Past, Present and Future Trends" *Navigation: Journal of The Institute of Navigation* Vol. 58, No. 2, Summer 2011.

[39] RXTE Science Operations Facility, "XTE ASM Catalog," [online], http://rxte.gsfc.nasa.gov/docs/xte/SOF/ASMCatalog.html [retrieved 20 November 2012].

[40] Gendreau, K. C., Arzoumanian, Z., and Okajima, T., "The Neuton-star Interior Composition ExploreR (NICER): an Explorer mission of opportunity for soft X-ray timing spectroscopy," *Proceedings of SPIE in Space Telescopes and Instrumentation: Ultraviolet to Gamma Ray*, volume 8443, September 2012. doi: 10.1117/12.926396

[41] Winternitz, L. M., Hassouneh, M. A., Gaeber, J. A., Mitchell, J. W., Gavriil, F., Arzoumanian, Z., and Gendreau, K. C., "An X-Ray Navigation Ground Testbed," *27th Space Sim Conference*, Annapolis, MD, November 2012.

[42] Ghosh, P., *Rotation and Accretion Powered Pulsars* World Scientific Series in Astronomy and Astrophysics, Vol. 10, World Scientific Publishing Co. Pte. Ltd., Singapore, 2007.

[43] Bhattacharya, D., "Millisecond Pulsar," *X-Ray Binaries*, W. H. G. Lewin, J. van Paradijs, and E. P.J. van den Heuvel, Eds., Cambridge University Press, Cambridge, UK, 1995, pp. 223-251.

[44] White, N. E., Nagase, F., and Parmar, A. N., "The Properties of X-Ray Binaries," *X-Ray Binaries*, W. H. G. Lewin, J. van Paradijs, and E. P.J. van den Heuvel, Eds., Cambridge University Press, Cambridge, UK, 1995, pp. 1-57.

[45] King, A., "Accretion in Close Binaries," *X-Ray Binaries*, W. H. G. Lewin, J. van Paradijs, and E. P.J. van den Heuvel, Eds., Cambridge University Press, Cambridge, UK, 1995, pp. 419-456.

[46] Fraser, G. W., *X-Ray Detectors in Astronomy*, Cambridge University Press, Cambridge, UK, 1989.

[47] Wood, K. S., Meekins, J. F., Yentis, D. J., Smathers, H. W., McNutt, D. P., Bleach, R. D., Friedman, H., Byram, E. T., Chubb, T. A., and Meidav, M., "The HEAO A-1 X-ray Source Catalog," *Astrophysical Journal Supplement Series*, Vol. 56, December 1984, pp. 507-649.

[48] Sheikh, S. I., Pines, D. J., Wood, K. S., Ray, P. S., Lovellette, M. N., and Wolff, M. T., "Spacecraft Navigation Using X-ray Pulsars," *Journal of Guidance, Control, and Dynamics*, Vol. 29, No. 1, 2006.

[49] Reichley, P. E., Downs, G. S., and Morris, G. A., "Use of Pulsar Signals as Clocks," *NASA Jet Propulsion Laboratory Quarterly Technical Review*, Vol. 1, No. 2, July 1971, pp. 80-86.

[50] Reichley, P. E., Downs, G. S., and Morris, G. A., "Time-of-Arrival Observations of Eleven Pulsars," *Astrophysical Journal*, Vol. 159, January 1970, pp. L35-L40.

[51] Allan, D. W., "Millisecond Pulsar Rivals Best Atomic Clock Stability," *41st Annual Frequency Control Symposium*, IEEE, Philadelphia, PA, 1987, pp. 2-11.

[52] Downs, G. S. and Reichley, P. E., "Techniques for Measuring Arrival Times of Pulsar Signals I: DSN Obsevations from 1968 to 1980," NASA Jet Propulsion Laboratory, California Institute of Technology, Pasadena CA, NASA Technical Reports NASA-CR-163564, 15 August 1980.

[53] Downs, G. S., "Interplanetary Navigation Using Pulsating Radio Sources," *NASA Technical Reports N74-34150*, 1974, pp. 1-12.

[54] Wallace, K., "Radio Stars, What They are and the Prospects for Their Use in Navigational Systems," *Journal of Navigation*, Vol. 41, No. 3, September 1988, pp. 358-374.

[55] Shearer, A. and Golden, A., "Implications of the Optical Observations of Isolated Neutron Stars," *Astrophysical Journal*, Vol. 547, February 2001, pp. 967-972.

[56] Chester, T. J. and Butman, S. A., "Navigation Using X-ray Pulsar," *NASA Technical Reports N81-27129*, 1981, pp. 22-25.

[57] Wood, K. S., "Navigation Studies Utilizing The NRL-801 Experiment and the ARGOS Satellite," *Small Satellite Technology and Applications III*, Ed. B. J. Horais, International Society of Optical Engineering (SPIE) Proceedings, Vol. 1940, 1993, pp. 105-116.

[58] Hanson, J. E., *Principles of X-Ray Navigation*, Ph.D. Thesis, Stanford University, 1996, URL: http://il.proquest.com/products umi/dissertations/.

[59] Thomas, J. B., "An Analysis of Digital Phase-Locked Loops," *NASA JPL Publication* 89-2, February 1989.

[60] Becker, W. and Trumper, J., "Detection of Pulsed X-rays from the Binary Millisecond Pulsar J0437-4715," *Nature*, vol. 365, pp. 528-530, Oct. 1993.

[61] Sala, J., Urruela, A., Villares, X., Estalella, R., and Paredes, J. M., "Feasibility Study for a Spacecraft Navigation System Relying on Pulsar Timing Information," *European Space Agency Advanced Concepts Team ARIADNA Study*, vol. 3, no. 4202, p. 23, 2004.

[62] Pines, D. J., "XNAV Program: A New Space Navigation Architecture," *Advances in the Astronautical Sciences Guidance and Control 2006: Proceedings of the 29th Annual AAS Rocky Mountain Guidance and Control Conference*, vol. 125, AAS-06-007, Breckenridge CO, February 2006.

[63] Woodfork, D. W., "The Use of X-ray Pulsars for Aiding GPS Satellite Orbit Determination," Master's of Science Thesis, Air Force Institute of Technology, 2005, URL: http:://www.afit.edu.

[64] Golshan, A. R. and Sheikh, S. I., "On Pulse Phase Estimation and Tracking of Variable Celestial X-Ray Sources,"*Proceedings of the 63rd Annual Meeting of the Institute of Navigation*, Cambridge, MA, April 2007, pp. 413-422.

[65] Sheikh, S. I., Golshan, A. R., and Pines, D. J., "Absolute and Relative Position Determination Using Variable Celestial X-Ray Sources," *30th Annual AAS Guidance and Control Conference*, American Astronautical Society, Breckenridge, CO, 3-7 February 2007.

[66] Rodin, A. E., "Optimal Filters for the Construction of the Ensemble Pulsar Time," *Monthly Notices of the Royal Astronomical Society*, vol. 387, 2008, pp. 1583-1588.

[67] Emadzadeh, A. A. and Speyer, J. *Navigation in Space by X-ray Pulsars*, Springer, New York, 2011.

[68] Doyle, P. T., "The Development of a Simulator System and Hardware Test Bed for Deep Space X-ray Navigation," Master of Science Thesis, University of Minnesota, 2013.

[69] Deng, X. P., Hobbs, G., You, X. P., Li, M. T., Keith, M. J., Shannon, R. M., Coles, W., Manchester, R. N., Zheng, J. H., Yu, X. Z., Gao, D., Wu, X., and Chen, D., "Interplanetary Spacecraft Navigation using Pulsars," *Advances in Space Research*, vol. 52, pp. 1602-1621, Nov. 2013.

[70] Deng, X. P., Coles, W., Hobbs, G., Keith, M. J., Manchester, R. N., Shannon, R. M., and Zheng, J. H., "Optimal Interpolation and Prediction in Pulsar Timing," *MNRAS*, vol. 424, pp. 244-251, July 2012.

[71] Tran, N. D., Renaux, A., Boyer, R., and Marcos, S., "Performance Bounds for the Pulse Phase Estimation of X-ray Pulsars," *IEEE Trans. Aerospace and Electronic Systems*, Vol. 50, no. 1, January 2014, pp. 786-793.

[72] Hisamoto, C. S. and Sheikh, S. I., "Spacecraft Navigation using Celestial Gamma-Ray Sources," *Journal of Guidance, Control, and Dynamics*, vol. 38, Special Issue in Honor of Richard Battin, 2015, pp. 1765-1774.

[73] Zhang, X., Shuai, P., Huang, L., Chen, S., and Lihong, X., "Mission Overview and Initial Observation Results of the X-ray Pulsar Navigation-I Satellite," *International Journal of Aerospace Engineering*, vol. 2017, Article ID 8561830, 2017, pp. 1-7.

[74] Mitchell, J. W., Hassouneh, M. A., Winternitz, L. M., Valdez, J. E., Ray, P. S., Arzoumanian, Z., and Gendreau, K. C., "Station Explorer for X-ray Timing and Navigation Technology Architecture Overview," *Proceedings of the 27th International Technical Meeting of The Satellite Division of the Institute of Navigation (ION GNSS+ 2014)*, Tampa, Florida, September 2014, pp. 3194-3200.

[75] Mitchell, J. W., Hassouneh, M. A., Winternitz, L. M., Valdez, J. E., Price, S. R., Semper, S. R., Yu, W. H., Arzoumanian, Z., Ray, P. S., Wood, K. S., Litchford, R. J., and Gendreau, K. C., "SEXTANT — Station Explorer for

X-ray Timing and Navigation Technology," *AIAA Guidance, Navigation, and Control Conference*, ser. AIAA SciTech. American Institute of Aeronautics and Astronautics, Kissimmee, FL, Jan. 2015.

[76] Winternitz, L. M., Hassouneh, M. A., Mitchell, J. W., Valdez, J. E., Price, S. R., Semper, S. R., Yu, W. H., Ray, P. S., Wood, K. S., Arzoumanian, Z., and Gendreau, K. C., "X-ray Pulsar Navigation Algorithms and Testbed for SEXTANT," *2015 IEEE Aerospace Conference*, Big Sky, MT, March 2015, pp. 1-14.

[77] Rong, J., Luping, X., Hua, Z., and Cong, L., "Augmentation Method of XP-NAV in Mars Orbit Based on Phobos and Deimos Observations," *Advances in Space Research*, Vol. 58, No. 9, November 2016, pp. 1864-1878.

[78] Wang, S., Cui, P., Gao, A., Yu, Z., and Cao, M., "Absolute Navigation for Mars Final Approach Using Relative Measurements of X-Ray Pulsars and Mars Orbiter," *Acta Astronautica*, Vol. 138, September 2017, pp. 68-78.

[79] Ning, X., Gui, M., Fang, J., and Liu, G., "Differential X-Ray Pulsar Aided Celestial Navigation for Mars Exploration," *Aerospace Science and Technology*, Vol. 62, March 2017, pp. 36-45.

[80] Kai, X., Chunling, W., and Liangdong, L., "Performance Enhancement of X-Ray Pulsar Navigation Using Autonomous Optical Sensor," *Acta Astonautica*, Vol. 128, November 2016, pp. 473-484.

[81] Liu, J., Kang, Z. W., White, P., Ma, J., and Tian, J. W., "Doppler/XNAV-Integrated Navigation System Using Small-Area X-Ray Sensor," *IET Radar, Sonar, and Navigation*, Vol. 5, No. 9, December 2011, pp. 1010-1017.

[82] Ray, P. S., Wood, K. S., Fritz, G., Hertz, P., Kowalski, M., Johnson, W. N., Lovellette, M. N., Wolff, M. T., Yentis, D., Bandyopadhyay, R. M., Bloom, E. D., Giebels, B., Godfrey, G., Reilly, K, Parkinson, P. S., Shabad, G., Michelson, P., Roberts, M., Leahy, D. A., Cominsky, L., Scargle, J., Beall, J., Chakrabarty, D., and Kim, Y., "The USA X-ray Timing Experiment," *X-ray Astronomy: Stellar Endpoints, AGN, and the Diffuse X-ray Background*, American Institute of Physics (AIP) Proceedings, Vol. 599, 1 December 2001, pp. 336-345.

[83] Wood, K. S., Determan, J. R., Ray, P. S., Wolff, M. T., Budzien, S. A., Lovellette, M. N., and Titarchuk, L., "Using the Unconventional Stellar Aspect (USA) Experiment on ARGOS to Determine Atmospheric Parameters by X-ray Occultation," *Optical Spectroscopic Techniques, Remote Sensing, and Instrumentation for Atmospheric and Space Research IV*, Eds. A. M. Larar

and M. G. Mlynczak, International Society of Optical Engineering (SPIE) Proceedings, Vol. 4485, January 2002, pp. 258-265.

[84] Wood, K. S., Kowalski, M., Lovellette, M. N., Ray, P. S., Wolff, M. T., Yentis, D. J., Bandyopadhyay, R. M., Fewtrell, G., and Hertz, P. L., "The Unconventional Stellar Aspect (USA) Experiment on ARGOS," *American Institute of Aeronautics and Astronautics (AIAA) Space Conference and Exposition*, AIAA Paper 2001-4664, Albuquerque NM, August 2001.

[85] Winternitz, L. M., Mitchell, J. W., Hassouneh, M. A., Valdez, J. E., Price, S. R., Semper, S. R., Yu, W. H., Ray, P. S., Wood, K. S., Arzoumanian, Z., and Gendreau, K. C., "SEXTANT X-ray Pulsar Navigation demonstration: Flight system and test results," *2016 IEEE Aerospace Conference*, Big Sky, MT, March 2016, pp. 1-11.

[86] Winternitz, L. M. B., Mitchell, J. W., Hassouneh, M. A., Price, S. R., Semper, S. R., Yu, W. H., Ray, P. S., Wolff, M. T., Kerr, M., Wood, K. S., Arzoumanian, Z., Gendreau, K. C., Guillemot, L., Cognard, I., Demorest, P., Stappers, B., and Lyne, A., "SEXTANT X-ray Pulsar Navigation Demonstration: Additional On-Orbit Results," SpaceOps Conference, Marseille, France, May 2018.

[87] Doyle, P., Albrecht, C., and Gebre-Egziabher, D., "The High Altitude X-ray Detector Testbed Payload for the 2012 High Altitude Student Platform," Univestiy of Minnesota-Twin Cities, LSU HASP Program, Final Science Report, 2012, `URL:http://laspace.lsu.edu/hasp/groups/2012/science_report/Payload_03/UMN_2012_HASP_Science_Report.pdf`.

[88] Frick, S., DeLange, J., and Gebre-Egziabher, D., "The High Altitude X-ray Detector Testbed Payload for the 2014 High Altitude Student Platform," Univestiy of Minnesota-Twin Cities, LSU HASP Program, Final Science Report, 2014, `URL:http://laspace.lsu.edu/hasp/groups/2014/science_report/Payload_03/UMN_HASP2014_Science_Report.pdf`.

[89] Hanson, J., Sheikh, S., Graven, P., and Collins, J., "Noise Analysis for X-ray Navigation Systems," *Proceedings of the IEEE/ION PLANS 2008*, Monterey, CA, May 2008, pp. 704-713.

[90] Thomas, J. B., "Reformulation of the Relativistic Conversion Between Coordinate Time and Atomic Time," *Astronomical Journal*, Vol. 80, No. 5, 1975, pp. 405-411.

[91] Moyer, T. D., "Transformation from Proper Time on Earth to Coordinate Time in Solar System Barycentric Space-Time Frame of Reference - Part One," *Celestial Mechanics*, Vol. 23, 1981, pp. 33-56.

[92] Moyer, T. D., "Transformation from Proper Time on Earth to Coordinate Time in Solar System Barycentric Space-Time Frame of Reference - Part Two," *Celestial Mechanics*, Vol. 23, 1981, pp. 57-68.

[93] Martin, C. F., Torrence, M. H., and Misner, C. W., "Relativistic Effects on an Earth-Orbiting Satellite in the Barycenter Coordinate System," *Journal of Geophysical Research*, Vol. 90, No. B11, 1985, pp. 9403-9410.

[94] Sheikh, S. I., Hellings, R. W., and Matzner, R. A., "High-Order Pulsar Timing For Navigation," *Proceedings of the 63rd Annual Meeting of The Institute of Navigation*, Cambridge, MA, April 2007, pp. 432-443.

[95] Seidelmann, P. K., *Explanatory Supplement to the Astronomical Almanac*, University Science Books, Sausalito CA, 1992.

[96] Hobbs, G. B., Edwards, R. T., and Manchester, R. N., "TEMPO2, a new pulsar-timing package - I. An overview," *Monthly Notices of the Royal Astronomical Society*, Vol. 369, No. 2, June 2006, pp. 655-672.

[97] Nelson, R. A., "Relativistic Effects in Satellite Time and Frequency Transfer and Dissemination," *ITU Handbook on Satellite Time and Frequency Transfer and Dissemination*, International Telecommunication Union, Geneva, 2010, pp. 1-30.

[98] Sheikh, S. I. and Pines, D. J., "Recursive Estimation of Spacecraft Position and Velocity Using X-ray Pulsar Time of Arrival Measurements," *NAVIGATION*, Vol. 53, No. 3, Fall 2006, pp. 149-166.

[99] Bradford, R., Teukolsky, S. A., "Arrival-Time Analysis for a Pulsar in a Binary System," *Astrophysical Journal* Vol. 205, 1976, pp. 580-591.

[100] Anderson, K. D., Pines, D. J., and Sheikh, S. I., "Validation of Pulsar Phase Tracking for Spacecraft Navigation," *Journal of Guidance, Control, and Dynamics*, Vol. 38, No. 10, 2015, pp. 1885-1897.

[101] Durrett, R., *Essentials of Stochastic Processes* (Springer, New York, 1999).

[102] Bar-David, I., "Communication under the Poisson Regime," *IEEE Transactions on Information Theory*, Vol. 15, No. 1, January 1969, pp. 31-37.

[103] Cinlar, E., *Introduction to Stochastic Processes* (Prentice-Hall, Englewood Cliffs, NJ,1975).

[104] Papoulis, A., *Probability, Random Variables, and Stochastic Processes* (McGraw-Hill, New York, 1991)

[105] Rinauro, S., Colonnese, S., and Scarano, G., "Fast near-maximum likelihood phase estimation of X-ray pulsars," *Signal Processing* Vol. 93, No. 1, 2013, pp. 326-331.

[106] Ashby, N. and Golshan, A. R., "Minimum Uncertainties in Position and Velocity Determination using X-ray Photons from Millisecond Pulsars," *Proceedings of the Institute of Navigation 2008 National Technical Meeting*, San Diego, CA, January 2008.

[107] Stephens, S. A. and Thomas, J. B., "Controlled-Root Formulation for Digital Phase-Locked Loops," *IEEE Transactions on Aerospace and Electronic Systems*, Vol. 31, No. 1, January 1995.

[108] Devroye, L., "The Poisson Process", *Non-Uniform Random Variate Generation*, Springer-Verlag, New York, 1986, [online], http://luc.devroye.org/rnbookindex.html [retrieved March 15, 2012].

[109] Koralov, L. V., and Sinai, Y. G. *Theory of Probability and Random Processes*, Second Edition, Springer, New York, 2007

[110] Haykin, S. and Moher, M., *Communications Systems*, Fifth Edition, John Wiley & Sons, Inc., New Jersey, 2009.

[111] Kay, S. M., *Fundamentals of Statistical Signal Processing: Estimation Theory*, Prentice-Hall, New Jersey, 1993, Chap. 3.

[112] Becker, W. and Trumper, J., "The X-ray Luminosity of Rotation-Powered Neutron Stars," *Astronomy and Astrophysics*, Vol. 326, October 1997, pp. 682-691.

[113] Possenti, A., Cerutti, R., Colpi, M., and Mereghetti, S., " Re-examining the X-ray versus Spin-down Luminosity Correlation of Rotation Powered Pulsars," *Astronomy and Astrophysics*, Vol. 387, April 2002, pp. 993-1003.

[114] Becker, W. and Trumper, J., "The X-ray Emission Properties of Millisecond Pulsars," *Astronomy and Astrophysics*, Vol. 341, 1998, pp. 803-819.

[115] Kuiper, L. and Hermsen, W., "X-ray and Gamma-ray Observations of Millisecond Pulsars," *Proceedings of the 4th AGILE Science Workshop "X-ray and Gamma-ray Astrophysics of Galactic Sources"*, Dec. 2003, pp.47-55.

[116] Nicastro, L., Cusumano, G., Lohmer, O., Kramer, M., Kuiper, L., Hermsen, W., Mineo, T., and Becker, W, "BeppoSAX Observation of PSR B1937+21," *Astronomy and Astrophysics*, Vol. 423, 2004, pp. 1065-1072.

[117] Soderstrom, T, *Discrete-time Sochastic Systems*, Springer, London, UK, 2002.

[118] Gamelin, T. W., *Complex Analysis*, Springer, New York, NY, 2001.

[119] Kaplan, E. D., *Understanding GPS Principles and Applications*, Artech House, Boston, 1996.

[120] Vilnrotter, V. A., Hinedi, S., and Kumar R., "Frequency Estimation Techniques for High Dynamic Trajectories," *IEEE Transactions on Aerospace and Electronic Systems*, Vol. 25, No. 4, July 1989, pp. 559-577.

[121] Ward, P., "Performance Comparisons Between FLL, PLL, and a Novel FLL-Assisted-PLL Carrier Tracking Loop Under RF Interference Conditions," *Proceedings of the 11th International Technical Meeting of the Satellite Division of The Institute of Navigation (ION GPS)*, September 1998, Nashville, TN, pp. 783-795.

[122] Gelb, A., *Applied Optimal Estimation*, The M.I.T. Press, Cambridge, MA, 1974.

[123] Gunckel, T. L., "Orbit Determination Using Kalman's Method," *Navigaiton: Journal of the Institute of Navigation*, Vol. 10, No. 3, 1963.

[124] Montenbruck, O. and Gill, E., *Satellite Orbits*, Springer-Verlag, Berlin, 2000.

[125] Vallado, D. A., *Fundamentals of Astrodynamics and Applications*, Second ed., Space Technology Library, Kluwer Academic Publishers, Boston MA, 2001.

[126] Wie, B., *Space Vehicle Dynamics and Control*, American Institute of Aeronautics and Astronautics, Reston VA, 1998.

[127] Brown, R. G. and Hwang, P. Y. C., *Introduction to Random Signals and Applied Kalman Filtering with Matlab Exercises*, Fourth Edition, John Wiley and Sons, New York, 2012.

[128] Chen, G. Y. and Wang, Y. F., "Soft X-ray detectors for pulsar navigation," *IOP Conference Series: Earth and Environmental Science*, vol. 69, June 2017

[129] Guirisato, D., Andersson, H., Huovelin, J., Korpela, S., Lehtolainen, A., Mizohata, K., and Tikkanen, P. O., "Radiation Testing of the XFM X-ray Detector for the Lagrange Mission," *2020 IEEE Nuclear Science Symposium and Medical Imaging Conference (NSS/MIC)*, October 2020, pp. 1-5.

[130] Devore, J. L., *Probability and statistics for engineering and the sciences*, 4th Edition, Belmont:Duxbury Press, 1995.

[131] Toubou, P., Willemenot, E., Foulon, B., and Josselin, V., "Accelerometers for CHAMP, GRACE and GOCE space missions: synergy and evolution," *Bollettino Di Geofisica Teorica Ed Applicata*, Vol. 40, 1999, pp. 321-327.

[132] Beaussier, J. and Mainguy, A. M., "Improvement in the characterization of the Cactus accelerometer through results obtained from an experimental program," *La Recherche Aerospatiale*, August 1977, pp. 255-257.

[133] Bai, Y., Li, Z., Hu, M., Liu, L., Qu, S., Tan, D., Tu, H., Wu, S., Yin, H., Li, H., and Zhou, Z., "Research and Development of Electrostatic Accelerometers for Space Science Missions at HUST," *Sensors (Basel)*, Vol. 17, No. 9, September 2017.

[134] Iess, L. and Asmar, S., "Probing Space-Time in the Solar System: From Cassini to BepiColombo," *International Journal of Modern Physics D*, Vol. 16, No. 12A, 2007, pp. 2117-2126.

[135] Touboul, P., Foulon, B., and Willemenot, E.,"Electrostatic space accelerometers for present and future missions," *Acta Astronautica*, Vol. 45, No. 10, November 1999, pp. 605-617.